UNIAXIAL STRAIN AND HIGH MAGNETIC FIELD INVESTIGATION ON MATERIALS WITH NOVEL ORDER PARAMETERS
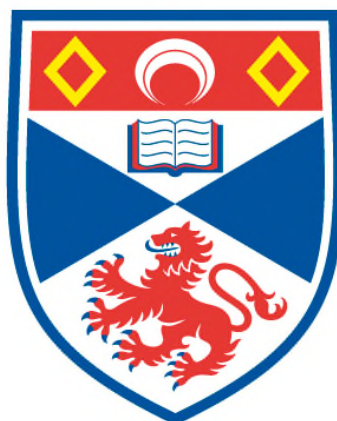
Lishan Zhao

**A Thesis Submitted for the Degree of PhD
at the
University of St Andrews**

2016

Uniaxial Strain and High Magnetic Field Investigation on Materials With Novel Order Parameters
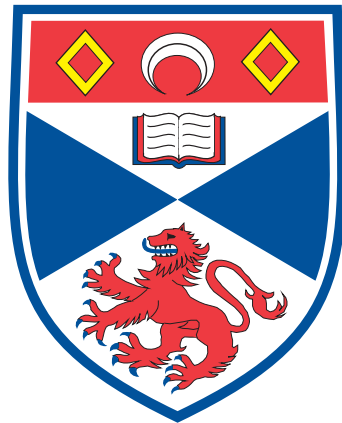
Lishan Zhao

This thesis is submitted in partial fulfilment for the degree of

Doctor of Philosophy at the University of St Andrews

December 2015

Declaration

Candidate's declarations

I, Lishan Zhao, hereby certify that this thesis, which is approximately 50000 words in length, has been written by me, that it is the record of work carried out by me and that it has not been submitted in any previous application for a higher degree.

I was admitted as a research student in September 2011 and as a candidate for the degree of Doctor of Philosophy in September 2011; the higher study for which this is a record was carried out in the University of St Andrews between 2011 and 2015.

Date   *Signature of candidate*

Supervisor's declaration

I hereby certify that the candidate has fulfilled the conditions of the Resolution and Regulations appropriate for the degree of Doctor of Philosophy in the University of St Andrews and that the candidate is qualified to submit this thesis in application for that degree.

Date   *Signature of supervisor*

Permission for publication

In submitting this thesis to the University of St Andrews I understand that I am giving permission for it to be made available for use in accordance with the regulations of the University Library for the time being in force, subject to any copyright vested in the work not being affected thereby. I also understand that the

title and the abstract will be published, and that a copy of the work may be made and supplied to any bona fide library or research worker, that my thesis will be electronically accessible for personal or research use unless exempt by award of an embargo as requested below, and that the library has the right to migrate my thesis into new electronic forms as required to ensure continued access to the thesis. I have obtained any third-party copyright permissions that may be required in order to allow such access and migration, or have requested the appropriate embargo below.

The following is an agreed request by candidate and supervisor regarding the electronic publication of this thesis:

Embargo on both of printed copy and electronic copy for the same fixed period of 6 months on the following ground: publication would preclude future publication.

Date   *Signature of candidate*

Date   *Signature of supervisor*

Abstract

At low temperatures, strongly correlated materials, which typically contain partially filled d- or f-electron shells, often exhibit phases with interesting properties, which may be of both research value and technological significance. The mechanisms of phase formation in them if could be clarified, are believed to be able to provide important insights not only into physics but also into the design of new materials. In this thesis, the experimental study of two strongly correlated materials, Sr_2RuO_4 and $CeAuSb_2$ is presented.

Sr_2RuO_4 is an unconventional superconductor, and a strong candidate for spin-triplet superconductivity. Its potential significance in relation to quantum computing also makes it of great scientific interest. In order to clarify the role of the Van Hove singularity (VHS) in its superconductivity, experimental study has been performed with the recently developed uniaxial strain methods. The experimental results suggest that as the sample is compressed towards the VHS, the transition temperature can be enhanced by a factor of ~ 2.3 whilst the upper critical field can be enhanced by a factor of more than ten. The experimental findings are intriguing and new possibilities are open for future study.

$CeAuSb_2$ is a Kondo lattice system which has been speculated to be close to a quantum critical point. The similarity between some of its low temperature properties and those of a well known quantum critical system $Sr_3Ru_2O_7$ makes it especially interesting. In this thesis, new magnetorestivity and torque magnetometry measurements are used to clarify its low temperature phase diagram, and reveal the strength of its magnetic anisotropy.

Acknowledgements

This thesis presents the results of four years of study, which was carried out mostly in St Andrews, and partially at the Max Planck Institute for Chemical Physics of Solids (MPI-CPfS) in Dresden, Germany. It would not have been possible without the help and support from many people.

First and foremost I would like to express my sincerest thanks to my supervisor, Prof. Andrew P. Mackenzie, who has not only given me the opportunity to explore the physics of strongly correlated materials but also supported me from every aspect. Over the past four years I have greatly benefited from his guidance and from the stimulating environment that he has been leading. I have learnt much from his physical insights, his open-minded spirit and his way of thinking. He also patiently helped me to improve my English language skills. I am also grateful to be given the opportunity to study in the MPI-CPfS during the last year of my PhD.

I want to give special thanks to Dr. Clifford Hicks, who has also offered me guidance over the past four years and supported me in many ways. I learnt many experimental skills from him. I also benefited enormously from the discussions with him and he always left an open door for my various questions. It was his invention of the uniaxial strain apparatus that made my work on Sr_2RuO_4 possible. His participation was also important for my research project on Sr_2RuO_4.

I would like to thank Dr. Alexander Steppke, with whom I closely collaborated on the work of Sr_2RuO_4. He not only contributed much to the project but also helped me improve my experimental skills on low temperature and low noise experiments. My carefulness was also improved through the collaboration with him.

My understanding of strongly correlated materials benefited much from the weekly seminars in St Andrews and those in the MPI-CPfS. I want to take the chance to thank Dr. Chris Hooley, Dr. Frank Kruger, Dr. Jonathan Keeling and Dr. Jean-Philippe Reid, who are working or used to work in St Andrews. I learnt much from them, not only at the seminars but also through informal discussions. The same gratitude is also given to the research fellows in the MPI-CPfS, especially to Dr. Manuel Brando, Dr. Dan Sun, Dr. Markus König, Dr. Elena Hassinger, Dr. Dmitry Sokolov, Dr. Frank Arnold and Dr. Pallavi Kushwaha. I also want to give my thanks to Dr. Andreas Rost, Dr. Alexander Gibbs, Dr. Mayukh Majumder, Dr. Christoph Geibel, Dr. Rodolfo Borzi, and Prof. Santiago Grigera, for the valuable discussions I had with them, which gave me insights in many aspects.

My work was supported by the mechanical and electronics workshops in St Andrews and at the MPI-CPfS in Dresden, and also by the cryogenic technicians in both places. Their work was extremely important for me to make progress with my project and to run my experiments. I thank all of them for their valuable help.

I want to express my special gratitude to Claudia Strohbach at the MPI-CPfS, who offered enormous help to me before and after I moved from St Andrews to Dresden. I also want to give my sincere thanks to Christine Edwards and Julie Massey in St Andrews. As the administrative staff of the CM-CDT, they are warm hearted and their hard work made my life as a PhD student easier in many ways.

My family has been constantly supporting and encouraging me. Their support and love is indispensable to any progress that I have ever made. I also wish to give my special thanks to Qianqian Zhang, who is now my fiancee, for her love and encouragements throughout my PhD. She made my four years study more pleasant.

Contents

Chapter 1

Introduction

Condensed matter physics deals with the physics of matter in which atoms are separated by $\sim 10^{-10}$m, like solids or liquids. In condensed matter physics, a typical question for a given material is why the material, in which all the constituent particles and the interactions between them are known, behaves as it does. For such a question, for all practical purposes one can neglect the nuclear interactions and gravity, and only needs to consider the electrons and atomic nuclei of the system. Theoretically, to describe such a system, one can write down the Schrödinger equation and a well defined Hamiltonian, in which the energy of the system is determined by the kinetic energy and the potential energy of the well known elementary particles, and then try to solve it. However the Coulomb interactions between these particles complicate the problem to such an extent that, even with the most powerful computers, there is still no hope to solve the problem accurately for systems containing substantially more than 10 particles [1], not to mention real systems typically consisting of 10^{20} particles or even more. Useful knowledge is thus always obtained under simplifications and approximations for systems of realistic size.

One example of the progress made under significant simplifications is band theory, which allowed us to understand why some materials are insulators and others are metals, and also greatly benefited the semiconductor industry. It is found to apply not only in nearly free electron systems but also in many systems where

the electron-electron interactions are appreciable. Interestingly the great success of standard band theory is achieved essentially in a non-interacting picture, in which the effects of other electrons on a given electron are either neglected or absorbed in an averaged field. The remarkable yet in some sense surprising success made of this effectively non-interacting theory was explained by Landau in his Fermi liquid theory. He pointed out that under some conditions the low energy eigenstates of the interacting system would have one-to-one correspondence with those of a non-interacting system, therefore, with some modifications the theory for a non-interacting electron system would still apply to an interacting system at low temperatures. The Fermi liquid theory turns out to be so robust that systems that could not be described by it have become especially interesting.

There are also systems in which the non-interacting picture ceases to be valid, for example in some of the so-called strongly correlated electron systems, where the electron-electron interactions are strong and the potential energy is large. (Although it is noted that strong interactions do not necessarily lead to violation of Fermi liquid theory.) When the electron-electron interactions can not be treated in a mean field way, the problem becomes a quantum many body problem with extremely high complexity, and for a given material it is generally too difficult to predict reliably what the ground state should be. The phenomenon that order of some form may spontaneously appear out of the complexity in these complicated systems has been termed 'emergence', which is one of the central topics in modern condensed matter physics research.

The diversity of ordering phenomena in strongly correlated electron systems has prominently advanced our knowledge of condensed matter physics. For example, it has been realised that superconductivity does not have to be *s*-wave, and it is also not necessarily incompatible with magnetism. Studies on transition metal oxides not only have revealed a complex phase diagram, in which the ground state could possibly be superconducting, magnetic or with no long rang order, but also have revealed that the ordered state could be microscopically inhomogeneous. [2] Phases with novel order may arise as a system is tuned towards a quantum critical point by an external non-thermal parameter (e.g. pressure, doping or magnetic field) [3]

and the novel order does not have to belong to the category of superconductivity [4]. The physics involved in these systems is so rich that even after several decades research we may have only uncovered the tip of the iceberg.

Presented in this thesis is the experimental work that I have performed on two materials, Sr_2RuO_4 and $CeAuSb_2$, both of which are strongly correlated electron systems with novel order parameters. Sr_2RuO_4 is a layered perovskite superconductor, which is especially interesting for researchers who care about superconductivity because it has been considered to be a strong candidate for spin-triplet superconductivity. [5] Understanding its superconductivity and clarifying the symmetry of its superconducting order parameter is an important yet unaccomplished task. In my work, I tried to investigate the effects of the Van Hove singularity[1] on its superconducting properties, with the recently developed uniaxial strain methods [6], which will be introduced in Chapter 3. Interesting results have been obtained and will be presented in this thesis. The second material, $CeAuSb_2$, is also a layered material but is a Kondo lattice system, which has been speculated to be close to a quantum critical point. [7] What made it interesting to me is the fact that this material exhibits a novel phase, in which the order parameter is not yet clear, when its low temperature antiferromagnetic order is suppressed by an applied magnetic field parallel to its interlayer direction. From some perspectives, the properties related to the novel phase of $CeAuSb_2$ appear to be reminiscent of those of an extensively studied quantum critical material, $Sr_3Ru_2O_7$. In this thesis, I will show my experimental study on its transport and magnetic properties down to approximately 20 mK and under magnetic fields up to 35 T. Some new physics has been discovered and previous proposals about the physics of $CeAuSb_2$ are questioned.

The arrangement of the thesis is as follows. An introduction to the general background physics is presented in Chapter 2, along with a brief introduction to the two subject materials. The experimental methods are mostly introduced in Chapter 3, with few exceptions that are covered in later chapters. Stressed in this chapter are

---

[1]A Van Hove singularity generally refers to a singularity in the density of states of its derivatives. More discussion of it will be presented in Chapter 4.

uniaxial strain methods, for which some details could not be found elsewhere in literature, and some refrigeration methods, which are generally important for low temperature physics. A detailed description of the work that I have performed on Sr_2RuO_4 is presented in Chapter 4, which includes a comprehensive introduction to the material, the motivation for my work, details of the measurements, the results and some discussion. Chapter 5 describes the work on $CeAuSb_2$ in a format similar to that of Chapter 4. The whose thesis is concluded with a summary of the work on the two subject materials and an outlook for future work, which is given in Chapter 6.

Chapter 2

Background Physics

In this chapter, I will introduce the background physics for the research I have performed on the two subject materials of this dissertation, Sr_2RuO_4 and $CeAuSb_2$. Section 1.1 introduces the basic physics of electrons in solids, beginning with the free electron gas model and ending with problems in strongly correlated electrons systems. Section 1.2 introduces a few microscopic models and phenomenological theories of (continuous) low temperature phase transitions that have been widely used to describe the physics in correlated electron systems. The complexity of the quantum many body problem is emphasised. The complicated and interesting situation related to a quantum critical point is mentioned in the end. Section 1.3 describes emergence phenomena in strongly correlated electron systems and the rich phases that could appear in systems with competing interactions. A brief introduction to the two subject materials is left to the end of this chapter. Longer and more comprehensive introductions to Sr_2RuO_4 and $CeAuSb_2$ will given in Chapter 4 and Chapter 5, respectively.

2.1   Electrons in condensed matter

Since the discovery of electrons (in 1897), they have been regarded crucially important in determining the properties of solids. Actually early models of solids,

like the Drude model and the Sommerfeld model, are almost purely theories of electrons, in which the ions are considered to be much less important [8] [9] When the Drude model was proposed, quantum mechanics was not available yet so it appeared as a classical model which treated the electrons as a classical gas. When the quantum effects of electrons (Pauli's exclusion principle) were taken into account by Sommerfeld in the free electron gas model, and the Maxwell-Boltzmann distribution used in the Drude model was thereby replaced by the Fermi-Dirac distributions, the Sommerfeld model came into being.

The main argument of Sommerfeld's theory is that the ground state of a Fermi gas, when described in momentum space, is formed by electron states that are completely occupied below a certain energy level ε_F (the Fermi level) and are completely unoccupied above ε_F (at zero temperature). Due to Pauli's exclusion principle, only electron states that are within a shell not more than $k_B T$ (or $\mu_B B$) away from the Fermi level can be susceptible to thermal (or magnetic) perturbations. Based on this, a series of important physical quantities, for example the specific heat C_v and the magnetic spin susceptibility χ, can be calculated for a given metal. Agreements between calculations and the measured quantities of many metals [9] proved the considerable success of the Sommerfeld model, given its simplicity and the crude approximations based on which it was constructed. In this theory the electrons are considered to be free and independent of each other, and the relaxation-time of the electrons is assumed to be independent of its position and velocity (the relaxation-time approximation). These approximations are indeed crude and what the more sophisticated theories developed later have done is mainly to reduce the inaccuracy brought by these approximations. [9]

A starting point of such improvements is to begin with a one-electron Schrödinger equation and to try to include the effects of the underlying regular lattice in solids by choosing an appropriate potential U for the Schrödinger equation:

$$-\frac{\hbar^2}{2m}\nabla^2\psi(\mathbf{r}) + U(\mathbf{r})\psi(\mathbf{r}) = \varepsilon\psi(\mathbf{r}) \qquad (2.1)$$

where $\hbar$ is the reduced Planck constant, m is the electrons mass and $\psi(\mathbf{r})$ is the

electron's wave function. (By considering the crystal lattice, the electrons in this problem have been changed from free electrons to Bloch electrons and quantities like the momentum are also changed correspondingly.) Equation 2.1 could be solved by perturbation methods, in for example the nearly free electron regime or in the tight-binding regime. The outcome of this is mainly the formation of energy bands. For real materials, to obtain a realistic band structure, the effects on an given electron of the presence of other electrons often needs to be taken into account and this is normally done with the so-called 'mean field theory'. What it does is to represent the effects of other electrons by an averaged field that alters the potential U. So the key task in finding the desired electronic structure to a great extent is to find an appropriate U and then solve equation 2.1, and eventually one still deals with a single electron problem.

With the help of high performance computers, band theory, which incorporates the ionic potential and the mean-field electron-electron interactions, has made remarkable progress. With it one can often predict whether a given material is a conductor or an insulator. A series of important quantities of a given material, for instance the electrical and the thermal conductivity can be calculated with the knowledge of the electronic dispersion.[9]

Actually the wide range in which this approach turns out to be successful is surprising, because essentially even if an appropriate U can be found the problem is still solved with an effectively independent electron approximation. The effect of other electrons on a given electron is regarded only to alter the ionic potential in a way equivalent to having a smoothly distributed negative charge, and the outcome is merely some modification to the structure of the N-electron wave function comparing with that of non-interacting electrons. However there is no obvious reason why the electron-electron interactions would only have such minor effects to the N-electron wave function, since the inter-electron spacing on average is not necessarily much longer than the interaction distance (the screening length). So how can we explain the surprising success of the results based on the independent electron approximation?

By considering this issue, we are leaving the regime of physics of non-interacting electrons. As we are going to see, electron-electron interactions could indeed have drastic effects on the N-electron wave function and on the equilibrium properties of many real materials, however the remarkable success of the independent electron approximation is not purely a coincidence. The first clue for this was provided by Landau, in the Landau Fermi liquid theory for materials with correlations.

2.2 Correlated electron systems

Correlated electron systems usually refer to those in which Coulomb interactions between electrons cannot be neglected, which are unlike for example alkali metals in which the electrons only have weak interactions and can be considered independent. Comparatively speaking, the electron-electron interactions in systems with d or f electrons (e.g. transition metal oxides and rare earth compounds) are usually more important than in s or p electron systems. The reason is that d and f electrons experience relatively strong ionic potential which tends to restrict them close to the ions and the short distance between electrons then results in strong Coulomb interactions, while in s or p electron systems the conduction electrons are more delocalised due to the relatively weak ionic potential and thus the mutual interaction is relatively weak.

As will be shown more clearly in the following discussion, the problem of a correlated electron system is essentially a complex quantum many body problem which is hopelessly complicated for brute force calculational approaches. In this regard, the Fermi liquid theory is also a good start point to introduce the physics of correlated electron systems, because as a phenomenological theory it can provide us insights on this extremely complicated problem.

2.2.1   Landau Fermi liquid theory and beyond

The Landau Fermi liquid theory was initially proposed for liquid ^{3}He [10] [11] [12] however it has been widely applied to metals with electron-electron interactions. The essence of Landau's theory can be summarised as follows. To deal with an interacting electron system, if we start off with a non-interacting system whose eigenstates are known and slowly (and adiabatically) turn on the interactions between the electrons, then although the eigenstate wavefunctions might be changed comparing with a non-interacting system, at sufficiently low temperatures (close enough to the Fermi surface) there could still be one-to-one correspondence between the new and the original states. This is called the 'adiabatic continuity'.

Due to the one-to-one correspondence mentioned above, the low energy excitations of the correlated system will have the same quantum numbers as the uncorrelated one. The difference is that in a correlated system the low energy excitations are not particle-hole pairs but quasiparticle-quasihole pairs, which reflect the difference in the eigenstate wave-functions. Further analysis predicts that the quantities calculated in the non-interacting picture, like the specific heat C_v, the compressibility κ and the magnetic susceptibility χ, will retain their form in the Fermi liquid theory, although with a renormalisation factor. For example, the specific heat C_v of a Fermi liquid can be expressed as

$$C_v \;=\; \frac{1}{3}\frac{m^\star p_F}{\hbar^3}k_B^2 T \tag{2.2}$$

where $m^\star$ refers to the effective mass of the quasiparticles, $p_F = \hbar k$ where $\hbar$ and k are the reduced Planck's constant and the crystal momentum respectively, k_B is Boltzmann's constant and T refers to temperature. The magnetic susceptibility can be expressed as

$$\chi \;=\; \frac{m^\star p_F}{\pi^2 \hbar}\frac{1}{1+F_0^a}\mu_B^2 \tag{2.3}$$

where μ_B is the Bohr magneton and F_0^a is a Landau parameter. Both C_v and χ are related to the density of states at the Fermi level and when compared with

their counter-parts for a Fermi gas, they are enhanced by a factor of $m^\star/m$ and $\frac{m^\star}{m}\frac{1}{1+F_0^a}$ (m is the free electron mass) respectively.

The predictions of the Landau Fermi liquid theory given above are important, because, since the Landau parameters are the only factors that are needed in this theory and they can be obtained experimentally, one can in principle model a correlated electron system (at low temperatures) by finding a set of parameters experimentally. This is simple and powerful, and in doing so valuable insights can be obtained to understand the low temperature properties of a correlated electron system, which is otherwise too difficult to achieve in brute force calculational approaches. Practically, the basic predictions of the Fermi liquid theory turned out to be so robust that the theory has been successfully applied to explain the low temperature behaviours of a wide series of materials.

Now let us consider the conditions under which this theory works. The concept of quasi-particles/quasi-holes is crucial for the Fermi liquid theory, however it should be noted that these quasi-particles/quasi-holes are only well defined close to the Fermi surface and only have a limited lifetime. Fermi's golden rule [2], the requirement of energy conservation and Pauli's exclusion principle in combination give rise to the following relationship between the quasi-particle scattering rate $1/\tau_\epsilon$ and the energy distance with respect to the Fermi surface [13]:

$$\frac{1}{\tau_\epsilon} \propto g_F^3 \epsilon^2 \tag{2.4}$$

where g_F is the density of states at the Fermi level and ϵ is the energy measured with respect to the Fermi surface. The quadratic relationship between $1/\tau_\epsilon$ and ϵ is the key factor which guarantees that for small enough excitation energy ϵ the quasi-particles are always long lived enough for the interactions to be turned on, because the energy corresponding to the scattering rate ($\propto \epsilon^2$) is always smaller than the excitation energy ϵ itself in the small ϵ limit. If this is true, at least a fraction of the originally non-interacting excited state should remain in the quasiparticle

---

[2] $\frac{1}{\tau_\epsilon} = \frac{2\pi}{\hbar}\sum_f |V_{if}|^2 \delta(\epsilon - \epsilon_f)$, where V_{if} is the scattering matrix element and ϵ is the quasi-particle energy, and i and f indicate the initial and final states respectively.

wavefunction [13] and the elementary excitations of the interacting system can be treated as almost independent quasiparticles. Equilibrium quantities can then be calculated with the quasiparticle spectrum and the density of states. This explains why the independent electron approximation would work in a wide range of materials at low temperatures.

Based on equation 2.4 a typical feature for a Fermi liquid is a T^2 quasi-particle scattering rate. When reflected in resistivity a T^2 dependence is normally seen for a metallic Fermi liquid state.

Things become more interesting when equation 2.4 is unsatisfied. If, for example, the scattering rate is not proportional to ϵ^2 but instead proportional to ϵ (as in the so-called marginal Fermi liquid), there will be no quasiparticles that are long-lived enough to let the interactions be turned on even at low temperatures. The violation of the adiabatic continuity will lead the Fermi liquid theory to fail. This could happen when there are long range interactions that are not screened in the system.

There are real systems in which the standard Fermi liquid scattering rate is not seen. For example, in the normal state of the high T_c cuprate superconductors temperature linear scattering rate was observed in optical transmission study [14]. Another case in which non-Fermi liquid behaviour has been extensively discussed is in the vicinity of a QCP where a continuous phase transition occurs at zero temperature. What is interesting there is not only the non-Fermi liquid behaviour itself but also the possible formation of new phases close to a QCP. This will be discussed later.

2.2.2 Microscopic models for strongly correlated materials

Since the problem in strongly correlated systems is a truly quantum many body problem, whose complexity goes beyond even numerical methods for realistic systems, simplification under certain approximations is needed in order to obtain insights on these systems theoretically. A model that has been broadly studied is

the Hubbard model, which in its unsimplified form appears as [15]

$$\mathcal{H} = -\sum t_{\alpha ij} c^{\dagger}_{\alpha is} c_{\alpha is} + \sum U^{\alpha\beta\gamma\delta}_{ijkl} c^{\dagger}_{\alpha is} c^{\dagger}_{\beta js'} c_{\gamma ks'} c_{\delta ls} \qquad (2.5)$$

where $c^{\dagger}$ (c) is the creation (annihilation) operator, t is the hopping integral, U is the interaction parameter, $s = \uparrow, \downarrow$ is the spin label, Greek letters are band indices, and Latin letters in the subscripts are labels of lattice sites. This Hamiltonian takes into account the kinetic energy (the first term) and the potential energy (the second term) of a multi-band system, and neglects effects like spin orbital coupling. If the second terms is comparable or even larger than the first term, the Coulomb interactions between electrons are strong and we can not treat them as perturbations to an originally uncorrelated system. It is also the second term that makes it extremely difficult to diagonalise the Hamiltonian.

For simplicity, if the system has only one band intersecting with the Fermi level and the interaction energy scale is smaller than the inter-band splitting[3], we can treat the system as a one band system (thus the band indices can be dropped). Assuming the onsite Coulomb interaction is identical for all lattice sites, if we neglect the direct inter-site interactions and the exchanges terms, equation 2.5 can be simplified to

$$\mathcal{H} = -\sum_{ij} t_{ij} c^{\dagger}_{is} c_{js} + U \sum_{i} n_{i,\uparrow} n_{i,\downarrow} \qquad (2.6)$$

in which $n_{is} = c^{\dagger}_{is} c_{is}$ and the meaning of the other symbols is identical to those in equation 2.5. Now only the inter-site hopping terms and the onsite Coulomb interactions remain, which reflect the delocalisation energy and the potential energy respectively. Quantum many body features still remain in this simplified model. It can be simplified further, if for example we only consider the nearest neighbour hopping and assume that the hopping parameter is the same for all atomic sites. The resulted Hamiltonian can be written as [16]

$$\mathcal{H} = -t \sum_{\langle ij \rangle} c^{\dagger}_{is} c_{js} + U \sum_{i} n_{i,\uparrow} n_{i,\downarrow} \qquad (2.7)$$

---

[3]This condition is not always satisfied in systems like rare earth compounds.

where $\langle\rangle$ denotes neatest neighbour terms.

The Hamiltonian expressed by equation 2.7 seems neat and it is essentially controlled by only two parameters if we use a dimensionless parameter U/t and the band filling factor n=N_e/N_{sites}. To obtain this Hamiltonian, as we have seen, a series of simplifications are adopted. As one might expect, there must be some parameter space that escapes our exploration in each step of simplification. However the physics covered by this simplified Hamiltonian is not at all as simple as one might naively imagine. Actually it is far from being completely understood and very rich physics can be learned from it. Indeed it is only completely solved in one dimension [17] and in higher dimensions we have to restrict our analysis to some certain limits.

In the $t \gg U$ limit, the interactions are weak and the kinetic energy is more important. In the opposite limit, i.e. the $U \gg t$ limit, the correlations are strong and the physics is more complicated. To get a flavour of the rich underlying physics in the strong interacting regime, two example models derived from the Hubbard model, the Heisenberg model and the t-J model, will be briefly discussed below.

The first interesting case comes near half filling ($n = 1$). With $n = 1$ since the conduction band is only half filled, by standard band theory one would expect a conductor. However in this case inter-site charge transfer is suppressed because an energy penalty of U has to be paid to enable it which is higher than the energy gain of t. Therefore there will be a energy gap $U - 2zt$ (where z is the coordinate number) that is derived from Coulomb interactions. What one ends up with is an insulator, the well known Mott insulator, which is distinct from band insulators.

Without other considerations the ground state of the Mott insulator would be magnetically highly degenerate since at each site the electron spin has two possible options (up or down). However this degeneracy can be lifted by virtual electron hopping (corresponding to the first term in equation 2.7), which in this case can be treated as a perturbation. Second order perturbation analysis [16] suggests that the electron hopping could lower the energy of the system (by an amount proportional to t^2/U) by aligning the neighbouring spins in an anti-symmetric fashion.

In other words, the ground state of the Mott insulator is an antiferromagnetically ordered state. In doing so, one can also rewrite the effective Hamiltonian by transforming the electron operators into spin operators thereby obtaining the quantum Heisenberg Hamiltonian:

$$\mathcal{H} = \frac{2t^2}{U} \sum_{\langle ij \rangle} \mathbf{S}_i \cdot \mathbf{S}_j + \text{const.} \tag{2.8}$$

where $\mathbf{S}$ is the spin operator with three components and is defined by $\mathbf{S}_i = c_{is}^{\dagger} \sigma_{s,s'} c_{is'}$ where σ is the Pauli spin matrices $\sigma = (\sigma_x, \sigma_y, \sigma_z)$. (In this expression, the i and j are gone over independently in the summation.) With a positive U now it is more evident that an antiferromagnetic ground state is favoured.[4]

The Heisenberg Hamiltonian has been extensively studied to describe the properties of strongly correlated materials like undoped copper-oxide materials (e.g. La_2CuO_4 and YBa_2CuO_6) [18] and frustrated spin systems (e.g. 2D triangular lattice systems) [19]. The rich physics captured by this model, that is related to for example magnetism, superconductivity and metal-insulator transitions, it is still being actively studied at the time of writing.

The Heisenberg Hamiltonian is mostly useful to study the electronic and magnetic properties of strongly correlated materials near half filling, while away from half filling, the $t-J$ model, which can also be derived from the Hubbard model, is found to govern the low energy excitations. The $t - J$ model is obtained by projecting out the doubly occupied states from the Hubbard model, and in a simple and explicit form it can be expressed as [20]

$$\mathcal{H}_{t-J} = \text{const.} - t \sum_{s,\langle ij \rangle} c_{is}^{\dagger} c_{js} + J \sum_{\langle ij \rangle} \left(\mathbf{S}_i \cdot \mathbf{S}_j - \frac{n_i n_j}{4} \right) \tag{2.9}$$

where $J = 4t^2/U$. The last term $n_i n_j/4$ in the second term refers to nearest neighbour density-density interactions, which is often omitted in the literature. Although the $t - J$ model was originally proposed by J. Spałek and coworkers

---

[4]The discussion in this subsection is focused on systems higher than 1D, since in 1D no long range order is permitted due to fluctuations.

[21] [22] to study possible ferromagnetic states in the extremely large U limit, this model has been extensively applied to study materials like doped copper oxide materials and others. The topics that have been discussed include but are not restricted to superconductivity, magnetism and quantum criticality, and thousands of papers related to it have been published.

The Heisenberg model and the $t - J$ model are two example models (derived from the Hubbard model) that have been extensively studied in condensed matter physics research. Although substantial progress has been made on these models and the parent Hubbard model, we are still not anywhere close to forming a complete description of them. Moreover one should remember that the Hubbard model itself is only an effective model in which some interactions (e.g. spin-orbit coupling) are omitted [15], and these interactions are not necessarily always unimportant. In real systems there are often other factors that have to be considered which further complicates the situation. For example, many metallic crystalline materials (e.g. rare earth compounds) contain localised magnetic moments, and electrons at these sites may simultaneously have onsite Coulomb interactions, interactions with the mobile electrons and mutual interactions between them. To describe the physics of these materials, the Anderson lattice model (or the Kondo model) [15] [23] is often applied. Kondo effects (describing the coupling between the localised and the conduction electrons) and Ruderman-Kittel-Kasuya-Yosida (RRKY) interactions (describing the indirect exchange interaction between the localised magnetic moments at different sites) may also have to be taken into account, the balance of which could give much room of variety of the equilibrium properties of these materials.

Overall, there are theoretical models that one can find to describe the physics of correlated electrons and rich information has been obtained by analysing these models, however due to the complexity of the quantum many problem, completely solving any of these models in dimensions higher than 1D is a formidable task that goes beyond the capability of our current theoretical tools. This situation makes phenomenological studies especially important, which will be introduced in the following subsection and the one next.

2.2.3 From classical to quantum phase transitions

An important aspect of research on correlated electron systems is the phenomenological study of phase transitions. In the following I will briefly introduce the basics of phase transitions, from Landau's theory of second order phase transitions to renormalisation group theory and then to quantum phase transitions. The aim here is not to give a comprehensive description of theories of phase transitions, instead it is only to outline the framework of the physics related to (mostly continuous) phase transitions, so one will not fine it much in-depth. For comprehensive and in-depth discussion on this topic, one can refer to, for example, [24] [25] [26] [27] [16]

2.2.3.1 Phases and ordering in condensed matter

Different phases of condensed systems show qualitatively different macroscopic behaviours. They are characterised by different quantities that reflect the degrees of ordering of these systems, which are usually called order parameters (OPs). [25] Examples of order parameters of some typical systems are given in Table 2.1. As one can see from Table 2.1, an order parameter can be a scalar, a vector or a tensor.

System	Transition	Order parameter
Liquid–gas	Condensation/evaporation	Density difference $\Delta\rho = \rho_{\text{liquid}} - \rho_{\text{gas}}$
Binary liquid mixture	Unmixing	Composition difference $\Delta c = c_{\text{coex}}^{(2)} - c_{\text{coex}}^{(1)}$
Nematic liquid	Orientational ordering	$\frac{1}{2}\langle 3\cos^2\theta - 1\rangle$
Quantum liquid	Normal fluid $\leftrightarrow$ superfluid	$\langle\psi\rangle$, ψ = wavefunction
Liquid–solid	Melting/crystallisation	ρ_G, G = reciprocal lattice vector
Magnetic solid	Ferromagnetic (T_{c})	Spontaneous magnetisation M
	Antiferromagnetic (T_{N})	Sublattice magnetisation M_{s}
Solid binary mixture	Unmixing	$\Delta c = c_{\text{coex}}^{(2)} - c_{\text{coex}}^{(1)}$
AB	Sublattice ordering	$\psi = (\Delta c^{\text{II}} - \Delta c^{\text{I}})/2$
Dielectric solid	Ferroelectric (T_{c})	Polarisation P
	Antiferroelectric (T_{N})	Sublattice polarisation P_{s}
Molecular crystal	Orientational ordering	$Y_{lm}(\theta, \phi)$

TABLE 2.1: The order parameters of some typical systems. [27]

The magnitude of an order parameter, which is used to distinguish the phases on opposite sides of a phase transition, is zero in the disordered phase and non-zero in

the ordered one. In general an order parameter is a function of some parameters, for example temperature, pressure or magnetic field. Thermodynamics suggests that ordered phases tend to form at low temperatures. [16] The reason is that at high temperatures, to minimise the thermodynamic potential (e.g. the Helmholtz free energy $F = E - TS$ or the Gibbs free energy $G = E - TS + PV$), the entropy of the system should be maximised, meaning that the system is disordered. At low temperatures though, thermal energy becomes less important and ordered states may form. When the temperature is sufficiently low and the potential energy dominates the low temperature ordered phase usually has a lower symmetry.

As the temperature is lowered, the transition between a disordered phase and an ordered one can be abrupt or continuous. In the former case the first order derivatives of the thermodynamic potential (e.g. the Helmholtz free energy F) will be singular and we say that the transition is of first order. In the latter case, the first order derivatives are not singular however the second order ones might be so, and if at least one of the second order derivatives diverge we say that the transition is of second order. This is the traditional classification of phase transitions. Figure 2.1 illustrates the change of the order parameter at a typical phase transition of the first (left panel) and the second (right panel) order.
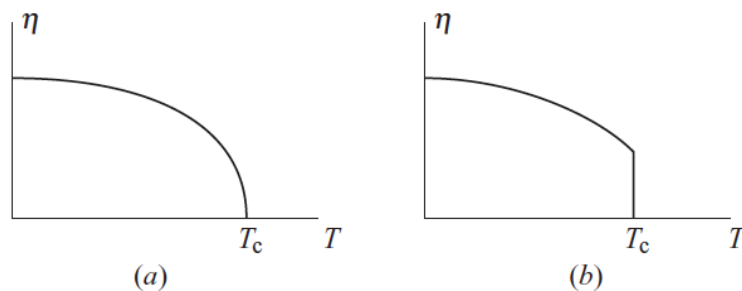
FIGURE 2.1: The order parameter η at a first order (left) and a second order (right) phase transition. At a first order transition there is a discontinuous jump in η while at a second order the change is continuous.

Most known phase transitions are first order [27], however for several decades much attention of condensed matter physicists has been drawn by phase transitions of second order due to the rich physics associated with them, for example critical

phenomena. Theoretical methods (e.g. the renormalisation group theory) developed to understand the second order phase transitions have also been extended to research areas beyond condensed matter physics (e.g. particle physics). In the following I will also mainly discuss second order phase transitions, or continuous phase transitions in modern terminology.

2.2.3.2   Landau's theory of continuous phase transitions

To study continuous phase transitions, L. D. Landau proposed a theory by expanding the free energy F as a function of the order parameter ϕ close to the critical temperature T_c. In a simple case in which the order parameter $\phi(\mathbf{r})$ is spatially homogenous and there are no external fields coupled to $\phi(\mathbf{r})$, the free energy F can be expressed by

$$F = \int \mathrm{d}\mathbf{r} \left[A + B\phi^2(\mathbf{r}) + C\phi^4(\mathbf{r}) \right] \tag{2.10}$$

where A is a constant which is unimportant, B and C are coefficients of the corresponding terms, each of which can be a function of the driving variables like temperature T or pressure P. Purely odd terms of $\phi(\mathbf{r})$ are neglected in this example for symmetry and stability reasons [16]. To satisfy the condition that $\phi(\mathbf{r}) = 0$ above T_c and that $\phi(\mathbf{r}) \neq 0$ below T_c, the coefficient B is supposed to change its sign from positive at $T > T_c$ to negative at $T < T_c$. Figure 2.2 illustrates the free energy F defined by equation 2.10, with A set to be zero and C assumed to be T independent, as a function of the order parameter ϕ above and below T_c. It shows that above T_c the phase is stabilised at $\phi = 0$ while below T_c at $\phi \neq 0$, which satisfies the requirements on ϕ mentioned above.

Linearising B close to T_c leads to $B = a(T - T_c)$ with a being a positive coefficient. With this, one can derive ϕ that corresponds to the minimum of F, which then determines the temperature dependence of ϕ below T_c. [16] In this specific case we have

$$\phi^2 = \frac{a}{2C} \left(T_c - T \right) \tag{2.11}$$
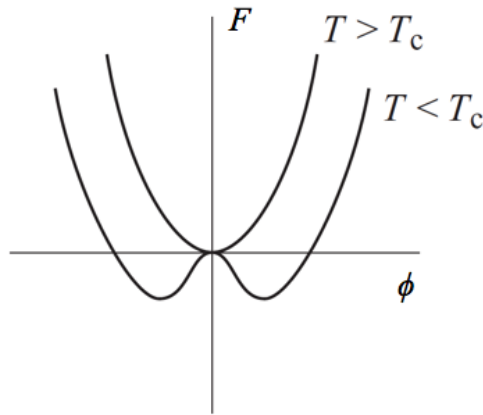
FIGURE 2.2: The free energy F (given by equation 2.10) as a function of the order parameter ϕ above and below T_c. It is seen that above T_c the minimum of F occurs at $\phi = 0$, while below T_c the minimum occurs at $\phi \neq 0$. In fact in this simple case, below T_c the minimum of F occurs at two points symmetric to $\phi = 0$.

Of course we can also verify the continuity of F itself at the transition, and obtain the temperature dependence of, for example, the specific heat c_v and other thermodynamic quantities.

Some of the physical importance of the analysis above is that it enables one to extract important information about the ordering of the system by experimentally studying the temperature dependence of the measurable quantities (e.g. c_v). However what really makes Landau's theory, which is essentially a mean field theory, of significance is its universality and flexibility.

To see the universality, one should note explicitly that Landau's theory of continuous phase transitions is based on expansions close to the critical point and the discussion puts no constraints other than symmetries on the order parameter, therefore the theory provides a unified description of the critical phenomena for all systems sharing the same type of symmetry of the order parameter. Close to the transition the order parameter can be expressed as a function of the reduced temperature $t = (T - T_c)/T_c$ with some exponent ν, and so do other quantities like specific heat and compressibility although the exponents may be different. These exponents are called critical exponents and are independent of the details of the

systems under consideration as long as they share the same symmetries (and dimensionality). Materials sharing the same value of critical exponents belong to the same universality class. More discussion of the universality of phase transitions will be given later.

The flexibility comes from the fact the form of the free energy F is not restricted to that shown in equation 2.10 and that coupling between the order parameter and other degrees of freedom in principle is allowed in the formalism. Actually one can add terms to equation 2.10 depending on the category of the system under consideration, or change the constraints on the coefficients, as long as F is still kept physical (thermodynamic principles should be respected). I will mention two well known examples here.

The first example concerns a ferromagnet. One can add a term containing the coupling between ϕ and the external field $h(\mathbf{r})$, and the free energy will be

$$F = \int d\mathbf{r} \left[B\phi^2(\mathbf{r}) + C\phi^4(\mathbf{r}) + Dh(\mathbf{r})\phi(\mathbf{r}) \right] \qquad (2.12)$$

In equation 2.13 D is a coefficient that reflects the coupling strength. The next step will be looking for ϕ that minimises F and analysing the field dependence of the order parameter at the transition. One can also calculate the susceptibility $\chi = (\partial\phi/\partial h)_{h\to 0}$ as T approaches T_c. The variational principle for the analysis is similar to that used for the simplest form of free energy in equation 2.10, and actually it is general.

The second example concerns the situation when the order parameter is spatially inhomogenous. Suppose that ϕ only varies slowly in space, one can add a single gradient term to the free energy and obtain the following free energy

$$F = \int d^3\mathbf{r} \left[C\phi^2(\mathbf{r}) + D\phi^4(\mathbf{r}) + G[\nabla\phi(\mathbf{r})]^2 \right] \qquad (2.13)$$

This is actually the Ginzburg-Landau functional which has been widely applied to study superconductors (and sometimes to study magnetic domain walls). Minimising this functional leads to the famous Ginzburg–Landau equation, analysis

based on which can provide deep insights on superconductivity.

Introduced above are just two examples in which the free energy has slightly more complicated form than that in equation 2.10. In principle the flexibility of this theory makes it possible to construct the free energy F of a suitable form depending on the situation one is dealing with. For example it can even be extended to describe first order phase transitions by allowing a non-zero ϕ^3 term in F. The wide application of Landau's theory of phase transitions and the insights that could be obtained from it makes it extremely important for studies on condensed matter physics especially on critical phenomena.

2.2.3.3 Beyond the mean field theory

Landau's theory of continuous phase transitions made remarkable success in studies related to the physics close to a continuous phase transition. However it is found that this theory is qualitatively correct but numerically inaccurate, in that the critical exponents predicted by it often contradict experimental results. [26] This is puzzling because close to the transition the order parameter expansion is supposed to work well and to lead to little inaccuracy. Historically this important problem was solved during the 1960s and 1970s, when the renormalisation group theory was developed, which led to much deeper understanding the nature of continuous phase transitions. [28] [29] A detailed description of the renormalisation theory is too much for this short introduction section, however it might be useful to introduce some important knowledge that one can learn from this theory.

(A) Close to a critical point, fluctuations of the order parameter are strong and they may significantly modify the behaviour of the thermodynamic quantities. The effects of fluctuations though, are not included in the standard Landau's theory of continuous phase transitions, which is essentially a mean field theory.

(B) The order parameter fluctuations in space are correlated, and the length scale of the correlation, which is called the correlation length ξ, goes to infinity at the transition. All short range interactions become irrelevant at the transition

and all length scales become equivalent. With ξ being the only important length scale that contributes to the singular behaviours of thermodynamic quantities, one can derive the universal scaling relationship between the critical exponents (e.g. Rushbrooke's identity, Widom's identity and Josephson's identity [16]).

(C) All the singular behaviour close to critical points can be classified into a limited number of universality classes.

(D) The dimensionality of a given system is important for classifying the system's universality class. There exist an upper critical dimension above which mean field theories can give correct results and a lower critical dimension below which fluctuations would forbid any order. A general tendency is that the fluctuations become less important as the dimension increases.

Overall the renormalisation group theory not only explains discrepancies between experiments and predictions of Landau's theory of continuous phase transitions but also provides us deep insights of phase transitions that could not be obtained by mean field analysis. All the discussion above, however, focuses on transitions at finite temperatures. Next we are going to see that fluctuations for quantum phase transitions, which occur at zero temperature, have different properties.

2.2.3.4   Quantum phase transitions

Continuous phase transitions that occur at zero temperature are different from those at finite temperatures. The critical behaviour close to a finite temperature continuous phase transition is governed by spacial order parameter fluctuations. As the temperature is lowered towards zero quantum fluctuations become more and more important. At $T = 0$K, temporal fluctuations are not negligible, and actually spacial and temporal fluctuations become intertwind at 0K. Quantum statistics is needed to describe quantum phase transitions and the physics related to a quantum phase transition can be different from a classical one (e.g. different scaling relationship). The driving force for quantum phase transitions can be non-thermal parameters (e.g. pressure, magnetic filed).

In some real systems there exists an ordered state below a critical temperature T_c, whose T_c can be gradually suppressed by application of pressure or some other non-thermal tuning parameter. When T_c is suppressed to zero we will have a quantum critical point (QCP). A QCP can be reached by tuning the control parameter g towards a critical value g_c while keeping the system at at 0 K, or alternatively if g is fixed at g_c it can also be approached by lowering the temperature. Of course absolute 0 K is never reachable experimentally, however, with modern cooling technology temperatures in the milli-Kelvin range or even lower are obtainable. A generic phase diagram close to a QCP is illustrated in Figure 2.3. The solid curve
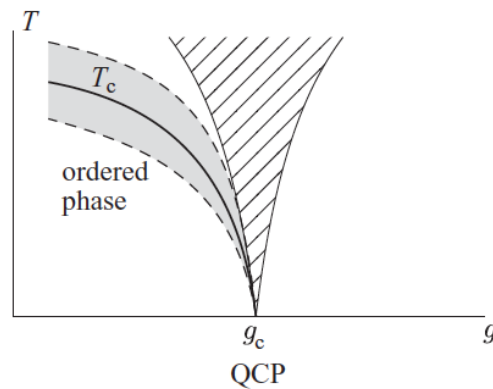
FIGURE 2.3: A general phase diagram in the vicinity of a quantum phase transition. [16]

represents the phase boundary between the ordered and the disordered phase. The grey area indicates the region where the critical behaviour is classical. Between the grey area and area marked by hatching is the usual thermally disordered phase. To the right of the area marked by hatching ($g > g_c$) is called the quantum disordered regime, which is normally characterised by quasi-particle excitations. The area marked by hatching (right above the QCP) is called the quantum critical area. In this area the properties of the system are strongly influenced by quantum fluctuations and unconventional behaviour (e.g. non-Fermi liquid behaviour) may be found in this area.

As we shall see in Chapter 5, physics related to a quantum phase transition/QCP is an extremely complicated topic. While much progress have been made since the 1970s following the pioneering work of J. A. Hertz [31], we are still far from

achieving a complete understanding on quantum phase transitions, as we do for their classical counterparts. Research on this topic has drawn wide attention for several reasons. To obtain a complete and systematic description of quantum phase transitions in their own right is one of them. Studying physics beyond the Fermi liquid picture also contributes to the motivation. Another important motivation is related to the possible formation of phases with novel order in the neighbourhood of a QCP, for example unconventional superconductivity, spin density wave or maybe order of other forms. [3] [4] [32] . The possible formation of novel phases is related to one of the central themes of research on correlated electron systems, 'emergence'. The rich phases and exotic ordering phenomena observed in correlated electron systems will be introduced in the next subsection.

2.3 Phase formation in strongly correlated systems

2.3.1 Exotic ordering phenomena

We have seen in the preceding subsections that the problem in strongly correlated electron systems is in general a quantum many body problem which we cannot solve completely. Even with the powerful renormalisation group methods, the results of calculations are often controversial because in the first place there are often uncertainties in determining which variables/interactions are important and which are not. However, out of this complexity nature provides us with relatively simple phases that form naturally. The rich ordering phenomena observed experimentally have to a large extent driven the research on these systems. Experimental research in recent years has proved that strongly correlated electron systems are really a realm of novel physics and we are still at an early stage in which accumulating experimental data and enriching our knowledge of novel order is still important for the possible formation of a complete understanding in the future.

Taking the transition metal oxides for example, as summarised by E. Dagotto [2], interesting phenomena observed in these systems include but are not restricted to high temperature superconductivity, colossal magnetoresistance (CMR), magnetism of different types, giant proximity effects, inhomogeneity at microscopic scales, possible spin-triplet pairing superconductivity, and possibly simultaneous spin, lattice and orbital ordering. In these materials there are often several competing interactions, too strong for the application of perturbation theory, and the outcome of these competing interactions is often surprising, for example giant responses to small perturbations and formation of different phases under slightly different conditions.

There are also strongly correlated systems with novel order of other categories, for example the Kondo lattice systems (often f electron based), iron based superconductors and many others. Actually the list of materials with novel order is now quite long.

Kondo lattice systems have shown us that physics related to superconductivity, magnetism and quantum criticality may appear in the same system, and physics in all these aspects may be captured by the Hubbard model. These topics and their inter-relationships have largely driven the research on strongly correlated electron systems, including that on the two subject materials of this thesis, Sr_2RuO_4 and $CeAuSb_2$.

2.3.2 Novel order parameters in Sr_2RuO_4 and $CeAuSb_2$

Sr_2RuO_4

Sr_2RuO_4 is a layered perovskite superconductor in which superconductivity was discovered in 1994 [33]. Historically it is the first discovered Cu free perovskite superconductor. It is isostructural to La_2CuO_4, the parent compound of cuprate superconductors $La_{2-x}Ba_xCuO_4$. However despite the structural similarity it shows properties distinct from those of cuprates in both its normal conducting and the

superconducting state. Its normal state is a Fermi liquid state with coherent electrical conduction in all three directions [34], contrasting the mysterious normal state properties of cuprates. The pairing symmetry has been argued to be spin-triplet pairing, which, if true, would make it a superconducting analogue of the superfluid ^{3}He. [5]

However the superconducting order parameter of Sr_2RuO_4 is still not well understood even today. The pairing symmetry of it is still controversial and the pairing mechanism remains unclear. The main research work that I have performed on Sr_2RuO_4, which is presented in Chapter 4 of this thesis, is to test its superconducting order parameter with the newly developed uniaxial strain techniques. As we shall see in Chapter 4, with this new method, new and interesting physics has been discovered, which provides new clues about how to understand the superconducting order parameter.

CeAuSb$_2$

CeAuSb$_2$ also has a layered structure, and it is a $4f$ electrons based Kondo lattice system which orders antiferromagnetically at approximately 6-7 K (depending on the gold site occupancy [35]). By applying a c-axis magnetic field, the Néel temperature T_N can be gradually suppressed. With $B_{\|c} = 5.3 \pm 0.2$ T, T_N can be suppressed to zero which potentially leads to a QCP. [7] Within this magnetically ordered state, there is a line of phase transitions that occur at approximately 2.8 T whose position shows little temperature dependence. Between this phase transition line and the field dependent phase boundary, there is an additional phase, related to which interesting physics has been discovered.

As we shall see in detail in Chapter 5, this additional, novel phase is marked, in resistivity, by a sharp increase at $B_{\|c} \sim 2.8$T and an abrupt decrease at the magnetic phase boundary. Accompanying the sharp changes in resistivity, two metamagnetic transitions are seen in magnetisation, each at one boundary of this novel phase. In heat capacity, the extracted magnetic contribution shows enhancements on both sides of the novel phase. [7] These features are reminiscent of those of $Sr_3Ru_2O_7$, a well known quantum critical system which, if clean enough, possesses

a spin density wave phase masking the position where the putative QCP is supposed to be located [3] [32] [4]. These similarities between two different systems makes it interesting to study whether there is some underlying physics in common.

The situation for $CeAuSb_2$ is different from that for Sr_2RuO_4 in that the former is not an extensively studied material, therefore I still needed to characterise it by carefully measuring, for example, the magnetoresistivity and torque in the presence of applied magnetic fields. A comprehensive introduction to the material, the work I have performed on it and the results obtained from the measurements will be presented in detail in Chapter 5.

Chapter 3

Experimental Methods

This chapter describes the experimental methods that were applied to perform the measurements on Sr_2RuO_4 and $CeAuSb_2$, the results for which are presented in Chapter 4 and Chapter 5 respectively. It contains two main sections. The first section describes the anisotropic strain methods that were applied for the measurements on Sr_2RuO_4, and the second one introduces some methods for refrigeration and a few probes used for the work on $CeAuSb_2$.

3.1 Uniaxial strain methods

Comparing with the uniaxial strain method, the uniaxial stress method is probably better known. The two methods are related but not identical. In this section I will firstly give a short introduction to strain, stress, and their relationship. Following it I will discuss the similarity and the difference between the two methods.

3.1.1 Strain, stress and their relationship

Stress describes the internal force distribution of an object and is defined by the force that acts on a unit area, while strain describes the extent to which an object

is deformed and is a dimensionless rate of the deformation. [36] Microscopically strain defines the relative atomic displacement.

In general, a stress can simultaneously have normal (either tensile or compressive) components caused by normal force components and shear components caused by tangential force components, therefore to properly describe stress one needs a stress tensor σ_{ij} in which $i, j = x, y,$ or z. There are also two types of strains: normal and shear strains, which means that to properly describe strain one also need a tensor (the strain tensor) ε_{ij} with $i, j = x, y,$ or z. In the linear region, the stress tensor is linked to the strain tensor by the generalised Hooke's law:

$$\sigma_{ij} = \sum_{kl} C_{ijkl}\varepsilon_{ij} \tag{3.1}$$

where C is a matrix that contains the elastic constants labelled by i, j, k and l and $i, j, k, l = x, y$ or z. The matrix C in principle can have $3^4 = 81$ components, however for a crystalline material, due to the symmetry properties of the material itself and the symmetrical form of σ_{ij} and ε_{ij}, the number of independent elastic constants is usually much less than that. For example, only six elastic constants are needed for a tetragonal crystal structure. They are usually relabelled by C_{11}, C_{33}, C_{12}, C_{23}, C_{44} and C_{66}, where 1=xx, 2=yy, 3=zz, 4=yz, and 6=xy.[5]. C_{11} and C_{33} describe the axial compression, C_{44} and C_{66} correspond to the shear modulus, and C_{12} and C_{23} describe the dilation on compression, i.e. the perpendicular strain response to an axial stress.

Let us consider the Hooke's law with an example of a homogeneous and isotropic material. In the linear regime it can be expressed by equation 3.2 [38]

---

[5]This is notation is the so called Voigt notation [37], which in principle should contain another term, 5=zx, which is not explicitly included for the case of a tetragonal structure as it is equivalent to 4=yz (x and y is equivalent).

$$\varepsilon_{xx} = \frac{1}{E}\left(\sigma_{xx} - \nu(\sigma_{yy} + \sigma_{zz})\right), \tag{3.2a}$$

$$\varepsilon_{yy} = \frac{1}{E}\left(\sigma_{yy} - \nu(\sigma_{zz} + \sigma_{xx})\right), \tag{3.2b}$$

$$\varepsilon_{zz} = \frac{1}{E}\left(\sigma_{zz} - \nu(\sigma_{xx} + \sigma_{yy})\right), \tag{3.2c}$$

$$\varepsilon_{xy} = \frac{\sigma_{xy}}{G}, \varepsilon_{yz} = \frac{\sigma_{yz}}{G}, \varepsilon_{zx} = \frac{\sigma_{zx}}{G}, \tag{3.2d}$$

in which E is Young's modulus, ν is Poisson's ratio which describes the ratio of transverse over axial strain and $G = \frac{E}{1+\nu}$ is the shear modulus. Alternatively if the strain components are known one can also express the stress components with the strain components.

3.1.2 Uniaxial strain methods vs. uniaxial stress methods

Both strain methods and stress methods can be used to study the equilibrium properties of materials. In linear regime, the non-zero strain and stress gives rise to an elastic energy term, which is given by [39]

$$W = \frac{1}{2}\sum \sigma_{ij}\varepsilon_{ij} = \frac{1}{2}\sum C_{ijkl}\varepsilon_{ij}\varepsilon_{kl} \tag{3.3}$$

Therefore with an applied strain the thermodynamic potential (e.g. the Gibbs free energy) could be changed, and and since all thermodynamic quantities are related to the free energy in some way, its change may lead to drastic change in macroscopic properties of a material especially when there are subtly balanced interactions in the material. An advantage that strain/stress methods possess is that they could have directional resolution, which is helpful for studies on symmetry properties of materials. A well known example of a method with directional resolution is ultrasound attenuation, in which the attenuation rate of ultrasonic waves in different directions can be measured (see e.g. [40]). The uniaxial strain method, developed for the measurements on Sr_2RuO_4 which will be presented next, also shares this advantage.

It should be noted that there is distinction between uniaxial strain methods and uniaxial stress methods. For the former, strain is the tuning parameter and it must be a well controlled quantity, whereas for the latter it is stress that is the well controlled tuning parameter. Technically the key difference between the two methods is, that for uniaxial strain methods the spring constant of the device should be much larger than that of the sample while for stress methods it is the other way round. In uniaxial stress methods, springs are usually used to obtain a well defined stress and to keep the forces exerted on the test sample constant. [41] As we shall see later in the strain device design though, to obtain a well defined uniaxial strain, this way does not work.

One thing I want to emphasise here is that, although (as we shall see later) in the design for our strain device, the displacement imposed on the test sample is uniaxial, the strain of the test sample is not exactly uniaxial. The reason is explained below. For a strain to be uniaxial, by definition, all components other than the uniaxial one have to be zero, which means for example if the loading is along the x direction then only the ε_{11} component in the strain tensor can be non-zero. (Similarly for uniaxial stress only the σ_{11} component can be non-zero.) However due to the Poisson's ratio (refer to equation 3.2), with an uniaxial loading the lateral strain components are not zero, therefore the strain generated by the strain device is anisotropic but not purely uniaxial. That said, what we were mostly interested in for the experimental work on Sr_2RuO_4 was the response to anisotropic lattice distortion, so whether the strain is strictly uniaxial or not is not so important.

3.1.3 Design of the strain device

As we shall see in Chapter 4, the experimental work that I have performed on Sr_2RuO_4 is inspired by the previous work done by C. Hicks *et al.* (see [6]). In their work, the authors achieved up to 0.23% strain with a Sr_2RuO_4 test sample (~ 1.5mm long) using a new type of strain device, which was described in detail in [41]. However the range of strain that was needed for my work was substantially

more than 0.5%. Therefore the strain device used in my work was an upgraded version of that of C. Hicks *et al.*, with improvements also in other aspects, for example the strain measuring scheme.

3.1.3.1 The schematic of the strain device
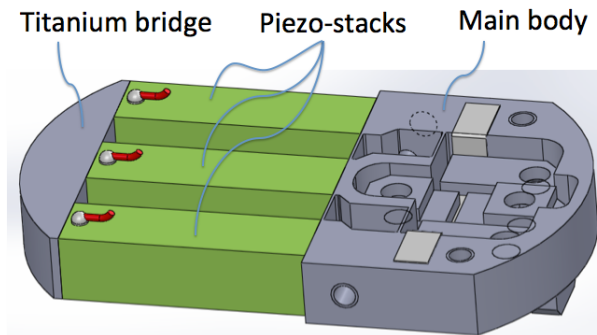
FIGURE 3.1: Schematic view of the strain device. It has three main parts: the main body, three piezo-stacks and a titanium bridge. The red wires from the piezo-stacks represent the electrodes of the stacks. The grey foil on the main body presents a silver foil used to improve thermalisation. For more description, see the main text.

Figure 3.1 shows the schematic view of the upgraded piezo-electric based strain device. The basic principle to generate uniaxial strain is identical to that of the strain device of C. Hicks *et al.*. As shown in Figure 3.1, the device is mainly composed of three parts, i.e. the main body of the device (made by titanium), a small titanium block as a bridge, and three piezo-electric stacks that are glued in parallel between the two former parts using Stycast 2850 epoxy. The central stack is glued to a movable titanium block, which is a part of the main body of the device but is only connected to the outer part through four thin thick foils.[6] The movable block can move in response to the expansion or shrinking of the piezo-stacks. It has a threaded hole, through which a 1 mm thick titanium plate can be firmly fixed to it with a screw. This titanium plate is one sample plate. The other sample plate is fixed opposite to it against the main body of the device, also with a screw. The two ends of the test sample are glued (with Stycast 2850) to the two sample plates respectively.

---

[6]The foils connecting the central titanium block and the outer part of the main body are machined with the same titanium slab through spark erosion.

The piezo-stacks are made of lead zirconium titanate (PZT) (standard commercial product) and they can shrink or expand depending on the sign of the applied electric voltage. When the central stack in Figure 3.1 expands, the central titanium block and the sample plate fixed to it will be pushed towards its opposite counterpart, and the sample, which is fixed between the two sample plates, will be compressed. Based on the same principle, if the central stack shrinks under a negative voltage, the sample will be tensioned. Operation of the outer two stacks also strains the sample, but with opposite sign: expanding the outer stacks tensions the sample, and shrinking them compresses the sample. By combining the deformation of them, one can maximise the strain available to the sample. The deformation of the stacks is uniaxial therefore the test sample will at least have a uniaxial strain component. The sample has to deform following the deformation of the piezo-stacks, because its spring constant is lower than that of the strain device, as explained in [41].

There are a few points worth being mentioned here about the strain device, although they have been pointed out in [41]. (A) In this design, the thermal contraction of the two sets of piezo-stacks cancels each other, thus it does not strain the sample as the device and the sample are cooled down. (B) The thermal contraction of titanium is similar to the lateral thermal contraction of the piezo stacks. This relaxes the mismatch of lateral strain at the ends of the stacks as they are cooled down. (C) The deformation of Stycast 2850 in contact with the sample needs to be considered for the sample strain determination. We will discuss this issue later.

3.1.3.2 Estimate the maximum strain scale

The uniaxial strain of the sample is proportional to the ratio between the uniaxial displacements of the piezo-stacks and the effectively strained sample length. Since the maximum displacement of the piezo-stacks is determined by their rated strain, the maximum strain of the test sample is proportional to the length of the piezo-stacks, provided the rated strain for stacks of different length stays constant.

Since the strain scale needed for my work substantially exceeded that obtained by C. Hicks *et al.*, I tried to enhance the maximum strain by using longer PZT piezo-stacks.

The functional length of the stacks is 18 mm. At room temperature the voltage range recommended by the manufacturer is -30V to 150V, and within this range the total displacement that a piezo-stack can generate is approximately 18 mm×0.15%=0.027 mm=27μm (0.15% is the rated strain of the stacks). So by simultaneously using the two sets of piezo-stacks, in principle, one can obtain total displacement of 54μm at room temperature. However previous work with similar piezo-stacks indicated that, at cryogenic temperatures (e.g.∼1K) the response of the piezo-stacks is only approximately 1/6 of that at room temperature, therefore the maximum low-temperature strain one would expect with the longer stacks might be approximately 54/6=9μm. At cryogenic temperatures though, the voltage limits of the piezo-stacks could be raised at least to -300V and 300V [41], which could at least double the maximum displacements of the piezo-stacks.

The typical length of samples to be strained with the strain device is approximately 1.5 mm, however, as we shall see later, the length over which the sample is really strained (which will be called 'strained length' hereafter) is approximately 600-700μm. It means that the strain applied to the sample (within the strained length) may well exceed 2%, which is significantly higher than that needed for the measurements (approximately 1.0%).

This was the expectation as the strain device was designed, practically however, it was found that the low temperature response of the long stacks applied in my strain device was substantially weaker than that of the relatively short ones applied by C. Hicks *et al.*. The maximum displacement obtained in the experiments was only approximately 7.7μm, which leads to a maximum sample strain of 1.16%. (The effective strain of the sample is actually even lower if one takes in to account the deformation of the Stycast 2850.) Nevertheless, as presented in Chapter 4, this maximum strain turned out to be adequate for the real measurements, and the experiments on the whole were successful.

3.1.3.3 Sample mounting and strain homogeneity

As mentioned earlier the two ends of the test sample should be fixed against the two sample plates respectively. To obtain high strain homogeneity I mounted the sample following the guidance given by C. Hicks *et al.* in [41].
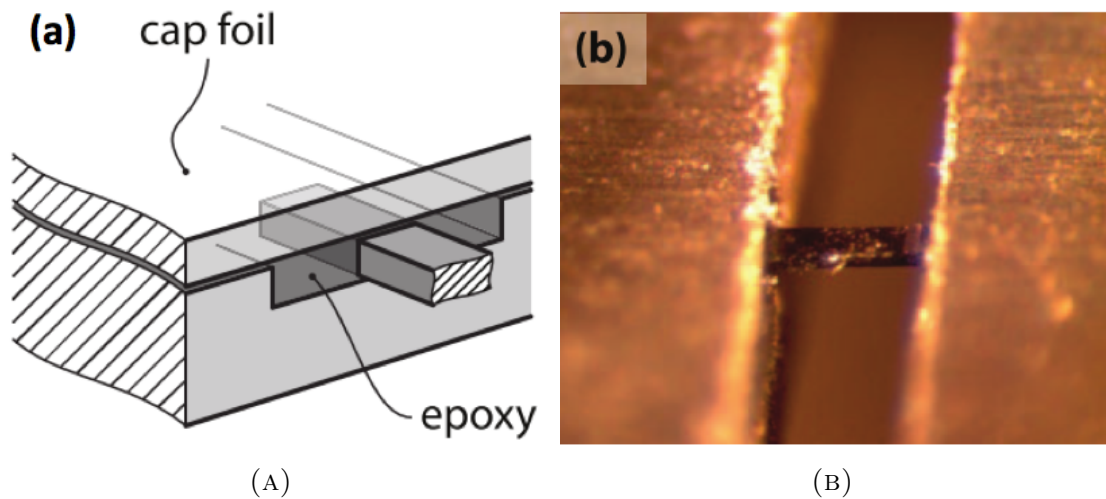
FIGURE 3.2: Illustration for sample mounting. Panel (A) shows in detail how the sample end is fixed and Panel (B) shows a mounted sample in real experimental environment. In both case a type of selected epoxy, Stycast 2850FT, is used to fill the space around the sample end. The cap foils helps to symmetrise the strain distribution, as described in the main text. [41].

The size of a typical sample used in the measurements was approximately 1.5mm long, 0.25mm wide and 0.05mm thick. It was of a rectangular-slab shape with a high aspect ratio. The sample was mounted in a way shown in Figure 3.2a. Each sample plate had an indentation milled in the middle, in which one sample end was placed. The indentation was filled by Stycast 2850, with the sample end embedded in it. (The Young's modulus of the epoxy ($\sim$15Gpa) is only approximately a tenth of that of the sample ($\sim$176GPa) [6].) A 100μm thick titanium cap foil was put on top of the indentation (and above the sample) to symmetrise the strain distribution when the sample was strained. This method of sample mounting was found to be able to improve the strain homogeneity and to stop the sample from buckling as it was strained. The strained length mentioned earlier is the length that is exposed between the two sample plates (see panel (B) of Figure 3.2).

To see exactly how the sample is strained, let us consider the case when it is compressed. As the two sample plates are pushed closer, the epoxy in the indentation also tends to move correspondingly, however the sample, which is in direct contact with it, tends to maintain its shape, therefore the epoxy feels a shear force in opposite direction to its movement. By Newton's third law the sample will experience a compressive force of the same magnitude. The strain distribution in neither the sample nor the epoxy is uniform. As shown in [41], in the epoxy, the displacement is biggest at the edge. In the sample, between the two sample plates the strain is highly homogeneous except close to the epoxy edge, where the strain has strong gradients. In the part of sample sitting in the epoxy, strain decays exponentially on entering the epoxy. There are a few parameters that control the length λ over which strain of the sample decays into the epoxy. For instance $\lambda = \sqrt{Etd/(2C_{66,e})}$, in which E is the Young's modulus, t is the thickness of the sample, d is the epoxy thickness, and $C_{66,e}$ is the shear modulus of the epoxy. Based on the simulation results by C. Hicks *et al.*, I tried to keep the epoxy thickness d above and below the sample both approximately $d = 10\mu$m, which equals to 20% of the thickness of the sample. (The indentation was milled such that its depth was 20μm more than the thickness of the sample.) With such parameters the sample's strain becomes highly homogeneous approximately 100μm beyond the epoxy edge, leaving a region in the middle where the strain is highly homogeneous and this is the region which the real measurements made use of (see Figure 3.3).

3.1.3.4 Strain measurement scheme

To ensure the reliability of the final data analysis it is important to know the strain of the Sr_2RuO_4 sample as accurately as possible. However, practically measuring the sample strain accurately is difficult. We can not infer the displacement of the piezo-stacks by observing the applied voltage because their response is hysteretic. Direct strain measurements are also technically unrealisable because the sample is too small. In the earlier work performed by C. Hicks *et al.*, they tried to measure the sample strain indirectly by attaching a resistive strain gauge between the sample plates. [41] [6] This method is not ideal though, because the resistance of
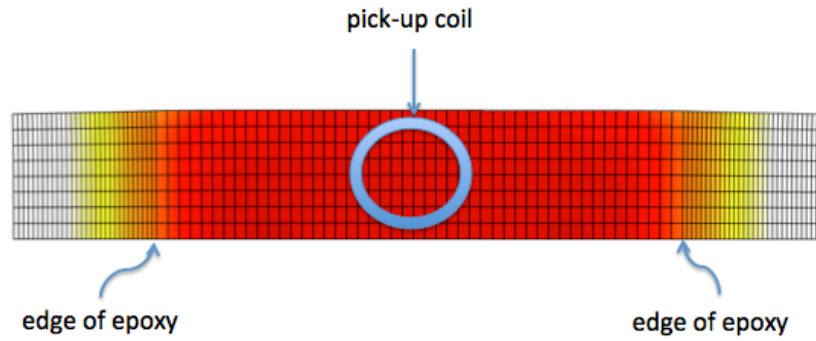
FIGURE 3.3: An illustration for the strain distribution in the sample as it is strained. Darker colour (red) means higher strain. The black grids are the mesh used in finite element analysis. It can be seen that the strain has big gradients close to the edge of epoxy, but is highly homogenous close to the middle of the sample. In real measurements a tiny coil was placed in the middle of the sample to sense the superconducting transition of the sample. The diameter of the coil is slightly smaller than the width of the sample. Therefore the strain of the part of the sample that was utilised in the measurements (i.e. the part underneath the pick-up coil) was homogenous.

the strain gauge is not only temperature dependent but also exhibits noticeable variation between different cool-downs. Moreover, in my work, application of an external magnetic field was needed and the magneto-resistance could make the measured resistance even less reliable. For these reasons I tried an alternative method, a capacitive method, to measure the displacements of the piezo-stacks under an applied voltage, through which we could infer the sample strain.

The basic idea is to make use of the fact that for a plate capacitor, there is one-to-one correspondence between its capacitance C and the distance l_c between the two conducting plates. The displacement caused by the piezo-stacks equals to the distance change between the two sample plates. To measure this distance change, I installed two conductive plates onto the strain device whose movement was in step with that of the two sample plates respectively.

A section view of the capacitive strain gauge is illustrated in Figure 3.4. The capacitor plates were actually two gold electrodes, each deposited on the top surfaces of a Macor[7] plate. The (electrically insulating) Macor plates were then glued to the titanium plug and the socket respectively (with GE varnish). In this way

---

[7]Macor is a type of machinable ceramic, which is electrically insulating and has little thermal contraction.
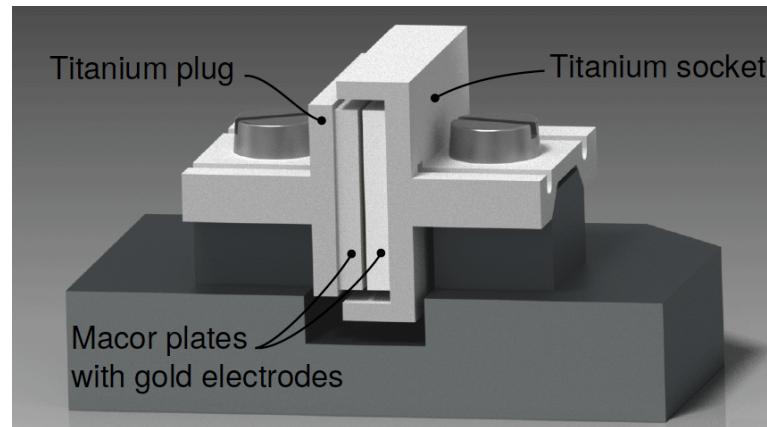
FIGURE 3.4: A sectional view of the capacitive strain gauge. To show clearly the inner structure of the strain gauge, the front wall of the titanium plug is cut away. The substrate was not eventually used

the capacitor electrodes were placed inside a cavity and were electrically partially shielded. Electrical shielding was necessary for the following reason. Due to the limited space available for the capacitive strain gauge, the dimension of the capacitor plates had to be small (approximately 10mm^2), and to leave enough space for the displacement measurements, the spacing between the plates could not be less than a few tens of micron. The consequence was that the capacitance could be no more than a few pF, which experimentally required careful control over the signal-to-noise ratio. (On the other hand, the cavity could not be completely closed because the capacitor electrodes needed to move freely along the axial direction of the piezo-stacks.)

The movement of the capacitor electrodes should be parallel to that of the sample plates and also parallel to that of the piezo-stacks, and the electrodes with the shielding titanium structures should be firmly fixed to the strain device. In order to realise this, a mating structure was designed, as shown in Figure 3.4. Each half of the shielding structure had an extended part perpendicular to it, underneath which there was a concave structure with a flat surface in the middle and two 45° bevels close to the side edges. Correspondingly the substrate had a bulge on each side, mating to the aforementioned concave structure. The substrate in Figure 3.4 is only for illustration (if the electrodes were fixed against the same substrate, they would not be able to move at all); practically the two bulges belonged to the

central titanium block and the main body of the strain device, respectively (refer to Figure 3.1, the bottom side) .

To make electrical connection between the measurement instruments and the capacitor electrodes, and to simultaneously keep the noise level low, I applied a pair of stainless steel coaxial cables to the Macor[8], each of which had a stainless steel core, surrounded by a layer of Teflon (insulating), and an outer jacket made of braided stainless steel. To connect the cores of the coaxial cables to the capacitor electrodes, each Macor plate and the corresponding titanium plug/socket had a thin hole prepared, whose size was just big enough to let the core of the coaxial cable and the inner insulation layer go through. The inner insulation layer was only stripped off close to the very end of the cables, which almost reached the top surfaces of the Macor plates. Gold was deposited into the holes of the Macor plates to make electric connection to the cores of the coaxial cables. To stabilise the coaxial cables, on each half of the strain gauge, the section of the cable close to the Macor plates was placed into the grooves shown in Figure 3.4, and was firmly fixed using Stycast 2850FT. (Only one groove was used on each side as only one coaxial cable was used on each side.) This worked well, and the electric connection between coaxial cables and the capacitor electrodes was stable during the operation.

The other ends of the coaxial cables were connected to an Andeen-Hagerling capacitance bridge (Model 2550A) to measure the capacitance. (The experimental fluctuation of capacitance turned out to be less than 0.1fF, small enough to be neglected for the data analysis.) By monitoring the capacitance, I was able to measure the change in the distance between the capacitor electrodes in real time. (I was only interested in the displacements brought by the piezo-stacks, and not interested in the absolute value of the spacing between the capacitor electrodes.) As one might expect, the sample may be slightly strained during the cool down due to the difference in thermal contraction between the sample and the titanium main body (of a section whose length equals to that of the strained sample length), however the concern could be partially relaxed since the capacitance corresponding to

---

[8]CX-SS25 Coax from CMR direct

zero strain could be known in the first place by direct measurement at room temperature. The displacement-capacitance relationship could be calibrated at room temperature with a Michelson interferometer, so assuming the calibration could be applied to low temperature measurements, one can read the displacement after the sample is cooled down, independent of temperature variation (within several degrees) and magnetic field. As we will see later, even with the room temperature calibration, there is slight uncertainty in determining the strain of the sample accurately, but for my purpose the slight uncertainty does not change the conclusions that one can draw from the measurements.

3.1.3.5 The whole probe

For the measurements on Sr_2RuO_4, low temperatures (as low as sub-Kelvin) and magnetic field were both needed. Therefore I used a dilution refrigerator (Kelvinox 25 from Oxford Instruments), whose base temperature was 50 mK, to generate the low temperature, and a three dimensional (3D) vector magnet ($1T \times 1T \times 9T$) to provide the magnetic field. A short introduction to the refrigeration method will be given later. Now let me introduce first the probe that was needed for the measurements.

During the measurements, the sample should be placed right in the field centre, and at the same time good thermalisation was also important. A probe was designed to fulfil these requirements, which was composed of the strain device, a copper frame, a hollow stainless steel tube, a copper plate and some additional small components. One end of the stainless steel tube was inserted in to the central hole of the copper plate, whose size matched the outer diameter of the tube, and the two were glued together with Stycast 2850FT. The other end of the tube was inserted into a whole of the copper frame, whose dimension was just big enough for the tube, and the two were also then glued with Stycast 2850FT. So the copper frame, the stainless steel tube and the copper plate were glued together, with the stainless steel tube in the middle; they together will be called the frame of the probe. The copper plate had several other holes through which it could be fixed

against the cold plate of the dilution refrigerator with screws. The length of the stainless steel tube was chosen such that when the stain device (with the sample mounted) was installed into the copper frame the sample would be situated in the field centre.
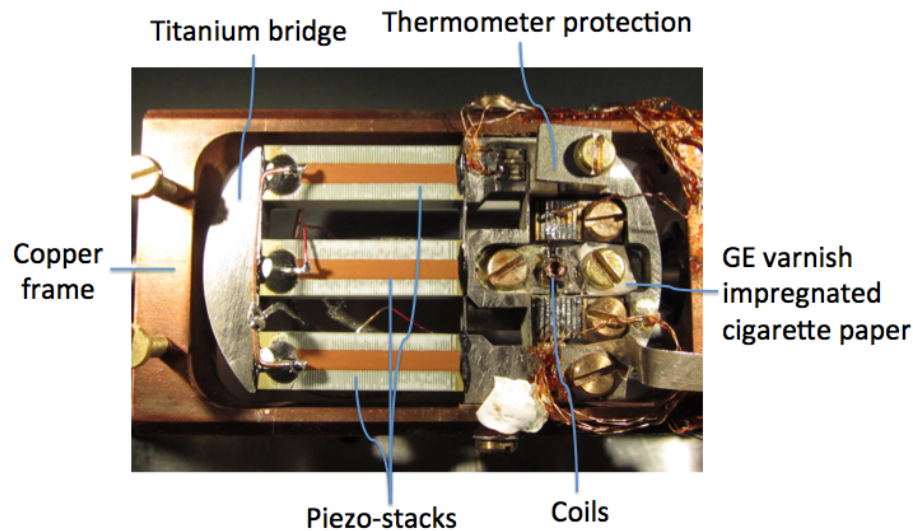
FIGURE 3.5: The real strain device used for the measurements on Sr_2RuO_4, installed into the copper frame of the probe. The strain device was fixed by two screws which could be seen on the top and bottom sides of the frame. The mounted sample is hidden underneath the coils for magnetic susceptibility measurements. A thermometer was installed underneath the thermometer protection structure. The sample plates and the test sample were electrically isolated from the rest of the strain device by two pieces of cigarette paper, as shown around the screws in the middle.

The copper frame was designed to accommodate the strain device and to fix it stably throughout the measurements. The main body of the strain device had a threaded hole (M2) on each side, and the copper frame had two corresponding holes which could let M2 screws go through (see Figure 3.5). To avoid too much lateral deformation of the stain device caused by the screws, they should not be screwed too tightly, however on the other hand, considering the thermal contraction, which was different for copper and titanium, the screws should be screwed relatively tightly because otherwise it would become too loose as the whole probe was cooled down. To achieve the right compromise, I used a crinkle washer for each screw to adjust the tightness, and the result turned out to be satisfactory.

In order to enable temperature sweeps, a heater should be installed on the probe and be thermally connected to the sample. The most convenient option for a heater was a resistor, and ideally a film resistor because bigger contact area means better heat conductance. However the strain device was too limited in size for a film resistor to be installed on, thus eventually I glued a 1000 Ω film resistor onto the copper frame with GE varnish. Then I used a piece of silver foil to enhance the thermal conductance between the copper frame and the strain device. A small thermometer was installed on the strain device (beneath the thermometer protection structure in Figure 3.5) to measure the temperature of the sample. To reduce the errors brought by the thermal time constant between the sample and the thermometer, I placed a piece of silver foil underneath both the thermometer and the sample plates. As we shall see in Chapter 4, the hysteresis in temperature up runs and temperature down runs was very small, which proved the validity of this method.

A 24-way connector and 12 pairs of twisted CuBe wires were used to make electrical connections from the bottom of the probe to the 24-way connector of the dilution refrigerator beside the mixing chamber, which was then linked to the measurement instruments in the laboratory. These wires were what were used to make connections for the thermometer, for the heater and for the coils for magnetic susceptibility measurements. CuBe wires were chosen because of their high thermal resistance.

Two heat sinks (not seen in Figure 3.5) were installed on the copper frame in order to thermalise the measurement wires and coaxial cables. The thermal time constant between the cold plate of the dilution refrigerator and the copper frame was found to be too long for the measurements, therefore I added a silver wire (0.5mm in diameter) to reduce it and the outcome turned to be good. One more thing to stress is that to drive the piezo-stacks at low temperatures, the maximum voltage needed was several hundred Volts, high enough to cause potential danger. Therefore I used a pair of coaxial cables (the same type as that used for capacitance measurements), for which the maximum operating voltage was 10 kV, to make electric connection between the stacks and the output terminals of a bi-polar high

voltage amplifier, that was home designed to drive the piezo-stacks. The high voltage amplifier could provide static voltages between -1000 V and +1000 V, with gain from 1 and 100. Even though coaxial cables were used for safety, all the connecting points (e.g. where connectors were used) were still carefully dealt with at all times during the operation, and the output voltages of the high voltage amplifiers monitored constantly.

3.2 Low temperature generation

The experimental work on Sr_2RuO_4 and $CeAuSb_2$, as presented in Chapter 4 and Chapter 5 respectively, was performed over a wide temperature and magnetic field range, and several different probes were used at different stages. In this section, I will briefly introduce the main pieces of apparatus that were used to generate the desired low temperature and the basic principles for their operation. They are a ^{3}He-^{4}He dilution refrigerator, a ^{4}He flow cryostat and an adiabatic demagnetisation refrigerator (ADR) with paramagnetic salt. For a more comprehensive description of similar apparatus in general and the underlying principles, one can refer to [42]. In this section, the corresponding probes that were used in combination with these apparatus will be also described briefly.

3.2.1 Dilution refrigerators

Dilution refrigerators are mostly important for temperature operation between 5 mK and 1 K. [42] They were used to study both subject materials of this work. For Sr_2RuO_4, a Kelvinox 25 dilution refrigerator was used in combination with a 3D vector magnetic (1T×1T×9T) for susceptibility measurements (under strain), while for $CeAuSb_2$ a top-loading dilution refrigerator was used in combination with a 35 T magnet (made of resistive coils) for resistivity and magnetic torque measurements. The physical principle is identical for the two types of dilution refrigerators and the main difference between the two is the way how the test

sample is mounted. For the former, the ^{3}He-^{4}He mixing chamber is always closed and one needs a probe to host the sample and to make connection to the cold plate of the refrigerator, as in the case described in the last section. In comparison, for the latter, the test sample will be directly placed in the ^{3}He-^{4}He mixing chamber, which gives better thermalisation at extremely low temperatures. The base temperature for a Kelvinox 25 dilution refrigerator is approximately 50 mK, and for the top-loading dilution refrigerator used in this work the base temperature is below 20 mK.

The cooling power of dilution refrigeration comes from the finite solubility of ^{3}He in a ^{3}He-^{4}He mixture even at zero temperature. Figure 3.6 shows the phase diagram of liquid ^{3}He-^{4}He mixture at saturated vapour pressure. Pure ^{4}He becomes a superfluid below 2.177 K, and this transition temperature can be suppressed if a portion of ^{3}He is added. The Lambda line in Figure 3.6 represents the line of
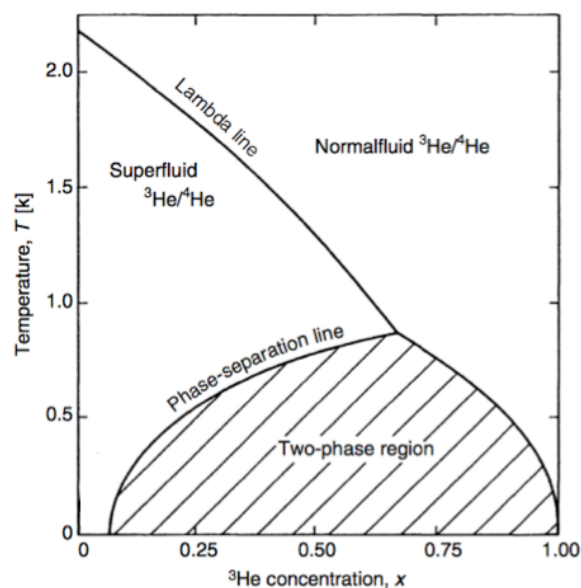
FIGURE 3.6: The phase diagram of liquid ^{3}He-^{4}He mixture at low temperatures. [42]

superfluid transitions. When the ^{3}He portion exceeds 67.5%, the superfluid phase does not form anymore. The corresponding critical temperature at this critical ^{3}He portion is 0.867 K, below which there is a mixed phase region (the hatched region). In this region, the liquid mixture separates into two phases, one ^{3}He rich and the other ^{4}He rich. (The density of the ^{4}He rich phase is slightly higher

so it stays at the bottom.) If one could drive the ^{3}He atoms from the ^{3}He rich phase to the ^{4}He rich phase, one would obtain a dilution process, from which a cooling power can be obtained. Practically this process is indeed realisable and it is actually the key step for dilution refrigeration.

^{3}He atoms are usually pumped out not directly from the mixing chamber, but instead from a chamber called the still, which is above the mixing chamber and is connected to the ^{4}He rich region of it with a thin tube. The temperature of the still is usually 0.7K, at which the vapour pressure of ^{3}He is much higher than that of ^{4}He, therefore in the still almost only ^{3}He evaporates and is pumped away. As the ^{3}He atoms are pumped away from the still, the osmotic pressure difference continuously drives more ^{3}He atoms from the mixing chamber to the still. [42].) On the other side, the ^{3}He atoms that have been pumped out are cooled down again by a liquid ^{4}He bath (at 4.2 K), a ^{4}He refrigerator (at$\sim$1.5 k) and heat exchanges above the mixing chamber, and the re-condensed liquid is injected to the ^{3}He rich phase again. Overall the dilution refrigeration process can be operated continuously.

To control the temperature of the still, usually a certain amount of heating power is applied to it during the operation. The temperature of the mixing chamber can also be controlled by using a heater to balance the cooling power. Usually this is done by PID control.

For non-top-loading dilution refrigerators, the bottom plate of the mixing chamber is usually thick and has several threaded holes to enable the installation of possible probes.

3.2.2 Adiabatic demagnetisation refrigeration

Adiabatic demagnetisation refrigeration is an old cooling method which can be dated back to the 1920s, and it was for a long time the main cooling method to reach temperatures substantially below 1K in laboratories before the dilution refrigeration method came into being. It is physically based on the magneto-caloric

effect. [42] Considering a paramagnetic material, which contains free magnetic ions (meaning that they do not interact with each other) with total angular momentum J (and magnetic moment μ), the total magnetic entropy can be expressed as

$$S \;=\; R\ln(2J+1) \tag{3.4}$$

in which R is the gas constant. If the entropy contributions from the lattice and electrons are much smaller than this term, they can be neglected. Suppose the magnetic moments are pre-aligned by an applied magnetic field H_i, when the magnetic field decreases, the magnetic entropy increases as disorder develops, however in an adiabatic process the total entropy is unchanged, therefore thermal energy is extracted for the magnetic disorder to develop and the temperature will be lowered. (For the same reason when the magnetic field increases the temperature would be raised.) The final temperature will be set only by the initial temperature and the ratio of the initial field over the final field.

Practically there are indeed paramagnetic materials that contain nearly free magnetic moments and have high magnetic entropy density (of the order of joules per mole). With such a material, if the field operation is slow enough so that the system is always maintained in thermal equilibrium, the demagnetisation refrigeration process can be realised. An adiabatic demagnetisation refrigerator can enable temperature sweeps between milli-Kelvin and a few Kelvin, and field sweeps at constant temperatures in this range. To achieve low temperatures, this method usually needs pre-cooling, but at the same time the combination with pre-cooling methods (e.g. by pumping pure ^{4}He) practically could make the temperature range more flexible.

In my work, an ADR was used for the low temperature electrical transport measurements on CeAuSb$_2$, the results of which will be presented in Chapter 5. The ADR was originally designed by Cambridge Magnetic Refrigeration (CMR) but was modified by people who used it previously. It has a low temperature stage (LTS) containing a paramagnetic salt pill. Above this LTS, there is a 1 K pot, which can pre-cool the whole LTS down to approximately 1.7 K by pumping ^{4}He

and thereby reducing the boiling point of liquid ^{4}He. When the pre-cooling process is finished, the LTS can be thermally disconnected from the rest of the apparatus. The probe I used for electrical transport measurements, which will be introduced next, was installed to the bottom of the LTS during the measurements.

The ADR electrical transport probe

The ADR electrical transport probe I used for the measurements on CeAuSb$_2$ was the same one as that used by J. Bruin for his work on Sr$_3$Ru$_2$O$_7$, which has been described in detail in [43]. The probe is shown in Figure 3.7. It has two sample platforms, each of which can accommodate a mounted test sample. The orientation of the mounted sample could be aligned by adjusting the relative hight of the three feet of the sample platform.

FIGURE 3.7: The ADR probe for low temperature transport measurements. It has two sample holders whose orientation can be adjusted by controlling the hight of its three feet. [43]

The probe is made of brass except the central stainless steel tube, which looks like a rod in Figure 3.7. It has 12 pairs of copper wires with polyester coating for measurements, which are heat sunk at the bottom of the probe, as seen in Figure 3.7. For my measurements I only used eight pairs, six for the transport samples and two for a Hall sensor (not seen in Figure 3.7) that was used to monitor the magnetic field. To thermalise the sample, one silver wire was added between the brass plate and the thermometry plate, before the whole probe was sealed.

3.2.3 ^{4}He refrigeration

3.2.3.1 ^{4}He refrigerator

Temperatures down to slightly below 1 K can be obtained by pumping on the vapour of boiling ^{4}He, whose boiling point is 4.2 K at one atmosphere. [42] Economically to reduce the cost, liquid ^{4}He is usually not directly pumped from the bath but is instead led to a small container through a thin tube with relatively high impedance before it is pumped. Some cooling power is inevitably lost to cool down the liquid from 4.2 K to its boiling point at reduced pressure, however approximately a half of it could still be useful to cool down some other object that one wants to cool down. In a dilution refrigeration system or the ADR system introduced in last subsection, this small container is called a 1 K pot which can bring the refrigerator's temperature down to approximately 1.5 K. It can also work independently as a ^{4}He cryostat with a base temperature of roughly 1 K-1.5 K (mainly depending on how well the system it is disconnect from objects at higher temperatures). When it is so, we would have pure ^{4}He refrigeration.

In my work, one ^{4}He refrigerator, which was equipped with a single axis rotator, was used for low temperature transport and torque magnetometry measurements on CeAuSb$_2$, as we shall see in Chapter 5. The mounted CeAuSb$_2$ was installed directly on the plate of the rotator so there was no specially designed probe for the transport measurements. For the torque magnetometry measurements presented in Chapter 5, two capacitive magnetometers were applied, one with a ^{4}He refrigerator, and the other with a dilution refrigerator. The physical principle for them is identical and will be presented in Chapter 5, thus here I skip the introduction to them.

3.2.3.2 ^{4}He flow cryostat

There was a ^{4}He flow cryostat that was used for CeAuSb$_2$ sample characterisation between room temperature and approximately 3.5 K, the cooling principle for which was also pumping on ^{4}He vapour. Its structure was simpler than that of

typical ^{4}He refrigerators though. For this setup, there was a closed sample space containing a little ^{4}He gas as thermal medium, and the cooling power came from flowing cold ^{4}He gas around it, which was injected into the space outside it through a transfer tube of a (movable) liquid ^{4}He dewar and was pumped out with a pump. The temperature was controlled by balancing the cooling power with a heater that was installed not far from the sample.
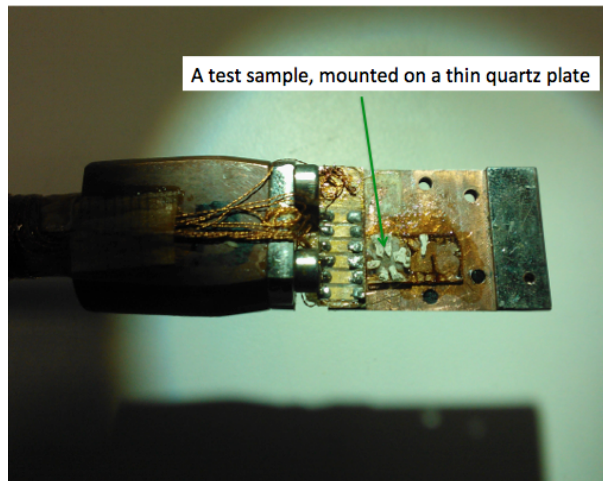
FIGURE 3.8: The probe for sample characterisation in the ^{4}He flow cryostat. One sample (as shown) can be mounted on the side shown and a second one can be mounted on the other side. The dark coloured glued in the figure below and around the quartz plate is GE varnish.

A probe that was designed for sample characterisation with this ^{4}He flow cryostat is shown in Figure 3.8. Two samples in principle could be mounted onto it for the same run, one on the side shown in Figure 3.8, and the second one on the other side. On the other side there was also a thermometer installed, to monitor the temperature of the probe and the samples. For my measurements the signal was usually amplified by room temperature transformers (SR554), before it was directed to lock-in amplifiers.

Chapter 4

Sr_2RuO_4

Sr_2RuO_4, as briefly introduced in Chapter 2, is the first discovered Cu free perovskite superconductor. [33] Through over twenty years research, it, as a strong candidate of p-wave spin triplet superconductivity [5] and a superconducting analogue of the superfluid ^{3}He, has been established as one of the classic unconventional superconductors. Research on Sr_2RuO_4 has not only deepened our understanding of the material itself but also benefited research on other superconductors (e.g. MgB_2 and iron-pnictides, see [44] and Ref. 94, 95 therein). Even so, after over twenty years of intensive research, fundamental questions about its superconductivity remain controversial, for instance the pairing symmetry and the microscopic pairing mechanism. Despite the difficulties, to understand its superconductivity is still of great significance and is still an active research topic.

An important issue in the research on Sr_2RuO_4 is the influence of Van Hove singularities in both its normal state and its superconducting state properties. [45] [46] [6] Of special importance is the γ band Van Hove singularity (γ-VHS), which is approximately 14 meV above the Fermi level as measured by angle resolved photoemission spectroscopy measurements [47]. However, approaching the γ-VHS, although being the closest one to the Fermi level, has been a formidable challenge by any traditional methods (e.g. application of magnetic fields) other than chemical doping, which brings extra effects (e.g. killing the superconductivity) by introducing extrinsic elements to the system. The difficulty comes partially from

the fact that 14 meV corresponds to a magnetic field of approximately 103 T, which is much larger than the highest (static) field that has been achieved up to date (which is 45 T[9]), and partially from the fact that it is difficult to preserve the superconductivity while tuning the system. Therefore it is highly desirable to approach this γ-VHS in a chemically clean way.

Inspired by the recent work of Hicks *et al.* [6] who successfully applied both compressive and tensile strain (in a controllable manner) to Sr_2RuO_4 and investigated the behaviour of T_c around zero strain, we realised the possibility of achieving higher compressive strain and thereby investigating the role of the γ-VHS. Presented in this chapter is my attempt to attack this problem by uniaxial strain techniques. It includes an introduction to both the normal state and the superconducting properties of the material, a more detailed description of the motivation of my research, the experimental work that I have performed and its results, and at the end, the discussion on the meaning of the results. Some future work is also suggested.

4.1 An introduction to Sr_2RuO_4

4.1.1 Basic properties of the strontium ruthenate family

4.1.1.1 Crystal structure

Sr_2RuO_4 belongs to the Ruddlesden-Popper strontium ruthenate series of layered perovskites, whose chemical formula can be generally described as $Sr_{n+1}Ru_nO_{3n+1}$, and is the single layer member with n=1. Its crystal structure is shown in Figure 4.1 (taken from Bruin, Doctoral thesis, 2012), together with that of its bilayer (n=2) counterpart $Sr_3Ru_2O_7$. It crystallizes in the K_2NiF_4-type structure which belongs to the tetragonal space group $I4/mmm$. The lattice constants at 300 K are $a = 3.87073(2)$ Å and $c = 12.7397(1)$ Å respectively, and upon cooling slight

---

[9]in the National High Magnetic Field Laboratory of Florida State University in Tallahassee, the USA

monotonic decrease was observed (e.g. at 15 K $a = 3.86190(3)$ Å and $c = 12.722$ $5(1)$ Å) [48].
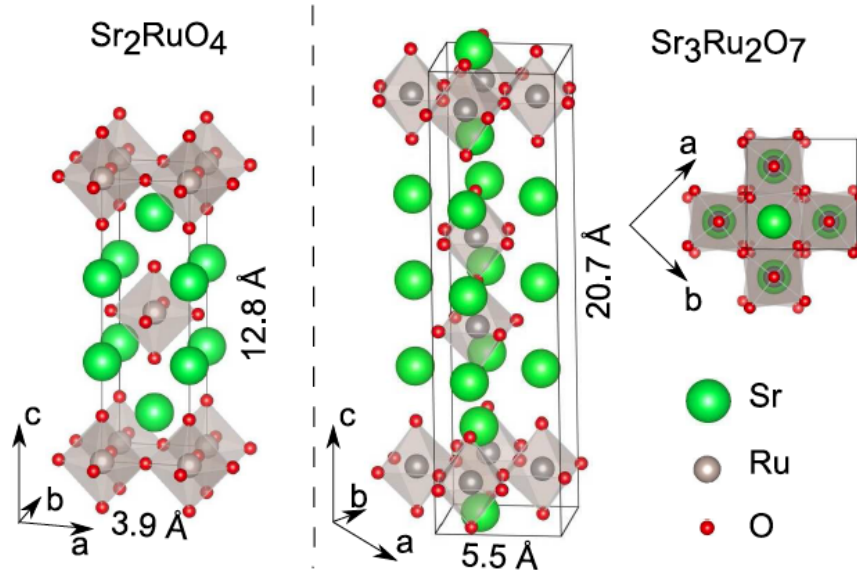
FIGURE 4.1: Crystal Structure of Sr_2RuO_4 and $Sr_3Ru_2O_7$ compounds [43]

In this series of compounds, each ruthenium atom is locally surrounded by 6 oxygen atoms, together forming a RuO_6 octahedron (see in Figure 4.1 the shaded octahedra). These RuO_6 octahedra are the fundamental building blocks, where most of the interesting physics happens. Within the ab plane, each RuO_6 octahedron shares its four lateral corners with its neighbouring RuO_6 octahedra thereby forming a RuO_6 octahedra layer, while along the c-axis, the number of stacked RuO_6 octahedra layers within a unit cell can vary. The number n of the $Sr_{n+1}Ru_nO_{3n+1}$ series actually refers to the number of vertically stacked RuO_6 octahedra layers within a unit cell. The compound in the $n \to \infty$ limit is $SrRuO_3$, the structurally three dimensional member, although there is not really an infinite number of layers in each unit cell (The unit cell is redefined in the case of $SrRuO_3$). The strontium atoms and the oxygen atoms at the vertical vertices of the RuO_6 octahedra are arranged into SrO spacer layers, which sandwich the RuO_6 octahedra layers.

While Sr_2RuO_4 is tetragonal[10], $Sr_3Ru_2O_7$ has lowered symmetry of the orthorhombic Bbcb space group, due to an approximately 6.8° counter rotation of the bilayer

---

[10]At the surface, in plane RuO_6 octahedra rotation was reported to result in lattice distortion [49].

RuO_6 octahedra about the c-axis[11] [50] [51]. This rotation leads to a $\sqrt{2} \times \sqrt{2}$ reconstruction of the unit cell and consequent reconstructions of its electronic structure [52], although the difference between the in plane lattice constants is extremely small ($a = 5.4979(4)$ Å, $b = 5.5008(1)$ Å). Symmetry lowering RuO_6 octahedra rotation (in more complicate manners) has also been reported in the triple-layer member $Sr_4Ru_3O_{10}$, and in the pseudo-cubic $SrRuO_3$, which results in space group symmetry of orthorhombic Pbam [53] and orthorhombic Pbnm [54], respectively.

4.1.1.2 Basic physics of the strontium ruthenate family

The $Sr_{n+1}Ru_nO_{3n+1}$ series is a family of compounds that has been intensively investigated from the perspectives of superconductivity, magnetism, quantum criticality and their interplay. The single-layer member Sr_2RuO_4, which is the subject matter of this work, is an unconventional superconductor with $T_c \leq 1.5K$ [55] and is a promising candidate superconductor for chiral p-wave order [5] [44]. The bilayer member $Sr_3Ru_2O_7$ is an itinerant metamagnet [56] and is interesting mainly because it is a magnetic-field-driven quantum critical system, and in addition when a magnetic field of approximately 8 T is applied along its crystal c-axis, it exhibits a novel phase [32] masking the putative quantum critical point in the temperature-field phase diagram. This novel phase, which has been identified as a spin density wave (SDW) phase recently[12] [4], is believed to be related to the quantum criticality of the system. Therefore $Sr_3Ru_2O_7$ serves as a good material to study phase formation in the vicinity of a quantum critical point. The triple-layer member $Sr_4Ru_3O_{10}$ shows rich magnetism (e.g. out-of-plane ferromagnetism and in-plane metamagnetism), hints of quantum critical fluctuations (e.g. non-quadratic temperature dependence of resistivity near the metamagnetic transition) [57] and striking features in electrical transport (e.g. several step-like drops

---

[11]The rotation angle is weakly temperature dependent (e.g. at 10 K it is approximately 7.8°).

[12]Actually it was discovered that it consists of two sub-phases next to each other with different wave-vectors.

in magnetoresistivity) [58] . The three dimensional member $SrRuO_3$ is a ferromagnet with an ordering temperature of 160 K [59] and a Fermi liquid ground state at low temperatures [60]. It is studied not only for fundamental physics but also for technical applications in, for instance, heterostructure devices. It can also work as an electrode material [61] , and is also studied because of the colossal magnetoresistance discovered in some ferromagnetic perovskites (e.g. (La,Ca)MnO3) [62].

For this family of compounds, as n increases, the electronic structure changes from quasi-two dimensional to three dimensional and at the same time the system empirically evolves towards ferromagnetism [57] [46]. Table 4.1 shows a brief summary of the evolution of the physical structure, the electrical transport anisotropy and the magnetism. The RuO_6 octahedra rotation in these materials is believed to have impact on the physics, in addition to leading to structural symmetry change. [49] [53]

Material	Point group	Space group	ρ_c / ρ_{ab}	Magnetism	SC?
Sr_2RuO_4	tetragonal	$I4/mmm$[48]	4000 (1.5K) [63]	non-magnetic [46]	Yes
$Sr_3Ru_2O_7$	Orthorhombic	Bbcb [51]	300 (0.3K) [64]	MM [56]	No
$Sr_4Ru_3O_{10}$	Orthorhombic	Pbam [53]	30 (2K) [57]	FM (c-axis) [57] MM (ab plane) [57]	No
$SrRuO_3$	Orthorhombic	Pbnm [54]	1.1 (2K)* [65]	FM [59]	No

TABLE 4.1: The Ruddlesden-Popper strontium ruthenate series $Sr_{n+1}Ru_nO_{3n+1}$. SC: Superconducting, MM: metamanetism, FM: ferromagnetism. $\star$: The resistivity anisotropy of $SrRuO_3$ was reported to be not much temperature dependent [65] , in contrast to that of the rest in the table.

4.1.1.3 A brief history of the research on the n=1 member Sr_2RuO_4

Sr_2RuO_4 was reported for the first time as early as 1959 [66], however intensive research on it did not begin until the late nineteen eighties and the early nineteen nineties, after the discovery of high T_c superconductivity in 1986 [67], especially after 1994 when superconductivity of itself was discovered [33]. Before the discovery of superconductivity in it, it was mainly of interest because it is isostructural to the high T_c cuprate superconductors (i.e. those sharing layered perovskite structures) and the possibility that its lattice match to the curates could lead to

technological applications.[13] On the physics side, at that time a key task regarding superconductivity research was to understand the pairing symmetry and the mechanisms responsible for the superconductivity of cuprate superconductors. It was not clear whether Cu is indispensable for high T_c superconductivity in oxides, and in the worldwide search for Cu free perovskite-like superconductors, Sr_2RuO_4 was the first to be discovered, although with a critical temperature. $T_c \leq 1.5K$ [33] [55]

The low superconducting transition temperature did not lower people's interest in Sr_2RuO_4 at all. In contrast, great effort was immediately made following the discovery of its superconductivity, to try to clarify both its normal conducting and superconducting properties, partially with the hope of obtaining useful information to help understand the high T_c superconductors. For the normal state, the high quality single crystals that could be grown enabled experiments that elucidated the nature of its normal state properties and the work of Mackenzie and Bergemann *et al.* convinced the community that the low temperature metallic state can be well described as a quasi-two dimensional Fermi liquid [46] [69], characterised by a set of Landau parameters. This is in contrast to the case of the cuprate superconductors whose normal state contains mysterious pseudo-gap or strange metal phases.

However, the superconducting properties of Sr_2RuO_4 turned out to be extremely interesting yet very difficult to understand. Within a few years of the discovery of superconductivity in Sr_2RuO_4, it was found that its superconductivity is unconventional, which is reflected in, for instance, the extremely high sensitivity to even non-magnetic superconductivities, the evidence for spin-triplet pairing [70] and the evidence for broken time reversal symmetry (from, e.g. muon spin-relaxation measurements [71] and Polar Kerr effect measurements [72] [73]). It was also proposed as a superconducting analogue of the A phase of the spin triplet superfluid ^{3}He [74] and indeed the combination of spin-triplet pairing, broken time reversal symmetry and tetragonal crystal symmetry narrows down the range of possible

---

[13]The early trials of image furnace growth of Sr_2RuO_4, which resulted in pure single crystals based on which superconductivity of it was discovered for the first time, were actually motivated by potential applications from the material science point of view (see [68]).

choices for the superconducting order parameter and favours a chiral *p*-wave order parameter (to be discussed in section 4.1.3.1) which is consistent with the proposal of T. M. Rice and M. Sigrist.

If this chiral *p*-wave order parameter is the correct one to describe the superconducting state of Sr_2RuO_4, it will have even broader importance, because in principle it should then support zero energy Majorana states based on half-quantum flux vortices, which are important for quantum computing (see, e.g. [75]). However, even today we have not found a theory that can explain all the experimental observations, and the full understanding of the order parameter of the superconducting state and the microscopic origin of the superconductivity still has not been achieved and due to its fundamental importance clarifying these issues is still highly desirable. This is still a goal of current research at the time of writing.

It should be acknowledged that, since the aim of this subsection is only to give a brief introduction to the research history of Sr_2RuO_4, not all the important results from the literature have been listed above, and that although complete understanding of the superconducting properties of Sr_2RuO_4 has not been achieved, substantial progress has been made from both the experimental side and the theoretical side.

4.1.2 Normal state properties

In this subsection I will try to briefly summarise the main observations of the normal state properties of Sr_2RuO_4 based on electrical transport, specific heat and magnetic susceptibility measurements, and explain how the normal state Fermi liquid picture was established. Emphasis will be given to aspects of the electronic structure, which are related to the discussion of the Van Hove singularities and the superconductivity.

4.1.2.1 Empirical observation

Electrical conductivity

Sr_2RuO_4 is a highly anisotropic metal which, although isostructural to the cuprate materials, shows very distinctive electrical conductivity. Typical temperature dependence of its DC resistivity is shown in Figure 4.2 [34].
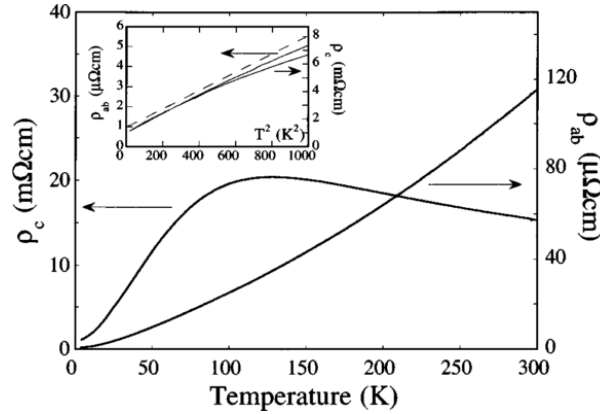
FIGURE 4.2: The temperature dependence of the DC resistivity of Sr_2RuO_4. ρ_c and ρ_{ab} represents the c-axis and in-plane value respectively. The inset shows ρ_c and ρ_{ab} as a function of T^2 below 32 K. [34]

The in-plane resistivity ρ_{ab} shows metallic behaviour upon cooling down to 3 K (the lowest temperature reported in that paper), with a residual resistivity of less than $1\mu\Omega$cm and a residual resistivity ratio (RRR) of approximately 300, which indicates good sample quality. The c-axis resistivity ρ_c however, on cooling first shows a continuous increase until a broad maximum is reached at approximately 130 K and then shows monotonic decrease below it. Both ρ_{ab} and ρ_c show T^2 dependence below approximately 20 K (see the inset), implying a low temperature Fermi liquid state, and at the same time the anisotropy ρ_c/ρ_{ab} (approximately 1400 for the work of Hussey *et al.*) stays essentially temperature independent. This temperature independent anisotropy (which is not seen in the isostructural cuprate materials) suggests coherent electrical conduction in all three directions, which is also implied by the AC optical conductivity measurements where a low frequency Drude peak has been observed to develop below approximately 30 K [76]. Upon cooling the c-axis electrical conductivity therefore experiences a incoherent-coherent crossover.

In summary, below approximately 20 K the electrical conductivity of Sr_2RuO_4 implies a low temperature Fermi liquid state.

Magnetic susceptibility

Unlike the electrical conductivity which shows high anisotropy, the magnetic susceptibility is only very weakly anisotropic and has a weak temperature dependence. Figure 4.3 shows the magnetic susceptibility obtained by Maeno *et al.* with a SQUID [14] magnetometer, between 5 K and 700 K in a magnetic field of 1 T (in the ab-plane and perpendicular to it).
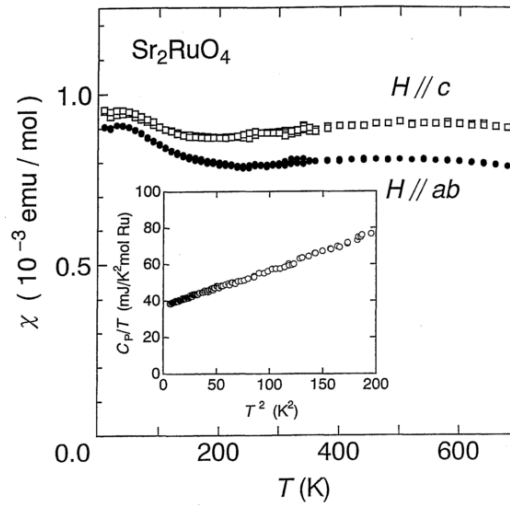
FIGURE 4.3: The magnetic susceptibility of Sr_2RuO_4 between 5 K and 700 K, in a magnetic field of 1 H. It is almost isotropic despite the structural anisotropy and the strong resistive anisotropy. [77]

The diamagnetic part from the core electrons is estimated to be 0.91 $\times 10^{-4}$ emu/-mol and the Van Vleck paramagnetic susceptibility (the orbital part) is estimated to be 1.54 $\times 10^{-4}$ emu/mol. Based on this and the data in Figure 4.3, the total paramagnetic susceptibility is concluded to be dominated by an enhanced Pauli susceptibility χ_0.

Specific heat

The specific heat of Sr_2RuO_4 at low temperatures, as shown in Figure 4.4, can be well described by $C=\gamma T+\beta T^3$, with γ and β estimated (based on the data in

---

[14]short for superconducting quantum interference device

Figure 4.4) to be 37.4 mJ/molK^2 and 0.197 mJ/molK^4, respectively [78]. The two terms, γT and βT^3, are the electronic and the phonon contribution respectively. The obtained γ is higher by a factor of 3-4 than that predicted by calculations based on local density approximation (LDA) [79] [80] and is higher by a factor of approximately 6.5 than that of RuO_2 [81], which is considered to be a normal d-band metal. Such enhancement is evidence for strong electronic correlations. It can also be seen in Figure 4.4 that C/T shows no resolvable difference between 0 T and 14 T.
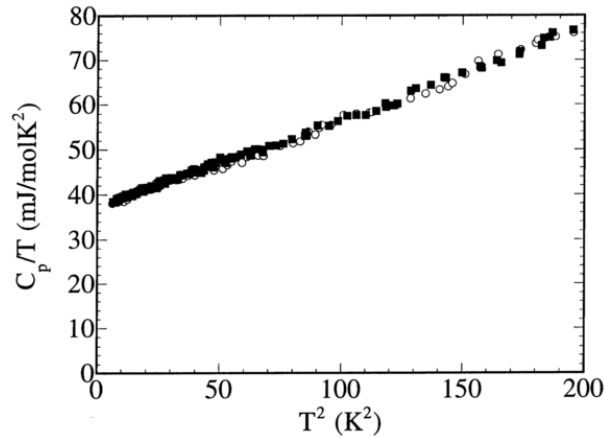
FIGURE 4.4: The specific heat of Sr_2RuO_4 in the form of C/T as a function of T^2, in zero field (filled squares) and 14 T (open circles) applied. [78]

The model which successfully fits the specific heat of Sr_2RuO_4 is consistent with the Fermi liquid theory of a metal and it is another evidence showing that Sr_2RuO_4 has low temperature Fermi liquid state in its normal state.

4.1.2.2 The electronic structure

To understand a metal it is generally important to know and to understand its electronic structure. For Sr_2RuO_4, a good start point to do so is probably to understand it with the general theories of transition metal oxides (TMOs). [82]

Qualitative understanding and calculations

The valence of Sr, Ru and O in Sr_2RuO_4 is expected to be +2, +4, and -2 respectively [46]. Thus for the Ru ions there are 4 electrons left in the 4d shell forming

the Ru^{4+} $4d^4$ electron configuration. The local RuO_6 octahedral crystal field environment splits the $4d$ shell into e_g (two fold, $d_{x^2-y^2}$, $d_{r^2-3z^2}$) and t_{2g} (three fold, d_{xy}, d_{xz}, d_{yz}) subshells, with the corresponding energy level of the latter lower than the former. Thus there are 4 electrons available to fill the Ru^{4+} t_{2g} level which can accommodate at most 6 electrons. We therefore may expect the Fermi surface to consist of pockets derived from these t_{2g} states plus some possible admixture of the oxygen $2p$ orbitals, with weak dispersion along the c-axis since the structure of Sr_2RuO_4 is highly two dimensional.

(A)　(B)　(C)
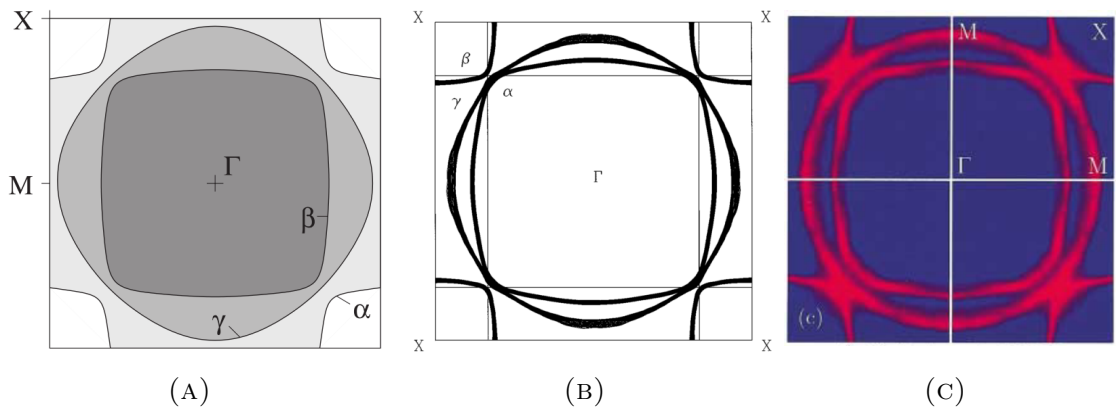
FIGURE 4.5: The Fermi surface of Sr_2RuO_4 [46] [83]

A two dimensional tight binding model based on the analysis given above, but completely ignoring the c-axis dispersion, can produce a qualitative Fermi surface, as shown in Figure 4.5a (taken from [46]), mimicking that from band structure calculations [79] [80] [84] [85] which is shown in Figure 4.5b (adapted from [83]).

From Figure 4.5a and Figure 4.5b, one can see that there are three Fermi surface sheets, labelled α, β and γ respectively following the notation in [69]. The two sheets centred at the Γ point of the Brillouin zone (c.f. Figure 4.5), i.e. the β and γ sheets, are electron-like, while the α sheet centring at the X point is hole-like. The α and β sheets are derived from the quasi-one dimensional Ru d_{xz} and d_{yz} orbitals which have weak hybridisation and from the Fermi surface shape in Figure 4.5 one can still see hints of their quasi-one dimensional origin. In comparison, the γ sheet is derived from the Ru d_{xy} orbitals, which may be extended enough to have overlap with orbitals of their diagonal Ru neighbours, therefore it is to some extent circular (or cylindrical when presented in a three dimensional fashion).

The 2D presentation of the Fermi surface in Figure 4.5 is of course not a complete description. While the basic features of the Fermi surface are commonly reproduced in the calculations, details of the electronic structure were dependent on the specific model employed. On the other hand accurate and quantitive information of the Fermi surface is believed to be of great significance to understand the superconducting properties of Sr_2RuO_4, thus experimentally detecting the Fermi surface is crucial. Fortunately for Sr_2RuO_4 it turns out to be possible to examine the Fermi surface topography to high accuracy through measurements of quantum oscillations and angle-resolved photoemission spectroscopy (ARPES) measurements. The former has especially brought significantly detailed information of the Fermi surface.

Experimental confirmation and refinement

In the following I summarise the main results of these experiments, but without giving detailed introduction to each of these experimental techniques, because these are not the experimental techniques used in this work. In-depth discussion of magnetic quantum oscillation can be found, for instance in [46] [86] [87] and comprehensive descriptions of ARPES can be found in several sources, for example [88] [89] [90].

ARPES is fundamentally based on the photoelectric effect [90]. It measures the energy and the momentum of electrons ejected from the sample under investigation, when a high energy photon beam (e.g. ultra-violet) is incident on the sample surface. The ability to simultaneously measure both the energy and momentum (of the ejected electrons) makes it suitable to directly map out the Fermi surface and also to provide information of the band dispersion. Early ARPES measurements on Sr_2RuO_4 [91] [92] however, showed results qualitatively different from those based on band structure calculations and that on the de Haas-van Alphen (dHvA) effects (to be discussed next) [69], due to issues like surface reconstruction and band reflection [83] [93]. Later Damascelli *et al.* managed to identify and further to overcome these problems, by varying the sample cleaving temperature and the photon energy [83]. The Fermi surface obtained by them is shown in Figure 4.5c,

where three Fermi surface sheets are clearly seen in comparison with the other two panels of Figure 4.5. The apparent touch of the γ and the β band is not real and is due to residual surface states and folded bands. The Fermi surface in Figure 4.5c agrees with that from calculations and that from the next-discussed dHvA measurements.

Central determination of the Fermi surface topology of Sr_2RuO_4 came from measurements of magnetic quantum oscillations, based on for instance angle-dependent magnetoresistance oscillations (AMRO), the dHvA effect, and microwave absorption effect [46]. In the presence of magnetic fields, the energy levels of moving charge carriers are quantised into discrete Landau levels. When these Landau levels are driven across the Fermi level, the periodic change of the density of states at the Fermi level will results in oscillations in observable quantities like conductivity (or equivalently resistivity), magnetisation and specific heat [86]. The oscillations in conductivity are usually called Shubnikov-de Haas effects and those in magnetisation usually called de Haas-van Alphen (dHvA) effects.

A typical dHvA signal measured by torque magnetometry is shown in Figure 4.6a [94] and the typical frequency spectrum is shown in Figure 4.6b. In Figure
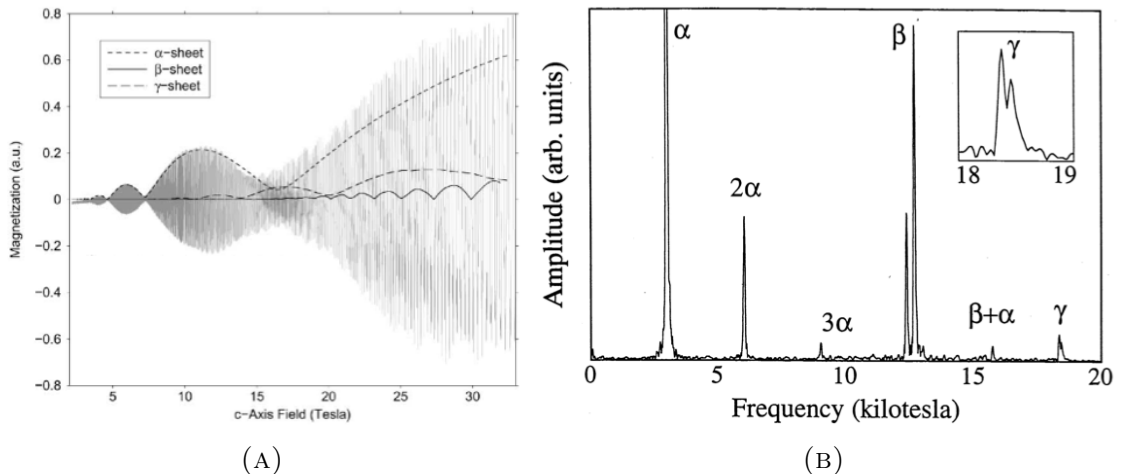
FIGURE 4.6: (A) Typical dHvA signal of Sr_2RuO_4 based on torque magnetometry measurements at 30 mK with the field applied at 4.53° off the c-axis. The black lines indicate the magnitude given by the three fundamental frequencies corresponding to the three Fermi surface sheets. [94] (B) Typical dHvA frequency spectrum of Sr_2RuO_4 [78]. Not only the three fundamental frequencies but also their harmonics are resolved. The splitting of the peak of the β sheet and the γ sheet (the inset) is due to the Fermi surface corrugation.

4.6b the peaks of the three fundamental frequencies are clearly distinguishable, corresponding to the three Fermi surface sheets α, β and γ, and in addition the harmonics and some fine features are visible, for example the splitting of β and γ which corresponds to the Fermi surface corrugation along the c-axis. The dHvA measurements at a series of field angles between the (001) and the (110) directions together with the AMRO measurements generated very detailed information of the Fermi surface topology (both in-plane and out-of-plane), with the help of the Fermi surface parameterisation methods developed by Bergemann *et al.* [46].

Fermi surface reconstruction

To accurately parameterise the Fermi surface geometry sheet-by-sheet, Bergemann *et al.* performed a cylindrical harmonic expansion on the local Fermi wave-vector of all the three Fermi-surface-sheet cylinders:

$$k_F\left(\phi, \kappa_Z\right) \;=\; \sum_{\mu,\nu \,\geq 0} k_{\mu,\nu}\cos\nu\kappa_Z \times \left\{ \begin{array}{ll} \sin\mu\phi & \mu \bmod 4 \equiv 0 \\ \cos\mu\phi & \mu \bmod 4 \equiv 2 \end{array} \right. \tag{4.1}$$

where $\kappa_z = ck_z/2$ with c being the height of the tetragonal unit cell, and ϕ is the azimuthal angle of $\boldsymbol{k}$ in the cylindrical coordinate system in k space. μ and ν are nonnegative integers.

For the β and γ sheets (centred on the Γ line), the four fold rotational symmetry and the mirror symmetry of the Brillouin zone only allow nonzero $k_{\mu,\,\nu}$ for μ being multiples of 4. Similarly for the α sheet the two fold symmetry, the mirror symmetry and the screw symmetry together only allows nonzero $k_{\mu,\,\nu}$ either for μ being multiples of 4 and ν even, or for $\mu \bmod 4 \equiv 2$ and ν odd.

Analysis of the dHvA and AMRO data, with the aforementioned cylindrical harmonic expansion and in addition an anomalous spin-splitting model (where linearly field dependent corrections were introduced to the warping parameters $k_{\mu,\,\nu}$), yielded a set of Fermi surface warping parameters, which are summaried in Table 4.2. These parameters are crucial to understand the c-axis dispersion and also form the basis of a full Fermi surface reconstruction, the results of which is shown in Figure 4.7. This model Fermi surface can quantitively reproduce all the dHvA amplitudes and moreover agrees with results of the resistivity measurements (e.g.
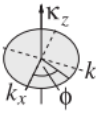
	k_{00}	k_{40}	k_{01}	k_{02}	k_{21}	k_{41}	k_{42}
α	304	−10	—	0.31	1.3	—	−1.0
β	622	−45	3.8	small	—	−0.6	small
γ	753	small	small	0.53	—	small	0.5

TABLE 4.2: The warping parameters of all three Fermi surface sheets of Sr_2RuO_4, in units of 107 m^{-1}. In the first row the corresponding corrugation of $k_{\mu,\nu}$ is illustrated. The long dash (not the minus sign), if appears, means that the according $k_{\mu,\nu}$ is forbidden for symmetry reasons. [46]
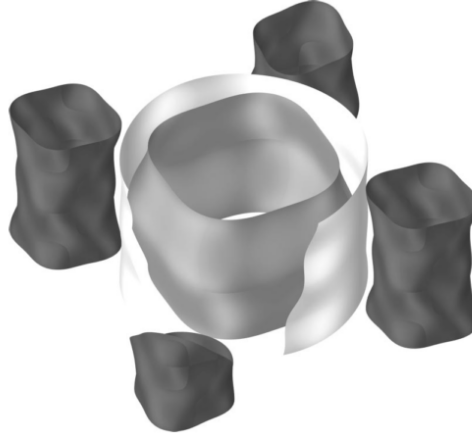
FIGURE 4.7: 3D presentation of the Fermi surface of Sr_2RuO_4, reconstructed based on the parameters in Table 4.2. For clarity the ripples along the c-axis are exaggerated by a factor of 15. The four dark coloured cylinders in the corners, the innermost cylinder and the one in-between shows the α, β and γ sheet, respectively. The latter two have been cut out for clearer illustration of the c-axis corrugation. [5]

resistivity anisotropy and the AMRO pattern [46]).

The measured dHvA frequencies, with uncertainties of 1%, are 3.04 kT, 12.77 kT, and 18.66 kT for the α, β and γ sheet, respectively, which only deviate from those of Mackenzie [69] by 0.3-0.8%. The extracted thermodynamic cyclotron masses (by Bergemann *et al.*), in units of the bare electron mass m_e, are $m_\alpha^\star = 3.3$, $m_\beta^\star = 7.0$, and $m_\gamma^\star = 16$, respectively, with uncertainties of 5%. In comparison the band masses for the three Fermi surface sheets are 1.1, 2.0, 2.9, respectively.

4.1.3 Superconducting properties

4.1.3.1 Order parameters for spin triplet pairing

Before discussing the detailed evidence for unconventional superconductivity in Sr_2RuO_4, it is necessary to briefly introduce some background physics about superconductivity, especially about spin singlet and triplet pairing and the corresponding order parameters.

For a conventional metal, according to the theory of Bardeen, Cooper and Schrieffer (the BCS theory), if there is any attractive interaction between the electrons at sufficiently low temperatures the Fermi liquid state is unstable to the formation of a coherent state consisting of paired electrons (i.e. the Cooper pairs). [95] The conventional attractive interaction is from electron-phonon coupling, which leads to Cooper pairs formed by electrons of opposite spins, whose total spin is $S=0$ (singlet) and orbital angular momentum is $L=0$ (s-wave). Accordingly the gap function $\Delta(\boldsymbol{k})$, which serves as the order parameter of the superconducting state, has a uniform sign of phase in k space, independent of the direction of the momentum vector $\boldsymbol{k}$ (although the magnitude of Δ may vary at different $\boldsymbol{k}$). Superconductors of this kind are called conventional superconductors or s-wave superconductors. However there could also be attractive interactions of other kinds which may lead to different gap functions with different symmetries; superconductivity with non-s-wave symmetry is called unconventional. The principle of understanding the symmetry of the Cooper pair wave-function is that, required by the anti-commuting relations of fermions, if the spin part of the pairing function is antisymmetric (S=0, spin singlet), the orbital part should be symmetric with $L=0$ (s-wave), 2 (d-wave) or other even numbers, while if the spin part is symmetric (S=1, spin triplet), the orbital part should be antisymmetric with $L=1$ (p-wave), 3 (f-wave) or other odd numbers.[15]

---

[15]In solids L and S are not necessarily good quantum numbers, especially when there is for instance strong spin-orbit coupling in presence, however this notation is generally used in the literature anyhow.

Different from case in the conventional superconductors, the gap function of unconventional superconductors does not have a uniform phase in $\boldsymbol{k}$ space, instead the summation of $\Delta(\boldsymbol{k})$ over all possible $\boldsymbol{k}$ equals to zero. It means that in contrast to conventional superconductors, the gap function could be destroyed by elastic scattering around the Fermi surface, due to for example non-magnetic disorder. As mentioned, Sr_2RuO_4 is of this kind, and as will be discussed there is good evidence indicating that it might even a spin-triplet superconductor with chiral p-wave order.

When one deals with the gap function of a triplet superconductor, the spin-degrees-of-freedom needs to be taken into account. Following the idea of R. Balian and N. R. Werthamer [96], if one starts off with a pair interaction potential that includes both parallel and anti-parallel spins and try to minimise the free energy $F \equiv <\mathcal{H}> -TS$, where $\mathcal{H}$, T and S refers to the Hamiltonian, the temperature and the entropy of the system respectively, one would end up with the following gap equation which is very similar to the s-wave case but is a 2×2 matrix:

$$\Delta^{\boldsymbol{k}} = -\frac{1}{2}\sum_{k'} V_{\boldsymbol{k},\boldsymbol{k'}}(\Delta^{\boldsymbol{k'}}/E_{\boldsymbol{k'}})tanh\frac{1}{2}\beta E_{\boldsymbol{k'}} \tag{4.2}$$

where $V_{\boldsymbol{k},\boldsymbol{k'}}$ is the pair interaction, $\beta = 1/k_B T$ with k_B being the Boltzmann constant, and $E_{\boldsymbol{k'}}$ satisfies $E_{\boldsymbol{k'}}^2 \equiv \epsilon_{\boldsymbol{k'}}^2 + \Delta_{\boldsymbol{k'}}^2$ with $\epsilon_{\boldsymbol{k'}}$ being the kinetic energy measured with respect to the Fermi energy.

R. Balian and N. R. Werthamer found a type of solution for Equation 4.2 and further introduced the so-called d-vector to express the gap function in a more compact and convenient way[16]

$$\Delta_0^{\boldsymbol{k}} = \begin{pmatrix} \Delta_{\uparrow\uparrow}(\boldsymbol{k}) & \Delta_{\uparrow\downarrow}(\boldsymbol{k}) \\ \Delta_{\uparrow\downarrow}(\boldsymbol{k}) & \Delta_{\downarrow\downarrow}(\boldsymbol{k}) \end{pmatrix} = \begin{pmatrix} -d_x(\boldsymbol{k}) + id_y(\boldsymbol{k}) & d_z(\boldsymbol{k}) \\ d_z(\boldsymbol{k}) & d_x(\boldsymbol{k}) + id_y(\boldsymbol{k}) \end{pmatrix} \tag{4.3}$$

---

[16]Equation 4.3 is actually from the notation of [44], which originated from the work of R. Balian and N. R. Werthamer.

With the d-vector $\boldsymbol{d}(\boldsymbol{k}) = (d_x(\boldsymbol{k}), d_y(\boldsymbol{k}), d_z(\boldsymbol{k}))$, the gap function in Equation 4.3 can be rewritten as

$$\Delta_{\sigma\sigma'}(\boldsymbol{k}) = i\left[(\boldsymbol{d}(\boldsymbol{k}) \cdot \sigma)\sigma_y\right]_{\sigma\sigma'} \tag{4.4}$$

where σ is the Pauli spin matrixes $\sigma = (\sigma_x, \sigma_y, \sigma_z)$. It is worth noticing that for a spin singlet superconductor only the off-diagonal terms in equation 4.3 are allowed to be non-zero, whereas for a triplet one the diagonal terms can also be non-zero.

The convenience of applying the d-vector is that, while having included all the information of the 2×2 gap function matrix, it transforms like a vector under spin rotations. The direction of the total spin of a Cooper pair is represented by the direction that is perpendicular to $\boldsymbol{d}(\boldsymbol{k})$, and the magnitude of the gap function magnitude can be evaluated by $\boldsymbol{d}(\boldsymbol{k})$:

$$|\Delta(\boldsymbol{k})|^2 = \frac{1}{2}tr\left(\Delta(\boldsymbol{k})\Delta(\boldsymbol{k})^\dagger\right) = |d(\boldsymbol{k}) \cdot d(\boldsymbol{k})^\star|^2 \pm |d(\boldsymbol{k}) \times d(\boldsymbol{k})^\star|^2 \tag{4.5}$$

If $|d(\boldsymbol{k}) \times d(\boldsymbol{k})^\star| = 0$ there is only one energy gap for the Cooper pairs and this case is called unitary, while if $|d(\boldsymbol{k}) \times d(\boldsymbol{k})^\star| \neq 0$, there could be two distinct gaps and it is called non-unitary. In the latter case, which is only possible for spin triplet pairing, intrinsic spin polarisation is expected since $|\Delta_{\uparrow\uparrow}(\boldsymbol{k})|^2 - |\Delta_{\downarrow\downarrow}(\boldsymbol{k})|^2 = i2[d(\boldsymbol{k}) \times d(\boldsymbol{k})^\star]_z \neq 0$.

The d-vector has been applied to describe the order parameters of the superfluid A, B and A1[17] phases of ^{3}He. [97] However, ^{3}He, although an excellent example of spin triplet pairing, is a superfluid rather than a superconductor, and in addition is isotropic with no constraint of crystalline lattices. Therefore searching for a superconducting analog of it in a crystalline solid has been an interesting topic. Sr_2RuO_4 is a strong candidate for spin triplet superconductivity based on a highly two dimensional metallic state. However, the possible d-vectors that can satisfy triplet pairing under tetragonal crystalline symmetry (neglecting the spin-orbit coupling) are not unique (see Table 4.3), and the final determination of the order parameter and a theory that can explain all the experimental observations has not been achieved yet.

---

[17]The A1 phase only exists in the presence of a magnetic field.

Unitary states $\mathbf{d}/\Delta_0$	Δ/Δ_0	Node	Time-reversal symmetry	^{3}He
$\hat{\mathbf{x}}k_x + \hat{\mathbf{y}}k_y$	$\sqrt{k_x^2 + k_y^2}$			BW
$\hat{\mathbf{x}}k_y - \hat{\mathbf{y}}k_x$	$\sqrt{k_x^2 + k_y^2}$			
$\hat{\mathbf{x}}k_x - \hat{\mathbf{y}}k_y$	$\sqrt{k_x^2 + k_y^2}$			
$\hat{\mathbf{x}}k_y + \hat{\mathbf{y}}k_x$	$\sqrt{k_x^2 + k_y^2}$			
$\hat{\mathbf{z}}k_x$	$|k_x|$	line		
$\hat{\mathbf{z}}(k_x + k_y)$	$|k_x + k_y|$	line		
$\hat{\mathbf{z}}(k_x \pm ik_y)$	$\sqrt{k_x^2 + k_y^2}$		broken	ABM
Nonunitary states				
$\hat{\mathbf{x}}k_x + i\hat{\mathbf{y}}k_y$	$|k_x + k_y|\uparrow\uparrow$ $|k_x - k_y|\downarrow\downarrow$		broken	
$\hat{\mathbf{x}}k_y - i\hat{\mathbf{y}}k_x$	$|k_y - k_x|\uparrow\uparrow$ $|k_x + k_y|\downarrow\downarrow$		broken	
$\hat{\mathbf{x}}k_x - i\hat{\mathbf{y}}k_y$	$|k_y - k_x|\uparrow\uparrow$ $|k_x + k_y|\downarrow\downarrow$		broken	
$\hat{\mathbf{x}}k_y + i\hat{\mathbf{y}}k_x$	$|k_x + k_y|\uparrow\uparrow$ $|k_y - k_x|\downarrow\downarrow$		broken	
$(\hat{\mathbf{x}} + i\hat{\mathbf{y}})(k_x + k_y)$	$2(|k_x + k_y|)\uparrow\uparrow$ $0\downarrow\downarrow$	line	broken	
$(\hat{\mathbf{x}} + i\hat{\mathbf{y}})(k_x + ik_y)$	$2\sqrt{k_x^2 + k_y^2}\uparrow\uparrow$ $0\downarrow\downarrow$		broken	A1

TABLE 4.3: Possible d-vectors allowed by symmetries of the tetragonal space group $I4/mmm$. [5]

4.1.3.2 Experimental evidence for unconventional superconductivity

1. Superconducting parameters

The measured and the estimated superconducting parameters are useful for the following discussion, so I summarise them in Table 4.4 [5]. The quantities, including the coherence length ξ, the penetration depth λ and the Ginzburg-Landau parameter κ in Table 4.4 are obtained with a single component Ginzburg-Landau theory, utilising the experimentally determined (in-plane and out-of-plane) H_{c2} and the thermodynamic critical field H_c. It is seen that the superconductivity in Sr_2RuO_4 is highly anisotropic, with an anisotropic parameter $\xi_{ab}/\xi_c = 20$.

2. non-s-wave superconductivity

According to Anderson's theory of dirty superconductors [98], for a conventional

Parameter			ab	c
T_c	(K)	1.50		
$\mu_0 H_{c2}(0)$	(T)		1.50	0.075
$\mu_0 H_c(0)$	(T)	0.023		
$\xi(0)$	(Å)		660	33*
$\lambda(0)$	(Å)		1900	3.0×10^4
$\kappa(0)$			2.6	46
ξ_{ab}/ξ_c		20		

TABLE 4.4: The superconducting parameters of Sr_2RuO_4 in its clean limit. H_c, ξ, λ and κ represent, respectively, the (thermodynamic) critical field, the coherence length, the penetration depth and the Ginzburg-Landau parameter. The quantities are defined for a field applied along the c-axis.[5]

superconductor (an *s*-wave superconductor), the superconductivity should be robust against elastic scattering. In contrast to conventional superconductors, however, Sr_2RuO_4 shows superconductivity that is extremely sensitive to non-magnetic impurities of, for example, Al or Si [55]. An impurity concentration of less than 430 ppm can already seriously influence or even destroy the superconductivity. It is also found that when the averaged impurity-impurity spacing becomes comparable with the in-plane coherence length ξ_{ab} ($\xi_{ab} \approx 900$ Å for samples with $T_c = 1K$ [99] and $\xi_{ab} \approx 660$ Å for samples with $T_c = 1.48K$ [55]), the superconductivity is destroyed. This is consistent with the prediction of the generalised pair-breaking theory for an unconventional superconductor [100].

In addition to the non-*s*-wave like impurity-effects, there are also other features indicating unconventional superconductivity. I will give two more examples here. One is that, in the combined nuclear magnetic resonance (NMR) and nuclear-quadrupole-resonance (NQR) studies, the spin-lattice relaxation rate $1/T_1$, which measures the energy transfer rate from the nuclear spins parallel to the applied field to the surroundings (the lattice), shows a steep decrease below the transition temperature with no coherence peak (the Hebel-Schlichter peak) and a T^3 dependence at even lower temperatures [101] [102]. Such behaviour is in contrast to the prediction of the standard BCS theory and implies an anisotropic gap structure. Another hint of non-*s*-wave superconductivity is the T dependence of the specific heat C_e, which is shown in Figure 4.8. The exponential T dependence of C_e for
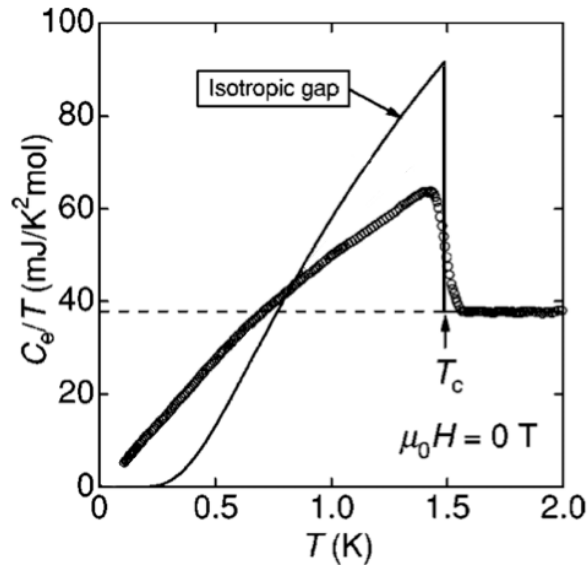
FIGURE 4.8: The electronic specific heat C_e of Sr_2RuO_4 as a function of temperature. For a standard BCS superconductor, the isotropic gap would give rise to an exponential temperature dependence of C_e below T_c, however, for Sr_2RuO_4 a linear temperature dependence is seen below T_c. In addition, the magnitude of the jump of C_e at T_c is only approximately 74% of the normal state value, which is substantially lower than the magnitude predicted by a standard BCS-like gap structure. Figure modified from [5] based on Fig. 1 of [103].

a standard BCS superconductor is not seen in Sr_2RuO_4, instead C_e shows a linear T dependence over a wide temperature range below T_c. Besides, the ratio of the magnitude of the jump of C_e with respect to its normal state value is only approximately 0.74, contrasting the well know value 1.43 for a standard *s*-wave superconductor.

3. Spin-triplet pairing

Shortly after the discovery of superconductivity in Sr_2RuO_4, T. M. Rice and M. Sigrist pointed out the possibility that it might be a superconducting analogue of superfluid of ^{3}He, based on the following facts: a) The two systems at low temperature are both Fermi liquids with strong correlations (for Sr_2RuO_4, the correlations are indicated by, for instance, the enhancements of γ and χ, cf. subsection 4.1.2.1); b) Some quantities of Sr_2RuO_4, like the mass enhancement factors of all Fermi surface sheets (≈ 4), the Wilson ratio ($\pi^2 k_B^2 \chi_0 / 3\mu_B^2 \gamma \approx 1.8$) and spin susceptibility enhancement (≈ 8) are roughly similar to those of liquid ^{3}He at atmospheric pressure; c) They are both in the weak coupling limit, indicated by the

small $T_{\mathrm{c}}/T_{\mathrm{F}}$ (10^{-3}-10^{-4} for both systems); and d) The 3D analogue of Sr_2RuO_4, $SrRuO_3$, is a ferromagnet below 160 K. [74] The analogy raised the possibility that Sr_2RuO_4 might be a superconductor with spin-triplet pairing, so they examined the possible order parameters (*d*-vectors) for triplet pairing under the symmetry constraint of a 2D square lattice, and compared the resulting states with those of the superfluid ^{3}He.

This comparison motivated the researchers to study the symmetry of the superconducting order parameter of Sr_2RuO_4, with particular hope to find evidence for spin triplet pairing. The identification of the order-parameter-symmetry can be studied either from the spin aspect of the Cooper pair wave-function or from the orbital aspect, and so far evidence has emerged from experiments sensitive to both. From the spin point of view, the NMR Knight shift measurements performed by K. Ishida *et al.* [70] [102] provided probably the most convincing evidence for spin-triplet pairing.

The Knight shift K is the difference between the NMR frequency of a nucleus when it is in a metallic environment and that of the same nucleus in a free ion. [104] It is a powerful technique to extract contributions of different sources to the total susceptibility in a metal or a superconductor (see, e.g. [105]), and for a superconductor in which the static susceptibility is not accessible due to the Meissner screening currents, the NMR Knight shift is particularly helpful to test the pairing symmetry. Specifically for Sr_2RuO_4, since the temperature dependent part of the Knight shift K (for a narrow band system) is from the Pauli paramagnetism of the conduction electrons and the Pauli susceptibility for a singlet superconductor is expected to vanish as $T{\to}0$ [102], if the measured Knight shift K (with an applied magnetic field H substantially smaller than H_{c2}) remains invariant when the sample is cooled deep into the superconducting state, there must be Cooper pairs in a triplet state of some form.

K. Ishida *et al.* performed a NMR Knight shift study with ^{17}O enriched[18] Sr_2RuO_4 samples that are close to the clean limit ($T_{\mathrm{c}} > 1.4$K). Their key result is shown

---

[18]The element substitution is to enhance the magnitude of the Knight shift signal.

in Figure 4.9 [70]. In their work, a field of 6.5 KOe was applied along the crystal a-axis (in the ab-plane), which resulted in two sets of inequivalent O sites in
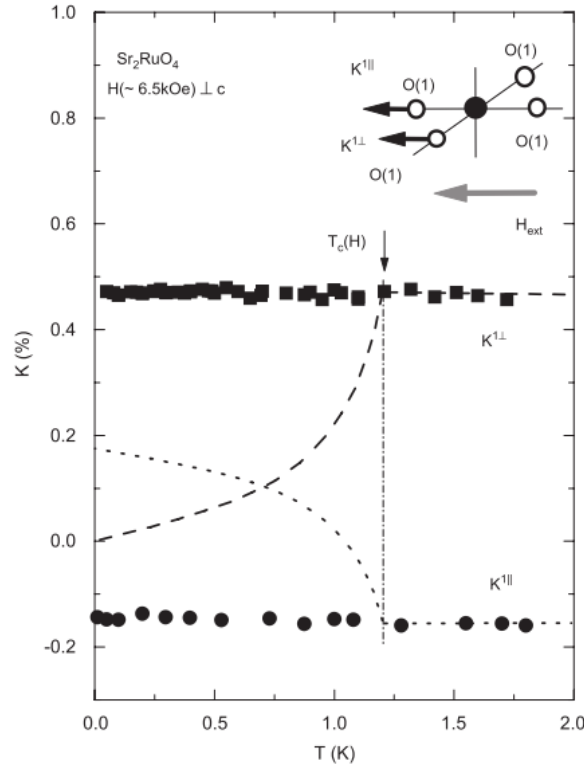
FIGURE 4.9: Temperature dependence of the Knight shift K for the two in-plane oxygen sites, with an in-plane field of 6.5 kOe. The dashed lines are expected value for a spin singlet $d_{x^2-y^2}$ state of a cuprate superconductor. The invariant K as the Sr_2RuO_4 sample was cooled into the superconducting state suggests spin triplet pairing. [70].

the RuO_6 Octahedra plane, due to the Rud-O$p\pi$ anti-bonding. For some oxygen atoms the Ru-O-Ru bonding direction was parallel to the field direction whereas for others the Ru-O-Ru bonding direction was perpendicular to the applied field, and they produced the Knight shift $K^{1\parallel}$ and $K^{1\perp}$, respectively, as shown in Figure 4.9. The orbital part of $K^{1\parallel}$ and $K^{1\perp}$ were estimated to be $^{17}K^{1\parallel}_{orb} = 0.18\%$ and $^{17}K^{1\perp}_{orb} = 0\%$, respectively. The remarkable feature in Figure 4.9 is that both $K^{1\parallel}$ and $K^{1\perp}$ remain invariant between 1.8K and 15mK. As explained above, such behaviour can only be consistent with the existence of spin triplet pairing.

Later [106] K. Ishida *et al.* performed similar measurements with ^{99}Ru enriched samples (again H ∥ab-plane), which gave a signal an order of magnitude higher than that from ^{17}O Knight shift studies. The ^{99}Ru NMR Knight shift also showed

an invariant K when T passed through T_c, thus reinforcing the conclusion of spin triplet pairing. To study the anisotropy of the spin susceptibility, H. Murakawa and K. Ishida *et al.* measured the Knight shift K by studying ^{101}Ru nuclear quadrupole resonance (NQR) spectra, with a small c-axis field[11] down to 20 mT [107] and an in-plane field down to 55 mT (for another experiment [108]). No temperature dependence of the Knight shift was observed in any of these experiments. Since the onset of superconductivity can be confirmed by, for example, the obvious decrease of $1/T_1$ signal (cf., e.g. Figure 13 in [108]) in the same setup, they conclude that, a *c*-axis magnetic field as low as 20mT can polarise the electrons in the superconducting state, or equivalently, can rotate the *d*-vector (so that it becomes perpendicular to the field). This essentially means that there is no resolved anisotropy in the spin susceptibility from these experiments.

The results of the Knight shift studies are consistent with that of polarised neutron diffraction work by Duffy *et al.* [109]. In their polarised neutron diffraction study, where the magnetisation density was measured with an in-plane magnetic field of 1T, no variance was observed when T passed through T_c.

For a superconductor like Sr_2RuO_4, which has a relatively simple electronic structure, the absence of reduction in spin susceptibility upon cooling through T_c in the Knight shift and the polarised neutron diffraction measurements, suggest that the Cooper pairs in Sr_2RuO_4 are very likely in a triplet state rather than a singlet state. It is worth mentioning that in a more recent work [110], half-height magnetisation steps were seen in torque magnetometry measurements with a micron-sized ring shaped sample. The authors interpret these as evidence for half quantum vortices, whose existence would support the spin triplet pairing scenario.

4. Odd parity superconductivity

As discussed above, to detect the symmetry of the Cooper pair wave-function, (in addition to studying the spin symmetry) one can alternatively study the symmetry of the orbital wave-function. An important experiment, focusing on the orbital parity, was reported by Nelson *et al.* in 2004 [111]. They successfully produced

---

[11]It is noted that this experiment is extremely difficult due to the low $H_{c2} \parallel$ c-axis (75mT)and the small Ginzburg-Landau parameter ($\kappa = 2.6$).

superconducting quantum interference devices (SQUID) of the type proposed by Geshkenbein *et al.* [112], each consisting of two $Au_{0.5}In_{0.5}$-Sr_2RuO_4 Josephson junctions, and tested the Josephson current dependence on the relative phase of the superconductor parameters of the two superconductors. The results of their work, which are briefly explained below, support the hypothesis that Sr_2RuO_4 has odd-parity pairing.

Theories [113] [114] [115] for a Josephson junction between a spin singlet superconductor (like $Au_{0.5}In_{0.5}$, which is an ordinary *s*-wave superconductor) and a spin triplet one with a magnetically active [19] interface predicts that the Josephson current j_s is sensitive to the orientation of the spin triplet order parameter with respect to the interface, or, is sensitive to the relative orientation of the *d*-vector. In particular, for a SQUID composed of two in-plane tunnel junctions on opposite surfaces of the triplet superconductor (as illustrated in Figure 4.10a), it is expected that if the *d*-vector is only along the c-axis, the critical current I_c will exhibit a minimum at zero magnetic field and it will oscillate with a varying field. If the two junctions are on the same side, the field-oscillating critical current will instead exhibit a maximum at zero field. Note that this assumes that in the experiment one could avoid the problem of unwanted magnetic flux passing through the SQUID, as learned from similar work on high T_c cuprate superconductors [116].

For the SQUID with two $Au_{0.5}In_{0.5}$-Sr_2RuO_4 Josephson junctions on opposite surfaces of the Sr_2RuO_4 sample (see Figure 4.10a), the critical current I_c as a function of the magnetic field, measured at a series of temperatures below its T_c ($\approx$0.4-0.55 K for the SQUID shown in Figure 4.10), is demonstrated in Figure 4.10b, and its counterpart for the SQUID with two junctions on the same side of the Sr_2RuO_4 sample is shown in Figure 4.10c.[20] $I_c(H)$ was measured at a series of temperatures to extrapolate the field dependence of I_c in the limit of zero induced flux for the SQUID, as an attempt to avoid the SQUID asymmetry problem (known for the phase sensitive test work on the high T_c cuprate superconductors, see [116]). It is seen that, as T approaches T_c, the critical current $I_c(H)$, for

---

[19]e.g. due to different spin-orbit coupling in the two superconductors.
[20]Note that in both cases the *c*-axis is perpendicular to the tunnelling current.
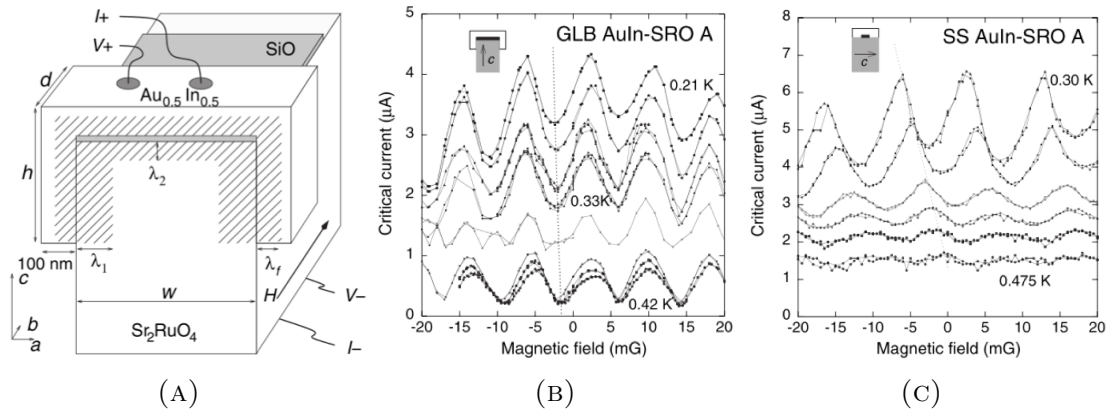
FIGURE 4.10: An example of the schematic of a $Au_{0.5}In_{0.5}$-Sr_2RuO_4 SQUID (Panel A) and the temperature dependence of the critical current as a function of magnetic field (Panel (B) and Panel (C)). In panel (A) the two junctions of the SQUID are both in-plane tunnel junctions and are on opposite sides of the Sr_2RuO_4 crystal. The top-surface (perpendicular to the c-axis) is insulated by a SiO layer. The results shown in Panel (B) are based on a SQUID of this kind. For the SQUID that gives rise to the results shown in Panel (C), the two junctions are on the same side of the Sr_2RuO_4 crystal. Panel (B) and Panel (C) show, respectively, the the critical current as a function of magnetic field, measured at a series of temperatures below the T_c of the SQUID. For interpretation of the data in Panel (B) and Panel (C), see the text. [111]

the junctions on opposite sides of the Sr_2RuO_4 crystal, approaches a minimum at $H = 0\ T$, whereas for those on the same side $I_c(H)$ approaches a maximum at $H = 0\ T$.

Assuming that the unwanted magnetic field has been successfully minimised (for details, see [111]), the observation discussed above suggests that under inversion the phase of order parameter has a phase change π, and therefore Sr_2RuO_4 has odd-parity pairing. In addition, the results suggest that the d-vector is aligned along the c-axis of the crystal in zero field. The odd-parity in the orbital function means symmetric spin pairing, i.e. spin triplet pairing, thus the results above are consistent with the observation in NMR Knight shift measurements. The establishment of the odd-parity pairing puts strong limits on the choice of order parameter.

5. Evidence for the breakdown of time-reversal symmetry in $\mathbf{Sr_2RuO_4}$

Since some of the allowed d-vectors for triplet superconductivity summarised in Table 4.3 (for example $\boldsymbol{d} = \Delta_0\hat{z}(k_x \pm ik_y)$, or those of the non-unitary states) correspond to superconducting states with broken time-reversal symmetry (TRS), to narrow down the possibilities for the choice of the d-vector, attempts were made to detect possible evidence for TRS-breaking.

If a superconducting order parameter breaks TRS, appearance of spontaneous internal magnetic fields becomes possible, for instance in the vicinity of defects and domain walls, when the superconductor enters the TRS-breaking state. [117]. Such small internal fields, in principle, can be probed by field sensitive probing methods, for example muon spin-relaxation (μSR) measurements. In μSR measurements, polarised muons are implanted in the sample, and their relaxation rate is measured statistically. This rate is expected to show an increase if in the sample under investigation there are small fields that are weak and broadly distributed (In comparison, uniformly ordered moments would give rise to muon spin precession.). The muon spin-relaxation rate Λ of Sr_2RuO_4 as a function of temperature, measured by G. M. Luke and the co-workers, is shown in Figure 4.11.

Filled squares in the two panels of Figure 4.11 represent the relaxation rate Λ parallel and perpendicular to the c-axis, respectively. Qualitatively similar enhancements of Λ can be seen in both directions, as the temperature goes below T_c. The fact that below T_c Λ can be strongly suppressed by a static field as small as 50 G indicates that at zero field the enhancements of Λ below T_c is due to (quasi-) static internal magnetic fields rather than fluctuating fields. Moreover the onset temperature of the enhancement in Λ seems to coincide with the T_c of the Sr_2RuO_4 sample in the experiment (verified with a sample whose $T_c = 0.9$ K). Therefore the data shown in Figure 4.11 are interpreted as evidence for TRS-breaking in the superconducting state of Sr_2RuO_4, and in addition the exponential form of the increase of Λ below T_c is attributed to broadly distributed fields of from dilute sources.
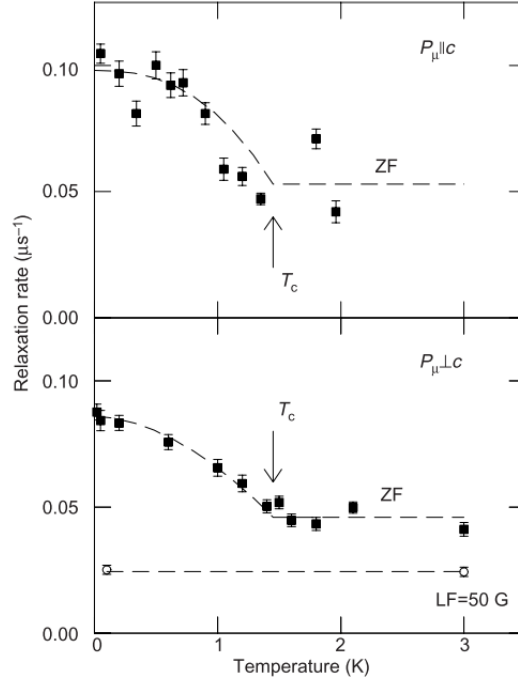
FIGURE 4.11: The muon spin relaxation rate Λ of Sr_2RuO_4. Filled squares in the upper panel and the bottom panel represent the relaxation rate parallel and perpendicular to the c-axis, respectively. For both directions Λ exhibits increase below T_c. Dashed curves are just guides to the eye. The two open circles in the lower panel represent the relaxation rate with a weak field of 50G applied perpendicular to the c-axis, measured above and below T_c respectively. No distinguishable difference of Λ can be seen below and above T_c in the presence of the small field.

Another important experiment that also indicates TRS-breaking in Sr_2RuO_4 is the polar Kerr effect measurements, reported by J. Xia *et al.* [72]. Their results are shown in Figure 4.12. The open circles refer to the rotation angle $\Delta \theta_K$ of the polarisation of the reflected light, whose corresponding incident light is linearly polarised and is normally incident to the Sr_2RuO_4 crystal surface. In $\Delta \theta_K$, the background rotation angle (from, e.g. the offset of the apparatus in zero field or the signal given by the apparatus in a finite field) has been subtracted.

It is clear from Figure 4.12 that a non-zero rotation angle of the polarisation appears and then develops as the Sr_2RuO_4 sample is cooled into the superconducting state, and the onset coincides with the sample's T_c, which is indicated by the T dependence of the in-plane resistivity ρ_{ab} in the same figure. This non-zero rotation angle of the polarisation of the reflected light, which is related to a (non-zero) off-diagonal term in the ac conductivity, should not appear for a system in
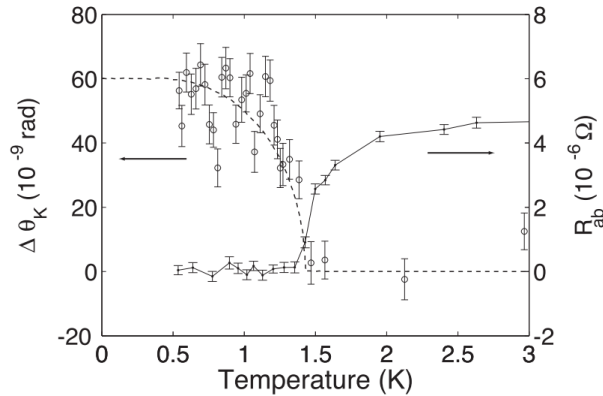
FIGURE 4.12: Temperature dependence of the polar Kerr effect of Sr_2RuO_4 (open circles), measured at zero field, and T dependence of the in-plane resistivity of the same sample (not measured simultaneously.) The dashed curve is a BCS-type fit to the temperature dependence of the gap size. Note that this fit was changed to a linear fit by A. Kapitulnik and J. Xia *et al.* in a later paper [73].

which TRS is conserved, therefore the data in Figure 4.12 strongly suggest the breakdown of TRS in Sr_2RuO_4. Other possibilities, for instance, vortex effects or magneto-thermal effects are also considered. However, the fact that the magnitude of the rotation signal shows no dependence on whether the field is present or whether the sample is field cooled, excludes the possibility of interpretation by vortex effects. Magneto-thermal effects are also unlikely, because the size of the rotation does not respect the power of the incident light in the power range used in the measurements [73]. The authors further show that if the Sr_2RuO_4 sample is pre-cooled with applied fields in opposite directions (e.g. -93 Oe and +47 Oe respectively), the resultant rotation angles after the field is removed exhibit opposite signs, implying that the chirality of the domains can be trained by a pre-applied field.

The combined results of muon spin-relaxation measurements and polar Kerr effect measurements coherently suggest that the TRS is broken in the superconducting state of Sr_2RuO_4. Moreover the interpretation of the magnetic field distribution in the observed square flux lattice also supports the argument of TRS breaking. [118] [119]The establishment of the breakdown of the TRS is very important to understand the superconductivity of Sr_2RuO_4. Unless the data interpretation were proved wrong, any proposed order parameter has to be reconciled with it,

placing a further constraint on the appropriate superconducting order parameter.

To summarise, in this subsection I have introduced the measured and estimated superconducting parameters, and then, following the discussion on impurity-effects, I discussed a series of experiments that unambiguously demonstrate the unconventional nature of the superconductivity in Sr_2RuO_4, for example, the NMR Knight shift measurements based on several atomic sites, the phase sensitive test of the order parameter, the μSR measurements and the polar Kerr effect measurements. The former two sets of experiments point to spin triplet pairing (from the spin and the orbit point of view respectively), and the latter two strongly suggest the breakdown of TRS in Sr_2RuO_4. These experiments provide extremely important knowledge regarding the superconducting properties of Sr_2RuO_4 and impose strong constraint to the choice of the order parameter. However these are not the only important experiments that have been performed on Sr_2RuO_4. In fact, to eventually establish the order parameter, as will be shown in next subsection, experimental facts in a wider range have to be considered.

4.1.3.3 Difficulties with interpretation in terms of a single-band chiral p-wave order parameter

1. The favoured chiral p-wave order parameter

When we examine the possible triplet order parameters that respect the D_{4h} point group symmetry, as listed in Table 4.3, we immediately realise that, if we restrict ourselves to the unitary states, the only d-vector allowing the breakdown of TRS is $\boldsymbol{d} = \Delta_0 \hat{z}(k_x \pm i k_y)$. This order parameter is consistent with all the experiments discussed in last subsection, and because it would be a superconducting analogue of the A phase of the spin-triplet superfluid ^{3}He, and may have important consequences regarding topological superconductivity, it has been especially emphasised in the literature and intensively investigated both theoretically and experimentally. The possible existence of Majorana fermions in a chiral p-wave superconductor and its possible applications in quantum computing/quantum information processing [120] [121] [122], have also attracted much attention.

The order parameter with $\boldsymbol{d} = \Delta_0 \hat{z} (k_x \pm i k_y)$ contains two degenerate sets of states, i.e. those of $k_x + i k_y$ and those of $k_x - i k_y$, with the orbital angular momentum of the pair-forming quasiparticles $L = +1$ and -1, respectively. Therefore the Cooper pairs corresponding to $\boldsymbol{d} = \Delta_0 \hat{z} (k_x \pm i k_y)$ can have either left-handed or right-handed polarisation, i.e. they are chiral. Since the pairing interaction with this d-vector lies in the p-wave channel, the order parameter of $\boldsymbol{d} = \Delta_0 \hat{z} (k_x \pm i k_y)$ is chiral p-wave order. The degeneracy of this order parameter is said to correspond to a series of peculiar properties [74] [123], for instance, the formation of domains with different chirality and edge currents at the domain boundaries and the sample edges. Many experiments have been carried out focusing on the effects of chiral domains. This is still a very active research direction about Sr_2RuO_4 at the time of writing, although here (to keep the structure of this dissertation balanced) I will only cover a few related experiments.

The observed phenomena in several published reports [124] [125] [126] have been attributed to the existence and/or dynamics of the chiral domains. For example, F. Kidwingira *et al.* studied the the critical current dependence on magnetic field and time $I_c(H, t)$, with Josephson junctions utilising orthogonal faces of Sr_2RuO_4 crystals, and observed unusual behaviour of $I_c(H, t)$ (e.g. so-called 'telegraph noise'), which was explained by chiral state transitions within a domain and domain-wall motions. [124] M. S. Anwar *et al.* fabricated Nb/Ru/Sr2RuO4 junctions, and carefully studied the $V - I$ dependence as a function of time at a series of temperatures. They observed unusual high-I_c-low-I_c switching behaviour, and interpreted the data with a model based on chiral-domain-wall dynamics. The work of T. Nakamura *et al.* is also consistent with the above two experiments. [125] It should be noted that a fundamental assumption of the data interpretation of these experiments is the existence of chiral domain walls, or in other words, the above data interpretation would have to be changed if the superconductivity in Sr_2RuO_4 is not of chiral order (with broken TRS). Similar ideas also apply to the interpretation of vortex coalescence data at intermediate out-of-plane field [127], which was speculated to be related to chiral domains too.

2. The insufficiency of a single band chiral *p*-wave order

Most single band chiral *p*-wave superconductivity scenarios for Sr_2RuO_4 assume that the superconductivity in this material is dominated by the γ band (the $4d_{xy}$ orbital) and this is a shared assumption among many reports and calculations in the literature. This assumption is arguably sensible because comparatively the effective mass renormalisation of this band is the strongest (c.f. subsection 4.1.2.2) and the chiral *p*-wave order parameter based on this single band model is consistent with many phenomena concerning the unconventional superconducting properties of Sr_2RuO_4. However, while this is true, it is not consistent with all of them.

The missing edge currents

As shown by M. Sigrist, K. Ueda and M Matsumoto [117] [128] [129], for a chiral *p*-wave superconductor, edge currents can arise in response to the spacial variation of the order parameter towards the sample edges/domain walls/inhomogeneities. Even though the counter-flowing Meissner currents can cancel the effects due to these edge currents in the bulk region of the superconductor, they can not completely screen them at these locations. Therefore the incompletely screened edge currents can induce spontaneous magnetism to the superconductor microscopically, although not macroscopically. Detection of the local fields is believed to be important to support the existence of the chiral domains. M Matsumoto and M. Sigrist estimated the magnitude of the local fields, based on a single band model, and obtained a maximum field magnitude on the order of 10 G close to the sample edges and domain walls. [129] Several efforts have been made up to date [130] [131] [132] [133], based on scanning SQUID imaging and/or scanning Hall probe microscopy, to detect the proposed local fields associated to the imperfectly screened edge currents, yet none of them have revealed a signal magnitude of even 1% of the predicted value.

Suppressed in-plane H_{c2} and the first order superconducting transition

For a type II superconductor, an external magnetic field can induce vortices with supercurrents circulating around them, and at the same time it tends to align the spins of the electrons in a Cooper pair. [134] Both effects have the possibility to destroy the superconductivity when the external field is sufficiently strong. For example a strong field can destroy the superconductivity by inducing vortices that are so dense that the neighbouring vortex-cores overlap with each other. This is often referred to as the orbital depairing effect. In some cases, when the energy gain by aligning the Cooper-pair electron spins (i.e. the Zeeman energy) exceeds the condensation energy, the field can also destroy the superconductivity before reaching the thermodynamically determined H_{c2}. This is often called the Pauli-depairing effect. In this case, the Zeeman energy is proportional to $(\chi_P - \chi(T))H^2$, where χ_P and $\chi(T)$ is the Pauli susceptibility in the normal state and the susceptibility in the superconducting state, respectively [135], and the sudden destruction of the superconductivity gives rise to a first order superconducting-state-normal-state (SS-NS) phase transition.

For Sr_2RuO_4, since the NMR and NQR work (as shown in subsection 4.1.3.2, part 3) has demonstrated that the Pauli susceptibility is unchanged across the superconducting-normal state transition, the energy gain by polarising the electrons is not expected therefore the Pauli-depairing effect should not be important in this situation. On the other hand, if the orbital-depairing effect is the deciding factor for the H_{c2}, theoretical analysis based on a single band chiral p-wave order parameter (i.e. $\boldsymbol{d} = \Delta_0 \hat{z}(k_x \pm ik_y)$) [136] suggests that for an external field that is parallel to the basal plane, as the temperature is lowered, H_{c2} should increase linearly with an increasing rate $-\epsilon \cdot \frac{\mathrm{d}H_{c2}}{\mathrm{d}T} \big|_{T_c}$, where ϵ is a numeric parameter and is predicted to be approximately 0.7.[21] However the experimentally determined value of ϵ is approximately 0.42-0.5 (see, e.g. [137] [138]), which is substantially lower than the predicted value. In comparison, the ϵ for a field parallel to the c-axis is experimentally estimated to be 0.78, which is not far from the value

---

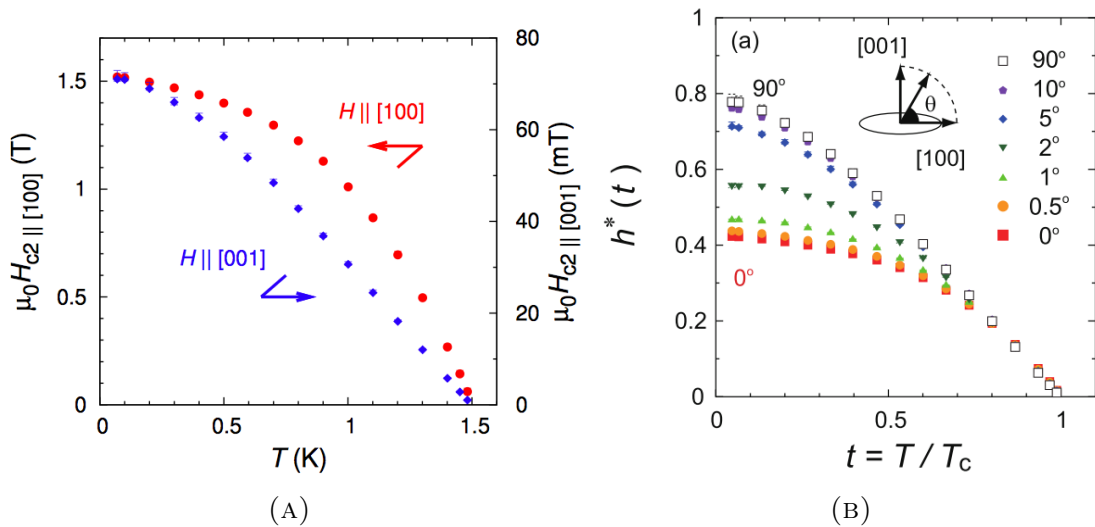[21]According to A. G. Lebed and N. Hayashi (2000), $\epsilon = 0.75$.

FIGURE 4.13: An H_{c2}-temperature phase diagram of Sr_2RuO_4. (A) H_{c2} versus T for both fields in-plane (red) and out-of-plane (blue). It is seen that for an in-plane field ($H \parallel 100$) the slope of $H_{c2}(T)$ deviates from that at T_c when T is lowered, while for an out-of-plane field the same slope persists upon cooling. Note that the field scales are different for the two cases. [137]. (B) $h^\star(t) = H_{c2}(T)/(\frac{dH_{c2}}{dT} |_{T_c})$ as a function of the reduced temperature $t = T/T_c$ at a series of angles. θ is the field angle with respect to the basal plane. The field lies within the plane defined by the [100] and [001] axises in this case. It is clear that the suppression of $h^\star(t)$ is only prominent when $\theta \le 5°$. Figure from [44], adapted from [137].

(approximately 0.73) predicted by E. Helfand and R. Werthamer for a type-II superconductor in the clean limit. [139] Figure 4.13a [137] shows the temperature dependence of H_{c2} for both field directions. It is noted that the anisotropy of the in-plane H_{c2} is small ($<0.3\%$, see e.g. [138]), so the suppression of $H \parallel ab$-plane is not much dependent on the detailed direction of the field in the plane.

Interestingly, it is found that this suppression of H_{c2} is only distinct when the field is within approximately $5°$ away from the basal plane (see 4.13b). Such strong field alignment dependence also makes spin-polarisation mechanisms unlikely. Thus overall the in-plane H_{c2} can be ascribed to neither orbital limiting nor spin limiting and remains as a challenge for interpretation.

Another unsolved puzzle is the recently discovered first order SS-NS phase transition below 0.8 K. [140] and specific heat [141] S. Yonezawa, T. Kajikawa, and Y. Maeno found through magneto-caloric effect measurements that, with the field precisely aligned in the basal plane, the SS-NS phase transition is surprisingly of

first order below approximately 0.8 K. Figure 4.14 shows the heat capacity (in the form of $\Delta C/T$) as a function of magnetic field, measured at a series of temperatures below T_c. The evolution from a high-temperature presumed second order
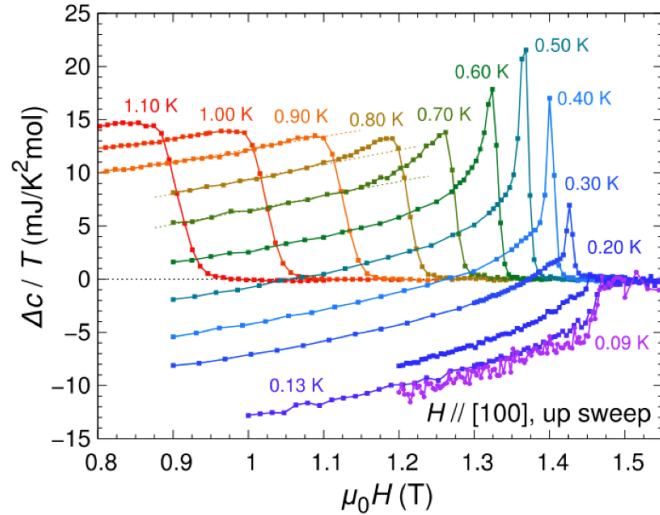

FIGURE 4.14: The heat capacity divided by temperature as a function of magnetic field for Sr_2RuO_4, measured at a series of temperatures below T_c. [141].

SS-NS transition to a low-temperature first order transition is marked by the development of the heat capacity peak as T is lowered, which reflects a discontinuous change of entropy. The reduction of the magnitude of $\Delta C/T$ below 0.5 K and the sign change at even lower temperature can also be explained by a first order transition, using the Clausius-Clapeyron relation (for details, see [141]). Moreover, it is found that the first order SS-NS transition is extremely sensitive to the field alignment ($\theta \leq 2°$) and to the sample purity. The origin of the strongly first order SS-NS transition below 0.8 K is also a question that has not been understood within in the spin triplet or any other scenario.

Line nodes in the gap structure

In the simplest case, the single band chiral p-wave order parameter $\boldsymbol{d} = \Delta_0 \hat{z}(k_x \pm ik_y)$ will give rise to an isotropic energy gap for a circular two dimensional Fermi surface, which leads to typical exponential temperature dependence of thermodynamic quantities (for an isotropic gap), similar to the case for an ordinary BCS s-wave superconductor. The fundamental reason for the exponential dependence for a fully gapped system is the fact that the thermodynamic quantities are governed by the density of states. [135] For the same reason, if the gap has (point

or line) nodes, the finite density of states below the gap will give rise to power law T dependence of the thermodynamic quantities. To clarify the gap structure for Sr_2RuO_4, many experiments have been performed. Evidences of the existence of low lying quasi-particle excitations and line nodes has accumulated, from the observation of power law T dependence of various quantities, for example, the coefficient of the electronic specific heat C_e/T ($\propto T$) [142], the nuclear spin-relaxation rate $1/T_1$ ($\propto T^3$, in very pure samples) [106], the thermal conductivity κ ($\propto T$) [143] [144], the London penetration depth [22] ($\Delta\lambda = \lambda(T) - \lambda(0) \propto T^2$) [145], and the ultrasound attenuation ($\propto T^{1.8}$, or $T^{1.4}$, mode dependent) [40].

Two things can be learned based on these experiments, beyond the many questions and arguments that can possibly arise regarding the data interpretation for almost each of the measured quantities mentioned above (for an overview and comments on these issues, see e.g. [5] [44]). One is that the a fully gapped state with the single-band chiral p-wave order parameter is disfavoured by the experimental data above, and the other is that a gap with vertical line nodes on a single two dimensional surface can not account for the observed phenomena either. Therefore, overall, the data above bring difficulties that are big enough to more or less exclude the possibility of single band chiral p-wave superconductivity, and strongly suggest the existence of line nodes, but at the same time, the positions of the line-nodes can not be fully determined based on these data. Further consideration of the line nodes will be given in the following subsection.

To summarise, in this subsection, I discussed the chiral p-wave order parameter $\boldsymbol{d} = \Delta_0 \hat{z}(k_x \pm i k_y)$, including the reason why it has been emphasised in the literature and some recent work regarding the topological superconductivity associated with it, and then I explained why the single band chiral p-wave scenario is not adequate to account for some of the observed experimental phenomena, with mainly three outstanding examples: the missing edge currents, the suppression of in-plane H_{c2} and the first order SS-NS transition with a precisely aligned in-plane field, and the existence of line nodes.

---

[22] It is noted that the explanation for the T^2 dependence of the London penetration depth is not straight forward, for more discussion, see [5].

4.1.3.4 Multi-band superconductivity and the controversy

In the last subsection, I pointed out that many experimental results are clearly incompatible with a single band chiral p-wave order parameter $\boldsymbol{d} = \Delta_0 \hat{z}(k_x \pm i k_y)$, even though it seems to be the only unitary p-wave state that is compatible with spin triplet superconductivity and the breakdown of TRS. Then an important question is, could the scenario of chiral p-wave superconductivity survive, if we take into account the multi-band effects and the fact that Sr_2RuO_4 is not a perfect 2-D superconductor? After all, unlike the cuprate superconductors, Sr_2RuO_4 has three bands crossing the Fermi level and it does have c-axis dispersion (although weak), as explained in subsection 4.1.2.2.

1. Multi-band effects

The approximation that all three bands contribute with similar strength to superconductivity of Sr_2RuO_4 could be applicable [146] when inter-band scattering is strong, as it will make the energy scale of superconductivity on different bands similar. However, as pointed out by D. F. Agterberg *et al.* [147], the different symmetry characters of the three bands crossing the Fermi level may lead to much suppressed inter-band scattering in Sr_2RuO_4 and therefore lead to gap opening at different temperatures, which can then result in unusual temperature dependences of thermodynamic quantities below T_c. The work of D. F. Agterberg *et al.* pioneered the theoretical research on the orbital dependent superconductivity in Sr_2RuO_4.

The idea of orbital dependent superconductivity was then extended by M.E. Zhitomirsky and T. M. Rice [146], who considered interlayer scattering. They proposed, based on their analysis, that there could be an active band in which a full gap opens and it may induce gaps that allow accidental line-nodes (even if they are horizontal) in the passive bands. Similar approaches have also been adopted by T. Nomura and K. Yamada [148] [149] and T. Nomura [150] though on the basis of intralayer scattering. In these reports, the following gap structure is discussed (see Figure 4.15), based on a three-band Hubbard model and a third order perturbation method focusing on the on-site Coulomb interactions. A main gap opens in the

γ band, which is the active band, and has gap minima along the Γ-M direction, while smaller gaps open in α and β bands with minima in the diagonal direction. The absolute gap minima appear in the β band. Using this gap structure, T. Nomura and K. Yamada were able to reproduce the temperature dependence of the heat capacity C/T (including the jump magnitude of C/T at T_c, down to 0.1 K) [149], the thermal conductivity (down to approximately 0.2 K), the ultrasound attenuation rate [150], and the NMR spin-lattice relaxation rate $1/T_1$ [151]. The anisotropy of the gap function is argued to be consistent with the field-orientation dependence of the specific heat, as measured by K. Deguchi *et al.* [152]
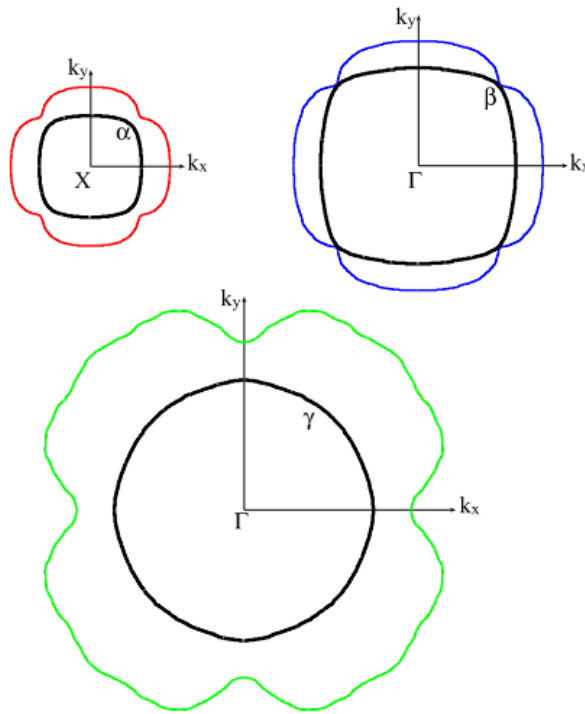
FIGURE 4.15: The gap structure of Sr_2RuO_4, proposed by T. Nomura. A big gap is open in the γ band (the active band), with minima along the $\Gamma - M$ direction. Smaller gaps open in the α and β bands with minima in the diagonal directions. The solid black curves illustrate the corresponding Fermi surface (in a 2D manner) and the distance between them and the coloured curves illustrate the gap magnitude. Figure taken from [141], based on Fig. 2 in [150].

As emphasised by T. Nomura and K. Yamada, chiral *p*-wave order parameter is allowed in this approach, which makes it appear to be consistent with most of the experimental results discussed so far. This gap structure and the underlying theory is also emphasised by Y. Maeno *et al.* in their recent review paper [44]. However, more recently, when E. Hassinger and the co-workers extended the

angle-dependent heat conductivity measurements down to approximately 50 mK, and they found that their heat conductivity data[23] showed inconsistency with the theoretical prediction of Nomura *et al.* below 0.2 K.

It is worth mentioning that, in line with the concept of multi-band superconductivity, there have also been other distinct calculations performed in order to clarify the pairing symmetry and the pairing mechanism. For example, S. Raghu, A. Kapitulnik, and S. A. Kivelson [153] applied renormalisation group analysis with a three-orbital Hubbard model and their results, which emphasise the role of the quasi-one dimensional d_{xz} and d_{yz} orbitals, are argued to be able to explain the absence of edge currents within the generalised chiral *p*-wave superconductivity scenario. Extension of this model, which includes spin-orbital coupling and inter-band hopping, is latter adopted by T. Scaffidi, J. C. Romers, and S. H. Simon [154], who argue that by including these effects the resultant gap magnitude and pairing magnitude can be drastically changed. However it is noticed that, these results do not support arguments of the breakdown of TRS in Sr_2RuO_4.

2. The controversy and future directions

As we have seen, although substantial progress has been made of our understanding about the superconducting properties of Sr_2RuO_4, so far we have not found a theory that is capable to explain all the experimental data, even with multi-band effects included. Beside this, there is often no consensus on the interpretation of experimental data on a specific topic. Actually, criticism can be found regarding almost each of the experiments mentioned above. One example is criticism of the evidence for triplet pairing.

The results of the NMR Knight shift measurements, and those of the SQUID based phase-sensitive measurements, which have been widely considered to be the key evidence for spin triplet pairing and consequently to favour the *d*-vector $\boldsymbol{d} = \Delta_0\hat{z}(k_x\pm ik_y)$, have been argued to be inconclusive by I. Žutić and I. Mazin [155]. For the NMR Knight shift measurements, they argue that the interpretation for the measurements with the field applied along the c-axis, which says that a magnetic

---

[23]E. Hassinger *et al.*, private communication.

field as small as 20 mT can readily rotate the d-vector from the c-axis to the ab plane, is rather unlikely. One of their arguments on this is that to allow such a d-vector rotation with a field of 20 mT, the spin-orbit coupling strength needs to be smaller than 1.1 μeV, which seems too small for Sr_2RuO_4. For the results of the SQUID based phase-sensitive measurements performed by Nelson *et al.*, I. Žutić and I. Mazin proposed an order parameter $\Delta \propto (k_x \pm ik_y)k_z$ and managed to qualitatively reproduce the results of Nelson *et al.* by considering the imperfect sample surface conditions and the weak c-axis dispersion of the Fermi surface. So I. Žutić and I. Mazin argue that the odd-parity is not the unique interpretation for the phase sensitive measurements. Based on the arguments above, they believe that the spin triplet pairing is not conclusive.

There are more examples of skepticism, not only about the data interpretation for experiments but also about the existing theories. At the time of writing, maybe the only consensus regarding the order parameter for Sr_2RuO_4 is that we have not arrived at an consensus. Many puzzles still need to be solved. However, above the obvious controversy, for further investigation, it seems that a few points have been generally appreciated by researchers. One is the necessity to consider multi-band effects to understand Sr_2RuO_4, or maybe in a more general sense, to understand a multi-band superconductor. Indeed, as mentioned in the beginning of this chapter, the concept of multi-band superconductivity has been proven useful to under some other superconductors (e.g. MgB_2 and iron-pnictides) [156] [157]. The second point is that the c-axis dispersion, which was emphasised by Bergemann *et al.* [46], should probably be treated more seriously in future research. Another point is the necessity to study the superconductivity of Sr_2RuO_4 experimentally in a band-by-band approach. It is not easy to apply discriminative methods to distinguish the origins of contributions to the superconductivity. However, if successfully applied, they surely have the potential to provide very useful information to nail down the order parameter, since there are many theories and arguments that have been proposed based on assumptions about the origin of dominating contributions. For example, the theory of S. Raghu, A. Kapitulnik, and S. A. Kivelson [153] emphasises the role of the quasi-one dimensional bands, while the earlier theories

of 'orbital dependent superconductivity' mostly assume the dominating role of the more two-dimensional γ band. The validity of the arguments on the breakdown of singlets and triplets by C. N. Veenstra *et al.*, at least to some extent, depends on where the superconducting gap mainly lives on. Another important aspect related to the band-by-band study, is the investigation on the VHS in Sr_2RuO_4. It is the topic of the next section.

4.1.3.5 A section-summary

In this section, I have presented an introduction to the unconventional superconductor Sr_2RuO_4, the subject matter of this chapter. It consists of three main parts, each covered in one subsection.

In the first part I introduced the basic properties of the strontium ruthenate family compounds, including the crystal structure, the principal research interest in each of these compounds and a brief research history specifically for Sr_2RuO_4. This part serves as an introduction to this material in a broad context.

In the second part, I presented the normal state Fermi liquid like properties in its electronic conductivity, magnetic susceptibility and specific heat. Following it the electronic structure was discussed. A qualitative interpretation was given first, which was then shown to be consistent with the experimental results of dHvA measurements, AMRO and the ARPES measurements (after the issues related to surface effects are solved). The procedure, and the outcome of the sheet-by-sheet Fermi surface reconstruction (developed by Bergemann *et al.*) was introduced.

Following the introduction to the normal state properties of Sr_2RuO_4, the unconventional superconducting properties were discussed. I introduced the *d*-vectors, which are widely used to describe the superconducting order parameter, summarised the experimentally extracted quantities and presented the experimental evidences for unconventional superconductivity. Special emphasis was given to those experimental results that have been widely considered to be evidences for spin-triplet pairing and those for the breakdown of TRS. In this regard, I firstly

emphasised physics of the chiral *p*-wave order parameter and then discussed the challenges to the chiral *p*-wave model. I pointed out that even in a multi-band approach there are experimental data which can not be explained with current theories and that at the time of writing, the pairing symmetry of Sr_2RuO_4 is still controversial. In the end, I listed a few directions that might be important for further study on this material.

4.2   The Van Hove singularities in Sr_2RuO_4

As mentioned in the introduction of this chapter, the role of the Van Hove singularities in Sr_2RuO_4, especially that of the γ band singularity, is important to the research on its superconductivity. In this section, I will explain it in details, after introducing the concept of Van Hove singularities and their possible applications in unconventional superconductivity.

4.2.1   VHSs in crystalline solids

Van Hove singularities generally refer to singularities in the density of states (DOS) or their derivatives, which may occur at anomalies in the band structure, for example, band edges or saddle points. These singularities are related to topological changes in band structures, and their existence is, as pointed out by L. Van Hove [158], fundamentally a consequence of the periodicity of the crystal structure. Because the DOS can peak or even diverge at a VHS, the electronic properties of a material can be drastically changed by the VHSs if they are close to the Fermi level. Therefore the role of VHSs in determining the properties of many crystalline materials, especially in unconventional superconductors, has drawn wide attention.

VHSs can occur at band maxima, minima or at saddle points, depending on the dimensionality. In 1D, close to a VHS, the DOS $g(\epsilon)$ is inversely proportional to the square root of the energy distance with respect to the VHS, i.e. $g(\epsilon) \propto 1/\sqrt{\epsilon - \epsilon_{VHS}}$. VHSs occur at band edges in 1D. In 2D, close to a VHS, the DOS has a logarithmic divergence: $g(\epsilon) \propto ln(W/(\epsilon - \epsilon_{VHS}))$, where W is the

(A)   (B)   (C)
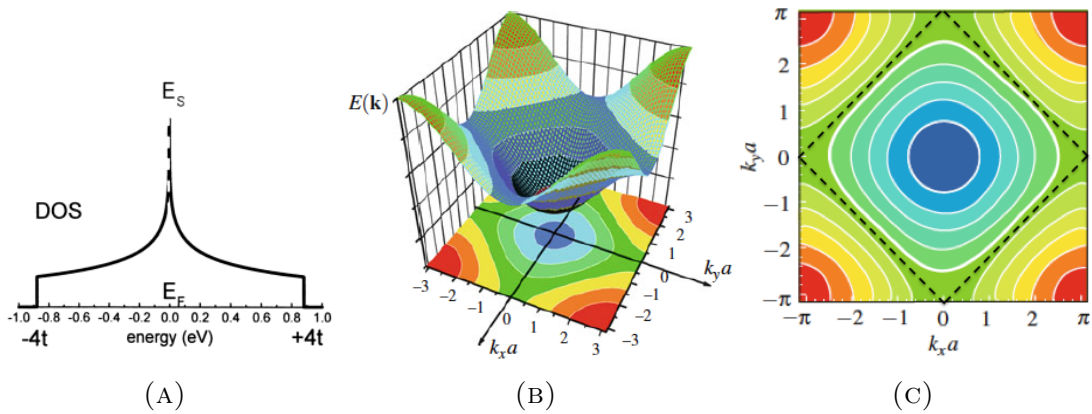
FIGURE 4.16: An example of the DOS, the electronic structure and the constant energy contours (at different cuts) of a 2D square lattice system. (A): The DOS distribution. t refers to the nearest neighbour interaction. The DOS shows logarithmic divergence at E_s, the position of the VHS. Such divergence is expected to occur at band saddle-points. [159] (B): The electronic dispersion relationship $E(k_x, k_y)$, presented in a 3D fashion. Four saddles points can be seen, at symmetric positions $(0, \pm\pi)$ and $(\pm\pi, 0)$. At these saddle points, VHSs can occur and have logarithmic divergence in the DOS.(C) Projections of constant E contours on the $(k_x a, k_y a)$ plane. If the Fermi level cuts the electronic dispersion surface below the saddle points, the Fermi surface (FS) will be electron-like, centred at the BZ centre, or if above the saddle points, the FS will be hole-like, centred at the BZ corners. Alternatively if the Fermi level exactly coincides with the saddle points, the FS, whose position is indicated by the dashed lines, will be simultaneously electron-like and hole-like, . [160].

band-width and $\epsilon - \epsilon_{VHS}$ is again the energy distance with respect to the VHS (see Figure 4.17a). Unlike in the 1D case, VHSs in 2D can occur not only at band maxima/minima but also at the saddle points of a band (see Figure 4.17b). The saddle point VHSs may have strong influence on the electronic properties of the material under consideration. In 3D, at a saddle-point VHS the DOS itself does not diverge however its derivatives do, and the DOS can have a peak (at the VHS). These VHSs are still of physical importance.

Around a saddle-point VHS, the Fermi surface topology undergoes an electron-like to hole-like crossover. Figure 4.16 illustrates an example of such a topological change of the FS at a VHS, based on a tight binding model for a 2D square lattice system. If the Fermi level is below the position of the VHS, E_s (i.e. below the energy level of the saddle-points), the FS will be electron-like, centred at the Brillouin zone centre, whereas if it is above E_s, the FS will be hole-like, centred at

the zone corners. Alternatively if the Fermi level is located exactly at the VHS, then the FS can be simultaneously electron-like and hole-like.

The example of the saddle-point VHS in Figure 4.16 is special, because the corresponding FS has perfect nesting and there can be diverging spin or charge susceptibilities at the nesting wave vectors, leading to instabilities at the VHS. However, in a more general context, it is not special at all to have a VHS that is related to instabilities of some sort. This is especially true in the 2D case, where the diverging DOS can lead to instabilities to a Fermi liquid state in the zero temperature limit. In higher dimensions (>2D), although interlayer interaction can truncate the divergence of the VHSs, a peak in the DOS can survive (the DOS integration under the peak is conserved) and still contribute to instabilities. Lifshitz analysed the consequence of a change in the Fermi surface topology for a 3D system and showed that phases transitions (Lifshitz transitions) can occur at or in the immediate vicinity of a VHS, which in turn can bring drastic changes in the system's thermodynamic quantities.

In addition to the VHSs discussed above, there is another type of VHS one can find in literature, which is called extended VHS [161]. Extended VHSs occur at so-called 'extended saddle-points', around which the band curvature does not change its sign. Instead, on one side of the extended saddle-points the band is extremely flat and the curvature goes to zero. This type of VHS is not a natural requirement of the crystal periodicity, however it can give rise to power law divergence in the DOS, because the band dimensionality is essentially reduced from 2D to quasi-1D close to the extended saddle-points (recall that in 1D the DOS has stronger divergence at a VHS).

4.2.2 VHSs in unconventional superconductors

Because VHSs can potentially be important in determining the electronic properties of crystalline materials, considerable effort has been made to study their possible roles in determining the properties of, for example, in high T_c cuprate superconductors [161] [160] [162] [163] [164], iron-based superconductors [165] [166]

[167] [168], MgB$_2$ [169] [170], strontium ruthenates and related materials [84] [45] [171] [47] [172] [173] [174] [175] and many other materials. Actually there are so many reports on VHSs related to different materials that there is simply no way to list all of them. Although not always the case, the research background is mostly related to superconductivity. As an example, the Van Hove scenario in high T_c cuprate superconductors, which is most relevant to the current project, is introduced briefly in the following.

Soon after the discovery of high T_c superconductivity in cuprates, several groups began to consider the potential influence of the VHSs embedded in the band structure of these quasi-two dimensional superconductors. For example, J. Labbe and J. Bok [176] calculated the electronic structure of La$_{2-x}M$CuO$_{4-y}$ (LMCO) compounds, with M possibly being Ba, Sr or Ca, in a tight-binding approach. They found that the band structure, in the tetragonal phase, have saddle-points at (0, $\pm\pi$) and ($\pm\pi$, 0) in the (k_x, k_y) plane of the reciprocal space, where the DOS shows logarithmic divergence, as expected. At roughly at the same time, renormalisation group (RG) approaches began to be developed by, for instance, I.E. Dzyaloshinskii [177] and H. J. Schulz [178]. Results of these and the subsequent studies have been used to explain both the normal state and the superconducting state properties of not only the LMCO compounds but also other high T_c cuprate superconductors. It is noted that the generalised VHS scenario, in which competing instabilities close to a VHS are taken into account, has been successful in explaining a series of unusual properties of the cuprates, for example the normal state transport properties (e.g. the T linear resistivity at optimal doping), the high T_c, the structural instabilities, the isotope effects, the doping effects and other properties [161].

An interesting point learned from the Van Hove scenario [176] [161] is that VHSs could introduce an electronic term into the pairing mechanism and modify the dependence of T_C on coupling strength. The cut-off energy in the VHS scenario is set by an electronic energy scale that is related to the band width and can be higher than the Debye energy, which is the cut-off energy in the standard BCS theory. In addition, there is an effective coupling strength $\tilde{\lambda}$ in the VHS scenario, but it influences the T_C only in the form of its square root in the exponent, unlike in the

BCS theory in which T_C is proportional to $\exp(-1/(\lambda-\mu^\star))$, where λ is the electron phonon coupling strength and $\mu^\star$ is the renormalised Coulomb interaction, given by $\mu^\star=\mu/(1+\mu\ln(W/\epsilon_D))$ with W being the band-width. This has been applied to explain the high T_c observed in these materials. However for Sr_2RuO_4, although there are also VHSs in it and it is isostructural to the high T_C cuprates, its T_c is very low (see last section). In-depth understanding on the role of VHSs in the superconductivity of Sr_2RuO_4 might be useful in a general sense to improve our knowledge on the interplay between VHSs and superconductivity.

4.2.3 The VHSs in Sr_2RuO_4

The VHSs in Sr_2RuO_4 were noticed shortly after the discovery of superconductivity in it, although understanding on them has been changed over years.

4.2.3.1 Theoretical studies

The early band structure calculations performed by T. Oguchi [79] for the first time suggested VHSs in two bands at approximately 0.25 eV above the Fermi level E_F, although they were not discussed by T. Oguchi and instead were only pointed out later by Singh [179]. Singh calculated the electronic structure of Sr_2RuO_4 independently and emphasised the VHSs in the vicinity of E_F. In his report, two DOS peaks were found close to E_F and were attributed to the two corresponding VHSs, located at approximately 0.06 eV and 0.26 eV above E_F, respectively. He further noticed that a VHS closer to E_F would occur at E_F if the bigger electron-like FS sheet (now generally known as the γ band FS) centred at the Brillouin zone centre (Γ point) just touches the zone boundary (the M point, c.f. Figure 4.5) and becomes a hole-like pocket centred at the zone corner (the X point). Such a VHS associated with a Fermi surface topology change is reminiscent of the typical circumstances in which a VHS occurs, as discussed in section 4.2.1, although in this case it occurs at a band maximum instead of a saddle point. A VHS close to the Fermi level was also obtained in the electronic structure calculations by P.

K. de Boer and R. A. de Groot, who in addition pointed out that there might be complexity due to possible surface magnetism. [84]

In 2000, T. Nomura and K. Yamada [45] calculated the FS and the DOS of Sr_2RuO_4 in a tight binding approach. In their calculations, they considered the experimentally determined [69] filling factors of each band and the FS topography. They emphasised that there are three VHSs originating from the three bands (α, β and γ, c.f. Figure 4.5) crossing the Fermi level, derived from the three Ru 4d orbitals (d_{xz}, d_{yz} and d_{xy}). Each of the three VHSs gives rise to a peak in the DOS spec-
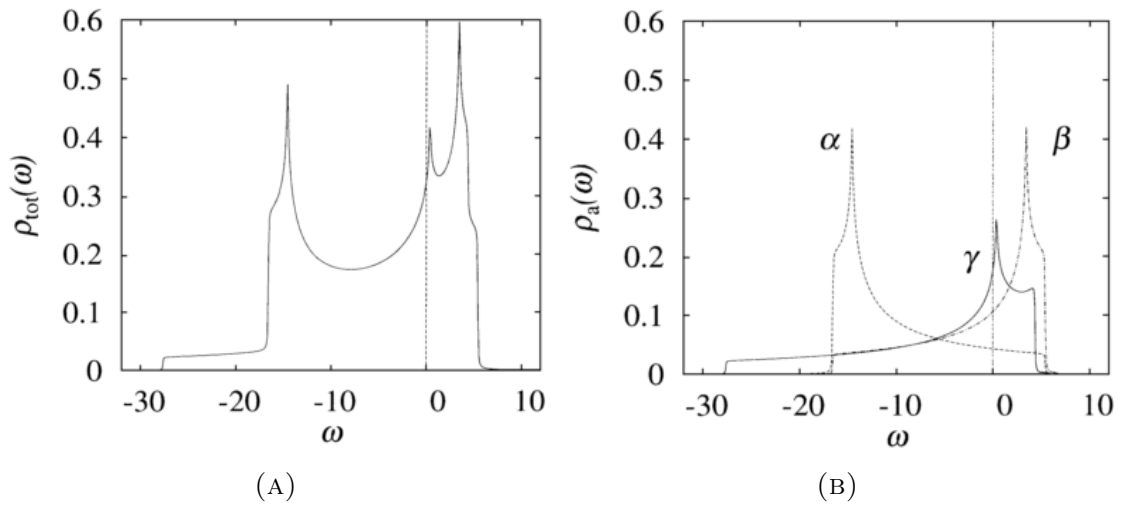

FIGURE 4.17: The DOS spectrum of Sr_2RuO_4 calculated by T. Nomura and K. Yamada within the MFA. (A) The total DOS $\rho_{tot}(\omega)$ versus the energy with respect to E_F where $\omega = 0$. The three obvious peaks in the DOS are caused by three VHSs. (B) The partial DOS $\rho_a(\omega)$, where $a = \alpha$, β or γ. It is seen that the γ-VHS is the one closest to the VHS. [45]

trum, as shown in Figure 4.17. The VHS from the γ band is the closest one to the Fermi level and is just above it, in agreement with the results of Singh. Their work also indicates that Sr_2RuO_4 is likely close to both FM and AFM instabilities and the proximity of the γ-VHS to the Fermi level may play an important role in determining its magnetic properties. Similar results (three VHSs) were also seen in the report of C. Noce and M. Cuoco [180].

Subsequent theoretical work related to the electronic structure of Sr_2RuO_4 mostly recognise the VHSs embedded in its band structure too, although, similar to the situation discussed above, the exact energy distance between them and E_F from

different groups varies. For example, the position of the γ-VHS was estimated by C. Bergemann [46] with a tight-binding approach to be 49 meV above E_F, while according to H. Iwasawa *et al.* (who did LDA + U band structure calculations) its position can be changed by effects of spin orbit coupling and the onsite repulsion U. [181] Nevertheless, the proposals related to the VHSs have been widely noticed. Bearing in mind the VHS scenario for cuprates, researchers have paid attention to the possible influence of VHSs in Sr_2RuO_4, especially to the γ-VHS, which is very close to the Fermi level.

4.2.3.2 Detecting the position of the γ-VHS

Since it is theoretically suggested that there might be a VHS situated close to the Fermi level, one may expect to see it probed by, for example, ARPES. However experimentally it turned out to be not straightforward at all. Early ARPES results [91] [92] seemed to be consistent with an extended VHS situated at approximately 20 meV below E_F, however they were later found have been interpreted incorrectly, as discussed in subsection 4.1.2.2. Effects of surface states and surface reconstruction were found to have misled the data interpretation [83] [182] and since then it has been generally accepted that there is no VHS originating from the bulk which is situated right below the Fermi level.

After the surface-state problem was overcome, substantial experimental progress with ARPES has been made to detect the position of the proposed γ-VHS, which is suggested to be only a few tens of meV above E_F. For example, by measuring the spectrum of the thermally excited electrons above E_F, H. Iwasawa *et al.* identified the γ-VHS at approximately 20 meV above E_F. [181] This result is not far from that obtained earlier by K.M. Shen *et al.* [47], who reported a slightly lower value of 14 meV, using essentially the same method. In the latter work, the γ-VHS was also approached by chemical doping. Their work will be introduced in the following part on chemical doping effects.

In summary the experimental detection of the position of the γ-VHS by ARPES has turned out to be successful and it is mostly likely between 14 meV to 20 meV above E_F.

4.2.3.3 Studies by chemical doping

Chemical doping is an effective method to tune the chemical potential and to study correlated electron systems. For Sr_2RuO_4, considerable efforts have been made to study the effects of chemical doping and the motivation is often related to the VHSs. The starting point of doping is either focused on the Sr^{2+} ions or focused on the Ru $^{4+}$ ions. In the former case, Sr can either be substituted by another alkali metal ion (e.g. Ca^{2+} [183]), which is isovalent, or by a transition metal ion (e.g. La^{3+} [47] [171]) which is non-isovalent, while in the latter case Ru^{2+} are substituted normally by another transition metal ion (e.g. Ti^{4+} or Ir^{4+} [184] [185]). Regarding the VHSs, the most relevant work might be the studies on the $Sr_{2-y}La_yRuO_4$ system in which a topological change in the γ FS sheet has been directly observed [47] [171].

In 2007 K.M. Shen *et al.* reported their study on the γ-VHS by a combination of chemical doping and ARPES measurements [47]. They studied $Sr_{2-y}La_yRuO_4$, in which Sr^{2+} ions are partially substituted by La^{3+}. The substitution is expected to introduce more electrons to the system while leaving the crystal structure minimally distorted. [171] Therefore the electron-like FS sheets (β, γ) should expand while the hole like FS sheet (α) should shrink correspondingly, and since the γ band FS is more sensitive to the increase of the electron concentration due to the proximity to the Fermi level, a topological change in the FS shape should be seen at a certain doping level, when the M point at the Brillouin zone boundary is touched. This expected change in the γ band FS was indeed observed by K.M. Shen *et al.* through ARPES measurements and is shown in Figure 4.18. It is seen in Figure 4.18 that from y = 0.18 to y = 0.27 the FS undergoes a topological change in its shape and its central position is also changed, thus the point at which the VHS occurs must be between y = 0.18 and y = 0.27. By making
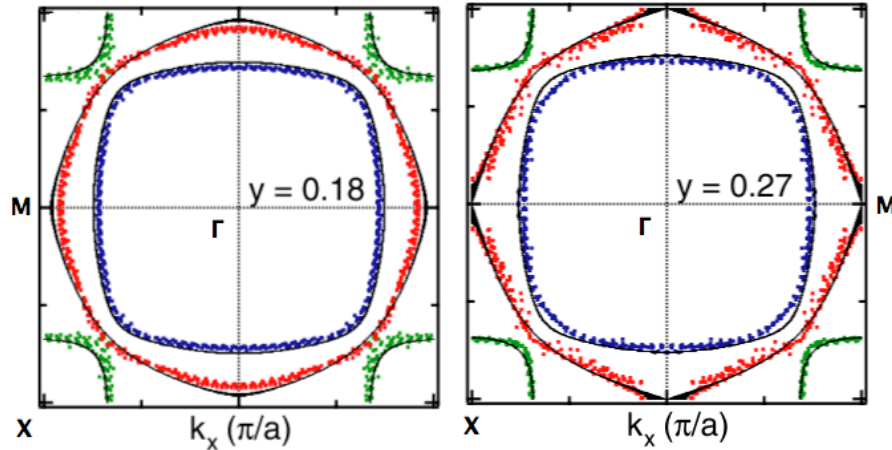
FIGURE 4.18: The FS of $Sr_{2-y}La_yRuO_4$, probed by APRES. The FS topography is shown for two doping levels, y = 0.18 and y = 0.27. It is seen that with y = 0.18, the γ band FS sheet is still centred at the Γ point (electron-like, similar to that of pure Sr_2RuO_4, c.f. Figure 4.5), while with y = 0.27 it becomes centred at the X point (hole-like) and a topological change has occurred. Black solid curves in the figure are the results obtained by a tight-binding (rigid-band shift) model. The figure is adapted from [47].

careful comparison with with the spectrum of the thermally excited electrons in pure Sr_2RuO_4, K.M. Shen *et al.* concluded that the γ-VHS is approached with y$\sim$0.2.

The results and conclusions of K.M. Shen *et al.* are consistent with the results obtained earlier by N. Kikugawa *et al.* [46] [171]. The ARPES measurements, in combination with dHvA and thermodynamic measurements have provided rich information about the evolution of several quantities as the system traverses the VHS. For example, from y = 0 to y = 0.27, the carrier number (per Ru) for the α and the β band FS sheet shows monotonic decrease and increase respectively, while for the γ band FS sheet, due to the electron-like to hole-like FS change at the VHS the initial carries number increase is interrupted at y$\sim$0.2. An interesting finding is that the electronic specific heat coefficient is enhanced upon approaching the VHS, and that the enhancement seems to be consistent with a picture of whole bandwidth ($\boldsymbol{k}$ independent) renormalisation. Another remarkable feature is that quantum oscillations survived with as much as 6% doping for all three main frequencies and as much as 10% for the α FS sheet. The superconducting transition temperature is suppressed to zero with y = 0.03. No longer range order is found in the La doped system as the VHS is crossed.

In summary, the studies by chemical doping have yielded considerable information in terms of the γ-VHS, especially in the sense that the proposed topological change in the FS shape has been directly observed by the combination of chemical doping and ARPES measurements. The dHvA and thermodynamic measurements performed upon moving to the VHS have also generated interesting results and new questions. In addition, although not discussed here, the vicinity to magnetic instabilities in phase space proposed by theories (e.g. [45]) are also (at least partially) verified, by for example the fact that magnetic order can be stabilised by 9% Ti doping [184]. Despite the success, chemical doping studies share a common problem, i.e. the superconductivity is always quickly suppressed, way before the VHS is reached, which makes more in-depth study difficult. This is one of the main reasons why the possibility to approach the VHS by uni-axial strain, which is a chemical clean method, offers me a valuable chance to attack this problem.

4.3   Approaching the VHS by uniaxial strain

The discussion above shows that studies on the VHSs in Sr_2RuO_4 are important to understand its superconducting and normal state properties. Although useful information has been obtained by chemical doping together with ARPES, dHvA and thermodynamic measurements, there are fundamental problems brought by the method itself, because chemical doping inevitably needs to introduce extrinsic ions to the system which rapidly suppresses the superconductivity and makes further studies impossible by the point when the VHS is approached. Therefore, to bring the VHS to the Fermi level without suppressing the superconductivity, if possible, will be highly desirable. Moreover, in the spirit of band-by-band study this type of work is also of great interest, because effects related to the FS distortion, if they could be observed, should be mainly associated with the γ band. In this section, I will introduce the possibility to approach the VHS without introducing atoms of extrinsic elements by applying a new method — piezoelectric based uniaxial strain technique.

4.3.1 Motivation

4.3.1.1 Suggestions from electronic structure calculations

C. Hicks *et al.* [6] showed that the FS of Sr_2RuO_4 can be altered drastically by applying strain along either of the principal axes. Figure 4.19 illustrate the FS shape of Sr_2RuO_4 (at $k_z = 0$) in the presence of 0.5% compression (blue curves) and tension (black curves), calculated with a Wien2K package [186]. It can be seen that the compression brings the γ FS sheet closer to the M point of the (2D) Brillouin zone boundary (and its symmetrical points), which is the Van Hove point. Further calculations suggest that stronger compression can enable the γ FS sheet to reach the M point, and when this happens, a topological change in its shape will occur, marking the arrival at the VHS. The FS sheet γ will change from an electron-like FS centred at the Γ point to a hole-like FS centred at the X point, similar to that shown in the right panel of Figure 4.18.
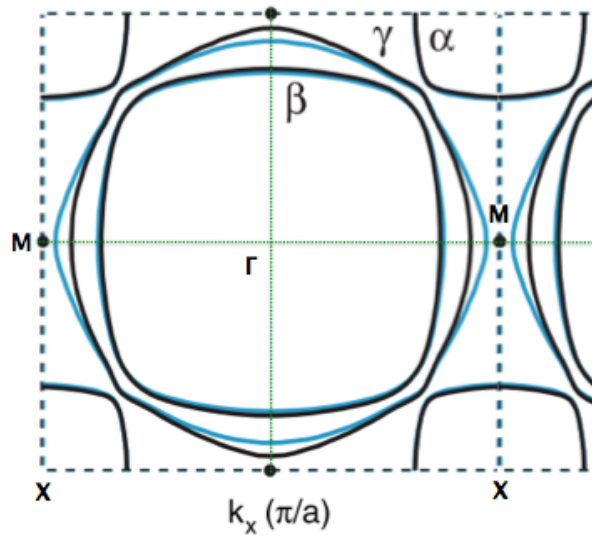

FIGURE 4.19: The FS deformation of Sr_2RuO_4 in the presence of uniaxial strain applied in the <100> direction. The blue and black curves show the FS under 0.5 % compression and tension, respectively. It is clear that the γ band FS sheet is brought closer to the M point, the Van Hove point. When the FS sheets from neighbouring Brillouin zones join each other at the M point, the VHS occurs. The dashed lines in the figure indicate the two dimensional Brillouin zone boundaries. Figure modified from [6] .

The magnitude of the strain needed to reach the γ-VHS, according to the electronic structure calculations, is in the range of 0.5% - 1.0%, which can likely be realised with improved piezoelectric based uniaxial strain method, as introduced in Chapter 3. Thus the uniaxial strain method technically provide a new and realistic method to approach the VHS in Sr_2RuO_4.

4.3.1.2 Motivations of the study

If the γ-VHS can really be traversed by the piezoelectric based uniaxial strain method, one can imagine a series of important experiments, which have never been possible by far, to understand the superconducting properties of Sr_2RuO_4, including the pairing symmetry, in a way that is highly controllable and convenient to operate.

The immediate effect one can imagine upon approaching the VHS is the response of the superconducting transition temperature T_c, hints of which have already been obtained from previous work done by C. Hicks *et al.* [6] , whose results are shown in Figure 4.20. They applied both tensile and compressive strain of magnitude up to
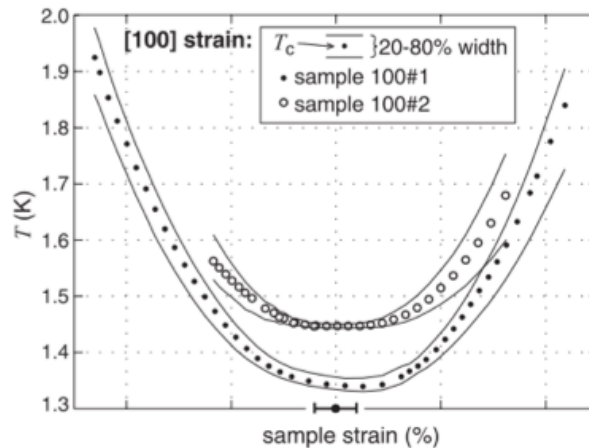

FIGURE 4.20: T_c of Sr_2RuO_4 versus strain parallel to the <100> direction (ϵ_{100}). Results from two samples are shown. Solid and open circles indicate the T_c, taken as the temperature at which 50 % of the jump of the in-phase susceptibility χ' at the SS-NS phase transition was observed. The black curves indicate the transition width, by marking the 20 % and 80 % points. For the description of the T_c dependence on ϵ_{100}, see the main text. Figure from [6] .

approximately 0.23 % and observed the response of T_c by measuring the ac susceptibility of the sample. Their focus was mainly to check whether the T_c dependence

on strain ϵ_{100} (parallel to the a or b axis) would show a V-shaped cusp around $\epsilon_{100} = 0$, as suggested by their theoretical analysis based on a two-component Ginzburg-Landau model for the chiral p-wave order parameter (shown in the supplementary material for their report). Interestingly the expected V-shaped cusp of T_c versus ϵ_{100} was not seen (at least not resolved within the experimental resolution), instead parabolic strain dependence of T_c was seen at $\epsilon_{100} > 0.03$ % and essentially zero strain dependence of T_c was seen at $\epsilon_{100} < 0.03$ %. Although their results do not obviously support the chiral p-wave order, they opened the possibility to approach the VHS with uni-axial strain techniques.

It is highly desirable to extend the compressive strain range to approach the VHS[24] and simultaneously observe the response in T_c, because it has the potential to provide valuable information about the pairing symmetry. The basic idea is the following. For a chiral p-wave order parameter, in the BCS theory by symmetry in reciprocal space there should be a phase difference of π in the order parameter on opposite sides of the M point in Figure 4.19, therefore the gap size should decrease on approaching this point. In contrast, if it is d-wave, there will be no such phase difference in the order parameter and an increase in T_c might be seen due to the increase of DOS on approaching the VHS. Therefore the response of T_c to ϵ_{100} is expected to reflect the pairing symmetry. Thus observing the response of T_c under compression that is strong enough to traverse the VHS is one of the main motivations of my research.

Another interesting quantity to measure, as an attempt to detect effects (in addition to the change of T_c) associated with the DOS enhancement upon approaching the VHS, is the upper critical field H_{c2}. By Ginzburg-Landau theory [134], $H_{c2} = \Phi_0/2\pi\xi^2(T)$, where $\Phi_0 = hc/2e$ is the flux quantum, $\xi(T) = \xi(0)[(T_c - T)/T_c]^{-\frac{1}{2}}$ is the temperature dependent Ginzburg-Landau coherence length, which in the $T \to 0$ limit is similar to the Pippard coherence length. Considering that the coherence length is related to energy gap size by $\xi(0) = \hbar v_F/\pi\Delta$ [187], where $\hbar$ is the reduced Planck constant, v_F is the Fermi velocity, and Δ is the size of the

---

[24]Too high a tensile strain will break the sample, thus is not wanted regarding the studies on the VHS.

superconducting energy gap, at $T = 0$, $H_{c2}\mid_{T=0} = \Phi_0/2\pi\xi^2(0) = \pi\Phi_0\Delta^2/2(\hbar v_F)^2$. Since the gap size Δ is proportional to $k_B T_c$, the upper critical field $H_{c2}\mid_{T=0}$ should be proportional to the square of the critical temperature T_c. However, given that the Fermi velocity in the Fermi liquid theory is closely related to the DOS by $g(E_F) = k_F^2/\pi^2\hbar v_F$ and that the DOS will be much enhanced upon approaching the VHS, the upper critical field $H_{c2}\mid_{T=0}$ may simultaneously be influenced by T_c and the non-constant v_F. Therefore experimentally it is interesting to see what the total outcome would be, as we drive the system towards the VHS. This is another important aspect of my research.

There are certainly more quantities one can consider to measure as the system approaches the VHS, the resistivity (in the normal state) for instance, however as mentioned earlier the current work is just a beginning of a series of potentially important experiments, and thus realistically I restricted myself to only measuring T_c and H_{c2}.

4.3.2   Measurement preparation

To observe the response of T_c or H_{c2} while tuning the system towards the VHS, two things need to be done. One is to apply a controllable and known uniaxial strain to the sample and keep it stable, and the second is to detect the superconducting transition under the applied strain, when the temperature or the applied magnetic field is ramped. For the former, a comprehensive description has been given in Chapter 3, covering methods to generate and to measure the applied strain, and guidance for sample mounting. Methods used to measure and to control the sample temperature have also been described there. Thus in this subsection I will mainly describe a few aspects beyond the description given in Chapter 3. These include the sample preparation, the sample mounting procedure, and the detailed methods used to probe the superconducting transitions.

4.3.2.1 Sr_2RuO_4 sample preparation

The single crystals of Sr_2RuO_4 used in this work were grown in the research group led by Y. Maeno in Kyoto University, with the floating-zone method in an image furnace, a method that is well known to be able to grow single Sr_2RuO_4 (and also $Sr_3Ru_2O_7$) crystals of very high quality. The superconducting transition temperature T_c exceeds 1.4 K, suggesting high crystal purity [55].
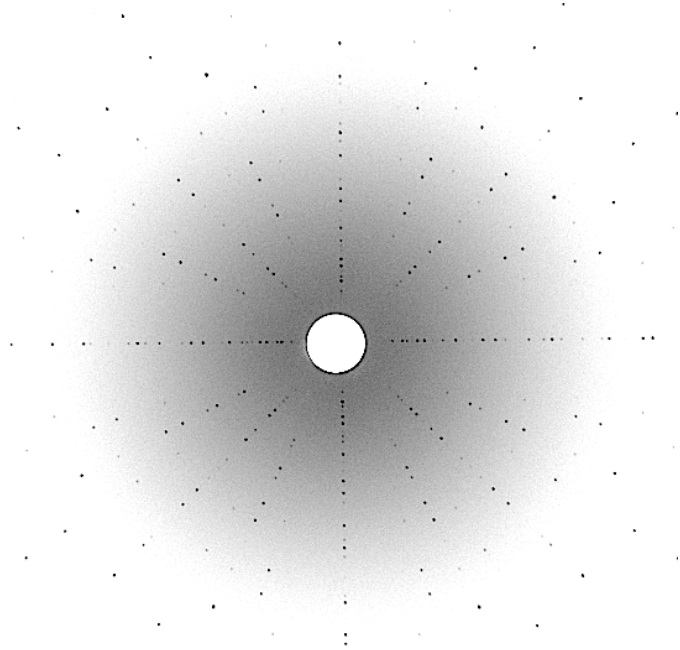

FIGURE 4.21: The Laue X-ray image for Sr_2RuO_4. The incident X-ray beam was normal to the *ab* plane of a cleaved sample. Intensity of the reflected X-rays is indicated by darkness. The reflected X-rays were collected using a photosensitive plate, which had a hole in its centre to guide the incident beam. The hole gave rise to the big white circular spot in the centre of the image. The X-ray pattern respects the symmetries of the crystal structure. By carefully comparing the collected Laue pattern with the results of simulation and repeating the same procedure after rotating the sample around its surface normal by a certain angle, we were able to determine the orientation of the crystal principal axes. The horizontal and vertical directions in the figure correspond to the directions of the a or b axis of the sample. No distinction of the two was resolved, as expected for a tetragonal crystal structure.

Since the desired strain needs to be applied in the <100> direction (parallel to either the *a* or *b* axis), the sample should be correspondingly cut along the <100> direction. The crystal orientation was measured with a Laue camera in the Centre for Science at Extreme Conditions in Edinburgh. For the Laue experiment, a sample with a cleaved surface (the *ab* plane) was firstly glued to an Aluminium holder

which was to be fixed onto a goniometer, and then was aligned such that the incident X-ray beam was perpendicular to its surface. The alignment was guaranteed by adjustments guided by a red laser beam whose path was set to coincide with the X-ray beam. The scattered X-rays were collected with a (photosensitive) cassette, which was then read out by an image processing machine FCR CAPSULA from Fujifilm. Figure 4.21 shows the collected X-ray scattering pattern. Regarding the orientation of the crystal principal axises, the horizontal and vertical lines in the figure correspond to the direction of the a or b axis of the sample, as described in detail in the figure caption.

After the crystal orientation was determined, I cut the crystal along the <100> direction to obtain rectangular-slice shaped samples whose dimensions are approximately 1.5 mm (length) * 0.25 mm (width) * 0.05 mm (thickness). (The 1.5 mm long edges are parallel to the <100> direction and the relatively wide surfaces are parallel to the *ab* plane.) The determination of sample dimensions followed the suggestions given by the finite element analysis discussed in Chapter 3. The crystal tended to cleave during the sample cutting process, which made the thickness of the cleaved samples typically vary between 0.03 mm to 0.07 mm. For later measurements, I chose those whose thickness were approximately 0.05 mm. The sample cutting was performed with a home made wire saw. The sample was installed onto a wooden sample holder, which was fixed against the wire saw. A 25 μm tungsten wire was driven to move over the crystal rapidly and simultaneously to gradually cut into the sample vertically. The abrasion was provided by SiC slurry (grain size less than 3 μm) that filled the gap between the tungsten wire and the sample.

The samples that had been cut into the right shape were then cleaned with ultrasonic methods, to remove residual SiC slurry grains and other possible contamination. After being cleaned, the samples were placed on top of a quartz plate and were heated up to 500 °C (in air) in a furnace for approximately 48 hours. The heat treatment was to release the internal stress at the sample edges, which were damaged during the cutting. The necessity of doing so came from the finding

that the sample edge could possibly have higher T_C than the bulk [25] and could be potentially hazardous to the experimental results.

Two conductive contacts were made for the sample to be measured, with 25 μm gold wires and silver epoxy 6838 from Dupont, each at one end and was situated only on one side of the sample. These contacts were used to check for sample fracture when the experiments were performed.

4.3.2.2 Sample mounting

The prepared Sr_2RuO_4 sample was mounted on to the strain device following the instructions described in Chapter 3 (c.f. Section 3.1.3.3). The device had two sample plates (see Figure 3.2 and Figure 3.5) installed on it with a thin slot in between, each supported and held one end of the sample with an indentation milled in the middle starting from the plate edge. The indentation was 800 μm long, 500 μm wide and 70 μm deep, and was milled such that when the plate was installed onto the strain device it was parallel to the long axis of the piezo-stacks. When both sample plates were installed and aligned, the two ends of the sample were fixed into the two indentations by Stycast 2850. Since each end of the sample only had approximately 350 μm embedded in the epoxy, there was still approximately 600-800 μm left (depending on the length of the whole sample) between the two sample plates, that was available for measurements. The sample was placed such that its long axis was parallel to the long axis of the piezo stacks. Since the indentation was approximately 70 μm deep while the sample was approximately 50 μm thick, the epoxy was approximately 10 μm thick below and above the sample close to the ends, respecting the suggestions from the finite element analysis. Also following the suggestion of the simulations, a narrow rectangular titanium slice (roughly 3 mm long, 0.2 mm wide and 0.1 mm thick) was placed over each end of the sample and on top of the sample plate, to symmetrise the strain on opposite sides of the sample.

---

[25] Alexander Gibbs, private communication.

After the sample was properly mounted and aligned, it was heated to 80°C together with the whole strain device for 2.5 hours to cure the epoxy.

4.3.2.3 Detecting the superconducting transitions

One of the key factors for the measurements is to detect the superconducting transitions at low temperatures, when the temperature or the magnetic field is ramped. A simple way to detect the transition at T_c or H_{c2} is to observe the response of the sample to a small AC magnetic field H_e ($H_e \ll H_{c2}$). The basics of the method are introduced below.

An excitation coil (150 turns, $\Phi = 3$ mm) was used to generate an AC magnetic field, which was placed such that its centre coincided with the middle of the sample. The middle of the sample was situated in the relatively homogeneous region of the AC field. A much smaller coil (35 turns, $\Phi = 0.18$ mm) was used as the pickup coil, to monitor the magnetisation of the sample. It was placed right on top of the sample (fixed by GE varnish), concentrically with the excitation coil. Therefore its centre also coincided with the middle of the sample. Due to the mutual inductance, the AC field generated by the excitation coil could induce an AC voltage in the pickup coil, which can be signalled by, for example, a Lock-in Amplifier. When the sample undergoes a superconducting transition, the field felt by the pickup coil will be rapidly changed due to the demagnetisation of the superconducting sample situated right underneath it, thus the induced voltage will be changed correspondingly. Therefore, by monitoring the AC voltage of the pickup coil one can in principle sense the superconducting transition.

A numerical estimate might be helpful to understand the magnitude of signals in the experiments. Close to the centre of the excitation coil, where the induced magnetic field is supposed to be relatively homogeneous, the AC field generated by the coil can be estimated by (assuming each turn has the same radius)

$$B_1(t) = \frac{N_1 \mu_0 I_1(t)}{2R_1} \tag{4.6}$$

where μ_0 is the magnetic permeability in vacuum, R_1 (= 1.5 mm) and N_1 (= 150) is the radius and the number of turns of the excitation coil, respectively, and $I_1(t) = |I_1|\sin(\omega t)$ is the time dependent current in the coil. Assuming the maximum of $I_1(t)$ equals to 150 μA and putting all the numbers in one would obtain $B_1(t) = 0.01$ mT, which is much smaller than the H_{c2} of Sr_2RuO_4 (75 mT for field parallel to the c-axis). The pick-up coil, which is placed in the central area of the excitation coil, is so small that the field it feels can be regarded homogeneous, and then the voltage induced in it can be estimated by

$$
\begin{aligned}
U_2(t) &= \frac{d\Phi_{12}}{dt} \\
&= \frac{d}{dt}\left(\frac{\mu_0 I_1(t)}{2R_1}N_1 N_2 \pi R_2^2\right) \\
&= \frac{\mu_0|I_1|\omega\sin(\omega t)}{2R_1}N_1 N_2 \pi R_2^2
\end{aligned}
\tag{4.7}
$$

where Φ_{12} is the magnetic flux penetrating the pickup coil, induced by the current in the excitation coil, ω is the frequency of the AC current, and all the rest variables have similar meaning as those in equation with the only difference being that the subscript 2, if appears, refers to the pickup coil. It can be seen from equation 5.1 that the maximum induced voltage in the pickup coil, which satisfies $U_{2-max} = \frac{\mu_0|I_1|\omega}{2R_1}N_1 N_2 \pi R_2^2$, is dependent on the frequency of the excitation current. Assuming $\omega = 5000$ Hz, and putting all the numbers in the equation, one obtains $U_{2-max} \approx 52$ nV. Since the pickup coil sits right on top of the sample and its diameter is smaller than the width of the sample, as the sample undergoes a superconducting transition, the signal change in U_2 should be of the same order of itself and it should be detectable by Lock-in amplifiers.

4.3.3 A short summary of the experimental conditions

When the experiment was performed, the temperature of the strain device was on the order of sub-Kelvin to Kelvin (below 10 K). To realise such low temperatures, as described in Chapter 3, a dilution refrigerator was used. The probe was installed underneath the cold plate of the mixing chamber of the dilution refrigerator, and

was sealed in the inner vacuum chamber (IVC) of the refrigerator. Twisted wires were adopted to reduce the noise level between the strain device and the 24-way connector on top of the insert of the refrigerator, and heat sinks were used at each stage to improve the thermalisation. The temperature was read out by a resistance bridge Lakeshore 370, which was also used to control the temperature of the strain device.

The current for the excitation coil was generated by a current source, consisting of a 1 kΩ resistor and the AC output voltage of a lock-in amplifier SR830. (The resistance of the rest of the circuit if much less than 1 kΩ.) Typical excitation current applied in the measurements was approximately 150 μA. To read out the AC susceptibility signals generated at low temperatures, the pickup coil was connected to an SR550 amplifier (gain = 100) before it was connected to the input of a lock-in amplifier SR830.

The capacitive method used to measure the applied strain has been described in Chapter 3, so it is not repeated here. One thing to mention though is that the resolution of strain is not limited by the resolution of the capacitance bridge but by other factors like the stability of the piezo-stacks.

The magnetic field needed to measure the upper critical field was generated by a three-axis vector magnet (9T$\times$1T$\times$1T). The vector magnet was used because it could significantly simplify the process to align the field to the desired direction. Details for the field alignment will be described in next section.

4.4   Measurements and results

The measurements I have performed on Sr_2RuO_4 mainly consist of two parts. One part is about the T_c dependence on the uniaxial strain ε_{100}, and the other part is about the dependence of the upper critical field H_{c2} on temperature at different uniaxial strains. These two parts of work and the corresponding results contribute to the main content of this section.

4.4.1 T_c dependence on the uniaxial strain

4.4.1.1 Tests under zero strain

At the beginning of the measurements, the influence of a few key experimental parameters on the results was tested, for example, the magnitude of the excitation current, the frequency for the AC susceptibility measurements and the temperature sweeping rate. The following set of parameters were eventually applied in the measurements, based on the results of parameter optimisation. The excitation currents was 150 μA, and the frequency was 5113 Hz. The temperature sweep rate was usually set to be 30 mK/min.[26] An example of the raw experimental data, obtained with the above-mentioned experimental parameters, is shown in Figure 4.22a.
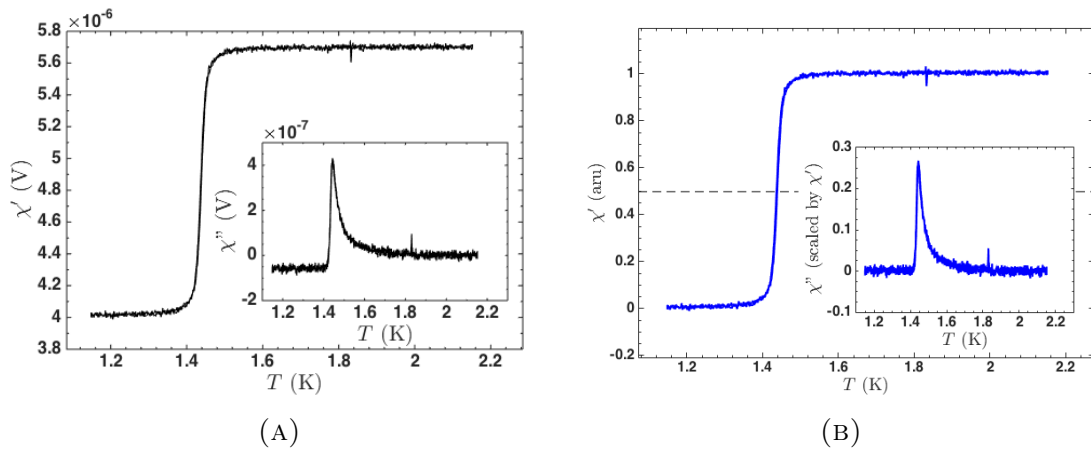

FIGURE 4.22: The AC susceptibility of Sr_2RuO_4, obtained with a sample cut along the <100> direction and measured with zero voltage applied to the piezo-stacks. (A) Raw data.The real part (χ') and the imaginary part (χ'') are shown in the main panel and the inset respectively. A neat and steep jump in χ' can be seen at approximately 1.45 K, indicating the superconducting transition of the sample. The peak in χ'' reflects the energy dissipation at the superconducting transition. (B) The rotated and normalised χ' (main panel), and the scaled χ'' (inset). For the explanation to the rotation and normalisation/scaling, refer to the text. The 50% level is indicated by a dashed line.

In Figure 4.22a, χ' and χ'' refers to the in-phase and out-of-phase part of the AC susceptibility, respectively. The steep jump in χ' and the anomaly in χ'' indicate

---

[26]In some temperature sweeps, the T sweeping rate was set to be 60 K/min far away from the the superconducting transitions (close to the transition, the sweeping rate was still 30 mK/min).

the superconducting transition at approximately 1.45 K. The features indicating the transition are neat and evident. Taking into account that the signal magnitude shown in Figure 4.22a has been amplified by a factor of 100 (due to the application of the amplifier), the magnitude of χ' in the normal state matches the estimate given in last section (55 nV, c.f. subsection 4.3.2.3).

For the data shown in Figure 4.22a, the voltage applied to the piezo-stacks was zero. The reading of the capacitive strain gauge was essentially identical to that at room temperature, indicating that the sample was at least very close to zero strain. This strain gauge reading is then taken as the reference level for the position of zero strain in subsequent measurements.

To quantitively extract T_c from the susceptibility data, the following procedure is adopted. Firstly the the imaginary part χ'' is rotated by an appropriate angle (usually around 2°) such that χ'' well below T_c equals that well above T_c, to eliminate phase shifts caused in other parts of the electric circuit. The real part χ' is rotated by the same angle. The rotated χ', measured with respect to the value well below T_c, is then normalised by magnitude of the total jump in χ' (i.e. the subtraction between χ' well above T_c and well below T_c.) The outcome is shown in Figure 4.22b. The rotated χ'', after being scaled by the jump-magnitude in χ' at the transition, is also shown in Figure 4.22b (the inset). Following the definition of T_c by C. Hicks [6] , T_c in most cases is taken as the 50% level of the superconducting transition. Whenever it is not, the reason will be explained and a new definition will be specified. This results presented in the following also follow this data processing procedure.

The difference between the T sweeping-up and sweeping-down curves was examined. In Figure 4.22, very little difference can be resolved between the two sets of curves. Quantitive analysis suggests that the difference in T_c is no more than 3 mK, which was small enough to be negligible for our data analysis.

4.4.1.2 Measurements under strains

Since practically the γ-VHS is only accessible through compression (tensioning the sample too much will break it before the VHS is approached), my attention to the T_c dependence on strain was mainly on its evolution under compression. With the uniaxial strain techniques introduced in Chapter 3, I successfully applied uniaxial displacement along the <100> direction up to 7.7 μm [27] to a sample whose length between the two sample plates was approximately 667 μm. However the finite element analysis suggests that about 20% of it goes into the epoxy surrounding the sample ends, and correspondingly the maximum of the displacement of the sample only approximately 7.7 μm$\times$80% = 6.16 μm. When evaluated in percentage, the maximum strain of the sample was approximately 0.92%.

Figure 4.23 (next page) shows the real and the imaginary part of the AC susceptibility as a function of temperature under a series of selected uniaxial strains, mainly under compressive strains. The negative sign indicates compression. The most prominent feature in Figure 4.23 is probably that the superconducting transition temperature can be enhanced up to 3.45 K by uniaxial compression and the enhancements show hints of saturation close to the highest applied compression. As the magnitude of ε_{100} is increased from zero (for compression), the superconducting transition is pushed to higher temperatures and at the same time the transition width is slightly broaden, which is reflected in both χ' and χ". This is possibly due to the strain inhomogeneity across the volume of the sample underneath the pickup coil. However, interestingly, on approaching $|\varepsilon_{100}| \approx 0.92\%$ the transition becomes sharp again, and actually the curves of χ' is sharpened so much that the onset of the transition can provide a well defined transition temperature T_c, and it seems unchanged above $|\varepsilon_{100}| \approx 0.86\%$. In Figure 4.23 a hump in χ' could be seen at approximately 3.3 K at $|\varepsilon_{100}| = 0.92\%$ (accompanying which a quasi-peak appears in χ"), however without further evidence it is not yet clear whether this hump is due to strain inhomogeneity or is intrinsic to the material.

---

[27]The scales of the applied strains were inferred based on the reading of the calibrated capacitive strain gauge.
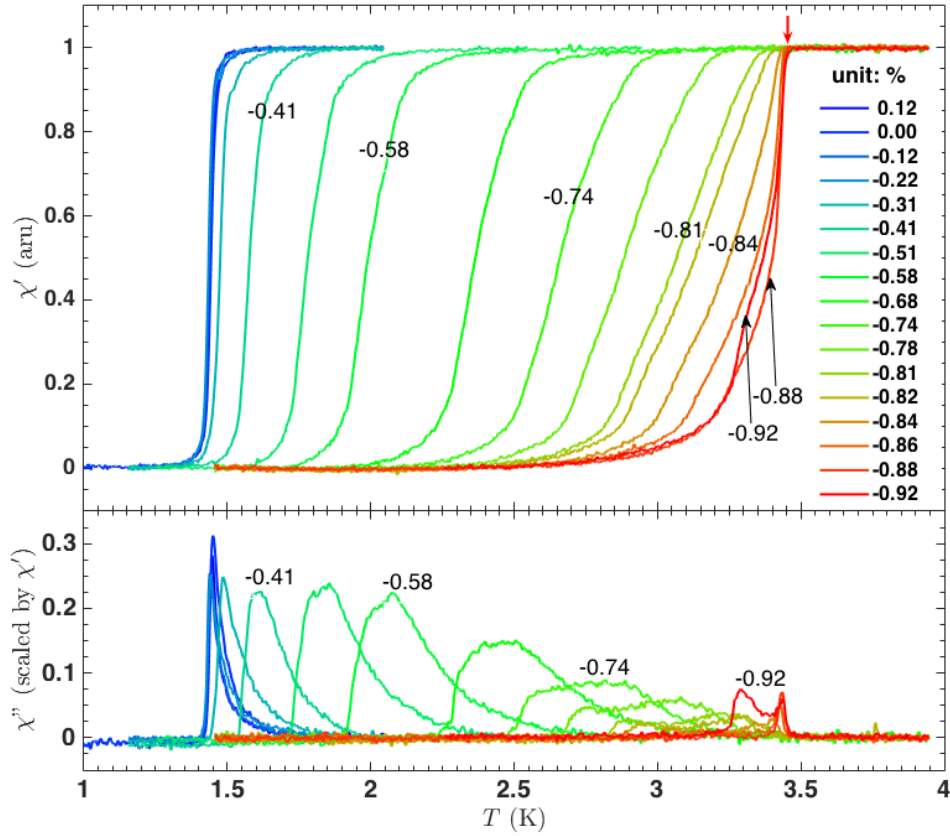
FIGURE 4.23: The AC susceptibility of Sr_2RuO_4 under uniaxial strains applied along the <100> direction. For the data shown, the imaginary part χ'' (lower panel) for each strain is rotated by a an appropriated angle such that χ'' well below T_c equals that well above T_c, to eliminate phase shifts caused in other parts of the electric circuit. The corresponding real part χ' is rotated by the same angle and the whole curve for each strain is normalised by χ' well below and χ' well above T_c. For each curve, χ'' shown in the figure was measured with respect to that at the lowest measured temperature and was scaled by the magnitude of the jump in χ'. A few strain scales are marked for the corresponding curves. The saturation point of the onset temperature for the transitions is marked by a red arrow in the upper panel.

To see the T_c dependence on ε_{100} more clearly, T_c is extracted following the procedure introduced on in subsection 4.4.1.1. Figure 4.24 shows T_c as a function of ε_{100}. From the main panel of Figure 4.24, the enhancements of T_c by compression are obviously seen. If one assumes that 0.92% compression is enough to traverse the γ-VHS, then the basic information one can learn from Figure 4.24 is probably that, T_c of Sr_2RuO_4 is enhanced rather than suppressed upon approaching the γ-VHS. This is an important conclusion, and will be discussed further in next section.
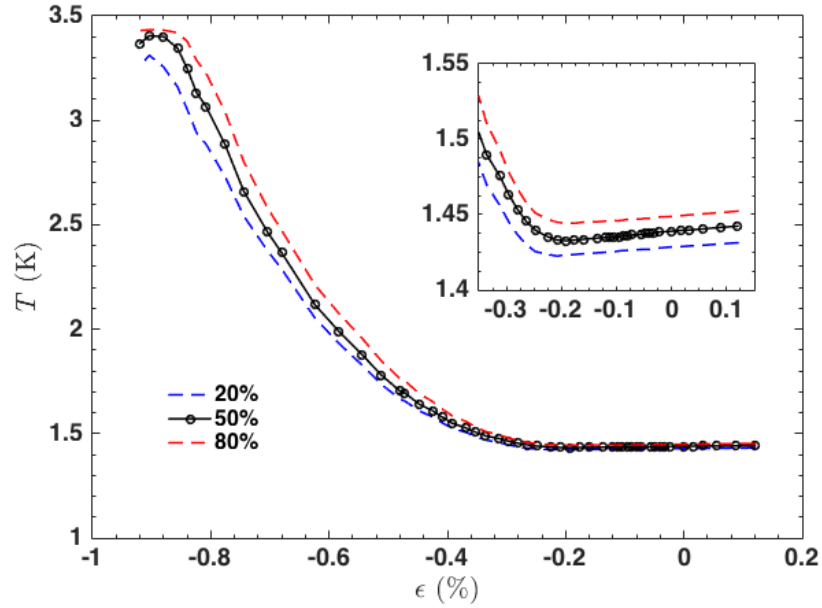
FIGURE 4.24: T_c versus ε_{100}. The solid black curve with open-circle markers shows the transition temperature defined by the position of 50% level. The enhancement of T_c by compression (above $|\varepsilon_{100}| \approx 0.2\%$) is evident. Above $|\varepsilon_{100}| \approx 0.86\%$ the T_c enhancements seem terminated. The small dip in T_c is associated with the appearance of the hump in χ', which is shown in Figure 4.23. It is thus not conclusively intrinsic to the material. In comparison, the 90% level only shows saturation above $|\varepsilon_{100}| \approx 0.86\%$. The dashed curves for 20% and 80% level are used to illustrate the transition width under different strains. It is seen that the transition width is slightly broadened as the compression magnitude is increased, consistent with the results shown in Figure 4.23. Interestingly, the T_c dependence on ε_{100} seems not symmetric around $\varepsilon_{100} = 0$, as shown in the inset. For more discussion, see the text.

More features can be seen in Figure 4.24. For example, above $|\varepsilon_{100}| \approx 0.86\%$, the enhancements of T_c do not continue, and a small dip is even seen in T_c. However, this small dip might be somewhat misleading, since it is related to the hump of χ' as shown in Figure 4.23. The onset temperature of the superconducting transition actually shows saturation instead of a dip above 0.86% compression. Although I am mainly interested in the high compression region, I noticed that around $\varepsilon_{100} = 0$, T_c shows a weak but resolvable decrease from weak tension to weak compression (see the inset of Figure 4.24). The enhancements of T_c occur only above $\varepsilon_{100} = -0.2\%$. This non-symmetric response of T_c around $\varepsilon_{100} = 0$ is for some reason not very consistent with the results of C. Hicks *et al.* [6] . However it does not change the main conclusion mentioned above.

4.4.2 H_{c2} under uniaxial strains

As discussed in section 4.3.1.1, the upper critical field H_{c2} is expected to provide useful information related to the γ-VHS. Therefore I studied the temperature dependence of $H_{c2} \parallel c$-axis at a series of fixed compressive strains, after aligning the magnetic field parallel to the c-axis.

To align the magnetic field parallel to the c-axis, I took advantage of the three-axis vector magnet, which can simultaneously generate a vertical field (z-field) and two orthogonal horizontal fields (x- and y-field). The sample was mounted such that its ab-plane was parallel to the direction of the z-field, so I only needed to find the c-axis direction of the sample in the horizontal field plane. This can be done with the x-field and the y-field. Firstly the temperature was set to be 1.45K, being in the middle of the superconducting transition and thus having a strong response to a small magnetic field. Then I varied the field angle in the horizontal plane with a fixed field magnitude of 2 mT, and simultaneously measured the AC susceptibility signal. The sample c-axis direction was determined by the symmetric point (the maximum) in the curve of χ' as a function of horizontal field angle.
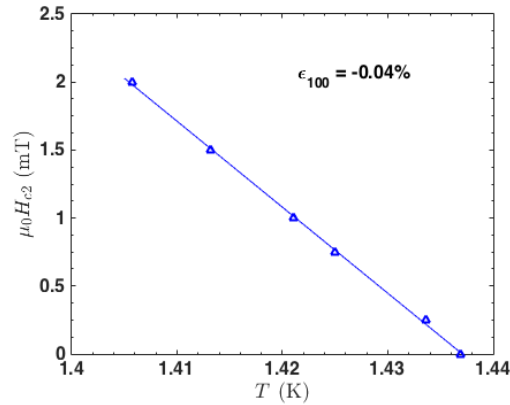

FIGURE 4.25: The temperature dependence of $\mu_0 H_{c2}$ in the proximity of $T_c \mid_{H=0}$, under a weak compressive strain of 0.04%. The solid curves in both panels represents a linear fit to the data.

With the field aligned, I tested the T dependence of $H_{c2} \parallel$ c-axis in the zero field limit. Figure 4.25 illustrates H_{c2} as a function of temperature under a weak compression of 0.04%. (The solid line in Figure 4.25 is a linear fit to the data.) It is seen that the T dependence of H_{c2} is linear. It is essentially identical to

that under zero strain, as shown by S. Kittaka *et al.* [137] (c.f. Figure 4.13a). Quantitively, the slope $\frac{\mathrm{d}H_{c2}}{\mathrm{d}T}\,|_{T_c}$ is approximately -63 ± 2 mT/K in both cases. As discussed in subsection 4.1.3.3, the linear T dependence of H_{c2} is expected by the Helfand-Werthamer theory (see, e.g.[139]). The consistency partially verified the field alignment and indicated a good starting point for the measurements under magnetic fields.

Next I tried to study the temperature dependence of H_{c2} under compression. Experimentally I tried two methods to do it. The first method is to fix the compressive strain and then to sweep temperatures at a series of constant fields, and the other
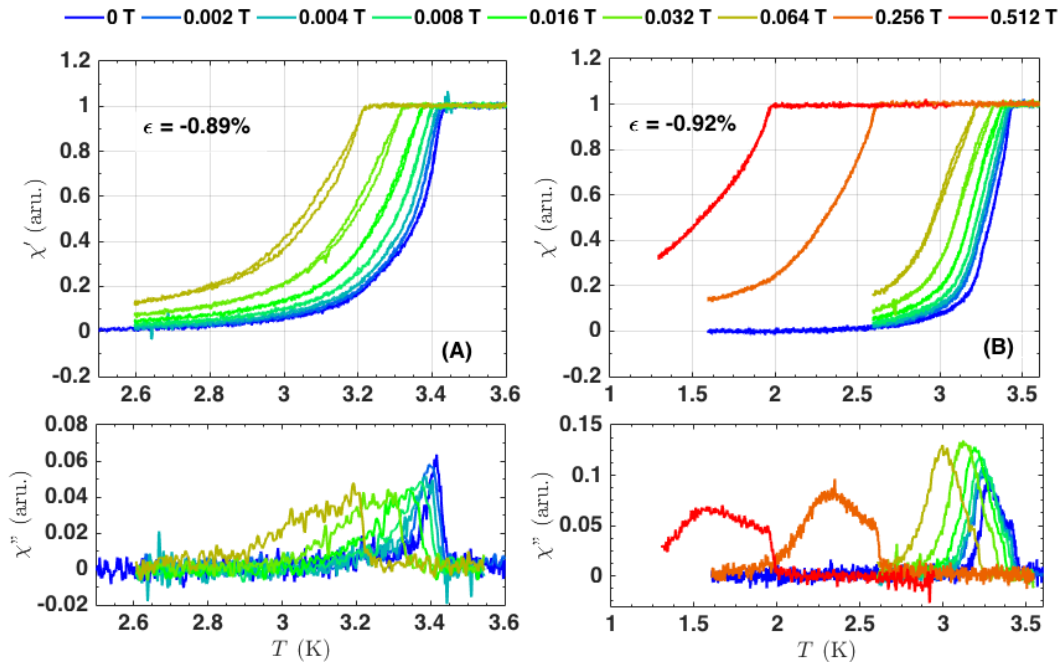

FIGURE 4.26: Temperature dependence of the real and imaginary part of the AC susceptibility, measured in the presence of a series of constant fields under two fixed strains. The two panels on the left show results under 0.89% compression, while the two on the right show results under 0.92% compression. T_c is suppressed by the applied fields in both cases, as expected, and the superconducting transition is broadened at the same time. With a mediate field (e.g. $B = 0.064$ T), some hysteresis could be distinguished between the T sweeping-up and the T sweeping-down curves, and it seems reproducible with both strains.

is to sweep magnetic fields at a series of constant temperatures (also with a fixed strain). Figure 4.26 illustrates the results of temperature sweeps under two representative strains, $\varepsilon = -0.89\%$ and $\varepsilon = -0.92\%$. It can be seen that the transition temperature T_c is suppressed by the applied magnetic fields, as expected. However

more important information in Figure 4.26 is that even under a high compressive strain, when an external magnetic field is applied to the sample, the broadening of the superconducting transition is still limited enough to enable one to properly define a T_c. Actually as shown in Figure 4.26 under such high strains, with the magnetic fields applied, T_c can still be well defined by the onset temperature of the transition, since the sharpening of the transition is well preserved in the presence of magnetic field. To my knowledge this is the first successful measurement of T_c of Sr_2RuO_4 both under high compressive uniaxial strain and in magnetic fields.

Some additional features can also be seen in Figure 4.26. For example, under an intermediate field (e.g. 64 mT), the T sweeping-up and the T sweeping-down curves of χ' showed some hysteresis, which seems reproducible under both strains. The reason for it is not clear at the moment. The hump seen at $\varepsilon = -0.92\%$ in χ' with no field gradually becomes less evident as the field is turned on and its strength increases.

In order to study the temperature dependence of $H_{c2}(T)$ under different compressive strains, I repeated similar temperature sweeps at constant fields under several fixed strains. For explicitness, two sets of well separated curves of $\mu_0 H_{c2}$ are selected to be shown in Figure 4.27, obtained with compressive strains of $\varepsilon = -0.72\%$ (blue) and $\varepsilon = -0.92\%$ (red) respectively. Bearing in mind the magnitude of $\mu_0 H_{c2}(T = 0)$ under zero strain, which is 75 mT, the most prominent feature one can see from Figure 4.27 is probably the strong enhancements of $\mu_0 H_{c2}$ by compressive strains. Taking the case of $\varepsilon = -0.92\%$ for example, at 1.56 K, the $\mu_0 H_{c2}(T)$ is already 512 mT (see the red solid curve), which is higher than the maximum of $\mu_0 H_{c2} \mid_{\varepsilon=0}$ by a factor of approximately 7. Based on Figure 4.27, an estimate of the $\mu_0 H_{c2} \mid_{\varepsilon=-0.92\%}$ in the 0 K limit (using a T_c defined by the onset of the superconducting transition) will be approximately 0.8 T, which is higher than that under zero strain (75 mT) by a factor of 10.7. This enhancement factor is obviously more than the enhancement factor of T_c^2, which is $T_c^2(\varepsilon = -0.92\%)/T_c^2(\varepsilon = 0) = 3.4^2/1.45^2 \approx 5.5$. This is another important conclusion and will be discussed later.
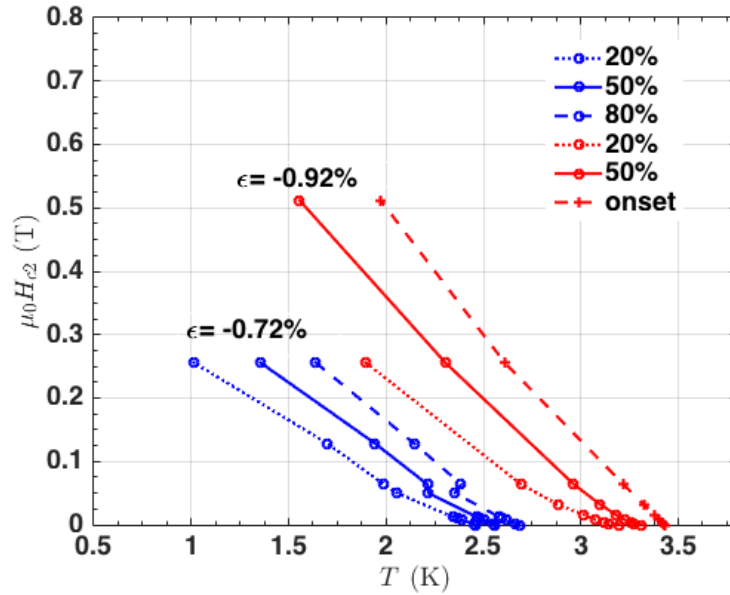
FIGURE 4.27: $\mu_0 H_{c2}$ as a function of temperature under two compressive strains, $\varepsilon = -0.72\%$ (solid blue curve with open circles) and $\varepsilon = -0.92\%$ (solid red curve with open circles). To show the transition broadening in the presence of a magnetic field, the positions corresponding to 20%, 50% and 80% transition levels are marked in the former case, and in the latter case 80% transition levels are replaced by the onset temperatures because for $\varepsilon = -0.92\%$ the onset gives a better definition of T_c. Comparing with the upper critical field under zero strain, which is 75 mT, $\mu_0 H_{c2}$ is obviously strongly enhanced in the presence of compressive strain. With $\varepsilon = -0.92\%$, the curve for $\mu_0 H_{c2}(T)$ given by 50% level seems super linear, however the superlinearity seems not obvious if the transition position is marked by the onset T_c (See the red dash-dot line with crosses).

In Figure 4.27, with $\varepsilon = -0.92\%$, the curves for $\mu_0 H_{c2}(T)$ based on T_c defined by criteria other than the onset of the transition seem superlinear in the small H limit. However since we know that due to the hump in χ' the only reliable T_c is defined by the onset temperature of the transition, the $\mu_0 H_{c2}(T)$ curve for which does not show obvious superlinearity, I will not conclude that the $\mu_0 H_{c2}(T)$ under high compressive strain shows an obvious positive curvature.

The temperature dependence of H_{c2} was also tested by field sweeps under a series of constant strains. The results are similar to that shown above and the results obtained under two selected strains ($\varepsilon = -0.27\%$ and $\varepsilon = -0.72\%$) are illustrated in Figure 4.28. By comparing Figure 4.28 with Figure 4.27, one can see that the T dependence of H_{c2} obtained by the two methods is similar, as expected.
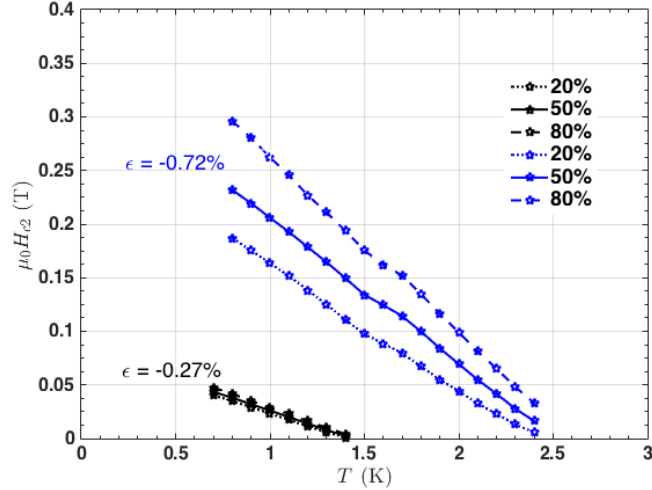
FIGURE 4.28: $\mu_0 H_{c2}$ versus temperature under $\varepsilon = -0.27\%$ (solid black curve with open stars) $\varepsilon = -0.72\%$ (solid blue curve with open stars). The position corresponding to 20% and 80% transition levels is also marked. The enhancements of $\mu_0 H_{c2}$ are also seen in field sweeps, expected.
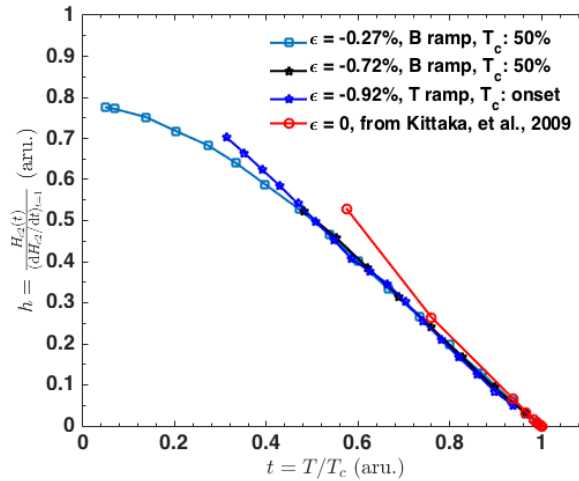

FIGURE 4.29: H_{c2} divided by dH_{c2}/dt in the zero field limit where t it the reduced temperature $t = T/T_c$. The data taken at $\varepsilon = -0.27\%$ and $\varepsilon = -0.72\%$ were obtained through field sweeps and the T_c was defined by the 50% level of the superconducting transition, while the data corresponding to $\varepsilon = -0.92\%$ were taken through temperature sweeps and the T_c was defined by the onset of the transition, which is prominently sharpen under this strain. The data corresponding to zero strain were obtained by digitising the data in Figure 4.13b, which was based on the work of Kittaka *et al.* in [137]. For the description of the data and the discussion, refer to the main text.

It is interesting to know whether the c-axis $H_{c2}(T)$ of the strained Sr_2RuO_4 sample obeys the same temperature of that of unstrained Sr_2RuO_4. To check this I plotted the c-axis $\mu_0 H_{c2}$ decided by the slope of $H_{c2}(T)$ in the zero field limit as a function of reduced temperature $t = T/T_c$, just as Kittaka *et al.* did in [137]

(c.f Figure 4.13b). The result of the comparison is shown in Figure 4.29. In Figure 4.29 I included the data obtained under three compressive strains, $\varepsilon = -0.27\%$, $\varepsilon = -0.72\%$ and $\varepsilon = -0.92\%$, the same with those shown in Figure 4.27 and Figure 4.28 and also the digitised data of Kittaka *et al.* from Figure 4.13b. It seems that in the regime where either the strain of the field is low the data show good consistency, whereas under high strain and high field (comparing to H_{c2}) hint of discrepancy can be seen. It will be very interesting in the future to see what will happen to the normalised $\mu_0 H_{c2}$ when the temperature is lowered further.

4.5   Discussion and conclusion

In section 4.4.1, the dependence of the Tc of Sr2RuO4 on compressive strain was presented. Despite of some details, the fundamental observation is that under substantial compressive strain, the γ-VHS, T_c of Sr_2RuO_4 is enhanced instead of being suppressed. Following the discussion in Section 4.3.1, in a naive single-band BCS picture, this conclusion does not support the scenario of p-wave superconductivity. If it were p-wave, the symmetry imposed phase difference of π on opposite sides of the M-point of the Brillouin zone might be expected to give rise to a suppressed T_c as the γ Fermi surface sheet is pushed towards the M-point by compressive strain. However to really determine whether this discovery disfavours p-wave superconductivity careful calculations will be needed.

The magnitude of the enhancement in T_c, induced by uniaxial strain, is as big 230%. The fact that the superconducting transition is broardened as the sample is compressed from zero strain could be explained by strain inhomogeneity in the region under neath the pickup coil. If we assume that the uniaxial strain applied to the sample is big enough to traverse the VHS of Sr_2RuO_4, then the re-sharpening of the transition at very high strain (close to -0.92%) might be explained by the possibility that although there is strain inhomogeneity in the region beneath the pick-up coil, as a higher and higher fraction of the sample in that region is driven to the VHS, a DOS plateau is reached and more and more of the sample in the

probed area becomes superconducting at the same temperature, which re-sharpens the transition curve of χ.

In subsection 4.4.2 I showed that even under substantial compression measuring T_c in the presence of a magnetic field is still possible using the piezo-electric based uniaxial strain methods. This made it possible to construct a $\mu_0 H_{c2}$-T phase diagram under strain. The experimental data suggest that under strain the enhancements of $\mu_0 H_{c2}$ goes faster than that of T_c^2. This in turn suggests an enhancement due to the increasing DOS as the γ-VHS is approached. (Otherwise if $\mu_0 H_{c2}$ is enhanced merely due to the enhancements of T_c^2, then when T_c is enhanced to 3.4 K, $\mu_0 H_{c2}$ would be approximately 0.39 T at $T = 0$ K, which is obviously too low comparing with the experimental results shown in Figure 4.27 and Figure 4.28.) The temperature sweeps at constant fields and the field sweeps at constant temperatures yielded similar results, as expected. Although $\mu_0 H_{c2}$ is much enhanced under compression, it, in the form normalised by dH_{c2}/dt in the zero field limit, still follows the same relationship with respect to reduced temperature t at least in the temperature range covered by the current measurements. A hint of deviation could be seen at low temperatures and under high compression but it is not clear whether it will develop when the temperature is lowered further.

Since I have only presented data from one sample in this chapter, a natural question concerns the reproducibility of the results that I have reported. The measurement is a very difficult one, and in addition to the fully successful run on which I have concentrated, I experienced many partially or completely failed runs. During my thesis research, two partially successful runs reached higher values of T_c (2.4 and 2.6 K) than had previously been published by our group, but they gave no additional information to that reported here. Finally, during the period when I was writing this thesis, and sixteen months after the run described here, my colleague Alexander Steppke succeeded in covering the same range of T_c on a different sample. The main qualitative features reported here (maximum Tc above 3.4 K and the transition sharpening near T_{c-max}) have now been repeated, and the new data give clearer evidence that a maximum is reached, with T_c slightly

dropping again at higher strains. I am therefore completely confident that the key results presented in this chapter are reproducible.

Some technical aspects of the work still require further investigation, however. In order to attempt these measurements, we worked with a '2nd generation' strain probe with several design changes over that used in the work of Hicks *et al* [6], and what might be a crucial change, namely the capacitive sensing of the strain. Although both the strain gauge used in the original work and the capacitive sensor used here were carefully calibrated, the strain scale that I report is over 50% larger per kelvin change of T_c than that measured by Hicks *et al.* Further work will be required to sort out this discrepancy, but I note that all the group's four rigs that have worked with capacitive strain measurement are discrepant from the strain-gauge-based design by approximately the same amount.

A second mystery is why I did not measure a symmetric Tc response around zero strain. The most likely reason is some mechanical failure of either the sample or the rig, but that would not fully explain my observation of a small but resolvable T_c change as I attempted to tension. Again, this will require further investigation, but I put little time into applying tensile strain, whereas the symmetric low-strain responses reported by Hicks *et al* were repeated on a number of samples.

These experimental issues aside, I note again that my main task was to apply large compression to my sample. This was clearly achieved, and, to my knowledge increasing T_c of any superconductor by a factor of 230% with strain has not been done before, even in materials without the disorder sensitivity of Sr_2RuO_4. That is my main result and achievement, and stands independent of details like settling the exact strain scale.

To summarise, the γ-VHS of Sr_2RuO_4 has been successfully studied with a chemically clean method, the uniaxial strain method. T_c is found to be enhanced by a factor of 230% (up to~3.4K) by compressive strains upon approaching the γ-VHS and accompanying its enhancements, the upper critical field $\mu_0 H_{c2}$ has been found to increase faster than T_c^2, indicating the increase of DOS as the sample is

compressed. A $\mu_0 H_{c2}$-T phase diagram has been constructed, which, although not very complete, provides important information related to the VHS.

Chapter 5

CeAuSb$_2$

As briefly mentioned in section 2.3.2, CeAuSb$_2$ is another layered material which shows intriguing physical properties at low temperatures. It is a correlated electronic system and the Sommerfeld coefficient of 100 mJ·K^{-2}·mol^{-1} suggests that it is a moderately heavy fermion system [188]. The interplay between magnetism and superconductivity in heavy fermion compounds has been a long standing topic in condensed matter physics. How these compounds' ground state and the corresponding order parameter evolve when they are tuned by some external parameters like pressure, magnetic fields or chemical doping is still not fully understood. Serving as a platform for studying such questions, CeAuSb$_2$ has become more complicated and interesting as the investigations of it have advanced. However, the research on CeAuSb$_2$ is still in its infancy, and many mysteries remain, for instance the order parameter in its high resistivity phase and the source of non-Fermi liquid behaviour in its paramagnetic state. This chapter will begin with a literature review of both theoretical and experimental research on CeAuSb$_2$ followed by the motivation for, and the methods of, the research that I have performed on it. The outcome of the research and the discussion on it concludes the chapter.

5.1   A review of CeAuSb$_2$

Research on CeAuSb$_2$ stemmed from the investigation of rare earth element(especially Cerium) and Uranium-based ternary compounds, which have quasi-two dimensionality in both their physical and electronic structures (see [188] Ref. 1-3 therein). The basic motivation is on one hand to study systematically the properties of these ternary compounds and on the other hand, as mentioned above, to understand the fundamental relationship between magnetism and superconductivity. CeAuSb$_2$ was reported for the first time by Sologub *et al.* in 1994 [189] to be an antiferromagnet below T$_N$ = 6K. After that as the sample quality was improved rich physical phenomena were discovered in its magnetic, electrical transport and thermodynamic properties [188] [190] [7] [191] [35] [192]. An important step was made in 2005. Balicas *et al.* [7] discovered a second transition in both magnetisation and electrical resistivity at a magnetic field of approximately 5.3±0.2 T applied along the interlayer direction and at the same time evidence of non-Fermi liquid properties was discovered in the paramagnetic state. In addition proximity to a possible QCP was proposed to explain the non-Fermi liquid behaviour close to the transition magnetic field. The physics of CeAuSb$_2$ then began to attract more attention [191] [35] [192].

In this section I will introduce the basic properties of this material as well as the (experimental and theoretical) effort that has been made to understand the underlying physics.

5.1.1   Crystal structure

CeAuSb$_2$ is isostructural with ZrCuSi$_2$-type (i.e. the HfCuSi$_2$-type) compounds, for instance, compounds sharing the chemical form CeTSb$_2$, with T being, for example Co, Ni, Pd, Cu or Ag [189] [190]. It crystallises in a tetragonal structure which belongs to the space group$P4/nmm$, as illustrated in Figure 5.1. The lattice constants are a=4.4081(3)Å and c=10.339(2)Å [189]. The atomic positions in

units of (*a*, *a*, *c*) are as follows: Ce in 2c(0.25, 0.25, 0.26), Au in 2a(0.75, 0.25,0.5), Sb1 in 2a(0.25,0.25,0.84) and Sb2 in 2c(0.75,0.25, 0) [193].

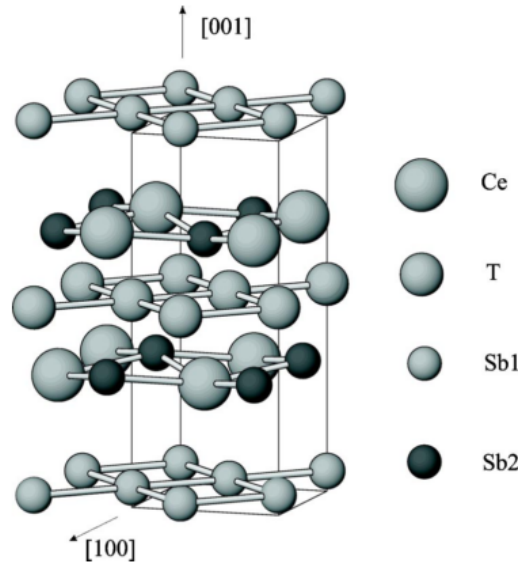FIGURE 5.1: Crystal Structure of Ce*T*Sb₂ compounds, in CeAuSb₂ *T* =Au. [188]

The microscopic structure of CeAuSb₂ can be understood as stacked CeSb-Au-CeSb-Sb layers. Alternatively it can be interpreted as binary Cerium antimonide intercalated by the transition metal Au atoms [188]. The structure of other compounds of this family can also be understood in a similar way. One thing to notice though, is that CeAuSb₂ is tetragonal whereas CeSb₂ is orthorhombic [194].

5.1.2 Magnetism

As mentioned above, CeAuSb₂ was first synthesised in 1994 by Sologub *et al.* [189]and was reported to be an antiferromagnet below $T_N = 6K$. After that its antiferromagnetism was reported by several other groups, for example, Thamizhavel *et al.* in 2003, L. Balicas *et al.* in 2005 and Seo *et al.* in 2012. The ordering temperature T_N varied somewhat between the reports, mostly ranging between 5 K and 6.8 K. Seo and the co-workers pointed out that the occupancy of Au-site has an important impact on the ordering temperature. [35] Specifically, samples of with Au-site occupancy of 99% have a $T_N = 6.8$ K while Au-site occupancies of

93% and 89% give rise to T_N of 6.0 K and 3.9 K respectively. This effect, which is related to disorder in the system, may play an important role in investigating this material and will be discussed again latter.
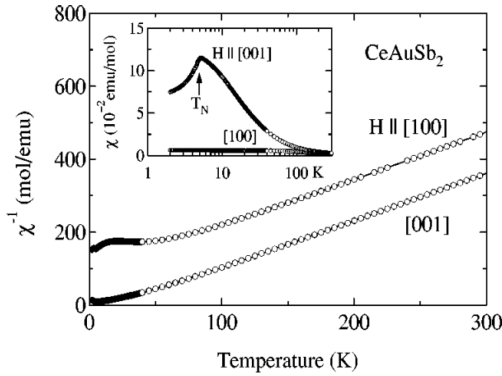

FIGURE 5.2: Temperature dependence of inverse magnetic susceptibility of CeAuSb₂. The inset shows the susceptibility. [188]
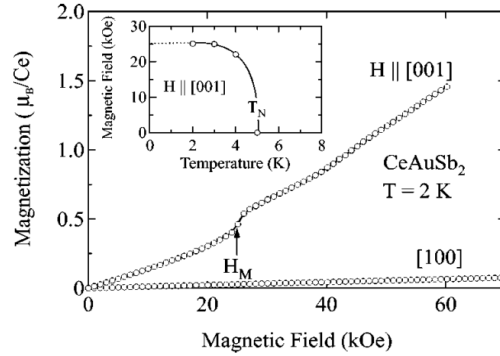
FIGURE 5.3: Magnetisation of CeAuSb₂ *vs.* magnetic field *H*. The inset shows the inferred temperature-field phase diagram. [188]

Some results of magnetic susceptibility measurements, from Thamizhavel *et al.*, are summarised in Figure 5.2 and those of magnetisation *M* in Figure 5.3. [188] From Figure 5.2 it is clear that above 100 K the magnetic susceptibility χ follows a Curie-Weiss law both in the interlayer direction and within the basal plane. The extrapolated Curie temperature and effective moment, for a magnetic field along the [001] direction and for a field in the basal plane, are summarised in Table 5.1, together with results of some other groups. Strong magnetic anisotropy can be seen from Figure 5.2 and the magnetic easy axis was determined as the [001] direction. The magnetic anisotropy was also reflected in the magnetisation as shown in Figure 5.3. With an increasing magnetic field, the magnetisation along the [001] direction develops more rapidly than that along the [100] direction. The in-plane magnetisation varies linearly with field up to 7 T (70 kOe in Figure 5.3). For magnetisation along the [001] direction, the linearity at low fields is interrupted at about 2.5 T by a metamagnetic transition which is clearly resolvable in Figure 5.3. At higher fields the approximate linearity continues up to about 6 T which was the highest field applied in this direction.

T_N (K)	θ_c (K)	θ_{ab} (K)	$\mu_{eff\text{-}c}$ (μ_B)	$\mu_{eff\text{-}ab}$ (μ_B)	Reference	Remarks
6.0		2.0		2.3	Sologub *et al.* 1994	a)
5.0	21	-69	2.49	2.50	Thamizhavel *et al.* 2003	
6.0	12.25	\	2.26	\	Balicas *et al.* 2005	b)

TABLE 5.1: The ordering temperature T_N, the Curie temperature θ and the effective magnetic moment μ_{eff} of CeAuSb₂. Remark a) The values for a field along the [001] direction and for one in the basal plane were not reported separately; b) '\' means no corresponding value was reported.

The behaviour of χ and M strongly suggests that the ground state is antiferromagnetically ordered because (i) the abrupt change in χ_c at about 5K indicates that the ground phase is ordered and ferromagnetism is not expected since there is no divergence in magnetic susceptibility close to the transition temperature; (ii) the magnetisation is zero in the absence of a magnetic field and it increases linearly as a magnetic field is increased from zero, showing no saturation with a field of several Tesla; (iii) no magnetic hysteresis was observed around zero field.

Although we know the magnetic easy axis is the c-axis, we do not know along which direction the spins are aligned, as a complicated magnetic structure may exist. An indication of the possible complexity is that there are different types of magnetic correlations in this system, suggested by the different signs of θ_c and θ_{ab} (positive sign accounts for ferromagnetic correlations and negative sign for anferromagnetic).

In 2005, Balicas *et al.* found that in the presence of a magnetic field along the [001] direction, below about 4.5 K, there exist two metamagnetic transitions. Figure 5.4 shows the magnetisation of CeAuSb₂ measured at 1.5 K, where two metamagnetic transitions are obviously seen. The first one occurs at $H_{MM} \approx 2.8$ T and the second one at $H_c \approx 5.3$ T. At $H > H_c$ the mag-

FIGURE 5.4: Field dependence of the magnetisation of CeAuSb₂ at 1.5 K. [7]

netisation quickly became saturated ($m = 1.65\ \mu_B$). Moreover it was found that

H_{MM} was only weakly temperature dependent, whereas H_{c} was strongly temperature dependent and actually it turned out that the latter corresponds to the antiferromagnetic-paramagnetic phase transition. It means that the phase boundary (below 4.5 K) in the temperature-field phase diagram shown in the inset of Figure 5.3 actually corresponds to a line of phase transitions (which occur at H_{MM}) within the magnetically ordered phase.
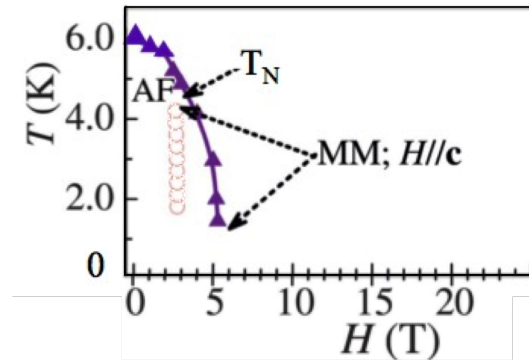

FIGURE 5.5: The temperature-field phase diagram of CeAuSb₂, for a magnetic field applied along the [001] direction. [7].

The revised temperature-field phase diagram is shown in Figure 5.5, reproduced based on the results of Balicas *et al.*. The solid purple line with triangular marks represents the boundary between the high temperature paramagnetic phase and the low temperature antiferromagnetic phase. In the absence of an external magnetic field, $T_{\mathrm{N}} = 6\mathrm{K}$ for their samples. With an increasing magnetic field applied along the [001] direction, T_{N} can be continuously suppressed towards zero, leading to a possible (field induced) QCP at H_{c}. The magnetically ordered phase is divided by a line of metamagnetic transitions, indicated by open (red) circles in Figure 5.5, into two sub-phases. Hereafter I will call the sub-phase on the left the antiferromagnetic A (AFM-A) phase and the one on the right the antiferromagnetic B (AFM-B) phase. As we are going to see, properties related to the AFM-B phase turn out to be very interesting and give rise to many open questions.

Balicas *et al.* also found that when the field was applied in the basal plane, one could hardly see a change in T_{N} even if the field was as strong as 16 T, which again indicates large magnetic anisotropy, consistent with the results of Thamizhavel *et al.*.

The two transitions reported by Balicas *et al.* was later confirmed by, for example, Strydom *et al.* in 2011, Seo *et al.* in 2012 and Lorenzer *et al.* in 2013, using different experimental methods. According to Lorenzer *et al.*, there even exist more phases. Figure 5.6 summarises the results of their (isothermal) magnetisation measurements. It was claimed that below 2 K, the peak of the field derivative of the magnetisation at 2.7 T was reduced in magnitude and became asymmetric as the temperature was lowered, and therefore the metamagnetic transition was split into two which in turn gave rise to the existence of another phase in between. Similar splitting was claimed for the other peak in the field derivative of the magnetisation at 5.4 T and it was argued that the two sub-peaks merged again at 0.5 K. The behaviour of the field derivative of

FIGURE 5.6: Magnetisation and its derivative of *RE*AuSb₂ with respect to magnetic field [192]

magnetisation at 5.4 T was ascribed to two characteristic temperatures that collapsed at 0 K. No subsequent reports either confirming or denying such behaviour have appeared so far and this is one of the things that my research aimed to investigate.

The valence of Ce atoms is important in the study of Ce based Kondo lattice systems and for CeAuSb₂ it was reported to be 3.02 by Flandorfer *et al.* based on their X-Ray absorption spectroscopy measurements [190].

The results introduced above represent a relatively complete summary of the measurements that have been performed so far on the magnetic properties of CeAuSb₂, mainly by magnetic susceptibility and magnetisation measurements. The next subsection will concentrate on the electrical transport measurements including
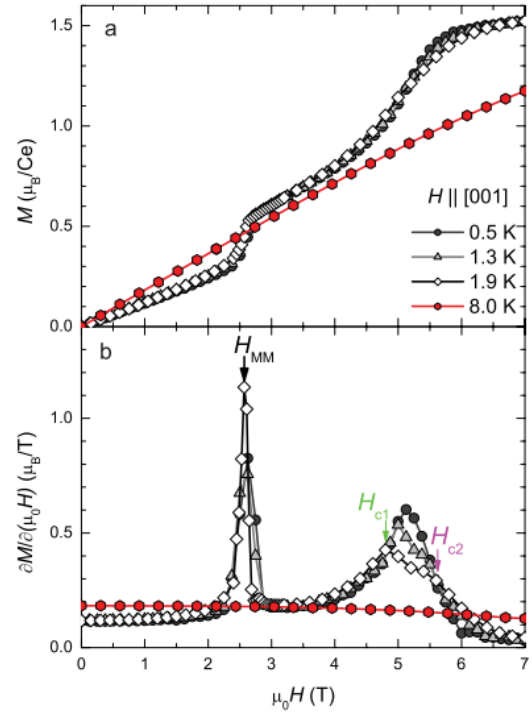
magnetoresistance measurements, and the one after it on specific heat measurements.

5.1.3 Electrical transport properties

The temperature dependence of electrical resistivity at zero field was measured for the first time by Thamizhavel *et al.* in 2003. The results are summarised in Figure 5.7. Distinct anisotropy in electrical resistivity was seen, which reflected the quasi-two dimensional nature of the material's electronic structure. At around 5 K, a change of the slope of the resistivity was seen both in the in-plane resistivity ρ_{ab} and in its out-of-plane counterpart ρ_c, which indicated the paramagnetic-antiferromagnetic phase transition. This is in line with the results of magnetic susceptibility measurements discussed above. The residual resistivity and the residual resistivity ratio (RRR) of their samples were approximately 30 $\mu\Omega$cm and 3, respectively.
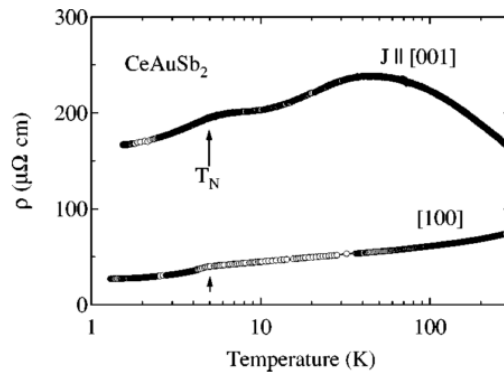

FIGURE 5.7: Temperature dependence of electrical resistivity of CeAuSb₂ [188]

The feature of ρ_{ab} at T_N was confirmed by Balicas *et al.* in 2005 and by Seo *et al.* in 2012. The former, whose samples had residual resistivity of 6-16 $\mu\Omega$cm, further observed that below T_N $\rho_{ab}(T)$ is proportional to T^2, indicating Fermi liquid behaviour in the ordered phase. However, above T_N the resistivity dependence on temperature became $\rho_{ab}(T) \propto T^\alpha$ with $\alpha \leq 1$ (see Figure 5.8) and was maintained when a magnetic field was applied along the [001] direction, until the field strength exceeded the threshold ($H_c = 5.3\pm0.2$ T) above which T_N dropped to zero. Figure 5.9 shows the exponent of $\rho_{ab}(T)$ in the field-temperature phase
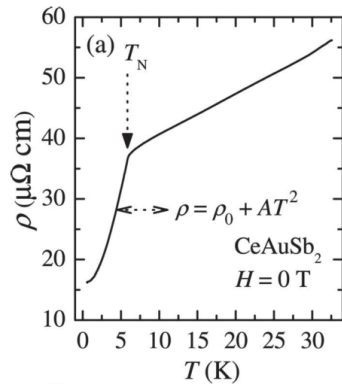
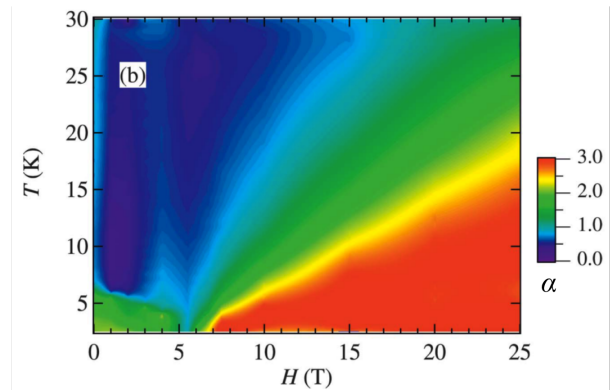FIGURE 5.8: Dependence of in-plane resistivity of CeAuSb₂ on temperature. [7]

FIGURE 5.9: Exponent of $\rho_{ab}(T)$ in the temperature-field phase diagram. [7]

diagram. Interestingly the quadratic temperature dependence of $\rho_{ab}(T)$ was not completely recovered even in the strong field region (where $H > H_c = 5.3\pm0.2$ T). The narrow $\alpha = 2$ region in the strong field zone should probably be considered to be in a process of continuous evolution between $\alpha \leq 1$ and $\alpha = 3$ therefore the Fermi liquid scattering rate is not necessarily seen in this zone. So overall, standard Fermi liquid transport is probably only seen in the antiferromagnetically ordered state (the AFM-A phase and the AFM-B phase) and the whole phase diagram is exotic. The mechanism responsible for the non-Fermi liquid behaviour in the paramagnetic state resistivity is not clear at present and is certainly worthy of further study. (One-magnon scattering was suggested as a candidate theory [7] [195] to explain the T^3 dependence of $\rho_{ab}(T)$ in the high field (spin polarised) paramagnetic phase, but even if it works, how exactly it can be applied to CeAuSb₂ is not clear at present.)

The magnetic field dependence of the in-plane resistivity was also studied by Balicas and co-workers in 2005. Figure 5.10 illustrates their results with a magnetic field applied along the [001] direction (i.e. the c-axis), at 22 mK. As one can see, the resistivity showed two transitions, each marked by an abrupt change of ρ_{ab}, as the magnetic field was ramped. The first transition occurred at $H_{MM} \approx 2.8$ T, indicated by a sharp increase in ρ_{ab}, after which a high resistivity phase was entered, while the second one occurred at $H_c = 5.3\pm0.2$ T, where ρ_{ab} plummeted to a value lower than that at zero field. When compared with the magnetisation results, the
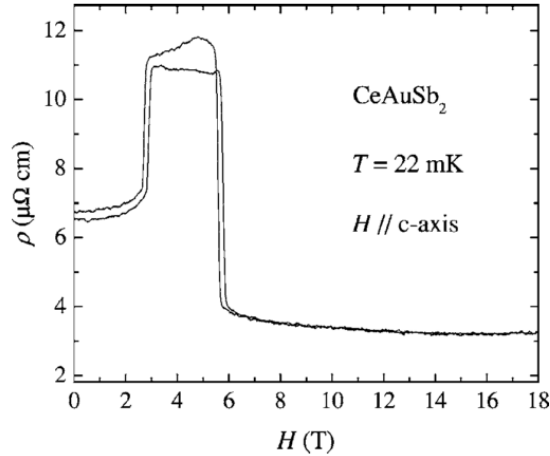
FIGURE 5.10: In-plane resistivity of CeAuSb₂ versus magnetic field H at 22 mK. [7]

first and the second resistive transitions correspond to the first and the second metamagnetic transitions, at the corresponding fields H_{MM} and H_c, respectively. So the existence of the antiferromagnetic B phase is also verified by the field dependence of resistivity. Interestingly, negative magnetoresistivity at fields above H_c was observed over a wide field range. Some hysteresis in the resistivity can be distinguished in Figure 5.10, which is particularly evident in the high resistivity phase (i.e. phase B). Whether the hysteresis is intrinsic is an important question and is one of the issues addressed in my research.

Lorenzer *et al.* also observed similar transitions in 2013, with samples of residual resistivity of about 37 $\mu\Omega$cm. In addition, they claimed that below 2 K there exists further transition-splitting at both transitions, by examining the field derivative of the resistivity (and the field derivative of the magnetisation, which was discussed in last subsection). However the putative splitting at the first metamagnetic transition was not observed in their Hall resistivity. Some anomalies at around H_c were seen both in the field derivative of magnetoresistivity and in Hall resistivity, and were argued to be the evidence of transition splitting. The results of my research though, together with some experimental results which will be shown later, suggest that although there might be some subtleties near H_c, transition splitting is not necessarily a correct interpretation. Besides, the comparatively high residual resistivity of their samples may have impact on the sample properties, because as

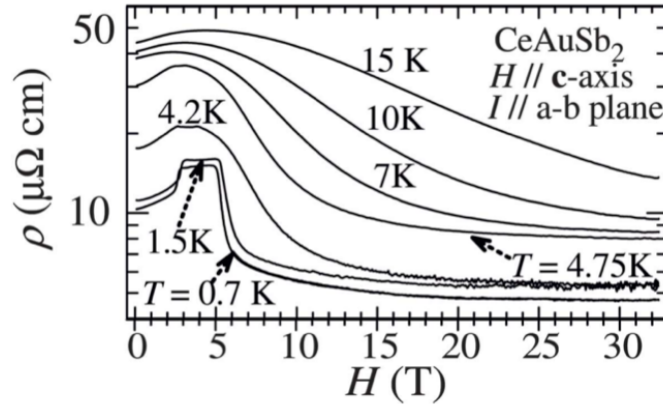indicated above there might be a subtle relationship between the sample quality and the properties of CeAuSb₂.

FIGURE 5.11: In-plane resistivity of CeAuSb₂ versus magnetic field H at constant temperatures. [7]

The temperature dependence of the magnetoresistivity is shown in Figure 5.11. The most interesting feature is the evolution of the two phase transitions. At low temperature, for instance $T \leq 1.5$ K, the two transitions were step-like, but as the temperature increased they became less prominent, and at $T \geq 4.75$ K they seemed to merge into one broad peak and became indistinguishable. This is in agreement with the phase diagram shown in Figure 5.5. Determination of how exactly the two phase transitions evolve as a function of temperature and how they merge is desirable to obtain a complete temperature-field phase diagram. This is also part of the motivation for my research.

It was already mentioned that CeAuSb₂ is possibly a quantum critical system. In this context the Hall resistivity can be helpful to understand quantum phase transitions in heavy fermions compounds. [196] Strydom and Thamizhavel measured the Hall resistivity ρ_H of CeAuSb₂ in 2011, at a few temperatures between 11 K and 1.8 K. The results are shown in Figure 5.12. With a magnetic field applied along the [001] direction and the current injected in the basal plane, below T_N (≈ 5.6K for their samples) weak Hall resistivity was seen below H_{MM} (about 2.6 T for their samples) and linear Hall resistivity isotherms were observed in the high field range, with almost identical slope and similar magnitude (cf. Figure 5.12a). In addition, an anomaly was observed around Hc. To extract this anomaly, the
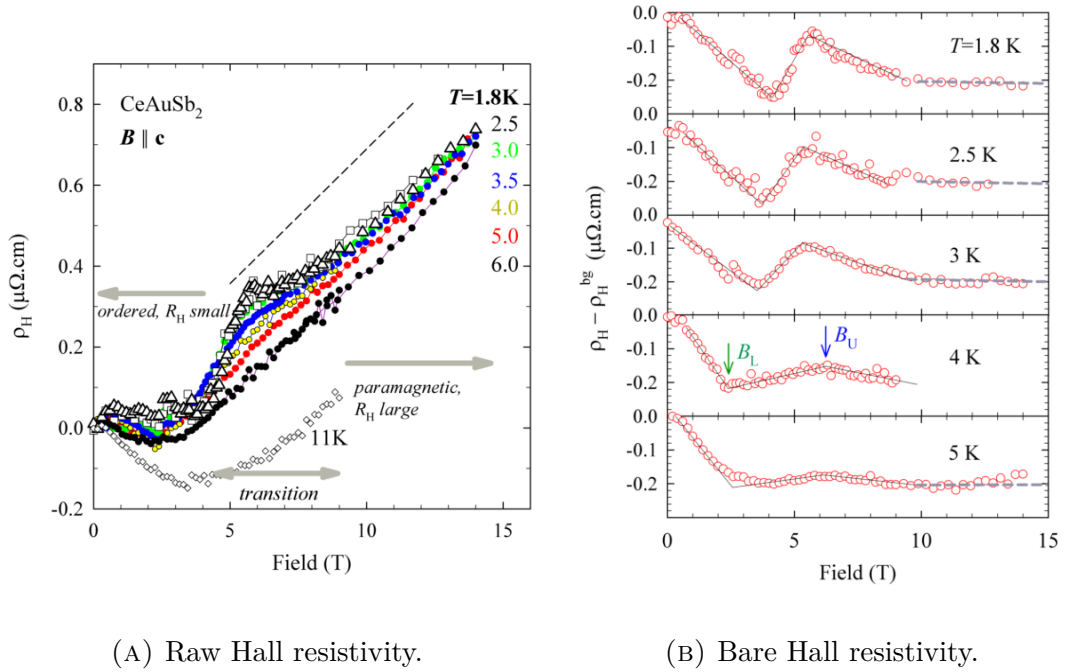
(A) Raw Hall resistivity.

(B) Bare Hall resistivity.

FIGURE 5.12: Field dependence of the Hall resistivity of CeAuSb2. In (B) the linear background was removed). [191]

authors subtracted the linear background from ρ_H and obtained the 'bare' Hall resistivity which is shown in Figure 5.12b. A local minimum (marked by B_L) and a local maximum (marked by B_U) can be clearly seen in the bare Hall resistivity. The two anomalies were argued to approach Hc from opposite directions as the temperature was lowered and to sharpen as it occurred. By extrapolating this behaviour to zero temperature the authors deduced a discontinuity in the Hall resistivity which was then ascribed to an unconventional local QCP in this heavy Fermion compound. Before I come into discussion on the validity of such argument, I should point out that the approaching and sharpening of the two anomalies, according to Lorenzer *et al.*, does not continue below 1.8 K [192]. Instead it was shown by Lorenzer *et al.* that the separation of the two anomalies in ρ_H stayed constant below 1.8 K (at least down to 0.15 K).

Even if the deduced discontinuity in ρ_H (at 0 K) were true, there would still be difficulty in making the unconventional local quantum critical scenario work for CeAuSb₂. A very brief interpretation is the following [196] [197]. Assuming that the RKKY interaction strength is small compared with the conduction

electron band width, a heavy fermion (Kondo lattice) system can undergo a quantum phase transition where disappearance of the magnetic order and the onset of Kondo screening occurs simultaneously and therefore a sudden change of the Fermi surface volume occurs at the transition, giving rise to a discontinuous change in the Hall resistivity. It means that when the phase boundary is crossed from the ordered side to the paramagnetic side, the local f-electrons will contribute to the electron density through hybridisation with the conduction electrons. However, in this picture a (heavy) Fermi liquid phase is expected in the paramagnetic side of the phase diagram, whereas the paramagnetic phase of CeAuSb$_2$, even the low temperature region is very unlike a heavy Fermi liquid phase (cf. Figure 5.9).

Overall, in terms of the electrical transport properties (at ambient pressure) of CeAuSb$_2$, although some useful information has been obtained, more detailed and careful work on samples of good quality is still highly desirable.

5.1.4   Pressure effects

As mentioned in the introduction, pressure has been widely used as a tuning parameter in condensed matter physics. For CeAuSb$_2$, Thamizhavel *et al.* examined the temperature dependence of resistivity under pressures up to 2 GPa and suggested that the ordering temperature T_{N} vanished at about 2 GPa.[46] However this was not verified by the (in-plane) resistivity measurements performed by Seo and the co-workers in 2012, under pressures up to 5.5 GPa.[47] According to Seo *et al.*, the ordering temperature T_{N} was not suppressed to zero under pressure even if the pressure exceeded 2 GPa significantly. Instead some more complicated behaviour emerged under the applied pressure.

Figure 5.13 shows the temperature dependence of the magnetic contribution of the resistivity ρ_{Mag} at a few pressures. The magnetic contribution was obtained by

---

[46]Although in FIG. 10 of [188], a current along the [001] direction was indicated, if one compares the magnitude of the resistivity at, for example 1 K, with that in FIG. 6 of the same paper, one would see that the current was more likely in-plane.

[47]Both groups claimed the pressures they applied to be hydrostatic, however with no knowledge of the pressure medium the hydrostaticity is preferably taken as a hypothesis.
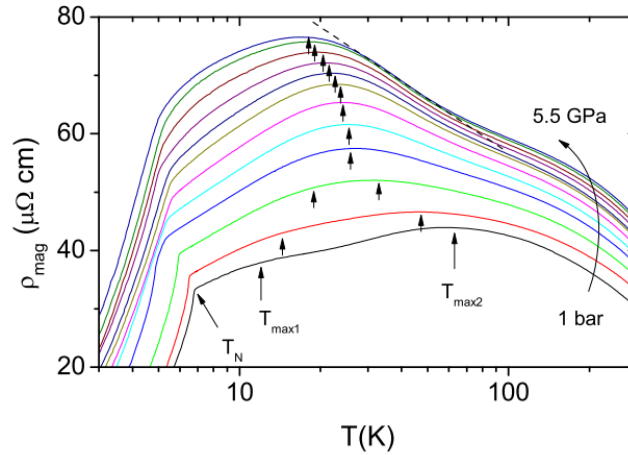
FIGURE 5.13: Temperature dependence of the magnetic contribution to resistivity ρ_{Mag} of CeAuSb$_2$ at pressures up to 5.5 GPa. [35]

subtracting the non-magnetic part, estimated based on the resistivity of LaAuSb$_2$ at ambient pressure, from the total resistivity. LaAuSb$_2$ was considered as the non-magnetic analogue of CeAuSb$_2$ and was expected to be much less pressure dependent. T_{N} in Figure 5.13 again indicates the Néel temperature. T_{max1} and T_{max2} indicate two broad maxima in ρ_{Mag}. The former was argued to be related to the Kondo hybridisation and therefore moved towards higher temperature with increasing pressure, while the latter was thought to be due to the crystalline electric field effects. They merged into one broad peak above 2.18 GPa. By examining the temperature derivative of the resistivity as a function of temperature below 8 K, Seo *et al.* obtained a temperature-pressure phase diagram which is shown in the lower half of Figure 5.14. (The upper half shows how T_{max1} and T_{max2} evolve under pressure, which has been already indicated in Figure 5.13.) A suppression of T_{N} was indeed seen with increasing pressure, but before T_{N} approached zero the process was interrupted by the emergence of a series of new phases.

It is not necessary at this point to discuss how precise this phase diagram is and how to define the boundary of these phases. The important message is that applying a hydrostatic pressure probably does not directly suppress the Néel temperature to zero thereby giving rise to a QCP. Instead there might be some unexpected complexity. Another thing which is clear is that no superconductivity was observed in hydrostatic pressures up to 5.5 GPa, at least above 1.2 K.
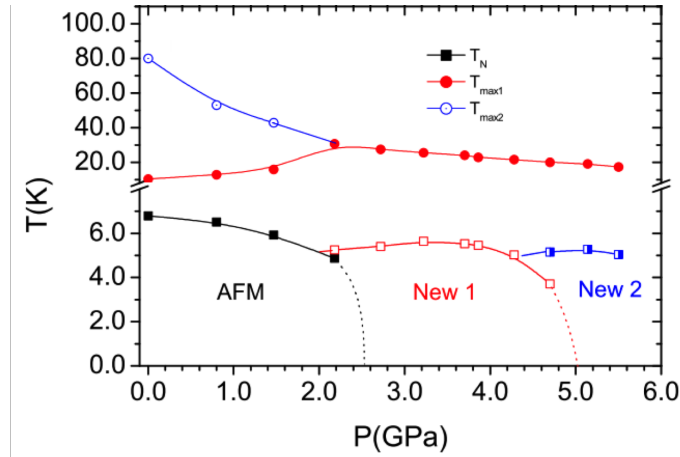
FIGURE 5.14: The temperature-pressure phase diagram of CeAuSb₂. The upper half shows the evolution of the two temperature scales, T_{max1} and T_{max2}, whose explanation is seen in the text. [35]

5.1.5 Specific heat measurements

The heat capacity (in the form of C/T) and the total entropy of CeAuSb₂ in the absence of magnetic field, measured by Thamizhavel *et al.*, are shown in Figure 5.15. The conspicuous peak in C/T manifested the magnetic phase transition. At T_N about 50% of the magnetic entropy of a free doublet (Rln2) was recovered. Below 3 K the heat capacity in Figure 5.15 looks linear (indicated by the dashed line) and Thamizhavel *et al.* extrapolated it to 0 K and obtained the Sommerfeld coefficient $\gamma \approx 90$ mJ·K^{-2}·mol^{-1}.
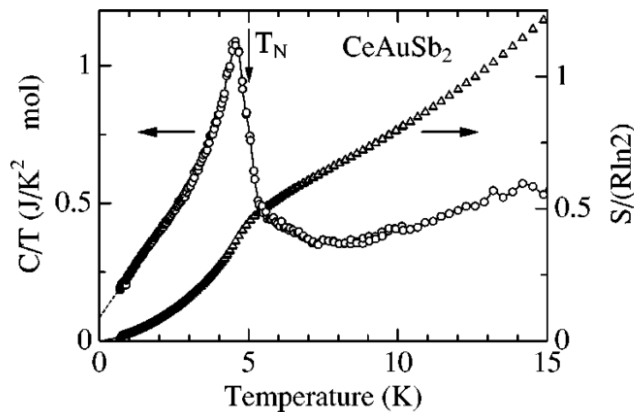

FIGURE 5.15: Specific heat and entropy of CeAuSb₂ versus temperature. [188]

Balicas *et al.* extended the measurement temperature down to below 400 mK in 2005 and in addition measured the heat capacity in several magnetic fields.
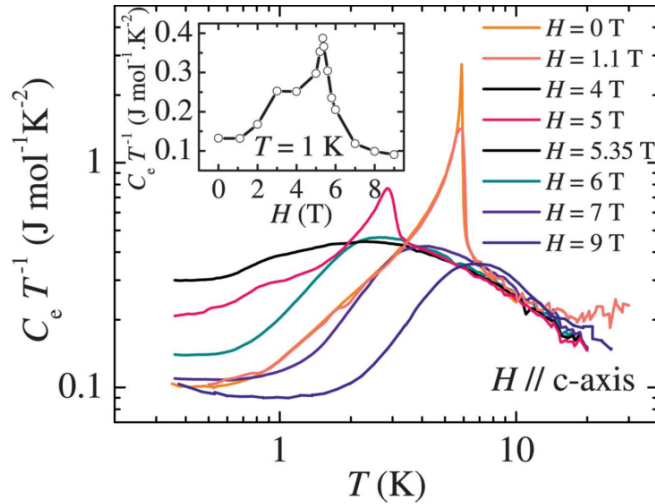
FIGURE 5.16: Temperature dependence of C_e/T of CeAuSb₂ at a few magnetic fields. The inset shows C_e/T, measured at 1 K, as a function of H. For the explanation of C_e/T, see the text. [7]

Figure 5.16 shows the magnetic contribution (C_e/T) to the heat capacity at a few magnetic fields. C_e/T was obtained by subtracting C/T of LaAuSb₂ at zero field from that of CeAuSb₂. An example of the subtraction is shown in Figure 5.17. The difference between C/T of CeAuSb₂ (the purple curve) and that of LaAuSb₂ (the black curve) corresponds to $C_e(\text{CeAuSb}_2)/T$. LaAuSb₂ in this context was considered as a non-magnetic analogue of CeAuSb₂, similar to that discussed in the resistivity measurement above.

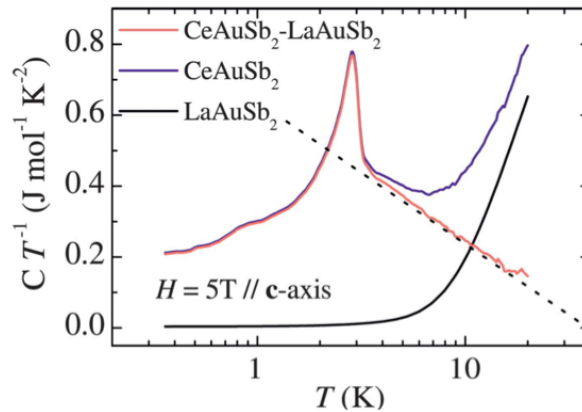FIGURE 5.17: Temperature dependence of C_e/T of CeAuSb₂ at 5 Ha few magnetic fields. [7]

Seen in Figure 5.16 and Figure 5.17, near H_c a logarithmic temperature dependence of $C_e(\text{CeAuSb}_2)/T$ was observed (above 3 K). This is interesting because in heavy fermion quantum critical systems such behaviour has been widely taken

as non-Fermi liquid behaviour due to quantum critical fluctuations. The reason why the $\ln T$ behaviour did not continue to very low temperature even close to H_c needs further study. The inset of Figure 5.16 shows the magnetic field dependence of C_e/T at 1 K. Obvious enhancement of C_e/T was seen near H_c and this was just a cut at this particular temperature as T was lowered towards zero. The enhancement of C_e/T close to H_c is consistent with the tendency of diverging effective mass of quasi-particles close to a QCP.

In summary, the results of heat capacity measurements discussed above are on the whole consistent with observations from magnetic and electrical transport measurements. Some non-Fermi liquid behaviour was observed in the paramagnetic phase, which is possibly related to quantum critical fluctuations. Many questions apparently exist which need further investigation.

5.1.6   Band structure calculation

In terms of the band structure of CeAuSb₂, unfortunately so far there has been only one publication seen in the literature, where first-principles calculation was done based on density functional theory (DFT), using the LDA+U method (local density approximation plus intra-atomic interaction) [193]. The main result of the calculation was that the density of states (DoS) near the Fermi level was argued to be mainly due to the Ce $4f$ electrons. The DoS close to the Fermi level and its projection of the Ce $4f$ and Sb 5p states is shown in Figure 5.18. From the bottom panel of Figure 5.18, it is clear that the DoS at the Fermi level is dominantly Ce $4f$ electron states. No Fermi surface was illustrated based on the calculations.
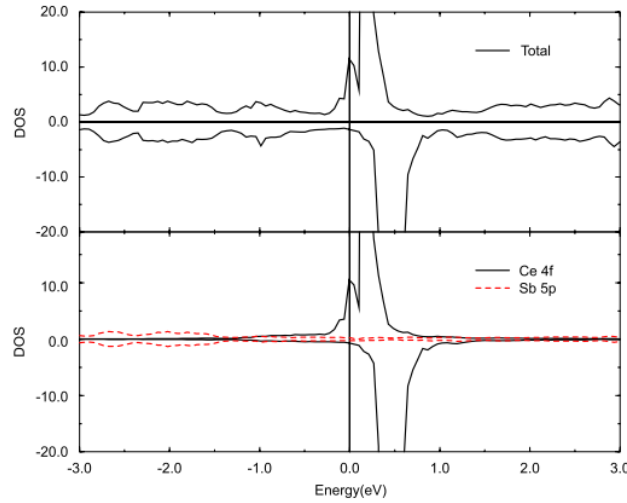
FIGURE 5.18: Desity of states of CeAuSb$_2$. Upper panel: total DoS, positive for majority and negative for minority; lower panel: projection of Ce 4f and Sb 5p states. [193]

5.2 A short summary and open questions

5.2.1 A summary of the literature review

From the experimental and theoretical results discussed above, some basic information can be extracted, which is important not only for our understanding about CeAuSb$_2$ but also for guiding future experiments. Therefore I am going to clarify these points as follows and then I will discuss some open questions about CeAuSb$_2$ which motivated my research.

From section 5.1 we learn that CeAuSb$_2$ is a paramagnet at room temperature and the inverse magnetic susceptibility is Curie-Weiss like. In the absence of external magnetic fields, as the temperature is lowered it orders antiferromagnetically below T_N, where T_N is the ordering temperature and depends on the Au-site occupancy. CeAuSb$_2$ is anisotropic both in magnetic susceptibility and in electrical resistivity. The Sommerfeld coefficient γ is about 100 mJ·K^{-2}·mol^{-1}, which gave rise to the argument of this compound being a moderately heavy fermion system. On the other hand, the fact that the effective magnetic moment per Ce ion is only slightly lower than that of the free Ce^{3+} ion suggests that the Ce 4f-electrons are mainly

local. The measured valence of Ce in it is +3.02 (at 300 K and 10 K) shows hints of valence variation from 3+ but it is not very conclusive.

In the presence of a magnetic field applied along the [001] direction, the ordering temperature can be continuously suppressed towards zero, leading to a hypothetical magnetic field tuned QCP. Within the magnetically ordered phase, a separate phase transition occurs at about 2.8 T which separates the magnetically ordered phase into two sub-phases. This phase transition, which is a weakly field dependent metamagnetic transition, can be identified, for instance, by an abrupt change in resistivity or in magnetisation. The phase transition (at H_c) between the ordered phase and the disordered one can be identified by a sudden change in resistivity or a peak in heat capacity, and it is also accompanied by a metamagnetic transition. Right below H_c, at very low temperature deviation from T^2 dependence of ρ_{ab} was observed. Outside the magnetically ordered phase, non-Fermi liquid behaviour has been observed. Representative features include:

1) $\rho_{ab}(T) \propto T^\alpha$ ($\alpha \leq 1$) at $T > T_N$ at zero field;

2) $\rho_{ab}(T) \propto T^\alpha$ ($\alpha \leq 1$) at $T > T_N$ at a finite field below or equal to H_c, (or at $T > 0$ K when $T_N = 0$ K);

3) $\rho_{ab}(T) \propto T^3$ at high fields and low temperatures;

4) $C_e/T \propto -\ln T$ close to H_c (above 3 K);

5) The coefficient A of the T^2 term of ρ_{ab} follows $(H\text{-}H_c)^{-1}$ as H approaches H_c.

The fourth and the fifth terms together with the anomalous exponent of ρ_{ab} (T) at H_c were argued to be the evidence of proximity to a magnetic field tuned QCP. Following this, a pressure induced QCP was proposed but was not realised with a sample whose $T_N = 6.8$K, by hydrostatic pressures up to 5.5 GPa, in contrast to the observation for a sample of $T_N = 5.0$ K. The origin of the difference remains unclear. For the sample of higher T_N, some unexpected features in resistivity was observed under pressure, suggesting possible existence of new phases at high pressures.

5.2.2 Open questions about CeAuSb$_2$

We have thus far summarised the main experimental and theoretical results about CeAuSb$_2$ in the literature. However, as indicated above, the information that has been accumulated cannot be completely understood with existing theories. Instead many questions arise from the observed properties. Here I will give a few examples of such intriguing open questions, which originally motivated my research.

As discussed above, CeAuSb$_2$ is argued to be close to a QCP. In the context of quantum criticality, as mentioned in Chapter 1 and Chapter 2, one of the reasons why it has attracted broad attention is the possible emergence of novel phases in the vicinity of a QCP. Outstanding examples include unconventional superconductivity in, for example, Cerium or Uranium based heavy fermion superconductors (e.g. CePd$_2$Si$_2$, CeIn$_3$ and URu$_2$Si$_2$), and the disorder-sensitive phase in the transition metal oxide Sr$_3$Ru$_2$O$_7$. Bearing in mind the possible formation of novel phases in the vicinity of a QCP, we notice that, for CeAuSb$_2$, some properties related to its antiferromagnetic phase B (cf. Figure 5.5) are surprisingly similar to those of the novel phase (i.e. the disorder-sensitive phase) of Sr$_3$Ru$_2$O$_7$, despite the two materials being quite different in nature. Some of the distinct similarities will be discussed in the following, after a very brief summary of the properties of Sr$_3$Ru$_2$O$_7$.

Sr$_3$Ru$_2$O$_7$ samples of high purity, grown by image furnace methods, show no magnetic order at low temperatures and are almost magnetically isotropic below 5 K [64] [56]. Upon cooling at zero field, a crossover appears at T^*, below which Fermi liquid behaviour has been observed (e.g. a T^2 dependence of resistivity). With a magnetic field applied parallel to the crystal c-axis, this crossover temperature can be continuously suppressed. For samples of residual resistivity $\rho_{\mathrm{res}} \approx 3~\mu\Omega$cm, results of magneto-transport, thermodynamic and magnetic measurements suggested the existence of a magnetic field tuned QCP at $H_{\mathrm{c}}(\mathrm{Sr_3Ru_2O_7}) \approx 7.8$ T $\parallel$ c axis [198]. However for samples of lower (by about an order of magnitude) residual resistivity, this putative QCP was found to be replaced by a novel phase, between 7.8 and 8.1 T. (At higher fields the Fermi
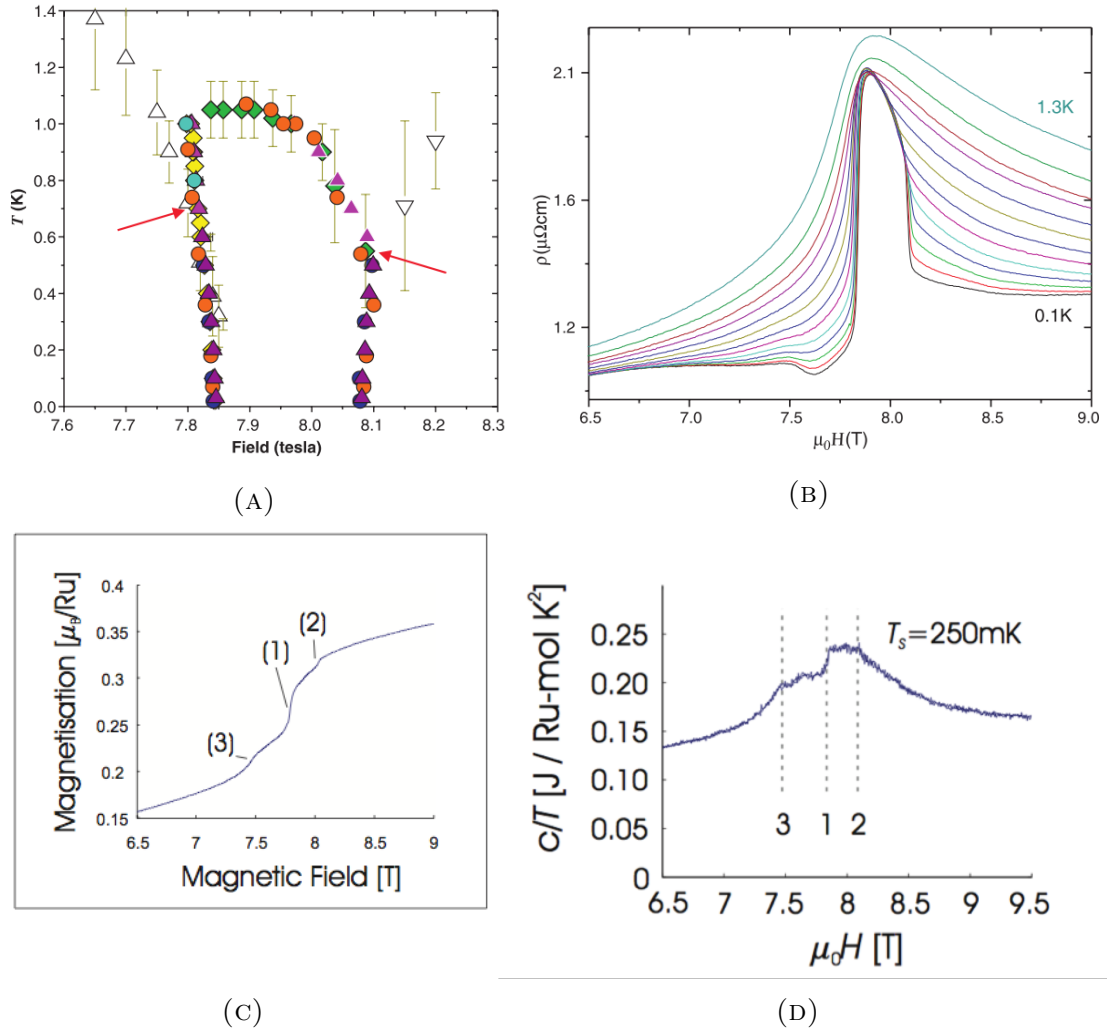
FIGURE 5.19: The novel phase and its related properties, of $Sr_3Ru_2O_7$. (A) The empirical phase boundaries, determined by measurements of ac susceptibility (the triangles), dc magnetization (the orange circles), resistivity (the diamonds) and magnetostriction (the blue circles). The red arrows indicated the critical temperatures below which the transitions are of first order (for the interpretation, see the text). At the dome, the transitions are of second order. [32] (B) The low temperature resistivity of $Sr_3Ru_2O_7$ as a function of magnetic field. [198] (C) Magnetization of $Sr_3Ru_2O_7$ close to the phase, as a function of magnetic field. For the meaning of the labels, see the text. [199](D) Specific heat (divided by temperature) of $Sr_3Ru_2O_7$ as a function of magnetic field, measured at 250mK. [199]

liquid behaviour was observed again for both cases). The formation of this non-superconducting phase appears to be related to the hypothetical QCP [32] and it is an excellent example manifesting the possible emergence of novel phases in the vicinity of a QCP. It has well defined phase boundaries (cf. Figure 5.19a) and accompanying its appearance interesting properties have been observed.

First, at very low temperature (e.g. 100 mK), the resistivity ρ (H) shows an abrupt increase at about 7.8 T, marking the entrance of the phase, and then at above 8.1 T, ρ (H) plunges to a value slightly higher than that below 7.8 T (shown in Figure 5.19b). Moreover, the magnitude of the coefficient A of the T^2 term of ρ (T) peaks as the field approaches the novel phase from either side of the field. [43] Second, two metamagnetic transitions appear at the lower and the upper critical field of the phase, respectively, as shown in Figure 5.19c. The labels (1) and (2) in the figure indicate the two metamagnetic transitions, and the label (3) corresponds to a crossover at about 7.5 T. Both the metamagnetic transitions are of first order, manifested by, for instance, a peak in the imaginary part of the ac susceptibility for each of them. Third, evident enhancement is observed in specific heat divided by temperature when the phase is approached from either side of the field (seen in Figure 5.19d).

If one recalls the properties of CeAuSb₂ that are related to the antiferromagnetic phase B, one can find similar behaviour in all the properties discussed above for the novel phase of Sr₃Ru₂O₇, despite of some minor difference in details. Such surprising phenomenological similarities in electrical transport, magnetic and thermodynamic properties give rise to a question: is there any underlying common mechanism in these two systems that lead to such similarities and if yes, what is it? This question is not trivial in that empirically one would expect different mechanisms for the magnetism in these two compounds. Sr₃Ru₂O₇ is an itinerant magnet [200] [174] with no f-electrons, whereas CeAuSb₂, as a Ce based Kondo lattice system, has regularly arranged local magnetic moments derived from the Ce 4f-electrons and shows hints of local magnetism, for instance, from its high temperature Curie-Weiss like magnetic susceptibility and the large effective magnetic moment per Ce ion. In addition, so far there is still not enough evidence

unambiguously manifesting that the AFM-B phase of $CeAuSb_2$ is related to a QCP, while for the novel phase of $Sr_3Ru_2O_7$, it is clearer that it is related to the putative QCP (although the driving mechanism of its formation is still not fully understood). Actually for $CeAuSb_2$, the existence of quantum fluctuations itself is probably still questionable. Nevertheless the phenomenological similarities do exist and to a good extent motivated my research. The fascination of a such comparison is that, if somehow some underlying physics could be identified, it will have far reaching consequences. For example if the comparison can provide us some insight about the mechanism responsible for the formation of the novel phase of $Sr_3Ru_2O_7$, it will be important information for understanding phase formation close to a QCP.

Clarifying the cause of the non-Fermi liquid behaviour of $CeAuSb_2$ is important, because an important question of modern condensed matter physics research is under what circumstances the standard theory of a metal, the Fermi liquid theory, will fail? In Chapter 2 some known examples have been briefly talked about, where non-Fermi liquid behaviour has been observed. These include but are not restricted to 1D Luttinger liquids, the strange metallic state of high temperature superconductors (HTS), heavy fermion compounds close to a QCP and some disordered systems (e.g. some doped semi-conductors and disordered heavy fermion compounds). Research on these systems at least tells us that non-Fermi liquid behaviour, like non-quadratic temperature dependence of resistivity, does not always imply the existence of a QCP. Actually, defining where a system is quantum critical (at very low temperature) could be difficult. For $CeAuSb_2$, we need more experimental results to try to determine how closely the non-Fermi liquid behaviour is related to a QCP. One question related to it is whether the phase transitions (in resistivity and magnetisation) of $CeAuSb_2$ at H_c are of first or second order. If the non-Fermi liquid behaviour is due to fluctuations of the order parameter (of the ordered phase), one would normally expect a second order phase transition at a QCP. However the observation of hysteresis of the transitions showed some sample dependence and no explicit conclusion was drawn. Therefore it still remains an important question to be answered. On the other hand, even if the non-Fermi

liquid behaviour turns out not to be directly related to a QCP, the question of its origin still needs to be addressed.

The non-Fermi liquid behaviour in CeAuSb$_2$ extends to ($H > H_{\rm c}$) regions far away from the possible QCP, implied by the T^3 temperature dependence of resistivity in the high field region of the temperature-field phase diagram (cf. Figure 5.9). It is therefore very exotic since in most heavy fermion compounds where quantum criticality is observed, the non-Fermi liquid behaviour is developed out of the heavy Fermi liquid phase, on both sides of the QCP. The latter is what current theories of quantum criticality usually account for. So even if the quantum fluctuations are proved relevant for the non-Fermi liquid behaviour, any applicable theory will have to cope with the non-Fermi liquid behaviour in the high field region. This can potentially be a challenge for the typical theories, like the Hertz-Millis theory and more recent theories with additional critical modes [201] [197] [202]. Related to this, the Hall resistivity discussed in sub-section 5.1.3, if can be reproduced in samples of better quality, will probably need alternative interpretation. The one-magnon scattering process, which is proposed to explain the unusual temperature dependence of the resistivity, usually predicts $\rho \propto T^3$ for half metals. For CeAuSb$_2$, the potential justification of its application is that the magnetisation appears to be saturated above $H_{\rm c}$, implying full polarisation of the spins which makes it similar to a ferromagnet at high fields. But the application is in no sense straightforward.

The last question I want to mention is related to the sample purity. Quantum critical systems are often found to be sensitive to disorder. [32] [203] It reminds us that we should always be careful of the sample purity when we think about the properties of the samples and the interpretation of them. Usually for metals the sample purity can be partially reflected from the residual resistivity and the RRR. For CeAuSb$_2$, as pointed out by Seo *et al.*, the Néel temperature can give us some extra information, because it reflects the Au-site occupancy. If one compares the experimental results of different groups with their samples' residual resistivity and ordering temperatures, some hint of disorder dependence can indeed be found. For example, the metamagnetic transition at $H_{\rm c}$ reported by Balicas *et al.* and Seo

et al., whose sample residual resistivity being 6-16 $\mu\Omega$cm and 4.4 $\mu\Omega$cm respectively, was not clearly resolved in the magnetisation measurements of Thamizhavel *et al.*, whose sample's residual resistivity being approximately 30 $\mu\Omega$cm. The transitions of resistivity reported by the two former groups are also much sharper than that by Lorenzer *et al.* whose samples' residual resistivity was approximately 37 $\mu\Omega$cm. In addition, according to Balicas *et al.*, the samples they used for resistivity measurements, which had different ordering temperatures (and residual resistivity), had different levels of hysteresis and they even claimed that one the measured samples showed no hysteresis at all. These experimental observations overall tell us that the sample purity might indeed be important to the properties of CeAuSb₂ and for further measurements the lower the residual resistivity the better, unless the disorder dependence of some properties is specifically studied.

The questions discussed above are interesting to me and as mentioned, they to a large extent motivated my research on CeAuSb₂. There could certainly be more questions one can ask but the situation at this stage is that, to push the research forward, obtaining a comprehensive summary of the properties based on samples of good quality is probably the first thing we should do. Started from here I have performed a series of measurements of electrical transport and torque magnetisation. Next I will show the experiments that I have performed and then I will show the results and discuss what they mean.

5.3 Experimental work

Having introduced the current status of the research and discussed the open questions about CeAuSb₂, in this section I will describe the experimental work that I have performed on CeAuSb₂, and show the results together with some basic analysis. The discussion on the meaning of these results will be left to section 5.4.

5.3.1 Electrical transport measurements

5.3.1.1 Sample preparation

The CeAuSb₂ crystals used for all the experimental work presented in this thesis were grown by Dr. Hideaki Sakai, using a flux method. Relevant crystal growth procedure can be found, for example, in [204] and [205]. An antimony self-flux was used in a vacuum to obtain pure single crystals. Slight variations in sample quality were found between samples from different growths. Samples from two batches were selected and used for the project, labelled hs-006 and hs-007; and their corresponding initial ratio of Ce:Au:Sb for sample growth was 1:4:8 and 1:5:10, respectively. The variation of initial ratio of the three constituent elements, at the time of the sample growth, was made in an attempt to achieve further improvement of sample quality. All these samples showed residual resistivity of 4-8 $\mu\Omega$cm (see Table 5.2). The lowest values reported elsewhere in the literature was 4.4 $\mu\Omega$cm [35], demonstrating that our samples are of good quality.

To verify that our samples are single-crystals and to determine the directions of the crystal principal axises, Laue experiments were performed in the Centre for Science at Extreme Conditions in Edinburgh, following the same scheme as that for Sr₂RuO₄. The resulting Laue pattern is shown in Figure 5.20, with the X-ray beam normal to the basal plane. The Laue pattern is very neat and shows obvious four fold symmetry, respecting the (tetragonal) crystal structure. By carefully comparing the Laue pattern and the simulated result for the same structure, we were able to distinguish the difference between the direction of the principal axes and the 45° direction, and then determined the horizontal and vertical direction in Figure 5.20 to be the principal axes (either a or b axis, which are equivalent for a tetragonal structure). With the crystal principle axes determined, in principle one can cut samples along any desired direction for measurements.

The shape of the as grown CeAuSb₂ samples was often that of thin plates, with typical thickness of 100-200 μm and the c-axis normal to the surface. This was ideal for in-plane resistivity measurements. However residual flux (originating from the
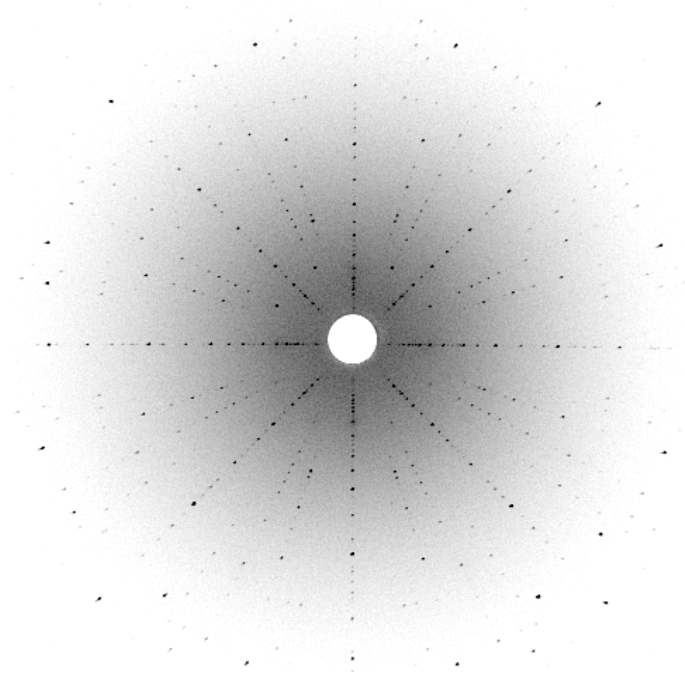
FIGURE 5.20: The Laue pattern of CeAuSb₂. The X-ray beam was normal to the basal plane. The white circular zone in the centre is resulted from the hole in the centre of the photosensitive board that is used to detect the scattered X-ray. Four fold symmetry can be clearly seen, reflecting the symmetry of the sample. The horizontal direction corresponds to either the a or b axis of the sample, which are equivalent for a tetragonal structure, and the vertical direction corresponds to the other axis.

sample growth) was sometimes found irregularly distributed on the surface of the sample. Since this might disturb the results of transport measurements, I chose flux-free areas to cut the needle shaped samples for the experiments, which was possible because these flux free areas could be of several mm². (In principle one could also polish the samples to remove the residual flux.) The sample cutting was performed with a commercial wire-saw (KD Unipress WS22), for which the principles are identical to that used for Sr_2RuO_4. The sample I ended up with had a relatively neat lateral interface. The typical size of the obtained needles was roughly 1.5 mm long, 200-300 μm wide and 100-200 μm thick.

The samples used for resistivity measurements were mounted in a typical four-terminal sensing configuration, which is widely used for accurate electrical resistivity measurements. The key idea is to separate the current contacts and the voltage contacts so that the extrinsic impedance of the circuit (e.g. the contact resistance and the wire resistance) does not come into the measured impedance

of the sample. A small difference made for our measurements is that two pairs of voltage contacts were prepared for each sample check that the current distribution was homogeneous.

A similar sample mounting scheme has been described in a few previous doctoral theses in our group (for instance, J. Farrell, 2007, J.-F. Mercure, 2008, J Bruin, 2012) and only minor changes were made for this work, which will be described at the end of this subsection.

To make the current contacts, a thin gold wire ($\phi = 50\ \mu$m) was attached to each end of the sample with conductive silver-epoxy 6838 from Dupont. For in-plane resistivity measurements, the current should be injected into the sample from the ends as homogeneously as possible. To do so, I tried to make the silver-epoxy spot size for the current contacts just enough to cover the whole end of the sample. Thin gold wires were also used to make voltage contacts and were fixed against the side surface of the sample with the same kind of silver epoxy. The voltage contacts should be made small to minimise the geometrical uncertainty, on condition of guaranteeing mechanical stability. The other terminals of the gold wires were fixed on a quartz plate with relatively big silver-epoxy spots, so that the mounted sample could be installed onto the probe together with the quartz plate, thereby reducing the risk of destroying the fragile contacts.

The sample mounting procedure used for this work only differs from that of J.-F. Mercure *et al.* in the silver-epoxy curing scheme. What they suggested to make contacts of very low resistance was to bake the silver epoxy (after it is placed in the right place) together with the sample at 450°C for 5 minutes. However this is not a good idea for CeAuSb₂ because, unlike strontium ruthenates which are oxidies being insensitive to oxygen, CeAuSb₂ has the risk of oxidisation at high temperatures in air.[48] Actually I found that leaving CeAuSb₂ at 450°C for one minute in air could already cause obvious oxidisation, and when it happened, the surface of the sample lost its lustre and turned dark. So the silver-epoxy was

---

[48]In principle one can also apply other types of conductive epoxy (e.g. Dupont silver epoxy 4929) which does not require high temperature curing, however, for this work Dupont 6838 was still used, because it is highly reliable at low temperatures.

baked at about 180°C for 2.5 hours (which was actually the standard curing scheme recommend by the user guide of the silver epoxy). With the help of ultrasound cleaning prior to the sample mounting, contact resistance was brought to $\leq 1\,\Omega$ for the current contacts and about 3-4 Ω for the voltage contacts, which was still high but usable.[49] (The contact resistance in principle can be controlled well below 1 Ω if the silver-epoxy can be cured, for example at 450°C for 5 minutes.)

5.3.1.2 Experimental conditions

The CeAuSb₂ samples were measured over a wide range of temperature (from room temperature down to 20 mK) and magnetic field (between 0 and 35 T), using probes and cryostats optimised for the desired measurements.

For primary sample characterisation (e.g. checking the RRR), the probe described in subsection 3.2.2 was used together with the ⁴He flow cryostat, which enabled us to ramp the temperature continuously from room temperature down to about 3 K. Low temperature in-plane resistivity measurements were firstly performed with the ADR, where two mounted samples were installed onto the transport-probe that was designed for the ADR (by J. Bruin, c.f. subsection 3.2.2), on which an un-calibrated Hall sensor was newly installed close to the samples. The work was done in the presence of a magnetic field up to 15 T and the Hall sensor enabled me to eliminate the influence of the hysteresis of the magnet, which turned out to be important for the hysteresis analysis (of the two transitions). After the low temperature in-plane magnetoresistivity measurements, where the magnetic field was always applied in the c-axis direction, field-angle variant magnetoresistivity measurements were performed at temperatures down to 1.4 K and in magnetic fields up to 9 T, with a ⁴He cryostat in combination with a 9 T magnet (see subsection 3.2.3.1). The field angle was rotated from parallel to the c-axis to be in the ab-plane and the obtained results showed interesting features, which made such measurements at even higher fields desirable. Further field-angle dependent

---

[49]Without ultrasound cleaning the semi-baked silver epoxy could give rise to contact resistance as high as 9 Ω.

magnetoresistivity (and torque magnetometry) measurements were therefore performed in the LNCMI (Laboratoire National des Champs Magnétiques Intenses) in Grenoble, France, where high magnetic field (up to 35 T) and low temperature (down to below 20 mK) could be achieved simultaneously. The probes and the corresponding cryostats have been described in Chapter 3, thus I will not repeat the description in the following.

5.3.1.3   Measurements at zero field

Since the residual resistivity and the RRR are believed to be indicative of sample quality, we measured the temperature dependence of the in-plane resistivity using the ^{4}He flow cryostat. Two samples were installed each time, and were measured between room temperature and 2-3 K. Six samples from the hs006 batch and two from the hs007 batch were measured, and the results are summarised in Table 5.2. The comparatively low residual resistivity and the high reproducibility of the results indicates that our samples have good quality. In addition the Laue pattern

Sample name	hs006-1	hs006-2	hs006-3	hs006-4	hs006-5	hs006-6	hs007-1	hs007-2
ρ_0	5.8	6.1	7.1	5.5	5.4	6.6	4.5	4.0
RRR	10.7	9.1	8.8	10.8	11.0	8.7	7.3	8.1

TABLE 5.2: The residual resistivity and the RRR of eight tested CeAuSb$_2$ samples. Six of the samples are from the hs006 batch and two are from the hs007 batch, as marked in the sample name. All samples are prepared using the method described in subsection 5.3.1.1.

suggests that our samples are single crystals. We thus believe that our samples are of good quality and this is a good start point of my work.

Figure 5.21a shows $\rho_{ab}(T)$ as a function of temperature. As the temperature is lowered ρ_{ab} decreases monotonically, and at about 6.3 K a sharp kink appears (marked by the red arrows in Figure 5.21a and its inset), indicating the magnetic transition. The temperature dependence of ρ_{ab} shown in Figure 5.21a is very similar to that of Seo *et al.* (c.f. FIG. 2 (a) in [35]). Careful examination reveals that there are three temperature ranges in which ρ_{ab} is linear in T but with different slopes: (1) approximately 120 K - 300 K, (2) approximately 11 K - 30 K

and (3) approximately 6.3 K (T_N) - 11 K. If one defines a temperature T^*_1 (≈ 11 K) for the position where the change occurs of the slope of $\rho_{ab}(T)$ (see the inset of Figure 5.21a), and another temperature T^*_2 (≈ 50 K) for the position of the broad kink in $\rho_{ab}(T)$, then by comparing our result with the that of Seo *et al.*, one would realise that T^*_1 and T^*_2 actually correspond to T_{Max1} and T_{Max2} in $\rho_{\text{Mag}}(T)$ in their work. So overall our result is in good consistency with that of Seo *et al.* at ambient pressure.
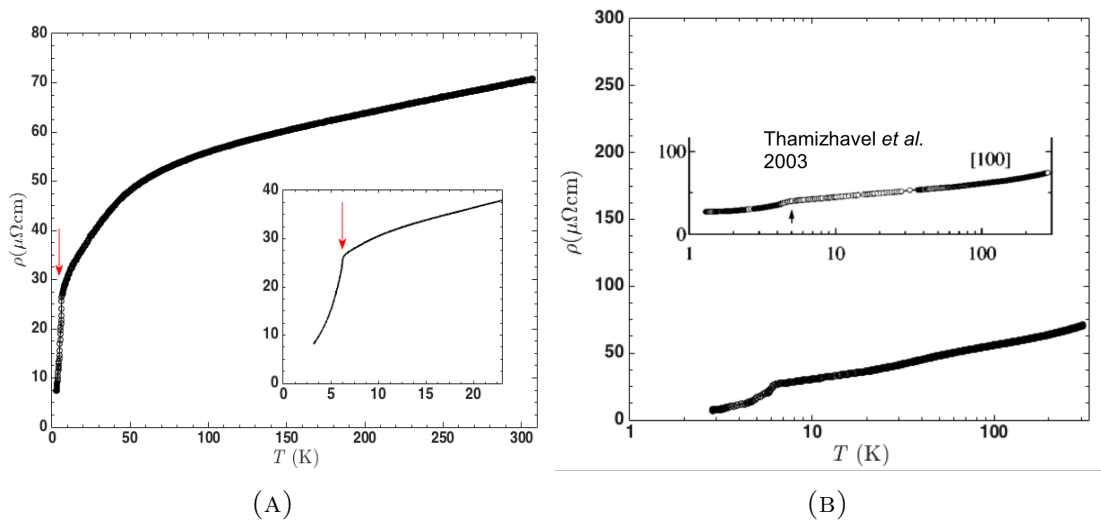

FIGURE 5.21: The temperature dependence of $\rho_{ab}(T)$ of CeAuSb₂. (A) $\rho_{ab}(T)$ on linear scales. Inset: $\rho_{ab}(T)$ below 25 K. The red arrows indicate the position of the magnetic transition. Note that at approximately 11 K, there is a small but noticeable change in the slope of ρ_{ab} (see the inset). (B) $\rho_{ab}(T)$ on semi-logarithmic scales, in comparison with the counterpart of Thamizhavel *et al.* (the inset, adapted from [188]). It is seen that for our sample ρ shows a sharper decrease at T_N and a more prominent hump at approximately 50 K.

The only other result of $\rho_{ab}(T)$ we can compare with is that of Thamizhavel *et al.*. Since their result was only shown on a semi-logarithmic scale, I did the same to our data for comparison, and the outcome is shown in Figure 5.21b. The results roughly look similar, although some differences are distinguishable. For example, the residual resistivity of our sample is lower by a factor of about 6 and the kink in ρ at T_N is sharper for our sample. Besides, the broad hump (which corresponds to the kink of $\rho_{ab}(T)$ at about 50 K) is more evident for our sample but is hardly seen for theirs.

Below T_N, the resistivity $\rho(T)$ shows T^2 dependence (see Figure 5.22), indicating Fermi liquid scattering rate in the magnetically ordered state. Therefore the ordered state can be regarded as a Fermi liquid state.
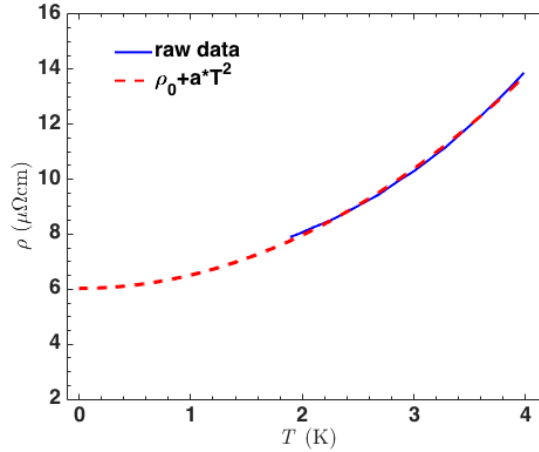

FIGURE 5.22: Temperature dependence of ρ_{ab} of CeAuSb₂ in the magnetically ordered state. It can be seen that $\rho_{ab}(T) \propto T^2$, which indicates Fermi liquid quasi-partical scattering rate.

5.3.1.4   Measurements in fields

Following the discussion of open questions in subsection 5.2.2, I performed low temperature resistivity measurements in the presence of magnetic fields, aiming for a comprehensive resistivity study of CeAuSb₂ at low temperatures.

Two samples, cut from the same bigger sample of the hs006 batch, were measured with the ADR transport probe that was mentioned in the previous subsection and was described in more detail in Section 3.2.3. The two samples, which were named hs006-S_A and hs006-S_B respectively, were both cut along the crystal principal axes (the a or b axis). Each sample had one pair of contacts for current injection and two pairs for voltage measurements. The two voltage contact pairs for hs006-S_A and one pair for hs006-S_B were connected to low temperature transformers while the other pair of hs006-S_B were connected to a room temperature transformer (SR554). (This arrangement was only due to the limited availability of low temperature transformers.) The gain was 100 for all transformers. The excitation current for

both samples was generated by a current source, composed of an AC voltage source (the AC voltage output of the lock-in amplifier SR830) and a 10 kΩ resistor, whose impedance is much higher than the rest of the electric circuit. A summary of the measurement parameters and the sample dimensions is shown in Table 5.3.

Sample name	W (μm)	t (μm)	L_1 (μm)	L_2 (μm)	Freqency (Hz)	I (μA)
hs006-S_A	160	130	250	280	71.13	100
hs006-S_B	250	150	733	846	81.13	100

TABLE 5.3: The experimental parameters of the resistivity measurements on hs006 samples. W: sample width; t: sample thickness; L_1: spacing between the first pair of voltage contacts; L_2: spacing between the second pair of voltage contacts; Freqency: measurement frequency; I: excitation current.

Figure 5.23 shows the primary results for $\rho(H)$ [50] as a function of magnetic field (which was ramped up first and then ramped down), measured at 300 mK, with an excitation current of 100 μA. The main features of $\rho_{ab}(H)$ are similar to those of Balicas *et al.*. Two abrupt changes of resistivity are observed at $H_{MM} = 2.8$ T and $H_c = 5.6$ T, respectively, which is consistent with their report. By comparing our result with the previous report, we can identify that at this temperature, below H_{MM} is the antiferromagnetic A phase, while between H_{MM} and H_c is the antiferromagnetic B phase and above H_c is the paramagnetic phase (cf. Figure 5.5). In the paramagnetic phase, the field dependence of $\rho(H)$ for our samples is also similarly weak at $H > H_c$.

The hysteresis in $\rho(H)$ of our sample showed distinct features. In Figure 5.23, one can see that hysteresis in $\rho(H)$ is not only observed in the high resistivity phase (i.e. the antiferromagnetic B phase, between H_{MM} and H_c), but also in the antiferromagnetic A phase (below H_{MM}). By carefully comparing Figure 5.23 and Figure 5.10 (from [7]), one can actually find that the hysteresis in the antiferromagnetic A phase could also be identified in the latter, although it is slightly less obvious. However Balicas *et al.* only recognised the hysteresis in the antiferromagnetic B phase and even stated that the other sample they measured showed no hysteresis at all (in either phase) [7]. In contrast, for our work, all the samples we measured showed the same hysteresis as that presented in Figure 5.23.

---

[50]I will ignore the subscript 'ab' hereafter when it does not cause confusion.
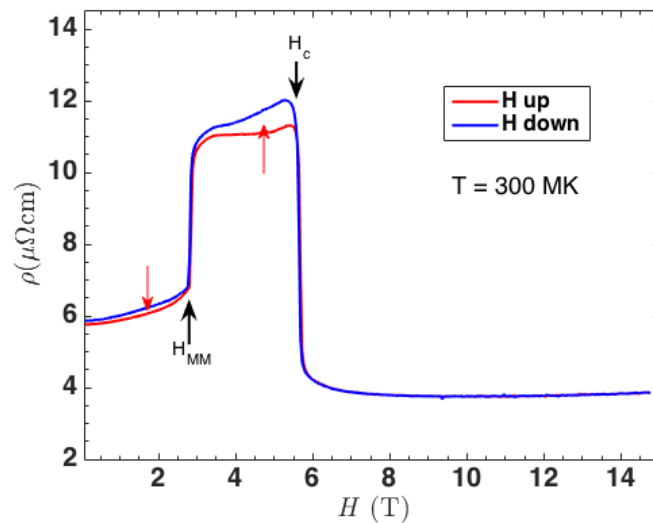
FIGURE 5.23: The resistivity of CeAuSb₂ as a function of magnetic field, measured at 300 mK. The red curve is for for field ramping-up and blue curve for field ramping down. The resistivity shows two abrupt changes, one at 2.8 T (indicated by the black arrow with label H_{MM}) and the other at 5.6 T (indicated by the black arrow with label H_{c}), in agreement with the results of Balicas *et al.* (cf. Figure 5.10). In addition, distinct hysteresis can been see in two regions, indicated by the red arrows in the figure. For more details, see the text.

Moreover, in the work of Balicas *et al.* (cf.Figure 5.10), some hysteresis at the two transition fields can be distinguished for the field increasing and decreasing curves, but it was ascribed by them to the time constant of their instruments. This in principle is possible, because in real measurements the field value provided by the magnet is usually obtained through calculation based on the excitation current of the magnet rather than through direct measurement. Due to the inductance of the magnet coils the set current cannot be established instantly, therefore the magnetic field estimated based on the set current may be slightly different from the real magnetic field in the centre of the coil where the sample sits. For field sweeps, the difference is further dependent on the field sweep rate. Although the argument of Balicas *et al.* may be true, it is not conclusive. To understand whether the phase transitions discussed above are of first or of second order though, it is desirable to make clear whether hysteresis of $\rho(H)$ at H_{MM} and H_{c} really exists and (if it exists) how it evolves with temperature.

Figure 5.24 (a) and (b) show the resistivity ρ of CeAuSb₂ as a function of H close to H_{MM}, and H_{c} respectively, both measured at 300 mK and at three different
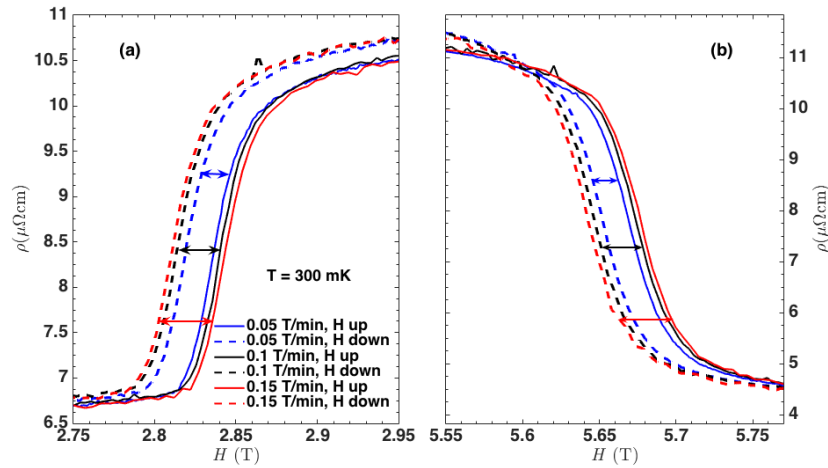
FIGURE 5.24: $\rho(H)$ of CeAuSb$_2$ close to H_{MM} (panel (a)) and H_{c} (panel (b)), measured at three different field sweep rates. The difference of $\rho(H)$ between field increasing and decreasing curves is dependent on the sweep rate, as expected.

field sweep rates. Evidently for both transitions discrepancy is seen between the field increasing and decreasing curves at each sweep rate and the strength of the discrepancy (indicated by the arrows whose colour is in agreement with the corresponding field sweep rate) depends on the field sweep rate, as expected. As shown, faster field sweeps generate a stronger discrepancy between the field increasing and decreasing sweeps, which makes sense. The question is whether there is hysteresis left as the field sweep rate approaches zero. The Hall sensor, which was installed close to the samples, enabled me to answer this question, because (at a constant temperature) the Hall signal is only dependent on the real magnetic field, irrespective of the field sweep rate. This essentially means that the Hall sensor can effectively work as a field indicator. The absolute value of the field cannot be read since the Hall sensor is not calibrated, however for our purpose it is already adequate.

The Hall signal close to H_{MM}, is shown in the left panel of Figure 5.25. The difference of magnetic field at a constant Hall voltage, between the field increasing and decreasing curves, is due to the time constant of the magnet. In this particular measurement (shown in Figure 5.25), which was performed at 300 mK and at a field sweep rate of 0.15 T/min, the Hall signal suggests that a 11 mT shift of the magnetic field for the field decreasing sweep can result in good agreement
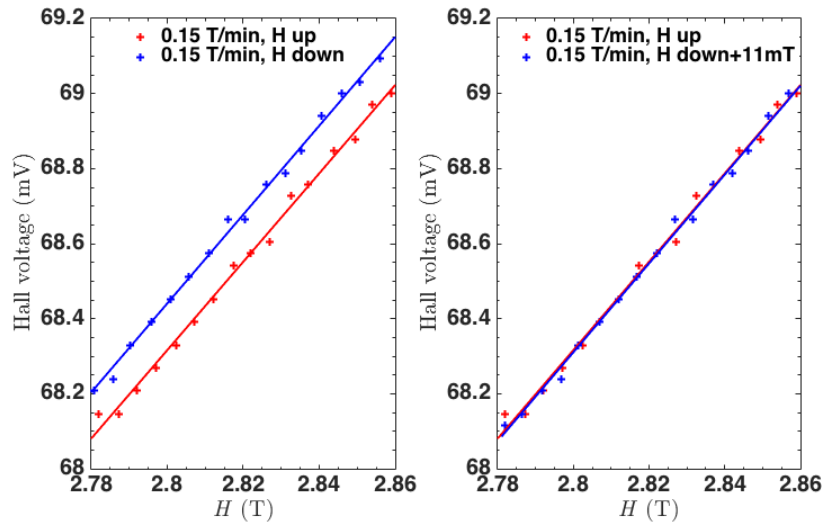
FIGURE 5.25: The Hall voltage close to H_{MM}, measured by the Hall sensor at a sweep rate of 0.15 T/min. Left panel: Raw data (plus marks) and the linear fit (solid lines). Some difference of the Hall signal between field increasing and decreasing sweeps can be clearly seen, which reflects the time constant of the magnet. Right panel: Evaluating the field discrepancy between the field increasing and decreasing sweeps. As is shown, in this case a 11 mT shift can adequately overcome the discrepancy.

with the field increasing sweep, thus the field discrepancy due to the instrument time constant can be evaluated as 11 mT. We can then remove the 11 mT field discrepancy from the original magnetic field difference in the resistivity measurement (close to H_{MM}) and see if there is any residual hysteresis. By applying this method to the field sweeps shown in Figure 5.24, the resultant residual magnetic difference is obtained and is illustrated in Figure 5.26.

As shown in Figure 5.26, at a certain temperature, the residual difference of $\rho(H)$ in H for each transition is a field-sweep-rate independent constant. It means that both transitions in resistivity are accompanied by intrinsic hysteresis, although the hysteresis at the magnetic transition (at H_{c}) is weaker. The hysteresis can be equivalently demonstrated by showing the resistivity as a function of the Hall voltage (see Figure 5.27), since the Hall voltage is an effective way of showing the magnetic field. As shown in Figure 5.27, within experimental resolution the difference for each transition between difference field sweeps indeed has the same magnitude, as expected.

It is possible to work out the width of the hysteresis of each phase transition (at
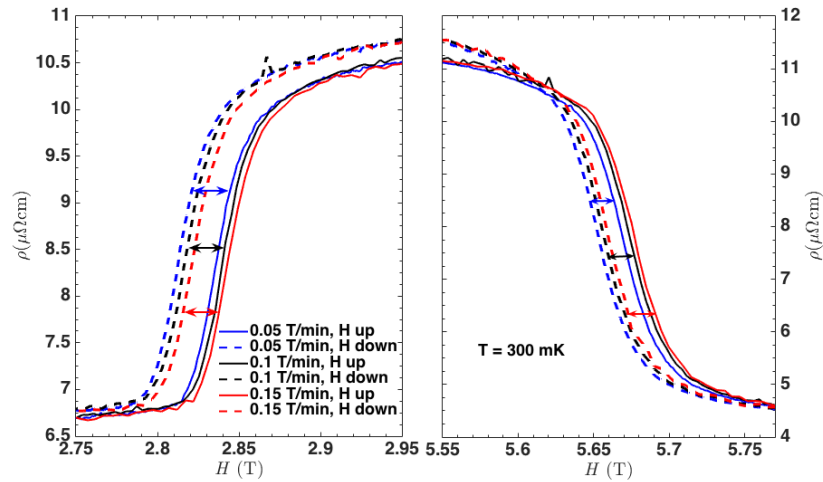
FIGURE 5.26: Residual difference of $\rho(H)$ of CeAuSb$_2$ close to H_{MM} (left panel) and H_{c} (right panel), measured at 300 mK and at three different field sweep rates. For both transitions the residual part becomes a constant, which corresponds to the intrinsic hysteresis of the sample at both transitions.
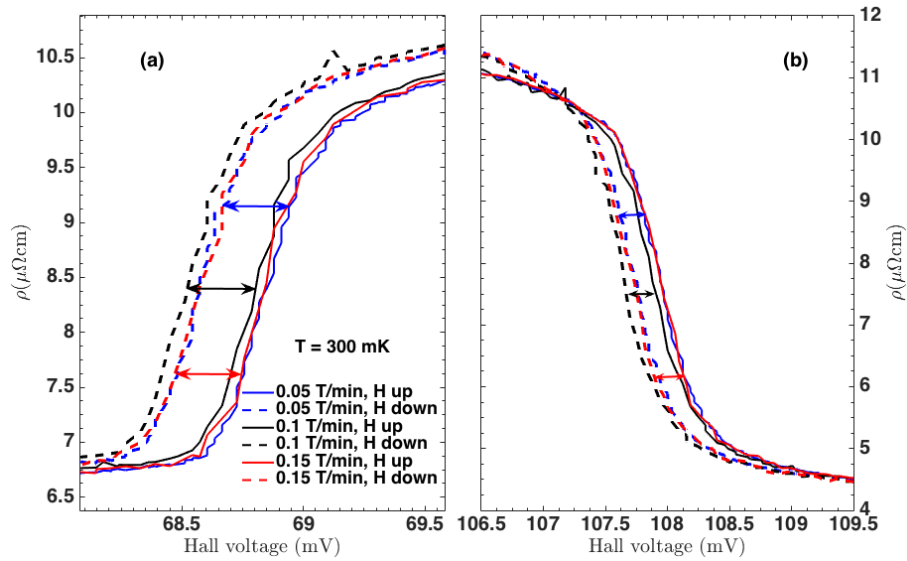

FIGURE 5.27: The resistivity ρ of CeAuSb$_2$ as a function of the Hall voltage, close to the two transitions, measured at 300 mK and at three different field sweep rates.

the measured temperature) although the Hall sensor is uncalibrated, because at least within the magnetic field range that covers the transition, the Hall signal is linearly proportional to the magnetic field (cf. Figure 5.25). For example, for the transition at H_{MM}, the result in Figure 5.27 makes it possible to evaluate the hysteresis in units of the Hall voltage while the proportionality between the Hall voltage and the magnetic field (in unit of T) shown in Figure 5.25 further enables

us to convert this Hall voltage into magnetic field in T (or mT). I applied this procedure to obtain the hysteresis of both transitions quantitively and the results obtained for measurements at different temperatures are shown in Figure 5.28.
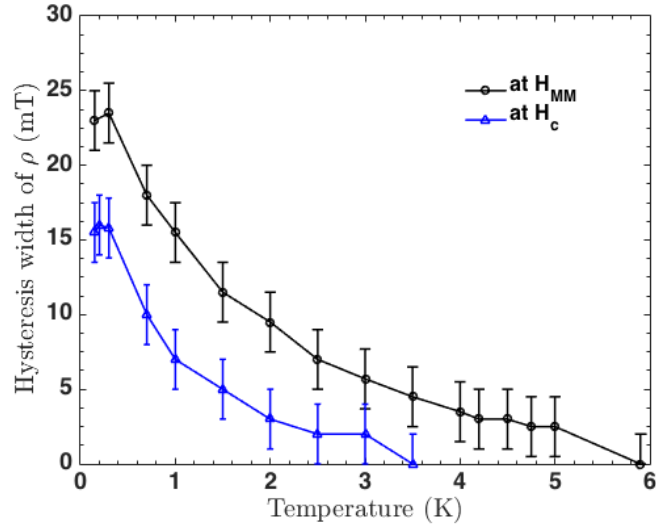

FIGURE 5.28: The width of resistivity hysteresis of CeAuSb$_2$ as a function of temperature.

The hysteresis of both transitions (shown in Figure 5.28) is strongly temperature dependent. Below 300 mK the hysteresis becomes saturated for both transitions within the experimental resolution, and the hysteresis at H_c is comparatively weaker. As the temperature increases the hysteresis for both transitions is suppressed quickly, and for the transition at H_c, above 3.5 K the hysteresis becomes unsolvable. For the transition at H_{MM} though, the hysteresis persists to higher temperature but also disappears at close to 6 K where the two transitions merge.

To carefully examine how the two phase transitions merge and to obtain a clear resistivity-field-temperature phase diagram is one of the tasks for this project. In line with the work for hysteresis analysis I performed isothermal magnetic field sweeps between 0 T and 7 T, with special attention paid to the region where the two phase transitions merge. The results are shown in Figure 5.29 and Figure 5.30. The former shows the resistivity-field-temperature diagram below 7 K while the latter shows $\rho(H)$ at several representative temperatures and in addition shows how the two phase transitions merge in detail (the inset). From Figure 5.29 and
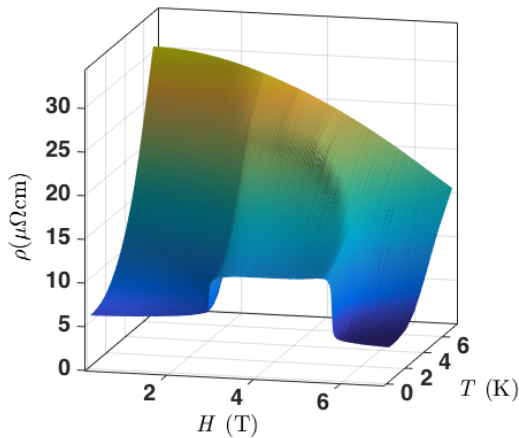
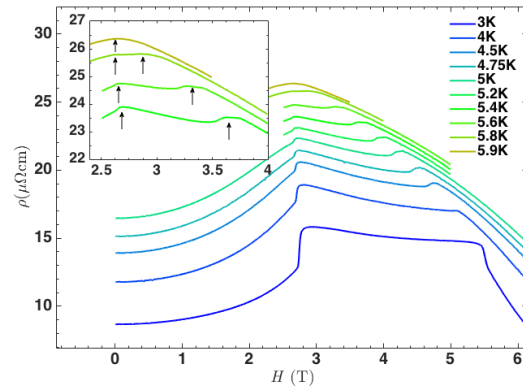FIGURE 5.29: The resistivity-field-temperature phase diagram of CeAuSb₂

FIGURE 5.30: The resistivity of CeAuSb₂ as a function of magnetic field at several selected temperatures. The inset shows how the two phase transitions merge into one.

Figure 5.30 it is clear that the phase transition at H_{MM} is only weakly temperature dependent while the one at H_c is strongly temperature dependent, consistent with the previous report ([7]). At approximately 6 K the two phase transitions merge into one and there is no hysteresis observed.

Field angle dependence of the resistivity

To understand the properties of CeAuSb₂ better, I performed isothermal resistivity measurements while ramping the magnetic field at a series of angles with respect to the c-axis direction, with a He-4 flow cryostat which is equipped with a single axis rotator. The magnetoresistivity ρ_M, defined as $\rho_m = (\rho(H)\text{-}\rho(0))/\rho(0)$, is shown in Figure 5.31 (based on the measurements with a sample that was cut from the hs006 batch and measured at 1.55 K.)

The magnetoresistivity in Figure 5.31 is interesting because it seems that the main outcome of tilting the magnetic field away from the c-axis is only to push the two transitions to higher fields, preserving the shape and magnitude of the response. To verify this, one can plot the magnetoresistivity as a function of the c-axis projection of the magnetic field, the outcome of which is presented in Figure 5.32.
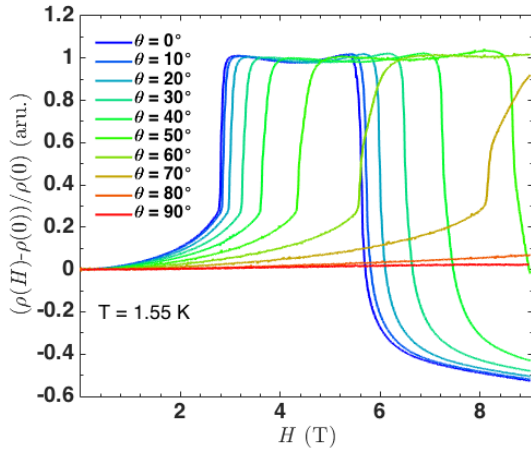
FIGURE 5.31: The field angler dependence of the magneto-resistivity measured at 1.55 K. θ in the legend represents the field angle with respect to the crystal c-axis.
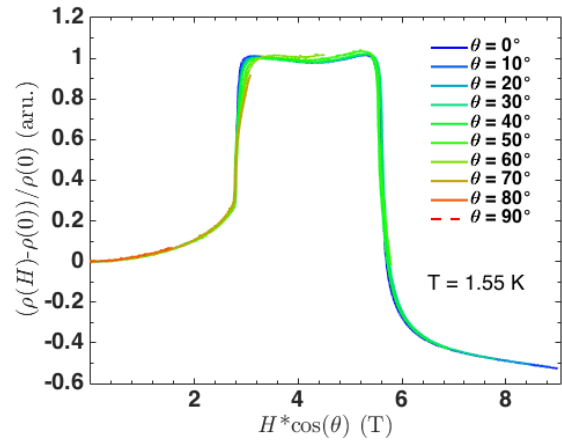
FIGURE 5.32: The magnetoresistivity of CeAuSb₂ as a function of the c-axis projection of the magnetic field (measured at 1.55 K).

From Figure 5.31 and Figure 5.32, it is noticeable that at high angles (e.g. $\theta \geq 60°$), the magnetoresistivity at the first phase transition (at H_{MM}) shows some fine structure, for example at $\theta = 70°$ a kink is seen at $\rho_{\mathrm{M}} \approx 0.6$, above which the slope of ρ_{M} is different. However this phenomenon was not clearly reproduced when another sample from the same batch was measured (in the LNCMI in Grenoble, France) with a dilution refrigerator in the presence of magnetic fields up to 35 T, whose direction can be tuned from parallel with the sample c-axis to parallel with the ab-plane.

FIGURE 5.33: The field angle dependence of the magnetoresistivity measured at temperatures below 100mK. θ in the legend represents the field angle with respect to the crystal c-axis.
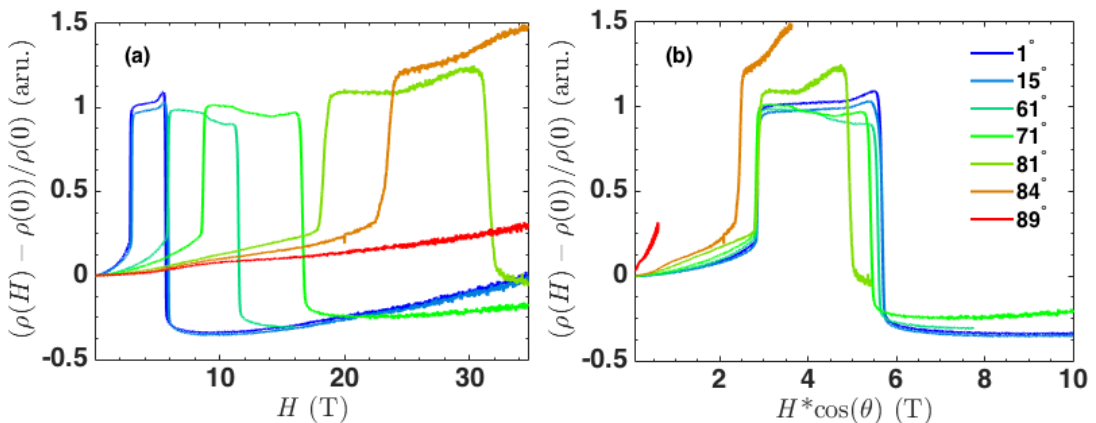
Figure 5.33 shows ρ_M as a function of magnetic field (panel (a)) and its c-axis projection (panel (b)), based on measurements on the second sample in fields up to 35 T and below 100 mK. The main features of ρ_M in Figure 5.33 are similar to those in Figure 5.31 and Figure 5.32. For example, the magnetic fields at which the two phase transitions occur, both increase as the field is tuned off the c-axis. In addition, the shape of the high resistivity phase is roughly preserved and similar collapse is seen when ρ_M is plotted as a function of the c-axis projection of the field. On the other hand the results shown in Figure 5.33 also have evident differences from those shown in Figure 5.31 and Figure 5.32. For example, when the magnetic field is applied close to the ab-plane (e.g. $\theta \geq 80°$), the width of the antiferromagnetic B phase deviates from the $1/\cos(\theta)$ scaling relationship (i.e. the scaled width of the antiferromagnetic B phase is reduced) and the magnetoresistivity shows enhancement in each phase. Moreover the magnetoresistivity below H_c shows different field dependence at different field angles, which is different from what was seen in Figure 5.31 and Figure 5.32, where only a kink of ρ_M was seen at the first transition. So at the moment it is difficult to draw firm conclusions on the detailed evolution of ρ_M close to the two transitions (or within the antiferromagnetic B phase), due to the sample dependence.

In Figure 5.33 (b), the scaled curve of ρ_M with $\theta \geq 84°$ exhibits a noticeable difference from the rest. However, for θ close to 90° a small deviation in θ can result in a relatively big change in the scaled field values, for example, a 1° reduction from 84° will result in a 0.4 T increase for the $(H\cos(\theta))$ scaled metamagnetic transition field H_MM and this would be enough to remedy the discrepancy in the scaling for this angle. Therefore the scaling deviation at high field angles is not absolutely clear.

In summary, the dependence of ρ_M on θ provides evidence that the observed behaviour is dominantly determined by the c-axis component of the applied magnetic field.

5.3.2 Torque magnetometry measurements

5.3.2.1 A brief introduction to torque magnetometry

When a magnetic sample is placed in a magnetic field, it will generally experience a force $\boldsymbol{F}_B = \nabla(\boldsymbol{m}\cdot\boldsymbol{B})$ and a torque $\tau = \boldsymbol{m}\times\boldsymbol{B}$, where $\boldsymbol{m}$ is the total magnetic moment of the sample and $\boldsymbol{B}$ is the applied field. If we only consider a sample that is placed in a homogeneous magnetic field and is uniformly magnetised, the force then vanishes and we are left with the torque.

Since the torque is the cross product of the magnetic moment and the magnetic field, if the direction of the magnetic moment is not collinear with the field, i.e. if the material placed in the field is magnetically anisotropic and the field is applied off its principal axes, there will be a non-zero torque exerted on the sample. For example, if the the sample under investigation has its c-axis as the magnetic easy axis, and the field is applied at a small angle θ (e.g. $\theta = 10°$) with respect to the c-axis in the bc-plane, the torque experienced by the sample will be

$$\begin{aligned}
\boldsymbol{\tau} &= \mathbf{m} \times \mathbf{B} \\
&= (m_b B_c - m_c B_b)\hat{a} \\
&= \mu_0 V (\chi_b H_b H_c - \chi_c H_c H_b)\hat{a} \\
&= \mu_0 V H^2 sin\theta cos\theta (\chi_b - \chi_c)\hat{a}
\end{aligned} \tag{5.1}$$

where μ_0 is the magnetic permeability in vacuum, V is the volume of the sample, χ is the magnetic susceptibility and $\hat{a}$ is a unit vector whose direction is parallel to τ (perpendicular to the bc-plane in this case). In equation 5.1 it is assumed that the magnetisation $\boldsymbol{M} = V\chi\boldsymbol{H}$ for both directions. From equation 5.1 one can see that the torque measures the magnetic anisotropy energy, and for a magnetically isotropic system there would be no torque expected in a magnetic field.

When the susceptibility anisotropy is sufficiently strong ($\chi_c \gg \chi_b$), the contribution to the torque from χ_b will be negligible and the magnetisation can then be

deduced from the torque as

$$|\mathrm{M}| \ \approx \ \frac{|\boldsymbol{\tau}|}{\mu_0 V H sin\theta} \qquad (5.2)$$

Note that the accuracy of equation 5.2 depends on the magnetic anisotropy. For for perfect 2D orbital moments it can be considered accurate, for systems of finite anisotropy it is just an approximation and is possibly bad if the magnetic anisotropy is not strong.

Equation 5.1 and 5.2 imply that, if one can measure the torque that a sample experiences in a known applied magnetic field, one in principle can infer the bulk magnetisation. It is an angle sensitive probing method, which when applied with the right probing apparatus can provide both qualitative and quantitive information of the magnetic properties (e.g. the magnetisation) of the sample with high sensitivity. For example, the micro-mechanical cantilever magnetometer designed by Schwarz *et al.* realised sensitivity as high as 10^{-13} J/T (or 10^{-10} emu in cgs unit). [206].

In the presence of intense magnetic fields, for sufficiently pure metals it is possible to observe quantum oscillations through torque magnetometry at low temperatures, due to the oscillatory magnetic susceptibility resulted from the quantised Landau levels. This is the famous de Haas-van Alphen (dHvA) effect. Detailed descriptions of it can be found in many textbooks, for instance [9], thus I will not repeat it here. The successful application in dHvA measurements is one of the reasons giving rise to the wide interest in torque magnetometry.

The torque experienced by the sample can be measured through different methods, for instance by capacitive, optical or piezo-resistive methods [207]. However, in the following I will briefly introduce the capacitive method here since for my work the torque of the sample was measured with small capacitive cantilevers.

The schematic of a classical capacitive cantilever magnetometer is shown in Figure 5.34. The capacitive magnetometer mainly consists of three parts, i.e. a cantilever with a thin rectangular beam with a comparatively wide end where the

sample to be measured sits, a substrate with a conductive surface underneath the cantilever end, working as a plate of the cantilever capacitor, and a spacer bridging the two parts above. The spacing between the cantilever and the substrate is usually small and the former two parts form a capacitor. In the presence of a magnetic field the sample's magnetic moments experience a torque which deflects the end of the cantilever thereby changing the capacitance between the cantilever and the bottom electrode. The torque of the sample is read out by measuring the capacitance change.
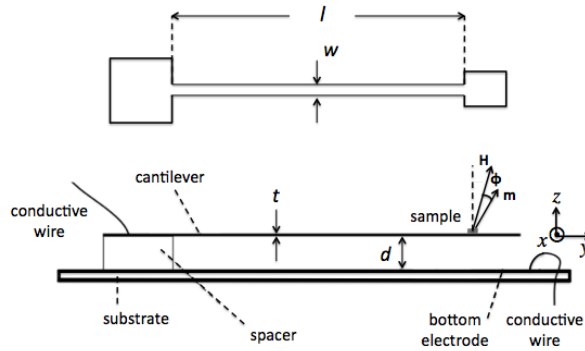

FIGURE 5.34: Schematic of a classical capacitive cantilever magnetometer. Upper panel: top view of the cantilever. Lower panel: side view of the magnetometer. The cantilever and the bottom electrode together form a plate-like capacitor and the torque of the sample is measured through the capacitance change due to the deflection of the cantilever end. Figure adapted from [207].

To the end of the cantilever, the torque τ of the sample is equivalent to one that is generated by a force $\boldsymbol{F} = F\hat{z}$, which is vertically applied at the end of the cantilever. Since the torque can be evaluated by

$$\boldsymbol{\tau} \;=\; \mathbf{r} \,\times\, \mathbf{F} \;=\; LF\hat{x} \;=\; \frac{Ewt^3}{4l^2}\Delta d\hat{x} \tag{5.3}$$

where *E, w, t* and *l* are the Young's Modulus, the width, the thickness, and the length of the cantilever, respectively, while Δd is the deflection of the end of the cantilever.

It shows that if we know the deflection of the cantilever end, in addition to the necessary parameters of the cantilever itself, we in principle can work out the torque. The deflection of the cantilever end can be estimated from the measured

capacitance change. Modelled as a simple plate capacitor, the cantilever capacitor's capacitance $C = \epsilon_0 A/d$, where ϵ_0 is the vacuum permittivity, A is the surface area of the capacitor plates and d is the spacing between the capacitor plates, respectively. If the spacing between the plates has a change Δd that is much smaller than the original spacing, i.e. $\Delta d/d \ll 1$, the capacitance change ΔC is proportional to the spacing change Δd:

$$\Delta C \approx \frac{\epsilon_0 A}{d^2}\Delta d = C\frac{\Delta d}{d} \tag{5.4}$$

Therefore the deflection of the cantilever end can be estimated as $\Delta \mathrm{d} = d\Delta C/C$ and the magnitude of the torque at the end of the cantilever can be evaluated as

$$|\boldsymbol{\tau}| = \frac{Ewt^3}{4l^2}\Delta d = \frac{Ewt^3 d}{4l^2}\frac{\Delta C}{C} \tag{5.5}$$

Thus eventually the measured capacitance provides quantitative information on the torque of the sample.

5.3.2.2 Measurements and results

The samples used for the torque magnetometry measurements were also from the hs006 batch. For primary measurements (in fields up to 9 T), the sample was cut in to a slab, whose dimensions were 250 μm$\times$250μm$\times$50μm, with its *c*-axis perpendicular to the square surface. The prepared sample was mounted onto a BeCu capacitive cantilever (similar to the one shown in Figure 5.35), which was installed on the rotation stage of the He-4 flow cryostat that was used for the angle dependent magnetoresistivity measurements. The sample was mounted such that the c-axis was perpendicular to the cantilever surface and one of its principal axises was parallel to the cantilever beam. The capacitance of the cantilever was measured by the Andeen-Hargerling 2550A capacitance bridge and coaxial cables were used to reduce the noise level.

The torque measured at 1.715 K, with the magnetic field applied 10° off the crystal c-axis, is shown in Figure 5.36. The two prominent jumps in torque τ correspond
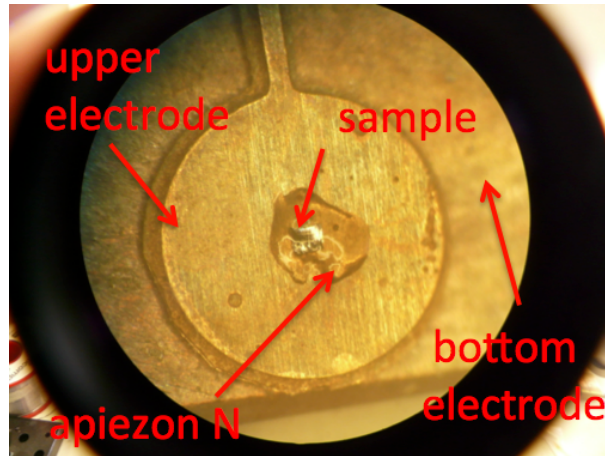
FIGURE 5.35: The capacitive torque cantilever with a CeAuSb$_2$ sample mounted on it. The sample was embedded in apiezon N grease [9] with its *c*-axis perpendicular to the cantilever surface. The sample was cut along its principal axes and was mounted such that one of the principal axes was parallel to the cantilever beam.

to the two metamagnetic transitions, at H_{MM} and H_{c} respectively, and in between is the antiferromagnetic B phase. Assuming that the magnetisation is dominantly
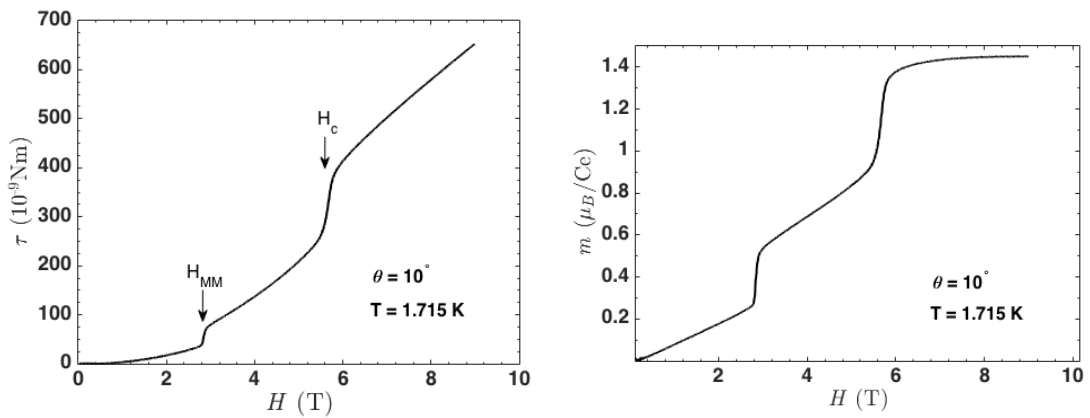
FIGURE 5.36: The torque of the CeAuSb$_2$ sample as a function of magnetic field, measured in capacitance change at 1.715 K and with the field 10° off c-axis.

FIGURE 5.37: The effective magnetic moment per Ce ion of CeAuSb$_2$, estimated based on the assumption of large magnetic anisotropy.

along the c-axis, one can estimate it through equation 5.2, and one can further estimate the effective magnetic moment per Ce ion. The result is illustrated in Figure 5.37, which is in agreement with the report of Balicas *et al.* (cf. Figure 5.4).

Two step-like jumps of magnetic moment are seen at the metamagnetic transitions and saturation is seen above the second transition.

FIGURE 5.38: Torque of CeAuSb$_2$ at 1.715 K as a function of magnetic field H, with H applied at variant angles θ (between the field and the c-axis). The black and purple arrows indicated the metamagnetic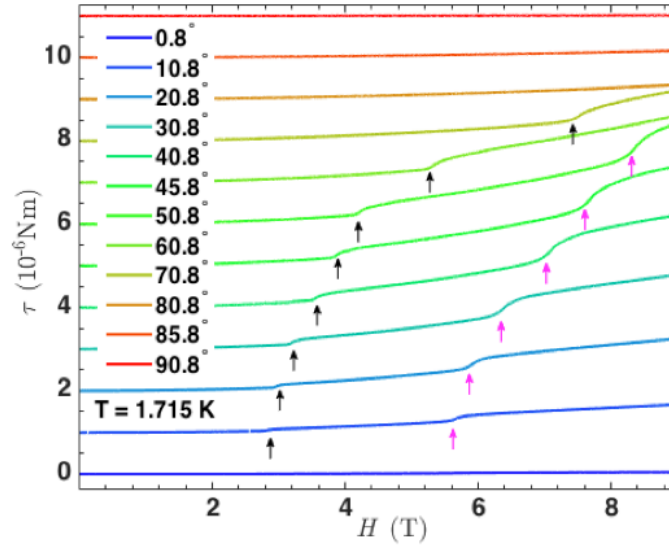 transitions at H_{MM} and H_{c} respectively. The curves are shifted by 10^{-6}Nm sequentially for explicitness.

The evolution of field dependence of the torque is shown in Figure 5.38. As the field is tilted away from the c-axis, the two metamagnetic transitions are pushed to higher fields simultaneously and the width of the antiferromagnetic B phase (between the two transitions) becomes wider, consistent with the observation of resistivity (cf. Figure 5.31 and Figure 5.33).

To check the role of the c-axis projection of the field H in regard of the phase transitions, I plotted the torque against $H\cos(\theta)$, shown in Figure 5.39. The result is similar to the observation in resistivity (cf. Figure 5.32 and Figure 5.33) in that the two metamagnetic transitions both occur when the c-axis projection of H is close to the transition field when $H \parallel$ c, although this approximation becomes less good when H is close the ab plane. If one plots $|\tau|/(\mathrm{H}\sin(\theta))$ as a function of $H\cos(\theta)$, one finds that all the curves roughly collapse (see Figure 5.40)[51].

---

[51]The anomalies close to 0 T are not important as they are due to the 'small denominator error' in $1/(H\sin(\theta))$ when H or $\sin(\theta)$ (or both) is very small.
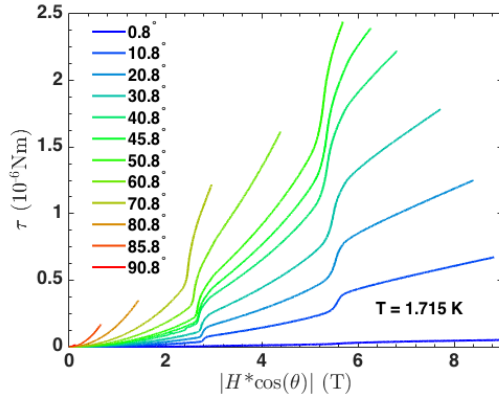
FIGURE 5.39: The torque of the CeAuSb₂ sample as a function of the c-axis projection of H, measured at 1.715 K.
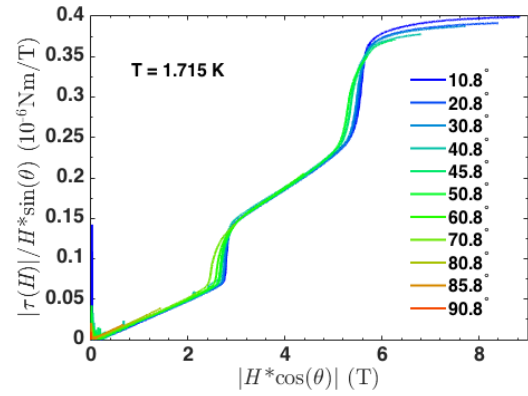
FIGURE 5.40: The total magnetic moment of the measured CeAuSb₂ sample, estimated by $|\tau|/(H\sin(\theta))$.

To see the two transitions at high field angles (H close to ab plane), higher magnetic fields were needed. The results of the torque measurements in fields up to 35 T (performed in the LNCMI, Grenoble, France) are shown in Figure 5.41. As seen in the figure, the main difference at high field angles is that the deviation of the two transition fields $1/\cos(\theta)$ becomes more evident (panel (B)) and the $|\Delta C|/H\sin(\theta)$ curves (as a function of $H\cos(\theta)$) show a poorer collapse. In addi-

(A)

(B)
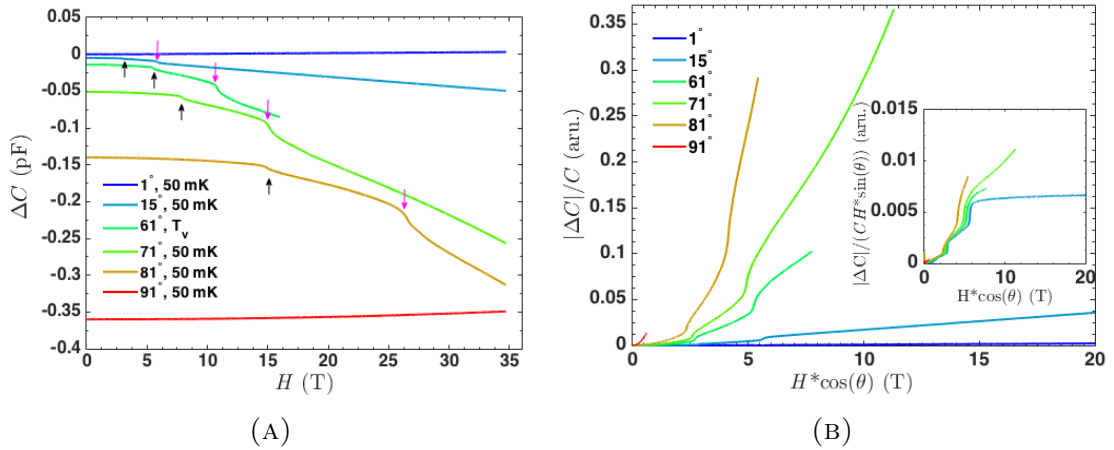
FIGURE 5.41: Torque of CeAuSb₂ measured by the capacitance change $|\Delta C|$ in fields up to 35 T. Panel (A): The magnitude of capacitance change $|\Delta C| = |C(H)\text{-}C(0)|$ at different field angles, (unevenly) shifted for explicitness. For the measurement at 61° the temperature was variant between 90 mK and 300 mK, however since τ is not very sensitive to T, it is still included for comparison. Panel (B): The magnitude of capacitance change (main panel) and $|\Delta C|$ divided by $H\sin(\theta)$ (inset) as a function of the c-axis projection of H.

tion, at high field angles $|\Delta C|/H\sin(\theta)$ grows linearly with respect to $H\cos(\theta)$ in the paramagnetic phase (above the second metamagnetic transition). However on the whole the behaviour of the torque at fields close to the ab plane are still not very different form that when H is close to c-axis.

Overall the results of torque magnetometry measurements are in agreement with the observation in resistivity discussed last subsection. The critical fields of both transitions show roughly a $1/\cos(\theta)$ relationship when the field is not too close to the ab plane, and the effective magnetisation curves (times the sample volume) at different field angles roughly collapse when plotted against the c-axis projection of H.

5.3.3   Discussion and conclusions

The hysteresis analysis with the help of the Hall sensor, as presented in section 5.3.1, suggests that at low temperatures both the phase transition on the left hand side of of the AFM-B phase and the one on the right hand side of it, are accompanied by weak but noticeable hysteresis in resistivity. However the temperature dependence of the hysteresis for the two phase transition lines is different. For the one to the left of the AFM-B phase, the hysteresis persists as the temperature increases until the transition line merges with the antiferromagnetic-paramagnetic phase transition line (at approximately 6 K for my samples). For the antiferromagnetic-paramagnetic phase transition, as the temperature increases the magnitude of the hysteresis in resistivity is quickly suppressed and becomes unresolvable at approximately 3.5K. So overall it seems that the AFM-B phase is surrounded by two first order phase transition lines on the two sides and one second order phase transition line on the dome.

If the antiferromagnetic-paramagnetic phase transition is second order at relatively high temperature ($\sim$3.5 K to T_N) and becomes first order as the transition temperature is suppressed towards zero, questions about whether there are really quantum fluctuations in this material will arise.

In my work, I also found hysteresis in resistivity between the field sweeping up and the field sweeping down curves in both the AFM-B phase and the AFM-A phase. In contrast to the finding of Balicas *et al.* [7], where resistivity hysteresis was only found in the AFM-B and not reproduced in all their samples, the resistivity hysteresis discovered in our samples turned out to be highly reproducible.

Based on the magneto-resistivity measurements I constructed a 3D phase diagram of ρ-T-H which showed the details of the evolution of ρ of CeAuSb$_2$ in magnetic fields and at different temperatures. This helped to clarify the boundary of the AFM-B phase, which one of the things that I planned to do. The angle dependent electrical transport measurements revealed that, as the magnetic field was turned from the c-axis towards the basal plane, the magneto-resistivity of ρ_{CeAuSb_2} was controlled by the c-axis projection of the field. The effects of tilting the field from the c-axis towards the basal plane was basically just to push the two transitions to higher fields.

The torque magnetometry measurements have yielded results that are consistent with those of the electrical transport. At the positions where the transitions were observed in resistivity, two metamagnetic transitions were observed and they were also pushed to higher fields when the field direction is tilted from the c-axis towards the basal plane.

The last thing to mention is that no evidence of further transition splitting has been found at either of the two phase transitions even at temperatures well below 1 K (neither in magneto-resistivity nor torque magnetometry measurements).

Chapter 6

Conclusions and future work

I have presented in this thesis the experimental work that I have performed on two strongly correlated materials, Sr_2RuO_4 and $CeAuSb_2$, and the corresponding results. Here I give a short summary to the work and the results, and then point out some potential work that might be meaningful for future research.

6.1 Sr_2RuO_4

To investigate the superconducting properties of Sr_2RuO_4, I tried to traverse its γ-band VHS with piezo-electric based uniaxial strain methods, and studied the superconducting transition temperature dependence on uniaxial strain along the [100] direction and the relationship between the transition temperature and the c-axis upper critical field H_{c2}. Simulation results suggest that to traverse the γ-band VHS, the strain scale needed would be between 0.5% and 1.0%. The experimental results showed that, for a sample whose transition temperature T_c is 1.45 K under zero strain, by applying a uniaxial strain ε_{100} of approximately 0.92%, T_c could be enhanced by a factor of 230%, to $\sim$3.4 K, and it seemed that T_c could not be enhanced further with higher strain. At the same time, the upper critical field H_{c2} showed an enhancement that was larger than T_c^2. These results, when considered

together with the simulation results, indicate that γ-band VHS has very likely been successfully transversed, without destroying the material's superconductivity.

Technically, results presented in this work have manifested the big advantage of the piezo-electric based uniaxial stain methods in achieving highly homogeneous strain. The superconducting transition reflected in the AC susceptibility signal was neat and was only broadened by a limited amount even when the sample was considerably strained. The strain homogeneity was also high enough to guarantee successful measurements on the upper critical field H_{c2}. Close to the highest applied strain the sharpening of the onset of the superconducting transition gave rise to a well defined T_c.

Regarding the pairing symmetry of Sr_2RuO_4, although in a naive BCS picture the results do not seem to favour the chiral p-wave scenario, it is difficult draw a clear conclusion at this point. The results presented here need proper interpretation based on careful theoretical calculations. This work, I believe, is only a starting point for the study with uniaxial strain methods on superconductivity of Sr_2RuO_4 from the perspective of approaching a VHS.

What is desirable next is not only theoretical calculations but also more experimental work. From the experimental point of view, it will be interesting to combine the uniaxial strain methods with more probing methods (A) to directly verify that the γ-band VHS has indeed been traversed, and (B) to study other equilibrium properties of Sr_2RuO_4 under uniaxial strain. For the former, ARPES is probably the most evident option, especially considering its previous successful application in studying the VHS of chemically doped Sr_2RuO_4 [47] [171]. Technically it is possible because a considerable section of the top surface of the sample is open to spectroscopy in piezo-electric based uniaxial strain methods. For the latter, data on for example specific heat or electrical resistivity will be useful to obtain better understanding on the change in physics when the sample is strained. Taking the specific heat for example, one may see the effects of enhancement of the DOS as the sample is strained, and if the chiral p-wave proposal were true and

the experimental resolution were high enough, one might expect to see two transitions in series as the strained sample is cooled from its normal state to the deep superconducting state.

6.2 CeAuSb$_2$

I have performed a series of electrical resistivity and torque magnetometry measurements on CeAuSb$_2$ at temperatures down to 20 mK and in fields up to 35 T. Based on the electrical resistivity measurements performed in the presence of a c-axis field, I obtained a detailed 3D topography of $\rho(T, H)$ (resistivity as a function of field and temperature) for CeAuSb$_2$ (refer to Figure 5.29). The resistivity hysteresis analysis suggests that the novel phase of CeAuSb$_2$, i.e. the antiferromagnetic B phase, is surrounded by two lines of weakly first order phase transitions on the left and the right hand side and a line of second order phase transitions on the dome. The fact that the magnetic-nonmagnetic state transition at $T \ll T_N$ is first-order casts questions on the validity of the arguments about the quantum fluctuations in this system, or on the origin of them if one believes in their existence. The angle dependent magneto-resistivity and torque magnetometry measurements suggests that CeAuSb$_2$ is magnetically highly two dimensional although it is electrically not so. The observed magneto-resistivity is dominated by the c-axis component of the magnetic field as it is tilted towards the ab-plane. This experimental work, based on samples of best quality available so far, showed consistency with most of the previously published results, except that no evidence was found of transition splitting at either of the two metamagnetic transitions in c-axis fields.

Since study of CeAuSb$_2$ is still at a relatively early stage, there is plenty of work that one could do to improve our understanding of it. For example to grow samples of even better quality is still highly desirable, because with pure enough samples one can at least expect to measure the dHvA signals which will help one to obtain information about its Fermi surface. So far this is not achieved yet, even with

our cleanest samples. Bearing in mind the knowledge learned from the research history of $Sr_3Ru_2O_7$, it might even be possible to find more new physics when the sample purity of $CeAuSb_2$ is further improved. Neutron scattering work will be helpful to obtain useful information about the material's magnetic structure in its ordered phases (in both the anti-ferromagnetic A phase and the anti-ferromagnetic B phase), which will be extremely important to understand its magnetic properties. There is also only limited information in the literature about its thermodynamic properties, for example specific heat. Thus careful specific heat measurements down to low temperatures (below 1 K) will still be meaningful. On the theoretical side, one would expect to see more work on the theoretical calculations of its band structure and the prediction of its Fermi surface topography. The interpretation of results obtained from electrical transport and torque magnetometry measurements needs to be put on the basis of careful calculations. A feature of interest highlighted by my work is the strong two-dimensionality of the responses to the phase transitions. Although the electronic structure would be expected to have some anisotropy, it is not clear that it would show the very strong magnetic anisotropy for which I have found evidence.

To summarise, interesting new physics has been discovered in my work on both Sr_2RuO_4 and $CeAuSb_2$, but there is still much room left for future theoretical and experimental research on both of them.

Bibliography

[1] R B Laughlin and D Pines. The theory of everything. *Proceedings of the National Academy of Sciences of the United States of America*, 97(1):28–31, 2000.

[2] Elbio Dagotto. Complexity in strongly correlated electronic systems. *Science (New York, N.Y.)*, 309(5732):257–62, jul 2005.

[3] ND Mathur, FM Grosche, and SR Julian. Magnetically mediated superconductivity in heavy fermion compounds. *Nature*, 394(July):39–43, 1998.

[4] C. Lester, S. Ramos, R. S. Perry, T. P. Croft, R. I. Bewley, T. Guidi, P. Manuel, D. D. Khalyavin, E. M. Forgan, and S. M. Hayden. Field-tunable spin-density-wave phases in $Sr_3Ru_2O_7$. *Nature Materials*, 14(4): 373–378, January 2015.

[5] Andrew Peter Mackenzie and Yoshiteru Maeno. The superconductivity of Sr_2RuO_4 and the physics of spin-triplet pairing. *Reviews of Modern Physics*, 75(2):657–712, May 2003.

[6] Clifford W Hicks, Daniel O Brodsky, Edward a Yelland, Alexandra S Gibbs, Jan a N Bruin, Mark E Barber, Stephen D Edkins, Keigo Nishimura, Shingo Yonezawa, Yoshiteru Maeno, and Andrew P Mackenzie. Strong increase of T(c) of Sr_2RuO_4 under both tensile and compressive strain. *Science (New York, N.Y.)*, 344(6181):283–5, April 2014.

[7] L. Balicas, S. Nakatsuji, H. Lee, P. Schlottmann, T. P. Murphy, and Z. Fisk. Magnetic field-tuned quantum critical point in $CeAuSb_2$. *Physical Review B*, 72(6):064422, aug 2005. ISSN 1098-0121.

[8] P. Drude. Zur elektronentheorie der metalle. *Annalen der Physik*, 306:566–613, 1900.

[9] N. David Mermin Neil W. Ashcroft. *Solid State Physics*. Brooks Cole, 1 edition, 1976.

[10] L D. Landau. The Theory of a Fermi Liquid. *Soviet Physics JETP-USSR*, 3(6):920–925, 1957.

[11] L D. Landau. Oscillations in a Fermi liquid. *Soviet Physics JETP-USSR*, 5(1):101–108, 1957.

[12] L D. Landau. On the theory of a fermi liquid. *Soviet Physics JETP*, 8:70–74, 1959.

[13] A. J. Schofield. Non-Fermi liquids. *Contemporary Physics*, 40(2):95–115, mar 1999.

[14] L Forro, GL Carr, GP Williams, D Mandrus, and L Mihaly. Far-infrared transmission study of single-crystal $Bi_2Sr_2Ca_1Cu_2O_x$ superconductors. *Physical Review Letters*, 65(15):1941, 1990.

[15] Assa Auerbach. *Interacting Electrons and Quantum Magnetism*. Springer-Verlag New York, 1 edition, 1994.

[16] Daniel I. Khomskii. *Basic Aspects of the Quantum Theory of Solids: Order and Elementary Excitations*. Cambridge University Press, New York, 1 edition, 2010.

[17] Elliott H. Lieb and F. Y. Wu. Absence of Mott Transition in an Exact Solution of the Short-Range, One-Band Model in One Dimension. *Physical Review Letters*, 20(25):1445–1448, jun 1968.

[18] Efstratios Manousakis. The spin- Heisenberg antiferromagnet on a square lattice and its application to the cuprous oxides. *Reviews of Modern Physics*, 63(1):1–62, 1991.

[19] N Elstner, R. R. P. Singh, and A. P. Young. Finite temperature properties of the spin-1/2 Heisenberg antiferromagnet on the triangular lattice. *Physical Review Letters*, 71(10):1629–1632, sep 1993.

[20] Jonathan Keeling. Quantum magnetism. University Lecture, 2012.

[21] K A Chao, J Spalek, and A M Oles. Kinetic exchange interaction in a narrow *s*-band. *Journal of Physics C: Solid State Physics*, 10(10):L271, 1977.

[22] K. A. Chao, J. Spałek, and a. M. Oleś. Canonical perturbation expansion of the Hubbard model. *Physical Review B*, 18(7):3453–3464, October 1978. doi: 10.1103/PhysRevB.18.3453.

[23] Robert M. White. *Quantum Theory of Magnetism*, volume 32 of *Springer Series in Solid-State Sciences*. Springer-Verlag, Berlin Heidelberg, 3rd edition, completely revised edition edition, 2007.

[24] Subir Sachdev. *Quantum Phase Transitions*. Springer Series in Solid-State Sciences. Cambridge University Press, 2nd edition edition, 2011.

[25] P. M. Chaikin and T. C. Lubensky. *Principles of Condensed Matter Physics*. Cambridge University Press, new edition edition, 2000.

[26] Leo P Kadanoff. Phases of matter and phase transitions; from mean field theory to critical phenomena. *Journal of Physics: Condensed Matter*, 12: 1496, 2009.

[27] Kurt Binder. Theory of first-order phase transitions. *Reports on progress in physics*, 50(7):783, 1987.

[28] Kenneth G Wilson. Renormalization group and critical phenomena. i. renormalization group and the kadanoff scaling picture. *Physical review B*, 4(9): 3174, 1971.

[29] Kenneth G. Wilson. Renormalization group and critical phenomena. II. Phase-space cell analysis of critical behavior. *Physical Review B*, 4(9):3184–3205, 1971.

[30] Hilbert v Löhneysen, Achim Rosch, Matthias Vojta, and Peter Wölfle. Fermi-liquid instabilities at magnetic quantum phase transitions. *Reviews of Modern Physics*, 79(3):1015, 2007.

[31] John A Hertz. Quantum critical phenomena. *Physical Review B*, 14(3): 1165–1184, 1976.

[32] SA Grigera, P Gegenwart, RA Borzi, F Weickert, AJ Schofield, RS Perry, T Tayama, T Sakakibara, Y Maeno, AG Green, et al. Disorder-sensitive phase formation linked to metamagnetic quantum criticality. *Science*, 306 (5699):1154–1157, 2004.

[33] Y Maeno, H Hashimoto, K Yoshida, S Nishizaki, T Fujita, JG Bednorz, and F Lichtenberg. Superconductivity in a layered perovskite without copper. *Nature*, 372(6506):532–534, 1994.

[34] NE Hussey, AP Mackenzie, JR Cooper, Y Maeno, S Nishizaki, and T Fujita. Normal-state magnetoresistance of Sr_2RuO_4. *Physical Review B*, 57(9):5505, 1998.

[35] S Seo, VA Sidorov, H Lee, D Jang, Z Fisk, JD Thompson, and T Park. Pressure effects on the heavy-fermion antiferromagnet $CeAuSb_2$. *Physical Review B*, 85(20):205145, 2012.

[36] Warren C. Young and Richard G Budynas. *Roark's Formulas for Stress and Strain*. McGraw-Hill Professional, 7 edition edition, 2002.

[37] Woldemar Voigt. *Lehrbuch der Kristallphysik*. Teubner Verlag, reprint of the 1st edition edition, 1966.

[38] L. D. Landau and E. M. Lifshitz. *Theory of elasticity*, volume 7 of *Course of Theoretical Physics*. Pergamon Press, 2nd english edition edition, 1970.

[39] Yakov Itin and Friedrich W. Hehl. The constitutive tensor of linear elasticity: Its decompositions, cauchy relations, null lagrangians, and wave propagation. *Journal of Mathematical Physics*, 54(042903), 2013.

[40] C Lupien, WA MacFarlane, Cyril Proust, Louis Taillefer, ZQ Mao, and Y Maeno. Ultrasound attenuation in Sr_2RuO_4: an angle-resolved study of the superconducting gap function. *arXiv preprint cond-mat/0101319*, 2001.

[41] Clifford W Hicks, Mark E Barber, Stephen D Edkins, Daniel O Brodsky, and Andrew P Mackenzie. Piezoelectric-based apparatus for strain tuning. *Review of Scientific Instruments*, 85(6):065003, 2014.

[42] Frank Pobell. *Matter and methods at low temperatures.* Springer Science & Business Media, 2007.

[43] Jan Adrianus Nathan Bruin. *Transport Studies of the Itinerant Metamagnet $Sr_3Ru_2O_7$ Near Its Quantum Critical Point.* PhD thesis, University of St Andrews, 2012.

[44] Yoshiteru Maeno, Shunichiro Kittaka, Takuji Nomura, Shingo Yonezawa, and Kenji Ishida. Evaluation of spin-triplet superconductivity in Sr_2RuO_4. *Journal of the Physical Society of Japan*, 81(1):011009, 2011.

[45] Takuji Nomura and Kosaku Yamada. Magnetic properties of quasi-two-dimensional ruthenates studied by mean field theoretical approach. *Journal of the Physical Society of Japan*, 69(6):1856–1864, 2000.

[46] C Bergemann, AP Mackenzie, SR Julian, D Forsythe, and E Ohmichi. Quasi-two-dimensional fermi liquid properties of the unconventional superconductor Sr_2RuO_4. *Advances in Physics*, 52(7):639–725, 2003.

[47] KM Shen, N Kikugawa, C Bergemann, L Balicas, F Baumberger, W Meevasana, NJC Ingle, Y Maeno, Z-X Shen, and AP Mackenzie. Evolution of the fermi surface and quasiparticle renormalization through a van hove singularity in $Sr_{2-y}La_yRuO_4$. *Physical Review Letters*, 99(18):187001, 2007.

[48] O Chmaissem, JD Jorgensen, H Shaked, S Ikeda, and Y Maeno. Thermal expansion and compressibility of Sr_2RuO_4. *Physical Review B*, 57(9):5067, 1998.

[49] R Matzdorf, Z Fang, Jiandi Zhang, T Kimura, Y Tokura, K Terakura, EW Plummer, et al. Ferromagnetism stabilized by lattice distortion at the surface of the *p*-wave superconductor Sr_2RuO_4. *Science*, 289(5480):746–748, 2000.

[50] H Shaked, JD Jorgensen, S Short, O Chmaissem, S-I Ikeda, and Y Maeno. Temperature and pressure effects on the crystal structure of $Sr_3Ru_2O_7$: Evidence for electronically driven structural responses. *Physical Review B*, 62 (13):8725, 2000.

[51] Ryoji Kiyanagi, Kenji Tsuda, Naofumi Aso, Hiroyuki Kimura, Yukio Noda, Yoshiyuki Yoshida, Sin-Ichi Ikeda, and Yoshiya Uwatoko. Investigation of the structure of single crystal $Sr_3Ru_2O_7$ by neutron and convergent beam electron diffractions. *Journal of the Physical Society of Japan*, 73(3):639–642, 2004.

[52] J-F Mercure, A W Rost, ECT O' Farrell, S K Goh, R S Perry, M L Sutherland, S A Grigera, R A Borzi, P Gegenwart, A S Gibbs, et al. Quantum oscillations near the metamagnetic transition in $Sr_3Ru_2O_7$. *Physical Review B*, 81(23):235103, 2010.

[53] MK Crawford, R L Harlow, W Marshall, Z Li, G Cao, R L Lindstrom, Q Huang, and J W Lynn. Structure and magnetism of single crystal $Sr_4Ru_3O_{10}$: A ferromagnetic triple-layer ruthenate. *Physical Review B*, 65 (21):214412, 2002.

[54] CW Jones, PD Battle, P Lightfoot, and WTA Harrison. The structure of $SrRuO_3$ by time-of-flight neutron powder diffraction. *Acta Crystallographica Section C: Crystal Structure Communications*, 45(3):365–367, 1989.

[55] AP Mackenzie, RKW Haselwimmer, AW Tyler, GG Lonzarich, Y Mori, S Nishizaki, and Y Maeno. Extremely strong dependence of superconductivity on disorder in Sr_2RuO_4. *Physical Review Letters*, 80(1):161, 1998.

[56] RS Perry, LM Galvin, SA Grigera, L Capogna, AJ Schofield, AP Mackenzie, M Chiao, SR Julian, SI Ikeda, S Nakatsuji, et al. Metamagnetism and critical

fluctuations in high quality single crystals of the bilayer ruthenate $Sr_3Ru_2O_7$. *Physical Review Letters*, 86(12):2661, 2001.

[57] G Cao, Luis Balicas, WH Song, YP Sun, Yan Xin, VA Bondarenko, JW Brill, S Parkin, and XN Lin. Competing ground states in triple-layered $Sr_4Ru_3O_{10}$: Verging on itinerant ferromagnetism with critical fluctuations. *Physical Review B*, 68(17):174409, 2003.

[58] ZQ Mao, M Zhou, J Hooper, V Golub, and CJ O'Connor. Phase separation in the itinerant metamagnetic transition of $Sr_4Ru_3O_{10}$. *Physical Review Letters*, 96(7):077205, 2006.

[59] JM Longo, PM Raccah, and JB Goodenough. Magnetic properties of $SrRuO_3$ and $CaRuO_3$. *Journal of Applied Physics*, 39(2):1327–1328, 1968.

[60] AP Mackenzie, JW Reiner, AW Tyler, LM Galvin, SR Julian, MR Beasley, TH Geballe, and A Kapitulnik. Observation of quantum oscillations in the electrical resistivity of $SrRuO_3$. *Physical Review B*, 58(20):R13318, 1998.

[61] XD Wu, SR Foltyn, RC Dye, Y Coulter, and RE Muenchausen. Properties of epitaxial $SrRuO_3$ thin films. *Applied physics letters*, 62(19):2434–2436, 1993.

[62] AP Ramirez. Colossal magnetoresistance. *Journal of Physics: Condensed Matter*, 9(39):8171, 1997.

[63] E Ohmichi, Y Maeno, S Nagai, ZQ Mao, MA Tanatar, and T Ishiguro. Magnetoresistance of Sr_2RuO_4 under high magnetic fields parallel to the conducting plane. *Physical Review B*, 61(10):7101, 2000.

[64] Shin-Ichi Ikeda, Yoshiteru Maeno, Satoru Nakatsuji, Masashi Kosaka, and Yoshiya Uwatoko. Ground state in $Sr_3Ru_2O_7$: Fermi liquid close to a ferromagnetic instability. *Physical Review B*, 62(10):R6089, 2000.

[65] G Cao, S McCall, M Shepard, JE Crow, and RP Guertin. Thermal, magnetic, and transport properties of single-crystal $Sr_{1-x}Ca_xRuO_3$($0< x< 1.0$). *Physical Review B*, 56(1):321, 1997.

[66] John J Randall and Roland Ward. The preparation of some ternary oxides of the platinum metals. *Journal of the American Chemical Society*, 81(11): 2629–2631, 1959.

[67] J.G. Bednorz and K.A. Müller. Possible High Tc Superconductivity in the Ba-La-Cu-O System. *Zeitschrift für Physik B: Condensed Matter*, 64:189–193, 1986.

[68] F Lichtenberg. The story of Sr_2RuO_4. *Progress in solid state chemistry*, 30 (3):103–131, 2002.

[69] AP Mackenzie, SR Julian, AJ Diver, GJ McMullan, MP Ray, GG Lonzarich, Y Maeno, S Nishizaki, and T Fujita. Quantum oscillations in the layered perovskite superconductor Sr_2RuO_4. *Physical Review Letters*, 76(20):3786, 1996.

[70] K Ishida, H Mukuda, Y Kitaoka, K Asayama, ZQ Mao, Y Mori, and Y Maeno. Spin-triplet superconductivity in Sr_2RuO_4 identified by ^{17}O knight shift. *Nature*, 396(6712):658–660, 1998.

[71] GM Luke, Y Fudamoto, KM Kojima, MI Larkin, J Merrin, B Nachumi, YJ Uemura, Y Maeno, ZQ Mao, Y Mori, et al. Time-reversal symmetry-breaking superconductivity in Sr_2RuO_4. *Nature*, 394(6693):558–561, 1998.

[72] Jing Xia, Yoshiteru Maeno, Peter T Beyersdorf, MM Fejer, and Aharon Kapitulnik. High resolution polar Kerr effect measurements of Sr_2RuO_4: evidence for broken time-reversal symmetry in the superconducting state. *Physical Review Letters*, 97(16):167002, 2006.

[73] Aharon Kapitulnik, Jing Xia, Elizabeth Schemm, and Alexander Palevski. Polar Kerr effect as probe for time-reversal symmetry breaking in unconventional superconductors. *New Journal of Physics*, 11(5):055060, 2009.

[74] TM Rice and M Sigrist. Sr_2RuO_4: an electronic analogue of 3He? *Journal of Physics: Condensed Matter*, 7(47):L643, 1995.

[75] Chetan Nayak, Steven H Simon, Ady Stern, Michael Freedman, and Sankar Das Sarma. Non-abelian anyons and topological quantum computation. *Reviews of Modern Physics*, 80(3):1083, 2008.

[76] T Katsufuji, M Kasai, and Y Tokura. In-plane and out-of-plane optical spectra of Sr_2RuO_4. *Physical Review Letters*, 76(1):126, 1996.

[77] Yoshiteru Maeno, Koji Yoshida, Hiroaki Hashimoto, Shuji Nishizaki, Shinichi Ikeda, Minoru Nohara, Toshizo Fujita, Andrew P Mackenzie, Nigel E Hussey, J Georg Bednorz, et al. Two-dimensional fermi liquid behavior of the superconductor Sr_2RuO_4. *Journal of the Physical Society of Japan*, 66(5):1405–1408, 1997.

[78] Andrew P Mackenzie, Shin-ichi Ikeda, Yoshiteru Maeno, Toshizo Fujita, Stephen R Julian, and Gilbert G Lonzarich. The fermi surface topography of Sr_2RuO_4. *Journal of the Physical Society of Japan*, 67(2):385–388, 1998.

[79] Tamio Oguchi. Electronic band structure of the superconductor Sr_2RuO_4. *Physical Review B*, 51(2):1385, 1995.

[80] Izumi Hase and Yoshikazu Nishihara. Electronic structures of Sr_2RuO_4 and sr_2rho_4. *Journal of the Physical Society of Japan*, 65(12):3957–3963, 1996.

[81] BC Passenheim and DC McCollum. Heat capacity of RuO2 and IrO2 between 0.54° and 10° k. *The Journal of Chemical Physics*, 51(1):320–321, 1969.

[82] PA Cox. The electronic structure of transition metal oxides and chalcogenides. In *Physics and Chemistry of Low-Dimensional Inorganic Conductors*, pages 255–270. Springer, 1996.

[83] A Damascelli, DH Lu, KM Shen, NP Armitage, F Ronning, DL Feng, C Kim, Z-X Shen, T Kimura, Y Tokura, et al. Fermi surface, surface states, and surface reconstruction in Sr_2RuO_4. *Physical Review Letters*, 85(24):5194, 2000.

[84] PK De Boer and RA De Groot. Electronic structure of magnetic Sr_2RuO_4. *Physical Review B*, 59(15):9894, 1999.

[85] A Pérez-Navarro, J Costa-Quintana, and F López-Aguilar. Electronic structure of Sr_2RuO_4 by means of local-density approximation plus strong correlation effects. *Physical Review B*, 61(15):10125, 2000.

[86] David Shoenberg. *Magnetic oscillations in metals*. Cambridge University Press, 1984.

[87] PD Grigoriev. Angular dependence of the fermi surface cross-section area and magnetoresistance in quasi-two-dimensional metals. *Physical Review B*, 81(20):205122, 2010.

[88] Andrea Damascelli, Zahid Hussain, and Zhi-Xun Shen. Angle-resolved photoemission studies of the cuprate superconductors. *Reviews of modern physics*, 75(2):473, 2003.

[89] Stephan Hüfner. *Photoelectron Spectroscopy*, volume 82 of *Springer Series in Solid-State Sciences*. Springer-Verlag Berlin Heidelberg, 3rd edition edition, 2003.

[90] Shigemasa Suga and Akira Sekiyama. *Photoelectron Spectroscopy*, volume 176 of *Springer Series in Solid-State Sciences*. Springer-Verlag Berlin Heidelberg, 1st edition edition, 2014.

[91] T Yokoya, A Chainani, T Takahashi, H Katayama-Yoshida, M Kasai, and Y Tokura. Extended van hove singularity in a noncuprate layered superconductor Sr_2RuO_4. *Physical Review Letters*, 76(16):3009, 1996.

[92] DH Lu, M Schmidt, TR Cummins, S Schuppler, F Lichtenberg, and JG Bednorz. Fermi surface and extended Van Hove singularity in the noncuprate superconductor Sr_2RuO_4. *Physical Review Letters*, 76(25):4845, 1996.

[93] H Ding, S-C Wang, H-B Yang, T Takahashi, JC Campuzano, and Y Maeno. Band reflection and surface reconstruction in Sr_2RuO_4. *Physica C: Superconductivity*, 364:594–599, 2001.

[94] C Bergemann, JS Brooks, L Balicas, AP Mackenzie, SR Julian, ZQ Mao, and Y Maeno. Normal state of the unconventional superconductor Sr_2RuO_4 in high magnetic fields. *Physica B: Condensed Matter*, 294:371–374, 2001.

[95] John Bardeen, Leon N Cooper, and J Robert Schrieffer. Theory of superconductivity. *Physical Review*, 108(5):1175, 1957.

[96] R Balian and NR Werthamer. Superconductivity with pairs in a relative p wave. *Physical Review*, 131(4):1553, 1963.

[97] D Vollhardt and P Wölfle. The superfluid phases of helium–3, 1990.

[98] Philip W Anderson. Theory of dirty superconductors. *Journal of Physics and Chemistry of Solids*, 11(1):26–30, 1959.

[99] Koji Yoshida, Yoshiteru Maeno, Shuji Nishizaki, and Toshizo Fujita. Anisotropic flux pinning in a layered superconductor Sr_2RuO_4. *Journal of the Physical Society of Japan*, 65(7):2220–2226, 1996.

[100] RJ Radtke, K Levin, H-B Schüttler, and MR Norman. Predictions for impurity-induced t c suppression in the high-temperature superconductors. *Physical Review B*, 48(1):653, 1993.

[101] K Ishida, Y Kitaoka, K Asayama, S Ikeda, S Nishizaki, Y Maeno, K Yoshida, and T Fujita. Anisotropic pairing in superconducting Sr_2RuO_4: Ru nmr and nqr studies. *Physical Review B*, 56(2):R505, 1997.

[102] Kenji Ishida, Hiroshi Murakawa, Hidekazu Mukuda, Yoshio Kitaoka, ZQ Mao, and Yoshiteru Maeno. Nmr and nqr studies on superconducting Sr_2RuO_4. *Journal of Physics and Chemistry of Solids*, 69(12):3108–3114, 2008.

[103] Shuji NishiZaki, Yoshiteru Maeno, and Zhiqiang Mao. Effect of impurities on the specific heat of the spin-triplet superconductor Sr_2RuO_4. *Journal of Low Temperature Physics*, 117(5-6):1581–1585, 1999.

[104] R. D. Parks. *Superconductivity: Part 1*. Dekker, 1st edition edition, 1969.

[105] Jacques Winter. *Magnetic resonance in metals.* Clarendon Press, 1971.

[106] K Ishida, H Mukuda, Y Kitaoka, ZQ Mao, H Fukazawa, and Y Maeno. Ru NMR probe of spin susceptibility in the superconducting state of Sr_2RuO_4. *Physical Review B*, 63(6):060507, 2001.

[107] H Murakawa, K Ishida, K Kitagawa, ZQ Mao, and Y Maeno. Measurement of the Ru 101-knight shift of superconducting Sr_2RuO_4 in a parallel magnetic field. *Physical Review Letters*, 93(16):167004, 2004.

[108] H Murakawa, K Ishida, K Kitagawa, H Ikeda, Z Q. Mao, and Y Maeno. 101ru knight shift measurement of superconducting Sr_2RuO_4 under small magnetic fields parallel to the RuO_2 plane. *Journal of the Physical Society of Japan*, 76(2):024716, 2007.

[109] JA Duffy, SM Hayden, Y Maeno, Z Mao, J Kulda, and GJ McIntyre. Polarized-neutron scattering study of the cooper-pair moment in Sr_2RuO_4. *Physical Review Letters*, 85(25):5412, 2000.

[110] J Jang, DG Ferguson, V Vakaryuk, R Budakian, SB Chung, PM Goldbart, and Y Maeno. Observation of half-height magnetization steps in Sr_2RuO_4. *Science*, 331(6014):186–188, 2011.

[111] KD Nelson, ZQ Mao, Y Maeno, and Y Liu. Odd-parity superconductivity in Sr_2RuO_4. *Science*, 306(5699):1151–1154, 2004.

[112] Vadim B Geshkenbeĭn, Anatoly I Larkin, and Antonio Barone. Vortices with half magnetic flux quanta in heavy-fermion superconductors. *Physical Review B*, 36(1):235, 1987.

[113] VB Geshkenbeĭn and AI Larkin. The josephson effect in superconductors with heavy fermions. *JETP Lett*, 43(6), 1986.

[114] A Millis, D Rainer, and JA Sauls. Quasiclassical theory of superconductivity near magnetically active interfaces. *Physical Review B*, 38(7):4504, 1988.

[115] Yasuhiro Asano, Yukio Tanaka, Manfred Sigrist, and Satoshi Kashiwaya. Josephson current in s-wave-superconductor/Sr_2RuO_4 junctions. *Physical Review B*, 67(18):184505, 2003.

[116] DJ Van Harlingen. Phase-sensitive tests of the symmetry of the pairing state in the high-temperature superconductors–evidence for $d_{x^2-y^2}$ symmetry. *Reviews of Modern Physics*, 67(2):515, 1995.

[117] Manfred Sigrist and Kazuo Ueda. Phenomenological theory of unconventional superconductivity. *Reviews of Modern physics*, 63(2):239, 1991.

[118] TM Riseman, PG Kealey, EM Forgan, AP Mackenzie, LM Galvin, AW Tyler, SL Lee, C Ager, D McK Paul, CM Aegerter, et al. Observation of a square flux-line lattice in the unconventional superconductor Sr_2RuO_4. *Nature*, 396 (6708):242–245, 1998.

[119] PG Kealey, TM Riseman, EM Forgan, LM Galvin, AP Mackenzie, SL Lee, D McK Paul, R Cubitt, DF Agterberg, R Heeb, et al. Reconstruction from small-angle neutron scattering measurements of the real space magnetic field distribution in the mixed state of Sr_2RuO_4. *Physical Review Letters*, 84(26): 6094, 2000.

[120] C.W.J. Beenakker. Search for majorana fermions in superconductors. *Annual Review of Condensed Matter Physics*, 4:113–136, 2013.

[121] Jason Alicea. New directions in the pursuit of majorana fermions in solid state systems. *Reports on Progress in Physics*, 75(7):076501, 2012.

[122] Martin Leijnse and Karsten Flensberg. Introduction to topological superconductivity and majorana fermions. *Semiconductor Science and Technology*, 27(12):124003, 2012.

[123] Manfred Sigrist. Broken time reversal symmetry in unconventional superconductors. *Physica C: Superconductivity*, 341:695–698, 2000.

[124] Francoise Kidwingira, JD Strand, DJ Van Harlingen, and Yoshiteru Maeno. Dynamical superconducting order parameter domains in Sr_2RuO_4. *Science*, 314(5803):1267–1271, 2006.

[125] Taketomo Nakamura, R Nakagawa, T Yamagishi, T Terashima, S Yonezawa, M Sigrist, and Y Maeno. Topological competition of superconductivity in $Pb/Ru/Sr_2RuO_4$ junctions. *Physical Review B*, 84(6):060512, 2011.

[126] MS Anwar, Taketomo Nakamura, S Yonezawa, M Yakabe, R Ishiguro, H Takayanagi, and Y Maeno. Anomalous switching in $Nb/Ru/Sr_2RuO_4$ topological junctions by chiral domain wall motion. *Scientific reports*, 3, 2013.

[127] VO Dolocan, C Veauvy, F Servant, P Lejay, K Hasselbach, Y Liu, and D Mailly. Observation of vortex coalescence in the anisotropic spin-triplet superconductor Sr_2RuO_4. *Physical Review Letters*, 95(9):097004, 2005.

[128] Masashige Matsumoto and Manfred Sigrist. Quasiparticle states near the surface and the domain wall in a $p_x \pm ip_y$-wave superconductor. *Journal of the Physical Society of Japan*, 68(3):994–1007, 1999.

[129] Masashige Matsumoto and Manfred Sigrist. Quasiparticle states near the surface and the domain wall in a $p_x \pm ip_y$-wave superconductor. *Physica B: Condensed Matter*, 284:545–546, 2000.

[130] Tsuyoshi Tamegai, Kohei Yamazaki, Masashi Tokunaga, Zhiqiang Mao, and Yoshiteru Maeno. Search for spontaneous magnetization in Sr_2RuO_4. *Physica C: Superconductivity*, 388:499–500, 2003.

[131] Per G Björnsson, Yoshiteru Maeno, Martin E Huber, and Kathryn A Moler. Scanning magnetic imaging of Sr_2RuO_4. *Physical Review B*, 72(1):012504, 2005.

[132] JR Kirtley, C Kallin, CW Hicks, E-A Kim, Ying Liu, KA Moler, Y Maeno, and KD Nelson. Upper limit on spontaneous supercurrents in Sr_2RuO_4. *Physical Review B*, 76(1):014526, 2007.

[133] Clifford W Hicks, John R Kirtley, Thomas M Lippman, Nicholas C Koshnick, Martin E Huber, Yoshiteru Maeno, William M Yuhasz, M Brian Maple, and Kathryn A Moler. Limits on superconductivity-related magnetization in Sr_2RuO_4 and $PrOs_4Sb_{12}$ from scanning squid microscopy. *Physical Review B*, 81(21):214501, 2010.

[134] Michael Tinkham. *Introduction to superconductivity*. Courier Corporation, 2012.

[135] Manfred Sigrist. Introduction to unconventional superconductivity. In *Lectures on the Physics of Highly Correlated Electron Systems IX*, volume 789, pages 165–243, 2005.

[136] K Maki, G-f Wang, and H Won. p-wave superconductors in Sr_2RuO_4 and bechgaard salts. *Journal of superconductivity*, 12(4):551–556, 1999.

[137] S Kittaka, T Nakamura, Y Aono, S Yonezawa, K Ishida, and Y Maeno. Angular dependence of the upper critical field of Sr_2RuO_4. *arXiv preprint arXiv:0906.2513*, 2009.

[138] ZQ Mao, Y Maeno, S NishiZaki, T Akima, and T Ishiguro. In-plane anisotropy of upper critical field in Sr_2RuO_4. *Physical Review Letters*, 84(5): 991, 2000.

[139] E Helfand and NR Werthamer. Temperature and purity dependence of the superconducting critical field, H_{c2}. ii. *Physical Review*, 147(1):288–294, 1966.

[140] Shingo Yonezawa, Tomohiro Kajikawa, and Yoshiteru Maeno. First-order superconducting transition of Sr_2RuO_4. *Physical Review Letters*, 110(7): 077003, 2013.

[141] Shingo Yonezawa, Tomohiro Kajikawa, and Yoshiteru Maeno. Specific-heat evidence of the first-order superconducting transition in Sr_2RuO_4. *Journal of the Physical Society of Japan*, 83(8):083706, 2014.

[142] Shuji NishiZaki, Yoshiteru Maeno, and Zhiqiang Mao. Changes in the superconducting state of Sr_2RuO_4 under magnetic fields probed by specific heat. *Journal of the Physical Society of Japan*, 69(2):572–578, 2000.

[143] Koich Izawa, Hidekazu Takahashi, Hidemasa Yamaguchi, Yuji Matsuda, M Suzuki, T Sasaki, T Fukase, Y Yoshida, R Settai, and Y Onuki. Superconducting gap structure of spin-triplet superconductor Sr_2RuO_4 studied by thermal conductivity. *Physical Review Letters*, 86(12):2653, 2001.

[144] MA Tanatar, M Suzuki, S Nagai, ZQ Mao, Y Maeno, and T Ishiguro. Anisotropy of magnetothermal conductivity in Sr_2RuO_4. *Physical Review Letters*, 86(12):2649, 2001.

[145] I Bonalde, Brian D Yanoff, MB Salamon, DJ Van Harlingen, EME Chia, ZQ Mao, and Y Maeno. Temperature dependence of the penetration depth in Sr_2RuO_4: evidence for nodes in the gap function. *Physical Review Letters*, 85(22):4775, 2000.

[146] ME Zhitomirsky and TM Rice. Interband proximity effect and nodes of superconducting gap in Sr_2RuO_4. *Physical Review Letters*, 87(5):057001, 2001.

[147] DF Agterberg, TM Rice, and M Sigrist. Orbital dependent superconductivity in Sr_2RuO_4. *Physical Review Letters*, 78(17):3374, 1997.

[148] Takuji Nomura and Kosaku Yamada. Roles of electron correlations in the spin-triplet superconductivity of Sr_2RuO_4. *Journal of the Physical Society of Japan*, 71(8):1993–2004, 2002.

[149] Takuji Nomura and Kosaku Yamada. Detailed investigation of gap structure and specific heat in the p-wave superconductor Sr_2RuO_4. *Journal of the Physical Society of Japan*, 71(2):404–407, 2002.

[150] Takuji Nomura. Theory of transport properties in the p-wave superconducting state of Sr_2RuO_4 – a microscopic determination of the gap structure. *Journal of the Physical Society of Japan*, 74(6):1818–1829, 2005.

[151] Takuji Nomura, Hiroaki Ikeda, and Dai S Hirashima. Theory of magnetic properties in the spin-triplet superconducting state of Sr_2RuO_4. *Journal of Physics and Chemistry of Solids*, 69(12):3352–3355, 2008.

[152] Kazuhiko Deguchi, ZQ Mao, Hiroshi Yaguchi, and Yoshiteru Maeno. Gap structure of the spin-triplet superconductor Sr_2RuO_4 determined from the field-orientation dependence of the specific heat. *Physical Review Letters*, 92 (4):047002, 2004.

[153] S Raghu, A Kapitulnik, and SA Kivelson. Hidden quasi-one-dimensional superconductivity in Sr_2RuO_4. *Physical Review Letters*, 105(13):136401, 2010.

[154] Thomas Scaffidi, Jesper C Romers, and Steven H Simon. Pairing symmetry and dominant band in Sr_2RuO_4. *Physical Review B*, 89(22):220510, 2014.

[155] Igor Žutić and Igor Mazin. Phase-sensitive tests of the pairing state symmetry in Sr_2RuO_4. *Physical Review Letters*, 95(21):217004, 2005.

[156] S Souma, Y Machida, T Sato, T Takahashi, H Matsui, S-C Wang, H Ding, A Kaminski, JC Campuzano, S Sasaki, et al. The origin of multiple superconducting gaps in MgB_2. *Nature*, 423(6935):65–67, 2003.

[157] Kazuhiko Kuroki, Seiichiro Onari, Ryotaro Arita, Hidetomo Usui, Yukio Tanaka, Hiroshi Kontani, and Hideo Aoki. Unconventional pairing originating from the disconnected fermi surfaces of superconducting $LaFeAsO_{1-x}F_x$. *Physical Review Letters*, 101(8):087004, 2008.

[158] Léon Van Hove. The occurrence of singularities in the elastic frequency distribution of a crystal. *Physical Review*, 89(6):1189, 1953.

[159] IK Bdikin and Eugene H Peterson. *Superconductivity Research Horizons*. Nova Publishers, 2007.

[160] Henri Alloul and Stephen Lyle. *Introduction to the Physics of Electrons in Solids*. Springer Science & Business Media, 2010.

[161] RS Markiewicz. A survey of the van hove scenario for high-t c superconductivity with special emphasis on pseudogaps and striped phases. *Journal of Physics and Chemistry of Solids*, 58(8):1179–1310, 1997.

[162] Julien Bok and Jacqueline Bouvier. Van hove scenario for high T_c superconductors. *Physica C: Superconductivity*, 460:1010–1012, 2007.

[163] AA Abrikosov. Theory of high-tc superconducting cuprates based on experimental evidence. *Physica C: Superconductivity*, 341:97–102, 2000.

[164] Alexandre Piriou, Nathan Jenkins, Christophe Berthod, Ivan Maggio-Aprile, and Ø Fischer. First direct observation of the van hove singularity in the tunnelling spectra of cuprates. *Nature communications*, 2:221, 2011.

[165] S Raghu, Xiao-Liang Qi, Chao-Xing Liu, DJ Scalapino, and Shou-Cheng Zhang. Minimal two-band model of the superconducting iron oxypnictides. *Physical Review B*, 77(22):220503, 2008.

[166] SV Borisenko, VB Zabolotnyy, DV Evtushinsky, TK Kim, IV Morozov, AN Yaresko, AA Kordyuk, G Behr, A Vasiliev, R Follath, et al. Superconductivity without nesting in lifeas. *Physical Review Letters*, 105(6):067002, 2010.

[167] V. I. Anisimov I. Leonov, S. L. Skornyakov and D. Vollhardt. Correlation-driven topological fermi surface transition in fese. *Physical Review Letters*, 115(106402), 2015.

[168] Delong Fang, Xun Shi, Zengyi Du, Pierre Richard, Huan Yang, XX Wu, Peng Zhang, Tian Qian, Xiaxin Ding, Zhenyu Wang, et al. Observation of a van hove singularity with gap nodes in KFe_2As_2. *arXiv preprint arXiv:1412.0945*, 2014.

[169] IR Shein, NI Medvedeva, and AL Ivanovskii. The band structures of superconducting mgb_2 and the isostructural compounds $CaGa_2$, AgB_2, AuB_2, $ZrBe_2$, and $HfBe_2$. *Physics of the Solid State*, 43(12):2213–2218, 2001.

[170] VG Tissen, MV Nefedova, NN Kolesnikov, and MP Kulakov. Effect of pressure on the superconducting T_c of Mgb$_2$. *Physica C: Superconductivity*, 363 (3):194–197, 2001.

[171] N Kikugawa, AP Mackenzie, C Bergemann, RA Borzi, SA Grigera, and Y Maeno. Rigid-band shift of the fermi level in the strongly correlated metal: Sr$_{2-y}$La$_y$RuO$_4$. *Physical Review B*, 70(6):060508, 2004.

[172] A Liebsch and H Ishida. Subband filling and mott transition in Ca$_{2-x}$Sr$_x$RuO$_4$. *Physical Review Letters*, 98(21):216403, 2007.

[173] QH Wang, C Platt, Y Yang, C Honerkamp, FC Zhang, W Hanke, TM Rice, and R Thomale. Theory of superconductivity in a three-orbital model of Sr$_2$RuO$_4$. *EPL (Europhysics Letters)*, 104(1):17013, 2013.

[174] A Tamai, MP Allan, JF Mercure, W Meevasana, R Dunkel, DH Lu, RS Perry, AP Mackenzie, David J Singh, Z-X Shen, et al. Fermi surface and van hove singularities in the itinerant metamagnet Sr$_3$Ru$_2$O$_7$. *Physical Review Letters*, 101(2):026407, 2008.

[175] PA Igoshev, V Yu Irkhin, and AA Katanin. Magnetic fluctuations and self-energy effects in two-dimensional itinerant systems with a van hove singularity in the electronic spectrum. *Physical Review B*, 83(24):245118, 2011.

[176] J Labbe and J Bok. Superconductivity in alkaline-earth-substituted la$_2$cuo$_4$: a theoretical model. *EPL (Europhysics Letters)*, 3(11):1225, 1987.

[177] IE Dzyaloshinskii. Superconducting transitions due to van hove singularities in the electron spectrum. *Zhurnal Eksperimental'noi i Teoreticheskoi Fiziki*, 93(4):1487–98, 1987.

[178] HJ Schulz. Superconductivity and antiferromagnetism in the two-dimensional hubbard model: scaling theory. *EPL (Europhysics Letters)*, 4(5):609, 1987.

[179] David J Singh. Relationship of Sr$_2$RuO$_4$ to the superconducting layered cuprates. *Physical Review B*, 52(2):1358, 1995.

[180] Canio Noce and Mario Cuoco. Energy bands and fermi surface of Sr_2RuO_4. *Physical Review B*, 59(4):2659, 1999.

[181] H Iwasawa, Y Yoshida, I Hase, S Koikegami, H Hayashi, J Jiang, K Shimada, H Namatame, M Taniguchi, and Y Aiura. Interplay among coulomb interaction, spin-orbit interaction, and multiple electron-boson interactions in Sr_2RuO_4. *Physical Review Letters*, 105(22):226406, 2010.

[182] KM Shen, A Damascelli, DH Lu, NP Armitage, F Ronning, DL Feng, C Kim, Z-X Shen, DJ Singh, II Mazin, et al. Surface electronic structure of Sr_2RuO_4. *Physical Review B*, 64(18):180502, 2001.

[183] Satoru Nakatsuji and Y Maeno. Quasi-two-dimensional mott transition system $Ca_{2-x}Sr_xRuO_4$. *Physical Review Letters*, 84(12):2666, 2000.

[184] M Minakata and Y Maeno. Magnetic ordering in Sr_2RuO_4 induced by nonmagnetic impurities. *Physical Review B*, 63(18):180504, 2001.

[185] SA Carter, B Batlogg, RJ Cava, JJ Krajewski, WF Peck Jr, and LW Rupp Jr. Mechanism for the metal-insulator transition in $Sr_2Ir_{1-x}Ru_xO_4$. *Physical Review B*, 51(23):17184, 1995.

[186] P. Blaha, D. Kvasnicka K. Schwarz, G. K. H. Madsen, and J. Luitz. *WIEN2k, An Augmented Plane Wave + Local Orbitals Program for Calculating Crystal Properties.* Karlheinz Schwarz, Techn. Universität Wien, Austria, 2001.

[187] James F Annett. *Superconductivity, superfluids and condensates*, volume 5. Oxford University Press, 2004.

[188] Arumugam Thamizhavel, Tetsuya Takeuchi, Tomoyuki Okubo, Mineko Yamada, Rihito Asai, Shingo Kirita, Andrei Galatanu, Etsuji Yamamoto, Takao Ebihara, Yoshihiko Inada, et al. Anisotropic electrical and magnetic properties of CeTSb$_2$ (T= Cu, Au, and Ni) single crystals. *Physical Review B*, 68(5):054427, 2003.

[189] O Sologub, K Hiebl, P Rogl, H Noël, and O Bodak. On the crystal structure and magnetic properties of the ternary rare earth compounds ReTSb$_2$ with

Re=rare earth and T=Ni, Pd, Cu and Au. *Journal of alloys and compounds*, 210(1):153–157, 1994.

[190] H Flandorfer, O Sologub, C Godart, K Hiebl, A Leithe-Jasper, P Rogl, and H Noël. On the cerium valence in ternary compounds CeMSb$_2$ and CeM'Bi$_2$; $M=$ Mn, Fe, Co, Ni, Cu, Zn, Pd, Ag, Au and $M'=$ Ni, Cu, Zn, Ag. *Solid state communications*, 97(7):561–565, 1996.

[191] AM Strydomt and A Thamizhavel. The hall effect in quantum critical CeAuSb$_2$. In *Journal of Physics: Conference Series*, volume 273, page 012015. IOP Publishing, 2011.

[192] K-A Lorenzer, AM Strydom, A Thamizhavel, and S Paschen. Temperature–field phase diagram of quantum critical CeAuSb$_2$. *physica status solidi (b)*, 250(3):464–467, 2013.

[193] T Jeong. First-principles study on the electronic structure of CeAuSb$_2$. *Physica B: Condensed Matter*, 388(1):249–252, 2007.

[194] Paul C Canfield, JD Thompson, and Z Fisk. Novel ce magnetism in CeDipnictide and Di-Ce pnictide structures. *Journal of applied physics*, 70(10): 5992–5994, 1991.

[195] Nobuo Furukawa. Unconventional one-magnon scattering resistivity in half-metals. *Journal of the Physical Society of Japan*, 69(7):1954–1957, 2000.

[196] S Paschen. Hall effect for classification of quantum critical points. *Physica B: Condensed Matter*, 378:28–30, 2006.

[197] Qimiao Si. Global magnetic phase diagram and local quantum criticality in heavy fermion metals. *Physica B: Condensed Matter*, 378:23–27, 2006.

[198] SA Grigera, RS Perry, AJ Schofield, M Chiao, SR Julian, GG Lonzarich, SI Ikeda, Y Maeno, AJ Millis, and AP Mackenzie. Magnetic field-tuned quantum criticality in the metallic ruthenate Sr$_3$Ru$_2$O$_7$. *Science*, 294(5541): 329–332, 2001.

[199] Andreas W Rost. *Magnetothermal Properties Near Quantum Criticality in the Itinerant Metamagnet $Sr_3Ru_2O_7$*. PhD thesis, University of St Andrews, 2009.

[200] SA Grigera, RA Borzi, AP Mackenzie, SR Julian, RS Perry, and Y Maeno. Angular dependence of the magnetic susceptibility in the itinerant metamagnet $Sr_3Ru_2O_7$. *Physical Review B*, 67(21):214427, 2003.

[201] P Coleman, C Pépin, Qimiao Si, and Revaz Ramazashvili. How do fermi liquids get heavy and die? *Journal of Physics: Condensed Matter*, 13(35): R723, 2001.

[202] Philipp Gegenwart, Qimiao Si, and Frank Steglich. Quantum criticality in heavy-fermion metals. *Nature Physics*, 4(3):186–197, 2008.

[203] Y Tabata, DR Grempel, M Ocio, T Taniguchi, and Y Miyako. Non-fermi-liquid scaling in $Ce(Ru_{0.5}Rh_{0.5})_2Si_2$. *Physical Review Letters*, 86(3):524, 2001.

[204] PC Canfield and Z Fisk. Growth of single crystals from metallic fluxes. *Philosophical magazine B*, 65(6):1117–1123, 1992.

[205] Paul C Canfield and Ian R Fisher. High-temperature solution growth of intermetallic single crystals and quasicrystals. *Journal of Crystal Growth*, 225(2):155–161, 2001.

[206] MP Schwarz, D Grundler, I Meinel, Ch Heyn, and D Heitmann. Micromechanical cantilever magnetometer with an integrated two-dimensional electron system. *Applied Physics Letters*, 76(24):3564–3566, 2000.

[207] Lu Li. *Torque Magnetometry in Unconventional Superconductors*. PhD thesis, Princeton University, 2008.